A STUDY OF UNSTABLE AXISYMMETRIC SEPARATION IN HIGH SPEED FLOWS

by

Michael Allen Kenworthy

Dissertation submitted to the Graduate Faculty of the
Virginia Polytechnic Institute and State University
in partial fulfillment of the requirements for the degree of

DOCTOR OF PHILOSOPHY

in

Aerospace Engineering

APPROVED:

A. K. Jakubowski, Chairman

J. A. Schetz

S. Baranowsky

R. L. Whitelaw

L. W. Johnson

March 1978

Blacksburg, Virginia

ACKNOWLEDGEMENTS

In a work of this nature one finds oneself indebted to a considerable number of people. I would like to take this space to acknowledge my supervising professors at the von Karman Institute for Fluid Dynamics,

; and at Virginia Polytechnic Institute and State University, Professor A. K. Jakubowski.

For the conduct of the test phase of this study I owe a great deal of thanks to , Chief Test Engineer of the VKI Supersonic/Hypersonic Laboratory. Additionally, I received considerable support from my fellow students, now

.

I am also greatful for the support given to me by my employer, ENSCO, Inc., who among other things made available the services of , my able typist.

Finally, but certainly most importantly, I thank my wife for standing by me through it all or at least the worst.

TABLE OF CONTENTS

Page

LIST OF FIGURES AND TABLES

LIST OF SYMBOLS

A	constant of proportionality in the expression for free interaction
a	speed of sound
B	constant of proportionality
C	Chapman's constant
c	specific heat
c_p	pressure coefficient
D	body diameter
d	spike diameter
F	time averaged fraction
f	frequency
H	boundary layer shape factor $(\frac{\delta^*}{\theta})$
K	constant of proportionality
ℓ	spike length
M	Mach number
$\acute{m}$	mass
$\dot{m}$	mass flux per unit time
N	reattachment parameter
n	ratio of momentum thicknesses
O	oscillation
P	pulsation
P_{t_2}	pitot pressure
p	pressure

R	ratio of Reynolds number; gas constant
Re	Reynolds number
Re_D	Reynolds number based on body diameter
Re_u	unit Reynolds number
r	radial coordinate or distance
r_a	spike radius
r_{sh}	body shoulder radius
S	Strouhal number; stable
T	temperature
t	time
u	velocity in the x-direction
v	velocity in the y-direction or r-direction
W	shear layer width
X	transformed streamwise coordinate
x	streamwise coordinate
Y	transformed normal coordinate
y	normal coordinate
z	non-dimensional velocity
α	separation angle
β	$\sqrt{M^2-1}$ or shock angle
γ	ratio of specific heats
Δ	change between two states
δ	boundary thickness; small change

δ	boundary layer displacement thickness
ε	thin skin dimension
η	non-dimensional transformed normal coordinate
ζ	non-dimensional Mangler shear length
θ	boundary layer momentum thickness
λ	non-dimensional axisymmetric shear length
μ	viscosity
ν	kinematic viscosity
ξ	non-dimensional 2-D shear length
τ	non-dimensional time
ρ	density
Φ	after body angle
Φ_D	body cone angle

Subscripts

c	refers to capture area
c	refers to collapse of foreshock
crit	critical
D	refers to main body
d	refers to dead air or separated region
f	final conditions
i	initial conditions
i	index = 1 or 3
j	refers to dividing streamline
ℓ	refers to portion of shear layer below the dividing streamline

r	reattachment
r_{pot}	available at reattachment
ref	reference value
r_r	required at reattachment
s	refers to normal shock
sh	shoulder
sℓ	refers to normal shock in the lateral direction
u	refers to portion of shear layer above the dividing streamline
x	unknown
o	stagnation value evaluated on dividing streamline
1	undisturbed free stream
2	conical conditions downstream of separation; plateau
3	conditions behind a normal shock (pulsation) conditions behind a reattachment shock (oscillation)
4	matched conditions between an oblique and normal shock
∞	inviscid free stream value

1. INTRODUCTION

1.1 Purpose and objective

The present study deals with the unstable flow which has been observed to exist for certain families of bodies in supersonic and hypersonic flow. Details of studies of this phenomenon are given in the literature survey (section 1.2). The term 'unstable' as it is used in this study pertains to a deterministic time dependent flow and should not be confused with unsteady flow phenomema, such as turbulence, with are time dependent but highly random. At present there exists little understanding of the cause of unstable flow nor does there exist any means of estimating the disturbance in terms of frequency and pressure. This is largely due to lack of data as is brought in section 1.2.

The purpose of the present study was, therefore, two-fold. First an attempt was made to determine what mechanism or mechanisms cause these unstable flows to exist. For this purpose detailed experiments were performed which allow the identification of the important parameters involved. Second correlations were developed to make possible engineering calculations of unstable flow in terms of frequency and pressure.

To accomplish these objectives an experimental study of spiked cones was carried out. Since it was evident from previous studies (section 1.2) that the change in shock

envelope is directly related to the instability, spark photography was employed as a means of documentation. Because a time-dependent pressure field must be associated with these phenomena, the pressure was measured on the cone face in order to obtain the time-averaged parameters of frequency and amplitude. The effects of Mach and Reynolds number as well as cone angle and spike length were examined. The parameters body shoulder radius, r_{sh}, and spike tip cone angle α_s, were held constant. Experiments were also conducted on specific models (i.e. cone angle and spike length) to obtain detailed information of the cycle history.

In the following chapter the equipment, measurement techniques and experimental program are outlined. The third chapter contains the presentation and discussion of the results of the time-averaged measurements. In the fourth chapter, results of time-dependent experiments are presented and discussed in order to lay the foundation for the theoretical analysis of Chapter 5. Conclusions are drawn in Chapter 6, and in Chapter 7 is demonstrated the practical use of the present study by comparison with a study of the ablating re-entry shapes.

1.2 Literature survey

Flow instabilities have long been of concern to design engineers. With the advent of supersonic flight a

number of new examples have been observed. As early as 1944, shortly after the first supersonic tunnels became operational, Oswatitsch (Ref. 1) reported the occurrence of an instability in connection with axisymmetric diffuser inlets equipped with conical centerbodies shown in Fig. 1a. More recent research has shown that this phenomenon, termed "buzzing" by diffuser inlet designers, is not limited to axisymmetric inlets, but is also associated with scoop-type inlets and perforated convergent-divergent diffusers (Ref. 2). This instability is encountered, for example, when a ram jet operates at off-design conditions causing the movement of the diffuser normal shock.

It is readily apparent that this instability will decrease the performance of a propulsion unit as well as cause serious structural and combustion problems. A few general theories were put forward based on internal mass flow considerations, e.g., see Refs. 3 and 4. In reference 4, an attempt was made to predict the frequency of this instability using a modified Helmholtz resonator model. As Trimpi (Refs. 5 and 6) pointed out the ram jet was actually better suited to quasi-one-dimensional model, and in fact, this latter model was in excellent agreement with experimentally obtained data. Although this form of instability is not the same as that to be studied herein, the principal features are similar to those of the mode of

instability later to be called pulsation.

Re-entry into the earth's atmosphere involves very high rates of heat transfer. Studies have indicated that large nose radii were the most practical solution to this problem for typical ballistic missile flight envelopes (e.g. Refs. 8 and 9). This, however, causes an increase in the drag which is also an undesirable effect. During the early 1950's, when considerable attention was being given to this problem, a compromise was reached by placing a slender rod at the apex of blunt bodies to create a conical separated region. Flow about certain classes of these bodies, which have been termed "spiked blunt bodies" was observed to be unstable. Although not all spiked blunt bodies cause unstable flow, a comprehensive review of studies of these shapes will be given in the next few paragraphs to provide a more complete background.

Jones (Ref. 10) found that at Mach 2.72 drag on hemispheres was reduced substantially by means of spikes and that the lowest drag coefficient was obtained with the longest spike for which the free shear layer remained laminar (Fig. 1b). Beastall and Turner (Ref. 11) arrived at the same conclusions for Mach numbers between 1.5 and 1.8. In the latter study, flat faced cylinders were used as opposed to the hemispherical models used by Jones, and Beastall and Turner observed unsteady flow for certain spike lengths. Also of interest is the fact that the

flow tended to stabilize when the spike was capped with larger angle cones whose base diameters were much larger than the spike diameter.

Hunt (Ref. 12) likewise concluded that a spike placed on a hemispherical blunt body in Mach 1.6 to 1.8 flow reduced the drag and that the principal parameter affecting drag was the spike length. The main purpose of Hunt's investigation was to study the effects of incidence on this drag reduction device. He found that the spike became less effective as a means of drag reduction as the angle of incidence increased. The drag reduction decreased from 50% at zero incidence to 33% at 5° angle of incidence to 18% at 10° to only 5% at 20°. Hunt found the angle of the spike tip cone to have negligible effect on the drag reduction.

Chapman (Ref. 13) showed theoretically that for a two dimensional laminar separated flow the value of heat transfer in the separated region was reduced to 0.56 of the value of an attached boundary layer. In the same analysis he estimated a 40% reduction of effective skin friction. Noteworthy also is the fact that he predicted that a turbulent separated flow would increase the heat transfer rate significantly above that of a similar laminar flow. Experimental programs were then initiated to investigate the practical application of controlled regions of separation. Specifically, these investigations were concentrated

on spiked blunt bodies.

Among the earliest investigators into the question of the effect of spikes on the heat transfer rate, even before Chapman's work (Ref. 13) was published, were Stalder and Nielsen (Ref. 14). Working in a range of Mach numbers of 0.12 to 5.04 and Reynolds number based on the body diameter, Re_D from 1.55 to 9.85×10^5, they concluded that the addition of the spike doubled the average heat transfer rate on hemispherical bodies regardless of spike length. It is obvious from spark shadowgraphs of the models at a Mach number of 2.67 and Re_D of 7.09×10^5 that the shear layer is transitional. Judging from the order of magnitude of Re_D it is most likely that all these results were obtained under conditions such that the shear layer was transitional if not turbulent. Another interesting point brought out in this study was the fact that the increase in heat transfer occurred over the region extending from the stagnation point to 45°, which encompassed the separated region. They, as earlier investigators, found a pressure drag reduction of 45% for the best case.

Bogdonoff and Vas (Ref. 15) working at a Mach number of 14 and an Re_D of 5×10^5, found that the spike was indeed an efficient means of not only reducing drag but the heat transfer as well. Results of tests carried out using a model with a ratio of spike length to body diameter, $\frac{\ell}{D}$ of 4 showed that for a hemispherical blunt body the drag was

reduced to $\frac{1}{10}$ and heat transfer to $\frac{1}{5}$ of the respective values without a spike, while the flat faced model ($\Phi_D = 90°$) showed reductions to $\frac{1}{40}$ and $\frac{1}{2}$, respectively. It was pointed out that the reason for the overall reductions in drag and heat transfer was related to the state of the shear layer which was purely laminar.

Also reported by Bogdonoff and Vas (Ref. 15) were two distinct forms of unstable flow which are now considered the two important modes of unstable axisymmetric separation. Despite the fact that there exists a large number of differing descriptive adjectives for these two modes, they will be referred to in the present study as oscillation and pulsation. Bogdonoff and Vas identified the general physical features as follows. The oscillation mode is characterized by the change in the shape of the foreshock as it oscillates between a convex and a concave configuration as illustrated in Fig. 2. The pulsation mode is manifest somewhat more dramatically as an excursion between two very different shock envelopes as illustrated in Fig. 3. One envelope consists of a conical foreshock emanating from the spike tip and intersecting the bow shock created by the blunt body (Figs. 3a and 3b). The other envelope is a single bow shock passing through the spike tip (Fig. 3c).

Crawford (Ref. 16) carried out a study of spiked hemispheres at a Mach number of 6.8 and a range of Reynolds numbers from $0.12\times10^6 \leq Re_D \leq 1.5\times10^6$. This allowed an investigation of the three cases of laminar, transitional and turbulent flow over the separated boundaries. Results showed that for the turbulent case, the total heat transfer to the model doubled in contrast to the laminar case which showed a decrease of approximately 50%. For transitional flow the heat transfer was a function of the position of the onset of transition. Once again the pressure drag was reduced in all cases as had been observed by previous investigators.

More recently, Holden (Ref. 17) has measured the heat transfer rates on spiked cones (Fig. 1c). Results of this study at Mach 10 showed that the most important factor which influences the total heat transfer to the body is the position of the point of shear layer reattachment. That is, for face reattaching flows the maximum total heat transfer increases with increasing reattachment angle. As had been observed previously, this can more than double the total caloric input in the worst case. In contrast it was seen that for shoulder reattachment the total heat transfer decreased with increasing spike length, reaching values as low as 20% of the unspiked values. It is important to note that these models are extremely yaw sensitive and any asymmetry in the flow produces very

large local heat transfer rates in the reattachment region. Also documented in this study were the unstable flows by this time recognized to occur with spiked blunt bodies. These results will be discussed later in detail.

Despite the now apparent disadvantages of using spikes as heat shields and drag reduction devices, other needs have spurred investigation in this field. For instance, Album (Ref. 18) and Wyborny (Ref. 19) have studied the effect of incidence on the aerodynamic coefficients on spiked blunt bodies. Findings in these two studies showed promise in using a spike as a means of aerodynamic control.

As flights in the high supersonic regime became routine, interest arose concerning the use of parachutes for stabilizing pilot ejection capsules and recovery of expensive test vehicles. Interest was further stimulated as parachutes were to be used in recovery of near space probes and satellites. Roberts (Ref. 20) and Maynard (Ref. 21) noted the presence of unstable flow seen by researchers of the spiked blunt body problem. This prompted work to be carried out at the Weapons Research Establishment, Australia which will be discussed later.

Studies made of entry vehicles for an unmanned Mars landing mission are usually aimed at satisfying two primary criteria. These are high drag characteristics to make use of the thin Martian atmosphere in braking and a lightweight

structure able to withstand the large impulsive loads encountered during such a maneuver. One class of shapes which seems to fulfill these criteria rather well is a bell shape known as a tension shell illustrated in Fig. 1d. Jones, Bushnell and Hunt (Ref. 22) found during their investigation of these shapes an unstable flow pattern characteristic of spiked blunt bodies.

Recently there has arisen evidence that these same flow instabilities may occur on a certain family of ablation shapes (Ref. 23). These particular shapes are formed during the high Reynolds number portion of re-entry when the boundary layer on the hemispherical nose experiences transition from laminar to turbulent flow. This causes the peak heat transfer rates to occur away from the stagnation point. On ablative surfaces the result is a concave conical shape as illustrated in Fig. 4, which in fact, resembles approximately the spiked blunt body. Studies of these shapes by Kenworthy and Richards (Ref. 24) and Abbett, Cooper and Dahm (Ref. 25) show that indeed flow instabilities similar to those of spiked blunt bodies do exist. This topic will be discussed in the final chapter.

In the references cited thus far with the exception of the diffuser buzzing problem, the phenomenon of unstable flow was considered to be an observation of secondary importance to the main study. There exists,

however, a limited number of investigations directed primarily at the topic of the unstable flow of spiked blunt bodies. The first of these appeared in 1952 by Mair (Ref. 26) who investigated the flow over spiked hemispheres, flat cylinders and a two dimensional equivalent model at a Mach number of 1.96 and an Re_D of 1.64×10^5. Under these conditions Mair found unstable flow for $\frac{\ell}{D} \leq 1.5$ and $\Phi_D = 90°$. Using various diagnostic techniques he accurately pieced together the history of the shock pattern from random spark photographs for a cycle of the pulsation mode. One important point brought out in this work was the fact that as the expanded foreshock collapses it is only a weak disturbance and a new bow shock is created as though the model were being impulsively started. Unfortunately for subsequent investigators Mair used the term oscillation for this phenomenon, and since he was working at a relatively low Mach number, he was not aware of the existence of the second mode which is now described as an oscillation. Mair also made an estimate of the frequency which yielded a Strouhal number, $\frac{fD}{u_1} = 0.12$.

Maull (Ref. 27) examined, for the hypersonic case M = 6.8, the region of reattachment in order to explain these flow instabilities. He found that rounding the shoulders stabilized the flow. That is, for the flat faced cylinder, $\Phi_D = 90°$, if the shoulder radius was zero,

there existed a relatively large range of $\frac{\ell}{D}$ for which the flow was unstable. As the shoulder radius, r_{sh}, was increased this range rapidly diminished, and at a value of r_{sh}/D somewhat less than $\frac{1}{2}$, a hemisphere, the flow was stable for all $\frac{\ell}{D}$ (see Fig. 5). This is in agreement with all previous work. Also presented was a very good idea of the influence of Mach number on the boundary between the oscillation mode and stable flow (see Fig. 6). Maull failed to make the distinction between different modes of instability, and, in fact, clouded the picture by labelling all unstable flow as "oscillation". He did, however, provide a good deal of insight into the driving mechanism behind pulsation by showing that the pressure imbalance caused by the strong shock-weak shock intersection would cause a mass reversal into the conical separated region. To substantiate this concept Maull showed that a shock pattern similar to that of the enlarged conical foreshock could be produced by a jet of air injected from the face of the cylinder into the incoming main stream. Maull also made an estimate of the frequency involved and arrived at a value of Strouhal number of 0.23, somewhat above Mair's estimation.

Wood (Ref. 28) showed there were five distinct types of flow over spiked cones depending on the cone apex half angle, Φ_D, and of course, a region of unstable flow which

occurred only for cone angles greater than the shock detachment angle. Here again, Wood considered all forms of instability as "oscillation". However, a number of interesting points were brought to light in this paper. Reattachment was strongly influenced by the body temperature, as was seen by the use of heated model. The hot model caused reattachment to move downstream to the shoulder. Two means of stabilizing, i.e., reducing the range of unstable flow parameters, were reported. The first was simply modifying the shoulder as had been observed earlier. The second was the injection of a small mass flow into the dead air region. Finally, Wood showed that the stable separated region could in reality be considered a dead air region by placing a spoiler disc in this region without altering the external flow pattern.

As was mentioned earlier, basic work was carried out to explore the use of conventional parachutes in supersonic flow. Robinson et al. (Ref. 29) conducted the first experiments designed to measure frequencies and amplitudes of instability. They arrived at the conclusion similar to that of Maull that the onset of instability occurs when the angle required to turn the separated flow parallel to the model face exceeds the shock detachment angle. A further condition is derived by considering the behaviour of the shock extremity, i.e., in the region of

reattachment, as the flow approaches the stable state. Results of calculations based on these assumptions are shown in Fig. 8. These results contradict those in Fig. 6. This is because Fig. 6 is the stability boundary between stable flow and oscillation while Fig. 8 exhibits the upper boundary of pulsation. Robinson et al. also reported a hyperesis effect in that the location of the pulsation upper boundary depended on whether one approached it by increasing or decreasing the spike length. The range of $\frac{\ell}{D}$ which caused pulsation did, however, decrease with increasing Mach number up to 2.8. The effects of spike diameter, d, as well as tip configuration were also investigated. Results showed $\frac{d}{D} \leq 0.25$ had little effect on the stability boundaries, but for $\frac{d}{D} \geq 0.5$ the spike diameter became an important parameter. Spike tip effects seemed to depend primarily on tip base diameter. The flow instability was most severe for the spike tip with diameter equal to the spike diameter. This was in agreement with Ref. 11. Also shown in this work was the effect of spike length on amplitude and frequency of instability which will be compared later with the results of the present study.

Holden (Ref. 17) also included information pertinent to the basic study of spiked blunt bodies. Diagrams similar to Wood's $\frac{\ell}{D}$ vs Φ_D plot were obtained at Mach numbers of 10 and 15 with an Re_D of 0.27×10^6. These are

shown in Fig. 9. Note the existence of six flow regimes. Holden documented both the oscillation mode which he labels type D flow, and the pulsation mode, type E. The existence of oscillation as an isolated region is most likely due to the experimental techniques and insufficient incrementing of parameters used to obtain the $\frac{\ell}{D}$ vs Φ_D plots. This point will be treated in detail later. Also shown in this work is the fact that oscillation is not only a change in the inflection of the separated region but a movement of the point of separation as well. This is an important point to remember when theoretically treating this phenomenon.

Finally, Kabelitz (Ref. 30) treated the spiked blunt body problem by a perturbation method applied to a simplified model of the stationary separated flow. That is, the driving mechanism was assumed to be entrainment by the shear layer which caused the separation and transition point to move forward. Although this is a valid effect of the instability and will, therefore, agree up to a point with the experimental trends, it cannot deal with either mode entirely satisfactorily. Kabelitz attempted for the first time to systematize the results of previous investigations, and he arrived at the conclusion that there existed three modes of instability: pulsation, oscillation and vibration. Of these he found the latter two to behave

in essentially the same manner and thus his findings are in agreement with those of Bogdonoff and Vas (Ref. 15).

2. EXPERIMENTAL APPARATUS

In this chapter are described the wind tunnels, models, instrumentation and test program of the experimental portion of the present study. Also given is a discussion of experimental uncertainty.

2.1 Test facilities

In order to examine experimentally the effect of Mach number on unstable axisymmetric separation tests were conducted in supersonic, S-1, and hypersonic, H-3, wind tunnels described in this section.

2.1.1 Hypersonic wind tunnel, H-3

The VKI hypersonic wind tunnel, H-3, is a blowdown facility with run times of up to five minutes. The flow is formed in an axisymmetric contoured nozzle yielding a uniform free jet 12 cm in diameter with a Mach number of 6.0 (Ref. 31). The test gas is air with maximum reservoir pressure of 4×10^6 N/m^2 and maximum reservoir temperature of 500°K. The free stream unit Reynolds number may be varied between 6×10^6/m and 36×10^6/m.

The open jet test section is located in a chamber which is evacuated to a pressure approximately equal to the free stream static pressure by means of a supersonic ejector. Models are mounted on a precision three-degree of freedom mechanism (pitch, yaw, and axial translation)

which in turn is attached to a rapid injection system. The test chamber incorporates large windows (30×50 cm) allowing optical visualization of the flow.

2.1.2 Supersonic wind tunnel, S-1

The VKI supersonic wind tunnel S-1 is a continuous closed circuit facility of the Ackeret type, driven by a 615 kW axial flow compressor. A silicagel dryer maintains the humidity level of the air during a run below 200 ppm at a stagnation pressure as low as 10^4 N/m^2. The stagnation pressure may be varied between 10^4 and 2.5×10^4 N/m^2. Stagnation temperature is approximately room temperature yielding a range of free stream unit Reynolds numbers between 1.1×10^6/m and 2.6×10^6/m at a nominal Mach number of 2.25.

The test section measures 40 cm × 40 cm and contains a precision three-degree of freedom traversing mechanism for model and/or probe support, as well as a variable incidence mechanism. The tunnel is equipped with two nozzle blocks which create nominal free stream Mach numbers of 2.0 and 2.25. Windows with diameters of 30 cm allow flow visualization to be made.

2.2 Models

During the present experiments two models were used. This was necessary for two reasons. First, the large model

(see 2.2.1) blocked the hypersonic wind tunnel for a range of $\frac{\ell}{D}$. Secondly, the use of two models increases effectively the range of Reynolds numbers of a wind tunnel. The important features of these models are given in this section.

2.2.1 Large model (D = 46 mm)

The "large" model was a 46 mm cylinder constructed of stainless steel 160 mm in length (Fig. 10). A set of seven interchangable conical noses was available with cone half angles from 30° to 90° in increments of 10°. The shoulder radius was zero. The noses were made of brass cylinders 94 mm long which were joined with the main body. The first large disturbance, i.e., the model support, was more than 3 body diameters (> 100 boundary layer thicknesses) downstream of the shoulder precluding any possibility of upstream influence.

Each nose was equipped with pressure transducer mounts for a Kistler and PCB transducer (see section 2.3.1). The pressure ports (1 mm in diameter and of the order of 1 mm in length depending on the cone half angle) were at a radial distance of 11.5 mm on the face 180° from one another. The port axis was parallel to the free stream direction for all nose sections. The resonance frequencies calculated for this type of port, taking into account the chamber volume of the transducer and viscous effects (Ref. 32), was just above 100 kHz. At the same radial position a chromel-alumel thermocouple was flush-mounted 90° from either pressure port.

Each nose tip was machined to accomodate an 8 mm diameter teflon center piece which served three purposes. First, it allowed one to change spike diameter by fabricating two or more center pieces for each cone half angle. Second, the teflon provided a pneumatic seal between the high pressure region in front of the face and the relatively low pressure region in the body interior (approximately equal to the wake pressure) and at the same time allowed the spike to move longitudinally. Third, the center piece isolated electrically the thin film gauges circuit from the metallic body.

The spike length could be changed continuously by means of a high speed motor at a speed of 1 cm/sec for a total change in length of 4 cm. A precision potentiometer ($\pm$ 0.1% full scale linearity) was incorporated in the transmission system to monitor the spike length with a digital voltmeter. Spike displacement could be recorded with an accuracy of $\pm$ 0.1 mm.

Two types of spikes were used. For the most part these tests were carried out using 3 mm diameter stainless steel rods ($\frac{d}{D}$ = 0.065) capped with a 15° half angle cone. A limited number of tests were conducted with 2.3 mm diameter ($\frac{d}{D}$ = 0.05 pyrex glass spikes also capped with 15° half angle cones.

2.2.2 Small model (D = 20 mm)

The "small" model was a 20 mm diameter brass cylinder 110 mm in length terminating with a 30 mm contoured boattail (Fig. 11). A set of seven conical brass noses were constructed with cone half angles from 50° to 90° in increments of 10° with two additional cones at 75° and 85°. Each nose added 5 mm to the overall length. The support was fixed 60 mm or more than 100 boundary layer thicknesses downstream of the cone apex to prevent upstream influence from the support.

Each conical nose contained a ported pressure mount on the face for the PCB transducer (see section 2.3.1) at a radial position of 5 mm with the port axis perpendicular to the surface. The pressure ports were 1 mm in diameter and approximately 1 mm in length. The calculated resonance frequency for this configuration including transducer chamber volume and viscous effects is slightly over 100 kHz (Ref. 32). A flush-mounted alumel-chromel thermocouple was installed.

The spikes used with this model were 1 mm drawn steel and were capped similarly to the spikes used with the large model, i.e., 15° half angle cones. In addition each interchangeable nose was equipped with a spike whose tip half angle, α_s, equalled the nose half angle, Φ_D ($\alpha_s = \Phi_D$). This spike was used for the case of $\frac{\ell}{D} = 0$ for its respective nose.

2.3 Model instrumentation

Due to the nature of the instabilities the instrumentation was required to be fast responding and extremely sensitive as well as robust. It was felt necessary in order to obtain a better understanding of these complex flows that both the frequency and some characteristic amplitude be measured over as much of the flow field as possible. Use was made of extensive experience in finally choosing the PCB pressure transducer which met all requirements for the measurement of the pressure at the model face. Platinum thin film gauges were chosen to obtain measurements of the streamwise elements of the flow fluid.

2.3.1 The PCB pressure transducer

The PCB pressure transducer employs the piezoelectric principle with a built-in low noise amplifier (integrated circuit) which accomplishes several ends at once. First, it yields a high signal-to-noise ratio, and moreover, a high level voltage output. Also inherent in this system is a fixed voltage sensitivity independent of cable length or capacitance and hence, cable movement. Thirdly, the low output impedance allows direct input into most readout instrumentation. Further, an integral accelerometer minimizes vibration sensititity and a discharge resistor automatically eliminates steady (d.c.) signal components. Therefore, this transducer was used almost entirely throughout the H-3 and S-1 test series.

Except for the earliest tests, the PCB model 112A21 quartz minigauge was employed. This gauge measures dynamic and sound pressure from 7×10 N/m^2 to 1.5×10^6 N/m^2. A sensitivity of 7.5×10^{-3} mV/N/m^2 is achieved by supplying an excitation voltage between $\pm$18 to 24 VDC at a 2 to 20 mA. This gauge has a resolution of 30 N/m^2 with 1% linearity. The acceleration sensitivity is rated a 1.5×10^{-9} N/m^2/g. The gauge itself has a pressure sensitive area 5.6 mm in diameter and an overall length including amplifier of 35 mm.

2.3.2 Platinum thin film gauges

For the purpose of documenting streamwise gradients a set of pyrex glass spikes were fabricated (see section 2.2.1). On these spikes were placed platinum thin film gauges. These gauges are rather sensitive means of measuring either surface temperature (resolution to the order of 0.01°K) or by means of analog circuits heat transfer rates (Ref. 33). For the purposes of the present work these were used in the thermometer mode.

The gauges themselves are simply a film of platinum which is diffused into the glass by raising its temperature to the softening temperation (~ 680°C). This creates a film of a good thermal conductor on a poor thermal conductor. Hence any change in surface temperature is indicated by a change in the resistance of the thin film of platinum. To measure this change in resistance each gauge was supplied

by a constant current of 1.5 mA obtained using a 500 VDC power supply in series with a 330 K ohm resistance. Since the resistance of each individual gauge was of the order of 100 ohm at room temperature and 150 at 200°C, even large changes in temperature would not affect this constant current supply. Note also this current was selected so that film temperature changes due to resistive heating would be negligible.

The leads along the glass spike were made with a silver paint baked on at a somewhat lower temperature than was used with the platinum (~ 500°C). The resulting resistance was of the order of one ohm. To these were soldered flexible wire leads to complete the circuit.

2.4 Flow visualization

In addition to measurement of the pressure on the model face several flow visualization techniques were used. These included both photographic and sublimation techniques outlined in this section.

2.4.1 Optical system

During the present work extensive use was made of the schlieren system installed in each tunnel. The S-1 installation used a single pass beam of collimated light which may be either continuous or spark generated (see section 2.4.2). In these tests only spark schlierens were obtained. In S-1

this was necessitated by the low density of the flow and the shock system being axisymmetric. A powerful light source was used in order that the optical system could be rendered very sensitive by using 80% to 90% cut-off with a knife edge.

The H-3 optical system is a double-pass system. A mirror, installed in the test chamber just outside of the free jet, reflects a point light source to an identical point which is then processed either as a focused shadowgraph or a schlieren. This double pass system is used because of its superior sensitivity; however, it suffers from the fact that a slight double image is created in the plane perpendicular to the plane of the light path.

2.4.2 Light sources

The light source used in the H-3 tunnel was a commercially available spark gap unit[1] of the arc discharge type stabilized by an argon jet. The spark energy was 1.25 joules with a duration of less than one microsecond. Also available in the same light source was a continuous lamp of 150W focused to a point in the anode gap of the arc discharge.

The light source used in the S-1 tunnel was also of the arc discharge type with a duration assessed at 1 μsec. This source was much brighter than the previously described

[1]Manufactured by Ernest Turner Electrical Instruments; Ltd, HIgh Wycombe, Bucks, England, RP 10845.

source. The least sensitive film available (400 ASA) was far too sensitive and therefore necessitated either filters or large cut off using a knife edge. This was also necessary to make the system sensitive enough to detect axisymmetric shocks since the optical system is focused in a plane coincident with the center line of the tunnel.

2.4.3 High speed film techniques

High speed films of flow instabilities were made with a 16 mm Kodak high speed camera with its rotating prism shutter removed. This modification was made since the camera was limited to a framing rate of 1500 per second. The camera was then employed in two distinctly different modes.

First, it was used in conjunction with the multiple spark source described in the previous section. That is, the camera was brought up to a speed of approximately 15 meters per second and then the multiple spark was discharged at a prescribed rate. The result was a shigh speed film of discrete images with sharp resolution due to short film exposure times.

The second technique, known as a streak technique, is somewhat analogous to a strip chart recorder as illustrated in Fig. 12. A continuous 150W light source replaces the spark source in the optical system and the

camera operates without a prism or shutter. The flow field is completely masked except for a slit 1 mm wide parallel to the spike and a distance of $\frac{D}{4}$ from it. The pulsating normal shock is seen as a dark point and acts effectively as a pen as the film moves at a right angle to the slit.

2.4.4 Sublimation technique

The use of the sublimation technique to identify regions of high shear and heat transfer rates is a standard tool in supersonic and hypersonic research. The model is first darkened with any suitable tooling dye and then sprayed with acenaphthene to obtain a uniform white coating. The acenaphethene layer, when exposed to areas of high shear and heat transfer, readily sublimates exposing the contrasting under-surface.

2.5 The synchronization technique

In order to obtain the data necessary to construct analytic models for the unstable spiked body problem, the spark photographs and the oscillograms of the pressure transducer output were synchronized. This was accomplished by means of the electro-mechanical system shown schematically in Fig. 13.

The system is activated by means of a double switch which when closed completes two circuits. One circuit triggers the oscilloscopes and at the same time initiates

a delay unit. The delay unit, after a prescribed period of time, approximately 0.5 ms, emits an electrical pulse causing the spark source to discharge. This discharge or spark which is the light source for the optical system is sensed by a photomultiplier whose signal is recorded on one of the two channels of the oscilloscope, thus documenting the precise position in the pressure wave when the photograph was taken. The second circuit activates the event markers of strip chart recorders used to record the tunnel reservoir conditions. This in conjunction with the tunnel calibration enabled one to take into account variations in reservoir conditions through non-dimensionalizing the data.

2.6 The test matrix

The experimental program was carried out in three series of tests.

The first series was conducted at a Mach number of 6.0 and a nominal free stream unit Reynolds number of 20×10^6 /m using the large model (D = 46 mm) which yielded a Reynolds number based on body diameter, Re_D, of 0.9×10^6.

The second series was also a Mach 6.0 flow but with a free stream unit Reynolds number of 6.5×10^6 /m employing the small model (D = 20 mm), resulting in an Re_D of 0.13×10^6. This test series forms the nucleus of the present study.

A third series was carried out at a Mach number of 2.21 with a free stream unit Reynolds number of 1.1×10^6 /m and 2.6×10^6 /m using the large models of the first series which resulted in Re_D's of 0.05 and 0.12×10^6.

These test series will be referred to as series I, II and III, respectively. The test conditions are summarized in Table 1.

2.7 Experimental uncertainty

The measurement of the principal parameters varied during the experimental portion of the present study involved the following error bounds:

a) geometric parameters of the model:

spike length, ℓ,	$\pm$0.1 mm
body diameter, D,	$\pm$0.01 mm
body cone half angle, Φ_D,	$\pm$0.2°

b) free stream and reservoir conditions:

Mach number, M	
H-3 (M_1 = 6.0)	$\pm$0.05
S-1 (M_1 = 2.21)	$\pm$0.01
reservoir pressure, p_{01},	
H-3	$\pm10^4$ N/m^2
S-1	$\pm10^2$ N/m^2
reservoir temperature, T_{01},	$\pm$5°K

TABLE 1 - TEST CONDITIONS

Series Number	M_1	D (mm)	Re_D	Range of ℓ/D	$\Delta\ell/D$ min.	Range of ΦD	$\Delta\Phi D$ min.	d/D	α_s
I	6.0	46	0.9×10^6	0-3	0.1	30^o-90^o	10^o	.065, .055	15^o
II	6.0	20	0.13×10^6	0-3	0.05	50^o-90^o	5^o	.05	15^o
III	2.21	46	0.12×10^6	0-3	0.1	30^o-90^o	10^o	.065	15^o
	2.21	46	0.15×10^6	0-3	0.1	30^o-90^o	10^o	.065	15^o

The resulting uncertainty in the free stream quantities of interest are given in Table 2.

The uncertainty in the measurement of the pressure wave is composed of three parts as shown in Table 3.

A summary of the uncertainties in the principal parameters of each test series is given in Table 4.

TABLE 2 - FREE STREAM UNCERTAINTY

Series Number	Re_u	u_1	P_{t_2}
I	±2.5%	±0.6%	±4%
II	±3.5%	±0.6%	±5%
III	±2.5%	±0.8%	±3.5%

TABLE 3 - PRESSURE WAVE UNCERTAINTY

	Frequency, f	Amplitude, Δp
Transducer calibration	0 [1]	2.5%
Oscilloscope calibration	1.5%	1%
Data reduction	0.5%	1%
Total	2%	4.5%

[1] Since the resonance frequency of the PCB gauge as specified by the manufaturers and also that of the port were one to two orders of magnitude above the frequencies of interest, uncertainty in the response was assumed negligible.

TABLE 4 - A SUMMARY OF EXPERIMENTAL UNCERTAINTY

Series Number	$\frac{\ell}{D}$ [2]	Φ_D	M	Re_D	$S=\frac{f_D}{u_1}$	$\frac{\Delta p}{P_{t_2}}$
I	±0.2%	±0.5%	±1%	±2.5%	±3%	±8.5%
II	±0.5%	±0.5%	±1%	±3.5%	±3%	±9.5%
III	±0.2%	±0.5%	±1%	±2.5%	±3%	±8%

[2] At $\frac{\ell}{D} = 1$

3. TIME AVERAGED EXPERIMENTAL RESULTS AND DISCUSSION

This chapter will present and discuss the experimental results in the form of time-averaged frequency and amplitude of the pressure field measured at the cone model face as a function to spike length, body cone angle, Mach and Reynolds numbers. Based on both the findings of Kabelitz (Ref. 30) and those of the present study, a system of classifying the modes of unstable axisymmetric separation is established. Following this a discussion is made first of the frequency and then pressure wave amplitude for each mode and important points are summarized in the final section.

For these discussions use will be made of smooth curves fitted using the least mean squares method to the mean values with bars indicating one standard deviation (see section 3.1). All data are given for reference in Appendix A in accordance with the series number outlined in section 2.6.

3.1 Data reduction and analysis

Previous investigations of unstable axisymmetric separation flow have reported that the phenomenon is periodic, e.g. Robinson et al. (Ref. 29) and Kabelitz (Ref. 30), which suggest treatment of the data by "time averaging". However, due to the nature of separated flows,

one would not expect this phenomenon to be purely periodic, and therefore, it is necessary to establish an appropriate method of data reduction and to evaluate the periodicity or coherency of the wave forms associated with these unstable flows.

It was found by sampling a large number of the pressure waves obtained that, in fact, there exists a primary frequency and an associated amplitude for each configuration studied (Figs. 14, 15, 16). Based on this observation the process of "time averaging" was approximated by the arithmetic mean of the appropriate quantity. In the case of frequency this was done by measuring the time required for a known number of cycles and dividing this time by the number of cycles to obtain the mean value. The process of obtaining the mean value of amplitude was somewhat more difficult since neither the values at the peaks or troughs were repeatable in all cases. This was overcome by measuring the vertical distance from the first discernable trough to the adjacent peak; then the vertical distance from the peak to the next trough and so on as illustrated in Fig. 17. These distances were summed and divided by the total number of measurements to obtain the mean value of amplitude.

Next it was possible to ascertain the repeatability of these wave forms and hence the validity of the use of their "time averaged" frequency and amplitude in the study

of unstable flow. This was done by calculating the standard deviation, σ, which is the rms error of the raw data relative to the mean value. In the case of frequency this meant measurement of the time of each individual cycle making up the overall sample measured to obtain the mean value.

A measurable pressure fluctuation was observed for unspiked models and models with spike lengths well beyond the stability boundary, i.e., stable conditions. This will be referred to as background noise since these configurations are nominally stable. The σ for these oscillograms was typically 50% of the mean value. Also the frequency was at least 50% above that of the unstable flow while the amplitude was one half to a third of the smallest unstable amplitude. The cause for these fluctuations is not readily apparent since calculations showed that the resonance frequency of the ports and pressure transducer cavity for small amplitude forced oscillation to be of the order of 100 kHz (Ref. 32). It is possible, however, that these ports operated as Helmholtz resonators to flow parallel to the model face. That is, the ports may be considered analogous to the side duct in a pipe flow which will amplify certain frequencies depending on the orifice and volume of the side duct. In fact, calculation of these "favored" frequencies based on the port diameter and cavity volume showed good agreement with the measured mean

value of the background noise.

In the regime of unstable flow the frequency of the pressure wave was characterized by a σ representing 5% of the mean value and the amplitude by 10%. Two small ranges of parameters generated unstable flows characterized by σ of between 20% and 30% of the mean value. From this one may conclude that the use of "time-averaged" or mean parameters is a valid approach in the analysis of unstable axisymmetric separated flows.

3.2 Classification system

A summary of the results of pressure wave amplitude measurements obtained during the Series II tests ($M_1 = 6.0$, $Re_D = 0.13 \times 10^6$) is shown in Fig. 18. Two distinctly different modes of unstable flow are observed, characterized by dramatically different levels in amplitude and separated by a well defined boundary. Furthermore, each mode has direct correspondence with one of the two different types of shock envelope extremes shown in Figs. 2 and 3. The lower level pressure amplitude is always present when the oscillating envelope (Fig. 2) is observed and the higher pressure levels are present only when the pulsating envelope is observed (Fig. 3). These observations are basically the same as those summarized by Kabelitz (Ref. 30). Therefore, flows of the first type will be called oscillation and those of the second type pulsation. The following sections

will present a detailed discussion of the pressure wave frequency and amplitude in each of these two regimes.

3.3 The upper boundary of oscillation

As the boundary between stable flow and oscillation, denoted as O/S, is approached from the stable regime by decreasing the spike length, the length of attached boundary layer decreases (Fig. 19). This observation was also made by Hunt (Ref. 12) and Crawford (Ref. 16). When the separation point reaches the spike tip, the conical foreshock is observed to ripple as shown in Fig. 19c. At this same point pressure measurements made on the model face begin to show a regular wave form with a definite frequency and amplitude. It was observed that the onset of oscillation was coincident in all cases with the establishment of leading edge separation. This is an important point, use of which will be made in the analysis of oscillation.

The precise value of $\frac{\ell}{D}$ at the O/S boundary, denoted $\frac{\ell^*}{D}$, is difficult to determine due to the relatively small difference between the amplitude of the oscillation pressure wave and the background noise in this region (see section 3.1 for a discussion of background noise). Also the pressure waves near the O/S boundary were not generally as coherent or repeatable as those observed well away from this boundary. In Fig. 20 is shown the O/S boundary as determined in the present study. Note that this is simply

the $\frac{\ell}{D}$ vs Φ_D plane of Fig. 18. The uncertainty of the value of $\frac{\ell^*}{D}$ is denoted by the vertical bars at each Φ_D studied. The uncertainty increases with decreasing Φ_D. It is interesting to note that for $\Phi_D \geq 75°$, $\frac{\ell^*}{D}$ is a relatively weak function of Φ_D.

These results agree well with those of Maull (Ref. 27) who found the boundary between stable and unstable flow, assumed here to be the same as the O/S boundary, to correspond to $\frac{\ell^*}{D} = 2.5$ for $\Phi_D = 90°$ in a Mach 6.8 free stream (Figs. 5 and 6). Investigations by Wood (Ref. 28) and Holden (Ref. 17) show results in good agreement with the present study with the exception that $\frac{\ell^*}{D}$ was reported to be zero at the shock detachment angle. This point is discussed in section 3.4.1.5. The rate of decrease in $\frac{\ell^*}{D}$ found by Wood (Fig. 7) shows good qualitative agreement with the present study. The interpretation of Holden's results (Fig. 9) is more difficult due to the existence of two regions of unstable flow which he neglected to distinguish between. However, the region of "D" oscillation indicates that $\frac{\ell^*}{D}$ is a weak function of Φ_D for $\Phi_D > 75°$ as was found in the present study.

Also shown in Fig. 20 is a broken line curve representing the O/S boundary based on an effective spike length. The effective spike length is the distance from the spike tip to the body shoulder parallel to the model axis. This,

in effect, presumes the conical portion of the body to be part of the "dead" air in the separated region. The O/S boundary is seen to correspond very nearly to a constant value of the effective $\frac{\ell^*}{D}$ for $\Phi_D \geq 75°$. This suggests that the onset of unstable flow is connected with a certain distance between the spike tip and model shoulder. Use will be made also of this point in the analysis of oscillation.

3.4 Discussion of the oscillation pressure wave

In this section are discussed the time averaged parameters of the oscillation mode, pressure wave frequency and amplitude.

3.4.1 The frequency of oscillation

Herein are presented the experimental findings of the effect on the frequency of the oscillation mode of the parameters; spike length, body cone angle, Mach number and Reynolds number.

3.4.1.1 The effects of model geometry

The plot of frequency in the form of Strouhal number ($S = \frac{fD}{u_1}$) versus the non dimensional spike length, $\frac{\ell}{D}$, in Fig. 21 shows the effect of model geometry on the frequency of oscillation for body cone angles greater than or equal to 75° at a free stream Mach number of 6.0 and a Re_D of 0.13×10^5 (Series II).

Kabelitz (Ref. 30) presents an oscillation wave ($M_1 = 8.8$, $Re_D = 0.37\times10^6$, $\Phi_D = 90°$, $\frac{\ell}{D} = 1.5$) with a Strouhal number of approximately 0.12. This agrees to well within the bounds of experimental accuracy with the present study.

There is a tendency for the larger Φ_D's to have somewhat higher frequencies than the lower. In particular $\Phi_D = 90°$ is generally 5% above $\Phi_D = 75°$ at all $\frac{\ell}{D}$'s for which oscillation was present for both models. However, within the limits of the experimental error, one may say that frequency is independent of Φ_D for $75° < \Phi_D \leq 90°$. Included in Fig. 21 is a hyperbolic curve which was adjusted to fit the extremes of the data. This curve is given by the equation

$$(\frac{\ell}{D})(S-0.03) = 0.14 \qquad (3.1)$$

3.4.1.2 Reynolds number effects

Figure 22 shows the oscillation Strouhal number of the Mach 6 data with $Re_D = 0.9\times10^6$ to agree well with Eq. 3.1 which represents the summary of data obtained at the same Mach number with an Re_D seven times smaller. The significance of the Reynolds number difference becomes apparent on comparing Figures 2 and 23 which are representative of their respective Reynolds numbers. The focussed shadowgraph of Fig. 2 shows the shear layer as a well defined white line throughout its entire length which

is generally accepted as proof of laminar flow. In contrast Fig. 23 shows the shear layer experiences transition soon after separation.

Thus, one may conclude that within these limits Reynolds number has no measurable effect on the frequency of oscillation regardless of the state of shear layer.

3.4.1.3 Mach number effects

To date the oscillation mode has been reported to exist only in hypersonic free streams. However, during the course of experiments at a free stream Mach number of 2.21, oscillation was observed only for the conditions $0.80 \leq \frac{\ell}{D} \leq 1.05$ and $\Phi_D = 70°$. An example is shown in Fig. 24. It is obvious that the range of model parameters which produce oscillation is greatly reduced at moderate supersonic Mach numbers relative to hypersonic Mach numbers and this in turn explains the lack of previous mention of this mode in the supersonic range.

In Fig. 25 sample Strouhal numbers obtained from pressure waves corresponding to the oscillation mode described above are compared with Eq. 3.1. The value of σ (see section 3.1) was 20% of the mean value which means that the oscillation pressure waves at supersonic speeds are not as coherent as at hypersonic speeds, and hence, one is limited to the conclusion that the Strouhal number of oscillation at supersonic speeds agrees approximately with that at hypersonic speeds.

3.4.1.4 Oscillation at Φ_D below 75°

Illustrated in Fig. 26 is the effect of model geometry on the frequency of oscillation for $\Phi_D < 75°$ with the free stream conditions: $M_\infty = 6.0$ and $Re_D = 0.13 \times 10^6$ (Series II). From this it is apparent that body geometry has a different influence on oscillation for $\Phi_D < 75°$ than for $\Phi_D > 75°$.

Beginning with the $\Phi_D = 70°$ model the agreement between experiment and the previously obtained curve fit (Eq. 3.1) is seen to be good for all values of $\frac{\ell}{D}$ except one, $\frac{\ell}{D} = 1$. The results of $\Phi_D = 70°$ at $\frac{\ell}{D} = 1$ are given in Fig. 27 compared with an example of oscillation $\frac{\ell}{D} = 1.3$, and stable flow, $\frac{\ell}{D} = 3$. There is seen to exist a difference between each of the three wave forms shown; i.e., although the wave form at $\frac{\ell}{D} = 1$ is less clear (σ [1] $\simeq 20\%$) than at $\frac{\ell}{D} = 1.3$ ($\sigma = 5\%$), it is more regular than the background signal ($\sigma \simeq 40\%$).

A further decrease of 10° in cone angle results in further modification to the frequency distribution with spike length. The $\Phi_D = 60°$ model exhibits only two values which agree with Eq. 3.1, $\frac{\ell}{D} = 1.2$ and $\frac{\ell}{D} = 1.5$. Figure 28 shows the results of $\Phi_D = 60°$ and $\frac{\ell}{D} = 1.2$ compared with neighboring values of $\frac{\ell}{D}$. The wave form at $\frac{\ell}{D} = 1.2$ is

---

[1] σ here is expressed as a percentage of the mean value.

quite regular with a σ of 5%. The frequencies of the neighboring $\frac{\ell}{D}$ have risen to a level nearly equal to the background level; however, they are somewhat more coherent than the background signal with $20\% < \sigma < 30\%$. Note also the amplitude of the two less regular wave forms of Fig. 28 are 2 to 3 times greater than the background amplitude shown in Fig. 27c. This point will be discussed later (see 3.4.2.4).

In Fig. 29a is shown the shock wave envelope of a third type of unstable flow which was encountered only for $\Phi_D \leq 75°$. Also shown is the lower neighboring $\frac{\ell}{D}$ which provoked the pulsation mode. Only a single photograph of the new mode is shown here because there was no significant change from this basic configuration of ripples or transverse pressure waves in the foreshock.

In Fig. 26 all points lying to the left of the symbol ←—|—→ were produced by shock envelopes identical to that of Fig. 29a. Note that the point of demarcation between these points and oscillation is a function of Φ_D. The standard deviation of the frequency was between 10% and 20% of the mean which shows these points to be within reasonable agreement with Eq. 3.1. For this reason the new instability will be referred to as the secondary form of oscillation, abbreviated 0_{II}.

In summary there are observed two departures from the behavior of S described in Section 3.4.1.1 as Φ_D is decreased below 75°. First, the frequency increases over certain ranges of $\frac{\ell}{D}$ below the boundary between stable flow and oscillation to levels approximately equal to that of the background noise. The extent of these ranges increases as Φ_D is decreased. Second, there appears a sub-class of the oscillation mode distinguished by its shock envelope that yields frequencies in agreement with Eq. 3.1.

3.4.1.5 Oscillation below the shock detachment angle

Until present it has been assumed, tacitly or otherwise, that separation caused by spiked cones with cone angles less than the shock detachment angle was stable. This is illustrated in Figs. 7 and 9. However, in the present study oscillation was observed to exist at a Φ_D of 50° and an $\frac{\ell}{D}$ unity in a free stream with a Mach number of 6 (Fig. 30b). Note that the conical shock detachment angle for Mach 6 is 55.5°. At $\frac{\ell}{D} = 1$ the pressure wave is seen to be quite regular with a standard deviation, σ, less than 5% of the mean value. In fact, the resulting Strouhal number was found to agree well with the oscillation frequency curve fit (Eq. 3.1) (Fig. 26). No secondary form of oscillation was found for the $\Phi_D = 50°$ model.

Also included in Fig. 30 are examples of flows at values of $\frac{\ell}{D}$ below and above unity which were stable. At

$\frac{\ell}{D}$ = 0.4 the flow exhibits leading edge separation and face reattachment (Fig. 30a). In contrast at $\frac{\ell}{D}$ = 2 the flow exhibits a non-leading edge separation but a shoulder reattachment (Fig. 30c). Note this is the same configuration observed for steady flows with Φ_D greater than the shock detachment angle. Only at $\frac{\ell}{D}$ = 1 does there exist both leading edge separation and shoulder reattachment and the flow is unstable.

3.4.2 The pressure wave amplitude of oscillation

Herein are presented the experimental findings of the effect on the pressure wave amplitude of the oscillation mode of the parameters; spike length, body cone angle, Mach number and Reynolds number.

3.4.2.1 The effects of model geometry

Figure 31 illustrates the effect of model geometry on the amplitude of the series II pressure wave (M_1 = 6.0 and $Re_D = 0.13\times10^6$). Each body cone angle shows approximately the same influence of $\frac{\ell}{D}$ on the pressure wave amplitude. As discussed in Section 3.1 there exists a finite pressure fluctuation associated with stable flow which is referred to as the background level. This is the cause for the pressure wave amplitudes at $\frac{\ell}{D}$ greater than 2.5 in Fig. 31. Decreasing the spike length results is an increase in the amplitude which is first noticeable

between the values of $\frac{\ell}{D}$ = 2.4 and 2.5. This trend continues until, at a value of $\frac{\ell}{D}$ equal to approximately two, a leveling off occurs in the amplitude. Further decreasing the spike length has little effect on the amplitude until the pulsation mode is encountered. This will be discussed in Section 3.5.

There also appears a distinct variation of the pressure wave amplitude with Φ_D in contrast to frequency which was found to be independent of Φ_D (see 3.4.1.1). The maximum value of the amplitude increases as Φ_D decreases. Also the boundary between pulsation and oscillation, indicated by the symbol P/O, occurs at successively lower values of $\frac{\ell}{D}$ as Φ_D is decreased. Note that at Φ_D = 75° a portion of the amplitude distribution exists as a broken line. This portion of the curve belongs to the secondary form of oscillation (see Section 3.4.1.4).

3.4.2.2 Reynolds number effects at hypersonic speeds

Data were recorded of the oscillation mode at two Reynolds numbers at Mach 6. At an Re_D of 0.9×10^6 the shear layer was found to be transitional as evidenced by Fig. 32, and at an Re_D of 0.13×10^6 the shear layer was laminar as illustrated in Figs. 2 and 27 (also see section 3.4.1.2). Based on this limited data as presented in Fig. 33 it is apparent that Reynolds number can play a significant role in determining the amplitude of the

oscillation pressure wave.

The most striking effect of increasing the Reynolds number is the increase in the maximum amplitude. For the $\Phi_D = 90°$ model this increase amounts to almost a factor of three going from an Re_D of 0.13×10^6 to 0.9×10^6. This is accompanied by a similar increase in the rate of increase in Δp with decreasing spike length. This rate is very nearly linear throughout the range of oscillating flow with no leveling off or "plateau" near the P/O boundary as was seen for the low Reynolds number case. The $\Phi_D = 80°$ model shows a reversal of trend at an $\frac{\ell}{D}$ of 1.50. After which occurs a second reversal, and the pressure wave amplitudes for the two Reynolds numbers are approximately equal when the high Reynolds number case blocked the tunnel.

Note that the pulsation/oscillation boundary, denoted by the symbol P/O, remains unchanged by changes in Reynolds number at $\Phi_D = 90°$, but has shifted to a lower value of $\frac{\ell}{D}$ at the higher Reynolds number with $\Phi_D = 80°$. It should be kept in mind, however, that these two cases are not strictly speaking comparable due to the differences in the state of the shear layer.

3.4.2.3 Mach number effects

As has been stated earlier the occurrence of the oscillation mode is limited to a very small range of parameters at moderate supersonic Mach numbers. During the

present study the only positive identification of oscillation was made at M = 2.21 using the $\Phi_D = 70°$ model for the range $0.80 \leq \frac{\ell}{D} \leq 1.05$. Furthermore, the pressure waves measured were found to be less repeatable under supersonic conditions than those of the hypersonic study. Thus, one may only conclude that the amplitude of the oscillation pressure wave at Mach 2.21 is approximately one tenth of the pitot pressure (Fig. 14). This is the same order of magnitude found for oscillation at Mach 6.

3.4.2.4 Oscillation pressure wave amplitude below $\Phi_D = 75°$

The effect of body geometry on the oscillation pressure wave amplitude for body cone angles, Φ_D, 75° and less is shown in Fig. 34. With the exception of $\Phi_D = 75°$ these distributions are quite different than those for $\Phi_D > 75°$ (Fig. 31). The results of $\Phi_D = 75°$ are included here because between $\frac{\ell}{D} = 0.6$ and $\frac{\ell}{D} = 0.8$ a new form of instability was observed which for reasons given in section 3.4.1.4 was subclassed as a secondary form of oscillation abbreviated 0_{II} (see Fig. 29). The boundary between 0_{II} and the primary form of oscillation, abbreviated 0_I, is denoted by the symbol $\leftarrow\!|\!\rightarrow$ with 0_{II} lying to the left of the vertical bar in all cases. The remainder of the pressure wave amplitude distribution, $\frac{\ell}{D} > 0.8$ is identical to distributions for $\Phi_D > 75°$.

The $\Phi_D = 70°$ model exhibits points of relative maxima and minima in contrast to the monotonic distributions for $\Phi_D > 75°$ (Fig. 31). The 0_{II} mode at values of $\frac{\ell}{D}$ slightly greater than the shock stand-off distance produced waves of larger amplitude relative to the background level but not as regular as those produced by the 0_I mode. The standard deviation, σ, of 0_{II} represented 40% of the mean value at the shock stand-off distance which gradually diminished to 10% at $\frac{\ell}{D} = 0.7$. At $\frac{\ell}{D} = 0.75$ the amplitude begins to decrease as $\frac{\ell}{D}$ increases reaching a minimum at $\frac{\ell}{D} = 1$. Recall from Section 3.4.1.4 that for the $\Phi_D = 70°$ model at $\frac{\ell}{D}$ 1 the frequency was seen to rise above the oscillation frequency curve fit (Fig. 26). These two phenomena, the rise in frequency and fall in amplitude, would seem to indicate a stabilizing of the flow, however, Fig. 27a shows the flow to be clearly unstable. A second maximum occurs at $\frac{\ell}{D} = 1.25$ followed by a minimum at 1.30 (Fig. 27b). This illustrates the rather dramatic effect small changes in spike length can have on the amplitude of oscillation. Continued increases in $\frac{\ell}{D}$ above 1.3 result in a gradual increase in amplitude to a maximum at $\frac{\ell}{D} \simeq 1.65$ and then a decay to stable flow. Independent traverses have shown these results to be repeatable.

The $\Phi_D = 60°$ model exhibits an oscillation amplitude distribution quite similar to that of $\Phi_D = 70°$. Beginning

at to shock stand-off distance ($x_s/D = 0.15$) an amplitude of more than 0.2 the pitot pressure is measured and found to be somewhat incoherent with σ equal to 40% of the mean value. The amplitude falls rapidly and at $\frac{\ell}{D} \simeq 0.5$ the change from 0_{II} to 0_I takes place. A relative minimum occurs at $\frac{\ell}{D} = 1.1$ followed by a maximum at 1.2 and another minimum at 1.25. Recall once again that at $\frac{\ell}{D} = 1.2$ the frequency was seen to conform to the oscillation curve fit. Also note that the amplitude at relative minima are only 80% to 90% above the background level. Due to relatively large standard deviation (30% of the mean value) of these signals and that of the background (50% of the mean value) it is difficult to classify these minima as stable or unstable flow. This point will be discussed later in section 5.2.7. A second maximum occurs at $\frac{\ell}{D} = 1.5$ and then a rapid decay to stable flow.

The frequency measured at $\frac{\ell}{D} = 1.5$ conformed to the curve fit as did the preceeding maximum.

Referring to the pressure wave amplitude distribution of the $\Phi_D = 80°$ series I ($M_1 = 6.0$ and $Re_D = 0.9\times10^6$) in Fig. 33 one sees a behavior similar to that of $\Phi_D < 75°$ series II ($M_1 = 6.0$ and $Re_D = 0.13\times10^6$). However, referring to Fig. 22 it is seen that the Strouhal numbers for $\Phi_D = 80°$ series I conform to the frequency curve fit (Eq. 3.1) throughout the range of $\frac{\ell}{D}$ which provoke oscillation. The conclusion is therefore that the similarity in the pressure

distribution does not reflect a similarity in cause. The difference most probably lies in the state or change in state of the shear later, i.e., laminar (series II) versus transitional (series I) (see Section 3.4.1.2).

One may interpret from Fig. 9 that Holden (Ref. 17) found results similar to these. That is, the isolated region of "D" oscillation may have been, in fact, a region of relative maximum amplitudes either in shock envelope movement or heat transfer fluctuations. Unfortunately this was but a minor point in Holden's work and was not covered in sufficient detail to make a further comparison.

There are two points of interest which should be emphasized here. First, as mentioned earlier, points od relative maxima in the pressure wave amplitude distribution correspond exactly to frequencies which conform to the curve fit for $\Phi_D \geq 75°$. Second, relative maxima for different Φ_D occur at nearly the same $\frac{\ell}{D}$ with a tendency to shift towards slightly smaller $\frac{\ell}{D}$ as Φ_D decreased.

3.4.2.5 Pressure wave amplitude below the shock detachment angle

The oscillation mode was found to exist only at a single value of $\frac{\ell}{D}$ for Φ_D less than the shock detachment angle during the series II tests (see Section 3.4.1.5). As illustrated in Fig. 30, the amplitude is only 5% of the pitot pressure, but the pressure wave itself is very

repeatable and is, in fact, more than twice that of the background measured for this model.

3.5 The pulsation boundary

3.5.1 Hypersonic case

The boundary between pulsation and oscillation was found to exhibit a rather unusual property. This property described as hysteresis has been reported in earlier investigations (Refs. 11 and 29). It was found early in the present study that the mode of instability observed for a given geometric configuration was strongly dependent on the conditions under which the model was injected into the flow if the value of $\frac{\ell}{D}$ was near the P/O boundary. Although the relatively higher Reynolds numbers encountered during the starting phase of the hypersonic tunnel seemed to favor pulsation, there were a few cases of oscillation occurring at these higher Reynolds numbers. It was not possible to test this phenomenon, as was done in the supersonic study using the traversing mechanism of the large model since that model blocked the flow at the P/O boundary for all Φ_D's except 90° (where, however, it blocked just below the P/O boundary allowing no space for hysteresis to occur). An attempt was made to correlate this flow multiplicity with the model body temperature which is indicative of the wall temperature at reattachment. This also was found to give apparently random results.

The random nature of this phenomenon leads one to suspect that another parameter or other parameters play a role in determining the mode of instability in the range of $\frac{\ell}{D}$'s near the P/O boundary. One parameter most likely to be the cause would be free stream turbulence which is itself random in nature. That is, the small changes in the unit Reynolds number or local flow direction may cause a change of mode.

In order to overcome this problem during the hypersonic test series, the convention was established of retracting the model from the flow once the desired conditions were established and re-injecting just before the data was taken. This in effect assured that the model was always started under identical conditions and removed the problem of flow multiplicity in all but two tests.

3.5.2 Supersonic case

In supersonic flow the boundary between pulsation and stable[1] flow also exhibited hysteresis but in a slightly different manner. With the ability to change spike length during a run, it was found that this boundary was a function of the direction from which it was approached. If, for example, the $\Phi_D = 90°$ model was started in a configuration which resulted in a pulsating flow and the spike length was increased slowly, the P/S boundary is encountered at a

[1] "stable" here is used to mean non-pulsating

certain $\frac{\ell}{D}$. On reversing the process the flow remained stable until an $\frac{\ell}{D}$ 10% to 15% below the previously mentioned $\frac{\ell}{D}$. There was also a change in these limits indicating a random or intermittent parameter was responsible. The spread between the upper and lower bounds diminished with decreasing Φ_D.

3.6 Discussion of the pulsation pressure wave

In this section are discussed the time averaged parameters of the pulsation pressure wave, frequency and amplitude.

3.6.1 The frequency of pulsation

Herein are presented the experimental findings of the effect on the frequency of the pulsation mode by the parameters spike length, body cone angle, Mach number and Reynolds number.

3.6.1.1 The effects of model geometry

The pulsation mode like the oscillation mode ($\Phi_D > 75°$) is characterized by a dependence of frequency on spike length but not on the body cone angle. This is illustrated in Fig. 35 for the series II results ($M_1 = 6.0$, 0.13×10^6). Above an $\frac{\ell}{D}$ of 0.5 the frequency is seen to decrease with an increase in spike length. Below this value, the frequency also tends to decrease with a decrease in spike length. However, pulsation at these low values of

$\frac{\ell}{D}$ is not manifest as described earlier. The wave form is quite irregular, e.g., the $\Phi_D = 90°$ model with an $\frac{\ell}{D}$ of 0.35 exhibited a standard deviation greater than 50% of the mean value.

The data was curve fitted using a least mean square technique resulting in the expression

$$S = 0.24 - 0.067 \frac{\ell}{D} \qquad (3.2)$$

This is shown by the straight line in Fig. 35.

Note that at M = 8.82 and $Re_D = 0.37 \times 10^6$ with a $\Phi_D = 90°$ model and $\frac{\ell}{D} = 1.0$ Kabelitz (Ref. 30) shows a pulsation wave with a Strouhal number of approximately 0.15 which agrees well with the values obtained in the present study.

3.6.1.2 Mach number effect

In order to determine the effect of Mach number on the frequency of pulsation, the series II high Reynolds number results ($M_1 = 2.21$ and $Re_D = 0.12 \times 10^6$) were curve fitted using the same method discussed in the previous section. The result was also a linear curve characterized by the expression

$$S = 0.25 - 0.076 \frac{\ell}{D} \qquad (3.3)$$

The data and the curve fit, a solid line, are shown in Fig. 36.

In Fig. 37 is shown a comparison of the above result with the result of Robinson et al. (Ref. 29) who investigated only the case of $\Phi_D = 90^c$. The frequencies measured in the present study are slightly higher than those of Robinson et al. but the overall agreement is good.

Also included in Fig. 36 is a broken line representing the curve fit of the series II data (Eq. 3.2). This comparison shows that to within the accuracy and bounds of the present experiment the frequency of pulsation is not affected by changes in the Mach number.

3.6.1.3 Reynolds number effects

As was done in the previous sections the series III low Reynolds number results ($M_1 = 2.21$ and $Re_D = 0.05\times10^6$) were curve fitted to obtain an idea of the effect of Reynolds number of the frequency of pulsation. The result is given as

$$S = 0.24 - 0.76 \frac{\ell}{D} \qquad (3.4)$$

This is shown in Fig. 38 as a solid line along with the data.

Also included in this figure is a broken line representing the curve fit of the high Reynolds number results at this Mach number for comparison. Again one must conclude due to the repeatability of the phenomena represented as error bars equal to one standard deviation

that for the range of parameters investigated Reynolds number changes do not affect the frequency of pulsation.

3.6.2 The pulsation pressure wave amplitude

Herein are presented the experimental findings of the effect on the pressure wave amplitude of the pulsation mode by the parameters, spike length, body cone angle, Mach number and Reynolds number.

3.6.2.1 The effects of model geometry

Figure 39 shows the effects of model geometry on the pulsation series II (M_1 = 6.0 and $Re_D = 0.13\times10^6$) pressure wave amplitude. Each curve shows the same general influence of changes in $\frac{\ell}{D}$. Beginning nearest the shock stand-off distance, the far left, the pressure amplitude increases to a maximum as $\frac{\ell}{D}$ is increased, and with the exception of $\Phi_D = 85°$ there is a slight decrease until the P/O boundary is reached. Also illustrated is that the pressure wave amplitude is a function of Φ_D. As Φ_D is decreased, the P/O boundary as well as the location of the peak value also moves to lower values of $\frac{\ell}{D}$.

One final similarity observed is that the maximum value of the pressure amplitude is of the same order of magnitude as the pitot pressure. Recall that the maximum oscillation pressure wave was typically one tenth of this value.

3.6.2.2 Mach number effects

In order to assess the effects of Mach number on the pulsation wave amplitude the results of high Reynolds number series II (M_1 = 2.21 and $Re_D = 0.12\times10^6$) were quadratically curve fitted using the least mean square technique. This is shown in Fig. 40 (see Appendix III for detailed data). Beginning at the shock stand-off distance, the far left of each curve, amplitude increases to a maximum just before the P/O boundary. The maxima are all again of the same order of magnitude as the pitot pressure, p_{t_2}. Robinson et al. (Ref. 29) reported maximum amplitudes of 0.75 p_{t_2} at M_1 = 2.2 and 1.25 p_{t_2} at M_1 = 2.8. This is considered a good agreement since the pressure transducer used by Robinson was flush mounted with a diameter equal to 25% of the model diameter differing from the system used in the present experiments.

The above observations are the same as were made of the hypersonic data. Therefore, in light of the accuracy and repeatability of the pressure wave amplitude, one may conclude that, for the two Mach numbers studied, Mach number had no effect either on the distribution or magnitude of the pressure wave.

3.6.2.3 Reynolds number effects

As was done in the preceeding section, the series III low Reynolds number results (M_1 = 2.21 and $Re_D = 0.05\times10^6$)

were curve fitted. These results are shown in Fig. 41. Again the pressure wave amplitude is seen to increase as the value of $\frac{\ell}{D}$ is increased from the shock stand-off distance to just before the P/O boundary and the maximum values are all of the same order of magnitude as the pitot pressure. Thus one may conclude that within the scope of these experiments Reynolds number has no effect on either the amplitude distribution or magnitude.

Robinson et al. (Ref. 29) also reported that the Reynolds number effect on pulsation was negligible. This point is further emphasized by the fact that to within the accuracy of both the present work and Robinson's work, there is no appreciable Reynolds number effect as the Re_D is varied from 0.05×10^6 (series III) to 0.5×10^6 (Robinson, Ref. 29), an order of magnitude.

3.7 Chapter summary

The present study of time averaged frequency and amplitude of pressure waves and stability boundaries is not the first of its kind; however, the range and resolution of the present study is far in excess of previous studies. Due to the volume of new facts found in this study it is necessary at this point to summarize important points for later references.

Beginning with the oscillation mode it was found that at Mach 6 neither the body cone angle nor Reynolds number, Re_D, had a measurable effect on frequency for $\Phi_D \geq 75°$. Results at Mach 2.21, although scarce, indicated that the frequency may also be Mach number independent. Findings of Kabelitz (Ref. 30) substantiate this. Thus, one may estimate the frequency of oscillation from Eq. 3.1.

In contrast it was found that the amplitude was a function of not only spike length but the body cone angle as well as Reynolds number. One may say, however, that sufficiently far from the O/S boundary the amplitude of the oscillation pressure wave is of the order of one tenth the pitot pressure at Mach 2.21 and 6. Also above a Φ_D of 75° there existed a characteristic distribution of amplitude with spike length which showed a momotonic increase as the spike length is decreased from the O/S boundary which eventually levels off before the P/O boundary is reached.

Below $\Phi_D = 75°$ at Mach 6 there were seen to exist two effects not observed above this value. First, fewer points of frequency conformed to the curve fit Eq. 3.1 as Φ_D was decreased, and the distribution of amplitude with spike length was changed radically from that found above $\Phi_D = 75°$. Note also that those values of $\frac{\ell}{D}$ producing frequencies conforming to the curve fit correspond to the

relative maxima in the amplitude distributions. Compare Figs. 26 and 34. Secondly, a subclass of oscillation was found which differed in shock envelope but exhibited frequencies which lay on the oscillation frequency curve fit. This subclass was referred to as the secondary form of oscillation and abbreviated 0_{II}. No similar effects were observed at M = 2.21 due to the limited range of parameters which produced oscillation.

Two important points were brought out in the study of the oscillation mode which will help to establish the cause for this instability. First oscillation was found to exist below the shock detachment angle which had heretofore been assumed impossible. Also it was seen that the unstable flow consisted of both leading edge separation and shoulder reattachment. Stable flows were found to exist with one or other of these attributes, but not both, suggesting these are the necessary conditions for the oscillation mode. Secondly, it was found that, at least for $\Phi_D \geq 75°$, the onset of unstable flow, oscillation occurred when the distance from the spike tip to body shoulder was a certain constant value.

The frequency of the pulsation mode was found to be independent of the body cone angle, Reynolds number, and Mach number to within the accuracy of these experiments for the cases studied. These findings are substantiated

by Robinson et al. (Ref. 30). Thus, one may estimate the frequency of pulsation from either Eqs. 3.2, 3,3 or 3.4.

As in the case of oscillation, the amplitude of the pressure wave was found to be affected in varying degrees by body cone angle, Mach number and Reynolds number. There did exist, however, a characteristic distribution of amplitude with spike length. This was a monotonically increasing curve as the spike length was increased from the shock stand-off distance to a point just before the upper limit of pulsation followed by a small decrease. The maximum value for these curves were of the order of the pitot pressure or ten times greater than the amplitude observed for the oscillation mode.

From the above, one may draw two general conclusions. First, the frequency of these phenomena seem to be more suited to analysis because they are independent of most parameters and seem to exhibit some universiality. Also recall that the frequency showed less data scatter and was characterized by 5% of the mean value in contrast to that of the amplitude at 10% of the mean value. For these reasons more attention will be given to the analysis of the frequency. Although the amplitude of the pressure seems to be affected by a number of parameters, it is still useful as a means of distinguishing oscillation and pulsation, and therefore, order of magnitude estimates will be

made to demonstrate the importance of the difference in the driving mechanisms behind these two modes of unstable flow.

Secondly, it was found by East and Wilkinson (Ref. 34) that two dimensional separated flows with Strouhal numbers based on step height of the order of 0.001 could not be treated by quasi-steady analysis. Since the Strouhal numbers of the flows under study are two orders of magnitude greater, it is obvious that they likewise will not be amenable to quasi-steady analysis and, therefore, information as to the time dependent nature is necessary to further the understanding of these phenomena. This is covered in the following chapter.

4. THE TIME DEPENDENT EXPERIMENTAL RESULTS AND DISCUSSION

In this chapter results are presented which demonstrate the time dependent characteristics of the two modes of unstable axisymmetric separated flow. This information is essential to the understanding of these flows and will be used as a basis for analyses made in the following chapter.

4.1 The oscillation mode

The history of an oscillation cycle is constructed by synchronizing spark photographs and the pressure wave measured at the model face. The pressure gradient in the streamwise direction is studied in order to obtain further information as to the relation of the separation and reattachment processes. Finally, a cycle of the secondary mode of oscillation is examined as was done for the primary mode.

4.1.1 The cycle

In order to gain some insight into the mechanism behind the oscillation mode a series of spark photographs were synchronized with pressure measurements made at the face of the model (Section 2.5). Results are given in Fig. 42 for $\Phi_D = 70°$, $\frac{\ell}{D} = 2.0$ series II ($M_1 = 6.0$, $Re_D = 0.13\times10^6$).

Beginning with Fig. 42a the cycle is approximately midway through its decompression, and separation is seen to be of the leading edge type. Figures 42a - 42e show the foreshock changing inflection as the pressure attains its minimum value. The inflection change begins at the tip and moves rearward. In Fig. 42e at minimum pressure, the shear layer is nearly a straight line. From Fig. 42f to Fig. 42h the separation point moves away from the tip as the pressure goes from its minimum to its maximum value. Note that the maximum pressure coincides with the apparent rearmost position of separation and also the steepest shear layer angle at reattachment. The separation point then reverses its course and by Fig. 42j has once again reached the spike tip.

In Fig. 43 are shown the results of the synchronization technique in less detail for $\Phi_D = 80°$ series I ($M_1 = 6.0$ and $Re_D = 0.9\times10^6$). Generally, good agreement is seen with series II in that the concave shape (Fig. 43a) occurs during the compression, and the concave shape (Fig. 43b) occurs during decompression.

The cycle of the oscillation mode at supersonic speeds exhibits a less pronounced but nonetheless a discernible change in the shock envelope as illustrated in Fig. 22 for $M_1 = 2.21$. The major difference in the two envelopes shown is the location of the intersection of the foreshock with

the aftershock. Note that the shock angle measured for the straight line portion of the shock emanating from the spike tip is the same for both photographs. The shock-shock intersection shown in Fig. 22a lies closer to the model than in Fig. 22b due to a curvature in the foreshock just upstream of the intersection causing a decrease of the shock strength in the vicinity of the model face. The pressure wave synchronization shows that this envelope (Fig. 22) corresponds to a pressure near the minimum value. Similarly, the pressure corresponding to the shock envelope of Fig. 22b is near the peak while the shock angle is larger than that of Fig. 22. Thus illustrated is the same correlation between shock angle and pressure on the model face for supersonic flow as was seen for hypersonic flow.

4.1.2 The streamwise gradient

In a steady separted flow the existence of the straight shear layer and the fact that across the shear layer $\frac{\partial p}{\partial y}$ is approximately zero assures one that there exists no streamwise pressure gradient with the exception of the small regions at separation and reattachment. The oscillation mode on the other hand has been observed to exhibit curved shocks (e.g., Fig. 2) which indicate that there exist streamwise pressure gradients, and hence, a fundamental difference between stable flow and oscillation.

Verification of the existence of this streamwise gradient was made using a $\phi_D = 90°$ model with an $\frac{\ell}{D}$ of 2 in a Mach 6 flow. This was accomplished using thin film gauges placed on glass spikes making it possible to correlate the phase angle between conditions near the spike tip and at the model face. The results are presented in Fig. 44 as two oscillograms; the upper with two traces from thin film gauges placed at different streamwise locations and the lower with a pressure wave obtained at the model face. Comparing the upper thin film trace ($\frac{x}{\ell} = 0.9$) with the pressure wave ($\frac{x}{\ell} = 1$), one sees that the two are similar in shape and that the phase angle is sufficiently small to demonstrate the proportionality of the thin film gauge output to pressure.

A comparison of the two thin film gauges, one located near the spike tip ($\frac{x}{\ell} = 0.1$) and the other near the model face ($\frac{x}{\ell} = 0.9$) reveals a large phase angle equal to approximately 180°. This shows that the minimum pressure at the spike tip corresponds in time approximately to the maximum at the face. This is essentially as anticipated since the spark photographs synchronized with pressure waves had shown the maximum pressure at the face to correspond to the largest shock angle in this vicinity while at the same time the shock angle near the spike tip was at a minimum value.

East and Wilkinson (Ref. 34), as mentioned earlier, measured similar phase angle in time dependent two

dimensional separated flows. They measured phase angles of 40° for Strouhal numbers based on step height and free stream velocity of 0.001. They showed analytically that the phase angle increases with increasing Strouhal number. The present results with a Strouhal number of 0.1 correspond to a phase angle of 180° which is in qualitative agreement with East and Wilkinson.

4.1.3 The secondary form of oscillation

The subclass of the oscillation mode, called the secondary form of oscillation (Section 3.3.1.4) was distinguished primarily by its shock envelope. In contrast to the rather simple concave to convex flexation of oscillation, the secondary form exhibited a series of transverse waves in the foreshock. A sequence of time synchronized spark shadowgraphs is shown in Fig. 45. This shows the transverse wave to be travelling in the free stream direction as the pressure rises at the face (Figs. 45a, b, c). Near the pressure peak, the conical foreshock appears to be undistrubed (Fig. 45c) after which time the transverse wave or waves begin to travel towards the spike tip as the pressure descends. They, however, never reach the tip and therefore, there always remains a finite portion of the foreshock which remains linear. The separation angle is, however, larger during the decompression than the compression although the separation remains

of the leading edge type.

4.2 The pulsation mode

The history of a pulsation cycle is constructed as was done for the oscillation mode. A specialized high speed photographic technique is employed to obtain further details of the pulsation cycle history.

4.2.1 The cycle

As was done for the oscillation mode, a synchronization was made between a series of spark photographs and the pressure wave measured at the face of the model. The hypersonic results are given in Fig. 46 and the supersonic results in Fig. 47.

In Fig. 46a the decompression has nearly been completed as the shock then begins its migration towards the model face. As it passes the half-way point, the minimum pressure is recorded at the face (see Fig. 46b). During the same portion of the cycle a compression/shock wave is being created at the face as though the model were being impulsively accelerated to supersonic or hypersonic speed. This wave in turn separates the spike boundary layer as may be seen in Fig. 46c, 3a, or 48a. The separation point then very rapidly moves towards the spike tip as the collapsing bow wave continues toward the face. In Fig. 46d the two waves have merged and the separation point has very nearly attained the spike tip. In Fig. 46e, the

separation point has reached the tip and the maximum value of pressure is recorded at the face.

This oblique conical foreshock then begins a lateral expansion as the pressure begins to decrease. This causes the shock-shock intersection to move towards the shoulder of the model. (Fig. 46f through 46h). In Fig. 46i, the shock-shock intersection has been displaced beyond the shoulder, and the original bow wave is being washed downstream. The foreshock continues its expansion as the pressure continues to decrease and achieves the bow wave characteristics at the start of the cycle (compare Fig. 46j with 46a).

The supersonic results presented in Fig. 47 show a similar history with some small differences. In Fig. 47a the expanded foreshock is seen as the decompression has been nearly completed, exactly as in the hypersonic cycle. In Fig. 47b, the first evidence of the formation of a new bow wave is seen. Here the reversal in pressure has already been obtained, whereas the collapsing bow wave was already halfway down the spike before this point in the pressure wave for the hypersonic case. The growth of this new bow wave is seen in Fig. 47c and 47d. By Fig. 47d the new bow shock is fully formed and has separated the spike boundary layer as was seen in the hypersonic cycle. The collapsing bow wave continues toward the face until it merges with the new bow wave at the free stream shock stand-off distance.

The separation point continues toward the tip, but the pressure at the model face does not decrease (Figs. 47e and 47f as in the hypersonic case). This is due to the relatively long time required for the separation point to reach the spike tip and results in the column of highly turbulent flow seen in Fig. 47d, 47e and 47f impacting on surface face during this period of time. In the hypersonic case, the separation point moved very much faster to the tip by-passing this feature. In Fig. 47g, the end of this pressure plateau is reached, and the foreshock begins expanding. Notice the formation of oblique shocks on the body downstream of the face. These are caused by the recompression of flow as it is overexpanded coming from the region of the face showing that there is a mass flux out of the foreshock region. The process of the expansion of the foreshock is shown in Figs. 47h through 47i. The pressure on the face decreases throughout this portion of the cycle as was the case in hypersonic flow.

Results presented by Robinson et al. (Ref. 29 show the same sequence of shock envelopes for the pulsation cycle at Mach 2.8 and Kabelitz (Ref. 30) at Mach 8.82. However, results of a similar synchronization technique used by Robinson are in disagreement with the above findings. That is, Robinson reports that the pressure on the model face decreases as the expanded foreshock collapses. However, as Mair (Ref. 26) pointed out, the flow encompassed by the

expanded foreshock in subsonic over the entire region and Fig. 46c where shock wave is forming at the body face indicating the flow has become supersonic. This situation is analogous to that of a body accelerating in a flow of constant static pressure and therefore the pressure on the model face must rise. Thus, it is physically impossible for the pressure on the model face to decrease indicating that the synchronization of Robinson is incorrect.

4.2.2 The shock history

In order to obtain a continuous record of the pulsation cycle a special technique was developed making use of a high speed camera without a prism (shutter) in conjunction with a continuous light source. By masking off the entire test section except for a single slit parallel to the model axis, the film became effectively the "roll of paper" in a strip chart recorder and the normal shock the "pen" (Fig. 13).

The results are shown in Fig. 49 for the $\Phi_D = 90°$ model with an $\frac{\ell}{D}$ of 1.3 in a Mach 6 flow. The flow direction is left to right. Note the light striation in the free stream, i.e., to the left of the strong shock. The slope of these correspond to a velocity within 3% of the free stream velocity as determined from a measurement of the reservoir temperature and tunnel calibration illustrating the validity of this technique. The large dark zone in the

middle of the photograph is a timing mark used to calibrate precisely the film speed. It should be kept in mind that these results vary somewhat with the radial position of the slit. The position chosen for this experiment was $\frac{D}{4}$ which reflects the overall details of the cycle.

These results are presented, in Fig. 50, as an x-t diagram. The cycle as represented begins at that point in time when the two strong shocks have just merged (Fig. 46d). Note that this distance is less than the shock stand-off distance for the unspiked body (see e.g. Liepmann and Roshko, Ref. 35). This is due to the fact that the shock stand-off distance is determined by a balance of mass crossing the normal shock and that escaping around the body. At the point $\tau = 0$ mass is being reversed towards the body axis caused by the large radial pressure gradient resulting in an effective body diameter smaller than the actual diameter. By $\tau = 0.1$ the bow shock has moved forward to the shock stand-off distance indicating that mass is now escaping only downstream. This corresponds approximately to Fig. 46e where the cycle is near its peak pressure. At $\tau = 0.36$ the normal shock appears at the spike tip corresponding to Fig. 46g. Recall that if the slit had been placed closer to the body axis, this appearance would occur sooner, and in the limit as the slit approaches the body axis, this would correspond to the beginning of the decompression and expansion of the foreshock (Fig. 46f). Note that between $\tau = 0$ and $\tau = 0.36$

there appears a darker oblique band which represents the path of the oblique shock in the x-t diagram.

From τ = 0.36 to 0.5 the bow shock at the spike tip remains stationary and the bow wave at the face recedes beyond the model shoulder at τ = 0.4. During this period the shock is expanding laterally corresponding to Figs. 46f through 46i. At τ = 0.5 the expanded foreshock begins to recede towards the model face and by τ = 0.75 has reached its terminal velocity equal to approximately 55% that of the free stream. Note that at τ = 0.8 depending on the cycle the birth of the new bow wave takes place at the model face. This point is near the minimum pressure as seen in Fig. 46b. The collapsing shock then merges with the new bow shock at τ = 1 and a new cycle begins.

5. THEORETICAL ANALYSIS

This chapter begins with a review of the method for calculating large steady separated regions. These flows by definition contain regions of interaction at separation and reattachment which are small compared to the length of the shear layer. Certain special cases observed near the stability boundary are discussed, i.e., leading edge separation and shoulder reattachment. Next concepts of unsteady flow are discussed and a working hypothesis of the driving mechanism for oscillation is presented. Using this hypothesis several physical features of oscillation are calculated and compared with experiment.

In the second half of this chapter the driving mechanism of pulsation is discussed and a physical model of pulsation is presented which is used to calculate frequencies as well as some details of the cycle which are compared with experiment.

5.1 Steady separated flows

The stable separated flows observed at or near the O/S boundary possess shear layers much longer than the lengths of the separation or reattachment regions as shown in Fig. 30. These types of flows are classified as large separated regions and in this section the method of calculating the important parameters of such flows based on body geometry and free stream conditions is discussed. Basically large separated regions may be thought of as consisting of two

independent processes, separation and reattachment, coupled by a third, the mixing process of the free shear layer. This is shown diagrammatically in Fig. 51.

5.1.1 The separation process

It has been observed by a number of investigators, e.g. Gadd, Holder and Regan (Ref. 35), Shuh (Ref. 37) and Chapman, Kuehn and Larson (Ref. 38) that there exists a class of separated flows which are free from the direct influence of the mode of inducing separation. Thus, the phenomenon near separation depends only on the simultaneous solution of the interaction of equations for the external flow with those of the boundary layer. This class of separation is known as "free interaction" and contains the subclass of compression corner and forward facing step separations such as the spiked blunt body of interest in the present study.

Chapman et al. have shown using an order of magnitude analysis that

$$C_{p_2} \equiv \frac{p_2 - p_1}{q_1} \sim C_f^{1/2} (M_1^2 - 1)^{-1/4} \qquad (5.1)$$

where the subscripts 1 and 2 refer to the conditions in the inviscid flow before and after the separation shock respectively. The conditions 1 are evaluated at the position furthest downstream in the induced pressure distribution at which the flow is essentially that of a non-separating flow. Equation 5.1 is applicable to both laminar and turbulent

flows for $M_1 > 1$ and for the range of conditions at which the constant of proportionality is evaluated. This equation has been shown to be valid and the constant of proportionality has been evaluated experimentally for laminar flow throughout the entire separation process up to the pressure plateau, region 2, and for turbulent flow up to the point of reversed flow (Refs. 39 through 44). Note also that Eq. 5.1 is valid for axisymmetric flow since the momentum equation is evaluated at the wall. For the case of laminar flow Eq. 5.2 becomes

$$C_{p_2} \sim Re_{x_1}^{1/4} (M_1^2 - 1)^{1/4} \qquad (5.2)$$

which is obtained by employing the laminar skin friction law. The constant of proportionality is evaluated experimentally which allows one to calculate the pressure in region 2, knowing the undistrubed free stream conditions and the length attached boundary layer, x_1. Also knowledge of C_{p_2} and M_1 allows one to obtain the separation angle, α, from the oblique shock equations. (See for example Ref. 45).

5.1.2 The reattachment process

In the calculation of large separated regions the reattachment process is considered to be the controlling factor (Needham, Ref. 46). At reattachment that part of the flow which is able to overcome the pressure rise passes downstream and that which cannot is reversed. In a steady

separated flow the mass reversed must equal that entrained by the shear layer from the separated region. This means that the streamline which divides the mass entrained from the separated region from that coming from upstream of the separation point must possess a pressure when brought to rest at the reattachment point equal to that required by the external inviscid flow. The former will be referred to as the potential pressure at reattachment, $p_{r_{pot}}$, and the latter as the required pressure at reattachment, p_{r_r},

$$p_{r_{pot}} = p_{r_r} \tag{5.3}$$

This distinction is not usually made since for steady flow these pressures are known a priori to be equal. However, for the purposes of later developments it is made here.

Chapman et al. (Ref. 38) have proposed that the potential reattachment pressure, $p_{r_{pot}}$, is equal to that achieved by an isentropic compression of the dividing streamline. Burggraf (Ref. 47) demonstrated by means of numerical techniques that this is indeed a valid model in spite to its simplicity. Thus one may write

$$p_{r_{pot}} = p_2 \left(1 + \frac{\gamma-1}{2} M_j\right)^{\gamma/(\gamma-1)} \tag{5.4}$$

where p_2 is the plateau pressure and M_j the Mach number on the dividing streamline. Note that since $\partial p/\partial y$ is

negligible across the shear layer the static pressure on all streamlines is equal to that of the external inviscid value in region 2, p_2 (Fig. 51).

Making use of an appropriate velocity-temperature relationship, one may obtain the potential pressure at reattachment as a function of the dividing streamline velocity. The Busemann integral, valid for adiabatic flows, yields

$$\frac{p_{r_{pot}}}{p_2} = \left\{ \frac{1 + \frac{\gamma-1}{2} M_2^2}{1 + \frac{\gamma-1}{2} M_2^2 (1-z_j^2)} \right\}^{\frac{\gamma}{\gamma-1}} \tag{5.5}$$

where z_j is defined as the ratio of dividing streamline velocity, u_j, to the external inviscid velocity in region 2, u_2 ($z_j \equiv u_j/U_2$). This parameter, z_j, will be treated in the following section.

Alternatively for the case of heat transfer the Crocco integral yields

$$\frac{p_{r_{pot}}}{p_2} = \left\{ \frac{\frac{T_d}{T_2}(1-z_j) + \frac{\gamma-1}{2} M_2^2 z_j + z_j}{\frac{T_d}{T_2}(1-z_j) + \frac{\gamma-1}{2} M_2^2 z_j (1-z_j) + z_j} \right\}^{\frac{\gamma}{\gamma-1}} \tag{5.6}$$

where T_d is the temperature of the "dead air" or separated region and T_2 is the static temperature in the inviscid external flow of region 2, the region downstream of the separation shock.

In earlier works such as Chapman et al. (Ref. 38), the required reattachment pressure was taken to be equal to the static free stream pressure downstream of the reattachment shock. However, as pointed out by Nash (Ref. 48) and Holder and Gadd (Ref. 49) this is contrary to experimental observation. Referring to Fig. 51 the reattachment pressure is seen to lie somewhere between the plateau pressure, p_2, and the free stream pressure downstream of the reattachment shock, p_3. Nash proposed a reattachment (or compression) parameter which relates the required pressure at reattachment to this pressure rise. This is defined as

$$N \equiv \frac{p_{r_r} - p_2}{p_3 - p_2} \tag{5.7}$$

Nash concluded from a survey of experiments conducted in the range $1.10 \leq M_1 \leq 3.85$ that although there existed some scatter, N was approximately constant with a value of 0.35 for turbulent reattaching flows.

Sirieix (Ref. 50) observed that a laminar shear layer reattaches half-way up the pressure rise or N = 0.5. This is also the value recommended by Cooke (Ref. 51) for laminar reattaching flow. Nash also noted that at supersonic speeds there is no pressure overshoot at reattachment.

Returning attention again to Eq. 5.3 it is apparent that in order to achieve this equality one must determine

the position and slope of the shear layer that will allow an appropriate transfer of energy to the dividing streamline. This point is discussed in the following section.

5.1.3 The shear layer

Chapman et al. (Ref. 38) show that in the case of free interaction the boundary layer displacement thickness and hence the boundary layer thickness itself is of the same order of magnitude as the region of interaction. Recall that large separated regions possess lengths of free shear layer much larger than the interaction region. Therefore, the boundary layer thickness at separation in these cases is much less than the free shear length which in turn is of the same order of magnitude as the step height or body radius. Thus one may conclude that free interaction is characterized by separation of boundary layers with thicknesses much smaller than the dimension of the object provoking the separation. This is seen to be the case in Fig. 30.

According to Nash (Ref. 48) so long as the boundary layer thickness at separation is small compared to the step height (or body diameter in the axisymmetric case), the velocity of the fluid in the separated region will be small ($M << 1$) and this region will be of almost constant pressure. This may be deduced from the facts that the separated region is a vortex possessing a point or points

of zero velocity and that at the reattachment point the fluid is brought nearly to rest with no mechanism to reaccelerate the flow. Thus, the flow in the separated region is relatively low speed and hence isobaric. This in turn means that the shear layer mixing process occurs in a zero pressure gradient environment. In this section mixing layer theories of shear layers in regions of constant pressure will be developed.

5.1.3.1 The two dimensional case

The process of energy transfer of compressible laminar shear layer in a zero pressure gradient environment was treated theoretically by Chapman (Ref. 52) and Lock (Ref. 53) for the two dimensional case with a zero boundary layer thickness at separation. The result of both studies was that the velocity on the dividing streamline is constant and equal to 0.587 of the velocity at the supersonic edge of the shear layer. Nash (Ref. 54) extended this to include a finite boundary layer thickness at separation for the incompressible case. Cooke (Ref. 51) derived an expression for the length of free shear layer as a function of dividing streamline velocity for two dimensional compressible shear layer including a finite boundary layer thickness at separation. This development is based on the assumption of self similar velocity profiles through the separation point and throughout the length of free shear

layer. Cooke's expression for a laminar free shear layer developing in a zero pressure gradient environment is

$$\xi = \frac{g}{(e+f)^3}\left[3ef \ln\left(\frac{e-z_j}{f+z_j}\right) + \frac{e^3(e+f)}{2(e-z_j)^2} - \frac{f^3(e+f)}{2(f+z_j)^2} + \frac{e^3}{e-z_j} - \frac{f^3}{f+z_j} + h \right] \tag{5.8}$$

where

$$e = 0.5873, \quad f = 0.7338, \quad \frac{g}{(e+f)^3} = 0.2675,$$

$$h = 0.5782, \quad = \frac{x_2 u_1 \nu_2}{x_1 u_2 \nu_1 n^2} \quad \text{and} \quad n = \frac{\theta_2}{\theta_1}$$

The non dimensional shear length, ξ, is the ratio of quantities upstream and downstream of the separation shock denoted by subscripts 1 and 2 respectively. These quantities are: x, the distance measured in the flow direction, thus x_1 is the length of attached boundary layer and x_2 the length of free shear layer; u is the free stream velocity and ν the kinematic viscosity. The momentum thickness, θ, is defined as usual in boundary layer theory:

$$\theta = \int_0^{\delta} \frac{\rho u}{\rho_\infty u_\infty}\left(1 - \frac{u}{u_\infty}\right) dy \tag{5.9}$$

where the ∞ conditions are the inviscid free stream values. A discussion of the assessment of the ratio of momentum

thicknesses, n, is given in Appendix B.

The non-dimensional dividing streamline velocity, z_j, is the dividing streamline velocity, u_j, divided by the velocity at the edge of the shear layer, u_2. Recall that in the present derivation the velocity in the separated region "below" the shear layer is taken as zero.

It should be noted, as Merritt (Ref. 55) pointed out, that the ratio of Chapman's constants, C_2/C_1 should appear in the definition of ξ due to the use of the Dorodnitsyn type transformation. Cooke tacitly sets this ratio equal to unity. This is a reasonable approximation since the ratio of Chapman's constants is equal to the ratio of static temperature across the separation shock raised to the $\frac{1}{4}$ power providing the viscosity is a power of temperature, $\mu \sim T^{3/4}$. Therefore except for strong shocks at high Mach numbers ($M > 10$) one may approximate the ratio of Chapman's constants in the expression of ξ as unity.

Results of Eq. 5.8 are plotted in Fig. 52. Cooke also arrived at nearly identical results using polynomial profiles. Appels (Ref. 56) also obtained values that differed very little from the above by using linear profiles. Finally, Denison and Baum (Ref. 57) solved the problem using Blasius profiles as initial profiles and an implicit finite difference method. These results are also shown in Fig. 52.

The comparison of Cooke and Denison and Baum shows appreciable differences for short shear lengths, $\log_{10}\xi < 0$. This is, of course, due to differences in initial profiles and methods of integration. Above the value of $\log_{10}\xi = 1$ the differences are seen to be quite small. Because Cooke's analysis involves no numerical integration and is simpler to implement, an analogous axisymmetric mixing layer theory will be developed.

5.1.3.2 The Mangler transformation

The compressible laminar axisymmetric mixing layer may be treated using the Mangler transformation (Ref. 58) and Cooke's analysis (Ref. 51). There, however, exists some doubt as to the validity of this approach in connection with the present study since the primary assumption is violated near the separation point due to the relatively small spike diameters being considered. The Mangler transformation will be used here for two reasons: first it will be employed only in the region of reattachment where all requirements of the transformation are met; and secondly, to compare with the results of a mixing layer theory based on the axisymmetric equations.

The basic restriction of the Mangler transformation requires that $W/r_0 << 1$ where W is the width of the shear layer and r_0 is the radial distance to the dividing streamline. This allows one to neglect certain terms in both the

momentum and energy equations and is equivalent to making the radial distance coordinate, x, only. The transformation is then accomplished by the change of independent variables governed by the relations

$$d\bar{x} = \left(\frac{r_0}{L}\right) dx \qquad \bar{y} = \left(\frac{r_0}{L}\right) y \tag{5.10}$$

where L is a characteristic fixed reference length. For the present development L will be taken as the length of attached boundary layer, x_1.

For a straight shear layer one may express radial distance to the dividing streamline as $r_0 = x \sin\alpha$ where α is the separation angle. Since the spike is assumed to have an infinitely small diameter and x_1 is in the undisturbed flow, the transformed variable, $\bar{x}_1$, equals the untrasformed variable, x_1. Thus the result of transforming the length of free shear layer may be written as

$$\frac{\bar{x}_2}{\bar{x}_1} = \frac{\sin^2\alpha}{3} \left(\frac{x_2}{x_1}\right)^3 \tag{5.11}$$

Defining a non-dimensional shear length, ζ , as

$$\zeta = \frac{\bar{x}_2 u_1 \nu_2}{\bar{x}_1 u_2 \nu_1 n_2}$$

where as before the subscripts 1 and 2 refer to conditions upstream and downstream of the separation shock respectively. The parameter n, the ratio of momentum thicknesses,

θ_2/θ_1, is discussed in Appendix B as mentioned earlier.

Substituting Eq. 5.11 into Eq. 5.12 the non dimensional shear length in terms of untransformed variables becomes

$$\zeta = \frac{\sin^2 \alpha}{3} \frac{x_2^3 u_1 \nu_2}{x_1^3 u_2 \nu_1 n^2} \tag{5.13}$$

With this expression one may make use of Cooke's result, Eq. 5.8 or Fig. 52, to determine, at least as a first estimate, the dividing streamline velocity for an axisymmetric shear layer. This, of course, is restricted to those regions where $W/r_0 << 1$.

5.1.3.3 A compressible axisymmetric laminar mixing layer theory

For model geometries under study the ratio W/r_0 at separation is not necessarily negligible compared to unity due to the face r_0 equals the spike radius, r_a, in this region, and the value of r_a for the present study is relatively small. This of course, means that in this region the Mangler transformation is not valid. Furthermore, Probstein and Elliott (Ref. 59) state that further generalization of the Mangler transform yields a set of "nearly" two dimentional equations. For these reasons there exists some doubt as to the reliability of using a Mangler transformation in the present study, and, therefore, a compressible axisymmetric laminar mixing layer theory based on the

work of Lock (Ref. 53) and Cooke (Ref. 51) is presented.

The formulation of the problem is essentially the same as that of Cooke; i.e., the mixing of a compressible laminar shear layer under constant pressure (velocity of separated region is zero) based on the assumption of similar sinusoidal profiles. Using the compressible axisymmetric boundary layer equations transformed to the incompressible plane by a Dorodnitsyn transformation, which implies a linear viscosity-temperature relation, a continuity of shear stress across the dividing streamline is established. This result is then integrated and solved simultaneously with the equation for momentum on the dividing streamline. In order to do this it is necessary to make the assumption $W/r_0 << 1$ except near the separation point where this requirement is relaxed to $W/r_0 < 0.25$. Details are given in Appendix C.

The result is identical to Cooke's analysis (Eq. 5.8) with the axisymmetric non-dimensional shear length, λ, defined as

$$\lambda = \frac{\sin^2\alpha}{3} \frac{x_2^3 u_1 \nu_2}{x_1^3 u_2 \nu_1 n_2} \left(\frac{x_1}{r_a}\right)^2 \qquad (5.14)$$

where r_a is the spike radius.

Comparing these results with the Mangler transformation one finds

$$\lambda = \zeta \left(\frac{x_1}{r_a}\right)^2 \qquad (5.15)$$

where x_1 is the length of attached boundary layer. Referring to Fig. 19 one sees that the ratio x_2/x_1 is relatively large and therefore small values of r_a will have little effect of z_j as determined from Fig. 52. Therefore, one may conclude that both treatments of the shear layer are reasonable within their regions of validity.

5.1.4 An outline of the calculation procedure

For reference an iterative scheme is presented here for the calculation of compressible axisymmetric laminar large separated regions which is essentially the same as that for two dimensional separation (see Needham, Ref. 46). The inputs are: the undisturbed free stream conditions (subscript 1) and body geometry, the length from the leading edge to the afterbody, ℓ, and the afterbody angle, Φ_D.

1) make an initial guess or estimate of the length of attached boundary layer, x_1;

2) calculate the separation angle, α, as outlined in section 5.1.1 (Eq. 5.2);

3) calculate the free stream conditions downstream of the separation shock, ρ_2, u_2 and v_2;

4) based on M_1 and Φ_D calculate the pressure downstream of the reattachment shock, p_3;

5) evaluate the required reattachment pressure, p_{r_r}, with $N = \frac{1}{2}$ (Eq. 5.7);

6) based on the geometry calculate the length of free shear layer, x_2;

7) evaluate the length of non-dimensional shear layer, λ;

8) obtain the dividing streamline velocity, z_j, either from Eq. 5.8 (with λ replacing ξ) or graphically from Fig. 52.

9) using z_j, calculate the potential pressure at reattachment, $p_{r_{pot}}$, from Eq. 5.5 for adiabatic flow or Eq. 5.6 for nonadiabatic flow.

10) if $P_{r_{pot}}$ is approximately equal to p_{r_r} terminate the scheme. If $p_{r_{pot}}$ is less than p_{r_r}, a longer length of shear layer is needed; hence, decrease x_1 and return to step 2 with the new value. If the reverse is true, increase x_2 and return to step 2.

5.1.5 Shoulder reattachment

Wood (Ref. 28) concluded that an understanding of reattachment near an expansion corner was of prime importance to the study of flow over spiked blunt bodies. This point is emphasised in Figs. 7 and 9 which show unstable flow to be bounded at all points by shoulder reattaching flow except for the unimportant case of spike lengths less than the shock stand-off distance. Wood also concluded that although the dividing streamline must always meet the face of the body, the outer part of the shear layer

may pass outside of the shoulder as illustrated in Fig. 53. By this mechanism, the deflection of the shear layer and the associated reattachment pressure rise can be very much less than the values required to turn the flow parallel to the model face. As a result the maximum pressure downstream of reattachment, p_x, will be significantly less than the pressure, p_i, that would be achieved in the event the flow was turned parallel to the body face. This is illustrated in Fig. 54 with the broken line representing the imaginary situation of flow turned parallel to the face and the solid line the pressure distribution affected by both the decreased compression angle and the influence of the expansion.

At present there exists no investigation, theoretical or experimental, as to the behavior on the value of p_x. However, one may propose the following argument as to the behaviour of p_x. Referring to Fig. 53 it is seen p_x will occur in a region of relatively high pressure due to the existence of the strong shock. In axisymmetric flow, the pressure behind a strong shock is no more than 4% less than the pitot pressure at Mach 2 and no less than 2% at Mach 5. That is, the pressure in the region adjacent to p_x varies little regardless of what occurs in the separation to region, and therefore, it is likely p_x will likewise be nearly constant. One may also argue that increases in the separation angle, α, cause rises in the

plateau pressure. However, p_x which is achieved by a compression from p_2 remains relatively constant since the compression turning angle is decreased. Thus, it is proposed that the assumption be made that p_x be treated as a constant for body cone angles above the shock detachment angle.

Some justification of this assumption has been provided as a recent study by Dolling (Ref. 60) of reattachment on convex ramps using the Lees-Reeves integral method. It was found that changes in the flow causing changes in p_2 had very little effect on p_x.

As Nash (Ref. 48) brought out, no pressure overshoot exists in the reattachment region in a compressible flow. That is, the pressure required at reattachment p_{r_r} must lie between the plateau pressure p_2 and the maximum pressure p_x. If p_x is approximated as a constant as argued above and p_2 is increased, it is obvious that p_x represents the upper limit of p_{r_r}.

5.1.6 Free interaction separation

Flow over spiked cones is classified as compression corner separation and hence, the separation process is free interacting (Refs. 38 and 51). This, of course, means that the separation angle, α, is a function of the length of attached boundary layer, x_1, and the undisturbed free stream conditions.

It was observed during the present study, as well as previous investigations (Refs. 17 and 28) that the stable configuration for body cone angles, ϕ_D, greater than the shock detachment angle was shoulder reattaching. This is shown to be the case in Figs. 7 and 9.

These two facts allow one to construct a simple model for large ϕ_D which simulates shoulder reattaching flow. Assuming a straight shear layer, there exists a unique value of x_1 which for a given model geometry and undisturbed free stream conditions will generate a separation angle of shear layer which reattaches at the body shoulder. This caluclation is based on the a priori knowledge of the location of the reattachment point and is therefore different from the calculation procedure outlines in section 5.1.4.

The results of such an analysis are shown in Fig. 55 with free stream conditions: $M_1 = 6.0$ and $Re_D = 0.125\times10^6$. Note the constant of proportionality, A, for the free interaction equation (Eq. 5.2) was obtained from the present experimental program (A = 2.0). The first point to notice is the decrease in the non dimensional attached boundary layer, x_1/D, as $\frac{\ell}{D}$ is decreased. This agrees well with the present experimental observations (Fig. 30) as well as previous investigations (Refs. 12 and 16).

The purpose of this analysis is to determine the effect of changes in $\frac{\ell}{D}$ on the potential pressure at reattachment, $P_{r_{pot}}$. The value of $P_{r_{pot}}$ for a given value of $\frac{\ell}{D}$ is obtained by evaluating the length of non dimensional shear layer knowing the separation geometry and resulting flow field. For this particular calculation, the Mangler variable, ζ, was used to minimize the number of input parameters and can be considered valid since the interest lies only in the region of reattachment (section 5.1.3.2 and 5.1.3.3). Making use then of Eq. 5.8 (ζ replacing ξ) one may obtain the non dimensional dividing streamline velocity, z_j. Figure 55 shows z_j to rapidly approach its maximum value for the range of $\frac{\ell}{D}$ considered as $\frac{\ell}{D}$ is decreased. The value of $p_{r_{pot}}/p_2$ is determined from Eq. 5.5 and is seen to continuously increase as $\frac{\ell}{D}$ decreases.

Thus one may conclude that for spiked cones with Φ_D greater than the shock detachment angle, the potential pressure at reattachment as supplied by the shear layer increases as $\frac{\ell}{D}$ decreases. Use will be made of this point presently in the analysis of oscillation.

5.1.7 Leading edge separation

The configuration of separation most amenable to theoretical analysis is obtained with a zero length of attached boundary layer, x_1. This is known as leading

edge separation and shown schematically in Fig. 56. The fact that no knowledge of the attached boundary layer is required makes the task relatively easy and also use may be made of laminar mixing layer theories based on zero thickness boundary layers at separation.

Leading edge separation is characterized by some very interesting properties. First of all, Chapman (Ref. 52) found that for compressible laminar shear layers with a linear viscosity-temperature relation, the dividing streamline velocity is constant and equal to 0.587 times the inviscid velocity downstream of the separation shock as mentioned previously. A corollary to this is that the velocity distribution is discontinuous through the separation point with a positive step at separation. The above value of z_j represents the limiting value of z_j for laminar mixing theories with finite boundary layer thicknesses at separation as the length of shear layer goes to infinity. This shows leading edge separation to be efficient in terms of energy input into the dividing streamline and is, in fact, truly an impulse.

Substituting the maximum value of z_j into Eq. 5.5 one obtains

$$\frac{P_{r_{pot}}}{p_2} = \left[\frac{1 + \frac{\gamma-1}{2} M_2^2}{1+0.65 \frac{\gamma-1}{2} M_2^2} \right]^{\frac{\gamma}{\gamma-1}} \qquad (5.17)$$

This equation illustrates two important facts for a steady separated flow with a laminar shear layer. First, $p_{r_{pot}}$ is seen to be independent of Reynolds number for leading edge separation. This was verified experimentally in Ref. 39. Second, these results are also independent of the inviscid shock relations.

Brower (Ref. 61) made use of the latter result to deduce the existence of a minimum wedge angle, Φ, for a given Mach number which can sustain leading edge separation. That is, as the wedge angle decreases so does the separation angle and a point is reached at which the shock strength is inadequate to sustain the required pressure ratio based on M_2. Brower also concluded that a maximum wedge angle for which leading edge separation was possible existed when the flow turning angle through the reattachment shock equals the shock detachment angle. With these conditions and the two dimensional shock relations Brower calculated the minimum and maximum wedge angles supporting leading edge separation as a function of undistrubed Mach number. This is shown in Fig. 57.

For the purpose of the present study this analysis was extended to the axisymmetric case using Brower's conditions and the cone charts in Ref. 45. These results are also shown in Fig. 57. The comparison of the two dimensional with axisymmetric results show that for a

given Mach number the minimum afterbody angle is less for the two dimensional case. This is a result of the fact that for a given Mach number a larger deflection angle is required to obtain the same static pressure increase across a shock for axisymmetric than for two dimensional flows. The maximum axisymmetric angle is seen to be considerably increased above the two dimensional case. This is, of course, due to the three dimensional relief afforded by axisymmetric flow.

Although it is not possible to achieve turbulent leading edge separation since by definition the early portion of the shear layer is characterized by relatively low Reynolds numbers, transition of the shear layer some where upstream of reattachment will alter the limits of leading edge separation discussed above. The most significant alteration will be achieved in the instance when the shear layer has sufficient time to develop a fully turbulent profile (recall that a high supersonic Mach numbers, the length of transition may become appreciable). In this case one may make use of the investigation of Korst, Page and Childs (Ref. 62) to determine the limits of leading edge separation. Korst et al. found that a two dimensional turbulent shear layer which develops in a constant pressure environment obtains a maximum non-dimensional dividing streamline velocity, $z_{j_{max}}$, with leading edge separation, or equivalently infinite shear

length, as was seen for the laminar case. The results of Ref. 61 presented in Fig. 58 show $z_{j_{max}}$ to be a function of Mach number in contrast to laminar flow. Note that the Mach indicated along the abscissa is the local free stream value and not to be confused with the undisturbed value upstream of the separation shock. As one would expect, the turbulent $z_{j_{max}}$ is somewhat larger than its laminar counterpart ($z_{j_{max}} = 0.587$) since turbulence increases the transport properties of shear flow. Finally, one may show by use of the Mangler transformation that the results of Fig. 58 are the limiting values of z_j for axisymmetric turbulent free shear layers.

Making use of this it is now possible to extend the analysis of the limits of leading edge separation to axisymmetric the laminar results. Note that the maximum body cone angle, Φ_D, which will support leading edge separation is only slightly increased over the entire range of Mach numbers going from laminar to turbulent flow. This is due to the fact that the flow after the separation shock is a very low supersonic flow in this case and hence, the turbulent $z_{j_{max}}$ is only slightly above the laminar value. The minimum value of Φ_D is, however, more strongly influenced due to the higher Mach numbers over the separated region as the separation angle decreases resulting in larger values of $z_{j_{max}}$ for turbulent flow.

Referring to Figs. 57 and 59, it is important to note that there occurs a dramatic decrease at approximately a Mach number of 3 in the maximum Φ_D which will support leading edge separation. Use will be made of this point in the following examination of oscillation.

5.2 The oscillation mode

Concepts of time dependent separation are introduced and used in conjunction with conclusions drawn from the previous section to form a working hypothesis of the oscillation mode. Use is then made of this hypothesis to correlate some of the experimental observations made in Chapters 3 and 4.

5.2.1 Time dependent separated flow

East and Wilkinson (Ref. 34) concluded from a study of separated flow over a forward facing step with an imposed time dependent step height that flows of this type characterized by Strouhal numbers based on step height, h, ($S = \frac{fh}{u_1}$) greater than 0.001 are not amenable to quasi-steady analyses. This is due to the phase angle between the separation and reattachment processes. Measurements of this angle with S = 0.001 showed that it attained values up to 40° and was itself time dependent. In an analysis carried out using a simplified perturbation of a corresponding steady separation the phase angle was

shown to be directly proportional to the Strouhal number. The Strouhal numbers encountered in the present study are two orders of magnitude greater than the above mentioned value and will obviously necessitate the use of more refined analysis techniques. Literature on transient or time dependent separated flows, in particular concerning the compressible case, is virtually non-existent, a finding also reported by East and Wilkinson.

For the purposes of later application the concept of the "bounding" streamline of an unsteady flow will be presented which in conjunction with prudent approximations will yield results which may be verified experimentally. The bounding streamline is defined as that streamline which separates mass entrained by the shear layer originating upstream of the separation point from mass scavenged by the shear layer from the separated region. This streamline, whose position with relation to the body is time dependent, is formed by the locus of particles which pass through the separation point and may be visualized as a dye streak created by a moving separation point which colors the fluid as it passes through this point. In the steady state case the separation point is stationary, and hence, the bounding streamline will coincide exactly with the classical dividing streamline.

Another useful concept for the understanding of time

dependent separated flows was put forward by East and Wilkinson (Ref. 34). Recognizing the fact that in a shoulder reattaching flow the position of the reattachment point is at or just upstream of the shoulder, it is obvious that a different streamline will be reattaching at each consecutive moment in time (in contrast to the behaviour of the bounding streamline). Fluid below this streamline will be reversed into the separated region and fluid above it will escape downstream. Hence, this streamline is termed the "escape" streamline by East and Wilkinson (Ref. 34) and may be visualized as the time dependent dividing streamline at reattachment. In the steady state case the escape streamline will likewise coincide with the dividing streamline since the reattachment streamline is always the same.

The importance of the bounding and escape streamline becomes clear when one considers the mass balance in the reattachment region. When at some instant in time the bounding streamline lies above[1] the escape streamline, the flow between these two streamlines originated in the separated region and is now passing downstream resulting in a net loss of mass from the separated region. When the situation is reversed and the bounding streamline lies

---

[1]This is based on the convention of the separated region lying "below" the inviscid flow.

below the escape streamline, there exists a mass influx to the separated region. For the case of a steady separated flow the bounding and escape streamline are coincident and, therefore, the mass scavenged equals the mass reversed as stated by Chapman, Kuehn and Larson (Ref. 34).

5.2.2 The energetic shear layer hypothesis

Findings of preceeding chapters and developments of preceeding sections of this chapter now make possible the formulation of a working hypothesis of the driving mechanism of the oscillation mode. Recall that in chapter 3 (section 3.4.1.5) it was determined from observation of experiment that the apparent necessary conditions for unstable flow were leading edge separation and shoulder reattachment even below the shock detachment angle. Later in section 5.1.7 it was found that as the spike length was shortened in a shoulder reattaching flow the result was a decrease in the length of attached boundary layer, x_1, a fact which had also been recognized experimentally. As a result of decreases in x_1 it was found that the potential pressure at reattachment, $p_{r_{pot}}$, is continually increasing. However, in section 5.1.6 it was seen that the required pressure at reattachment could not increase above the peak pressure downstream of attachment, p_x.

Thus, a hypothesis may be made as to the driving mechanism of the oscillation mode. That is assume a flow exists such that the following two conditions are met:

1) a large separated region exists (see definition given in the introduction of chapter 5); and

2) reattachment takes place in a compressible flow where the maximum pressure downstream of reattachment p_x can be approximated as a constant (e.g. a spiked blunt body).

If a sudden infinitesimal decrease in spike length occurs, a fluid element of the heretofore steady state dividing streamline will acquire a potential pressure at reattachment $p_{r_{pot}}$ exceeding p_x. When that element of fluid which possesses the excess pressure arrives at the point of reattachment, it will pass on downstream; thus causing the dividing streamline to become a bounding streamline. This will, of course, result in the adjacent streamline below the bounding streamline which possesses the $p_{r_{pot}}$ equal to p_x becoming the new "dividing" or escape streamline. As outlined earlier, the mass scavenged by the shear layer exceeds that reversed at reattachment creating a net mass flux out of the separated region.

The loss of mass in the separated region will after a certain time be felt at the separation point as a reduction in the pressure gradient along the spike. This results in

an increase of x_1 which will cause a decrease in $p_{r_{pot}}$. This effect will eventually be felt in the reattachment region causing the bounding streamline to return to the shoulder; however, due to the fact that as the fluid particle possessing this lower $p_{r_{pot}}$ constantly extracted from the separated region and as a consequence, $p_{r_{pot}}$ was constantly decreasing. Therefore the bounding streamline will lie below the escape streamline which as determined earlier is the condition for mass influx into the separated region. Again after a certain time this mass influx will cause the separation point to reverse its direction and x_1 will decrease. Consequently, $p_{r_{pot}}$ will increase which will eventually cause the bounding streamline to reverse its course and the process will repeat itself. This hypothesis will be referred to as the energetic shear layer hypothesis.

Briefly, the energetic shear layer hypothesis derives its name from the fact that for certain conditions the shear layer supplies a potential energy at reattachment which surpasses the ability of the model geometry to supply the necessary required pressure. Due to the fact that the separation and reattachment points are separated by a finite distance and "communicate" by means of fluid particles traveling at finite velocities, these processes remain

out of phase. In the following sections use will be made of the findings of chapters 3 and 4 to substantiate this new hypothesis.

5.2.3 The shock envelope history

The history of the changing shape of the shear layer and hence the shock envelope may be deduced by using the energetic shear layer hypothesis. To aid in this discussion use is made of a symbolic diagram which represents the bounding streamline as a locus of vectors. The magnitude of each vector represents the velocity, z_j, that will be attained in the region of reattachment based on the conditions at separation. For the case of leading edge separation this distinction need not be made since z_j is a constant along the bounding streamline; however, for the case of separation with a finite non dimensional shear length, λ, the velocity of a given particle increases as it progresses downstream. Finally, it must be emphasized that for the Strouhal numbers of interest, one must pay strict attention to the dynamics of the flow and not fall into the trap of making quasi-steady flow assumptions.

The analysis is began at that point in time corresponding to Fig. 42e, shown schematically in Fig. 60a. Because leading edge separation has been in existence for approximately a third of a cycle prior to this moment it is surmised that the velocity is uniform along the bounding

streamline at its maximum value. As a result of the abundance of energy present in this configuration, $p_{r_{pot}}$ exceeds the maximum possible p_{r_r} causing a streamline below the bounding streamline with the appropriate value of $p_{r_{pot}}$ to stagnate at the shoulder and thus become the new escape streamline. This causes the mass reversed to be less than the mass scavenged and hence a net mass flux out of the separated region. After the interval of time required for this to be felt upstream, the separation recedes towards the model face.

As the length of attached boundary layer, x_1, increases, the non-dimensional shear length, λ, decreases from effectively infinity to a finite value, reducing $p_{r_{pot}}$. Also note that as the separation process relaxes to a free interaction, the separation angle should also decrease. This situation is depicted in Fig. 60b. Here the downstream portion of the shear layer still possesses the excess $p_{r_{pot}}$ which began the mass loss. This is a result of the particles on the bounding streamline moving at a finite velocity between separation and reattachment causing a time lag. In Fig. 60d the last of the over energetic fluid has passed downstream, and now the energy deficient fluid is beginning to arrive in the reattachment region and is being reversed into the separated region. This corresponds to Fig. 42b.

Note also the increase in x_1 has further decreased α causing the concave shape and the maximum slope of the shear layer at the shoulder corresponds to the maximum pressure in the cycle.

After the time for the change in conditions of the separated region to be felt at the separation point, this point is forced towards the spike tip as illustrated in Fig. 60d. Once again the phasing of the separation and re-attachment processes will allow the mass influx to continue even after the separation point has attained the spike tip causing the convex separated region depicted in Fig. 60e. This configuration causes again mass loss to the separated region which allows the relaxation to the starting shape. During this time the pressure continues to fall at the model face until the shear layer begins again to increase its slope.

This illustrates that the energetic shear layer hypothesis may be used to explain qualitatively the shock envelope history and as a consequence the maximum and minimum pressures obtained experimentally on the model face. With some degree of confidence now established one may proceed to obtain quantitative comparison.

5.2.4 The frequency of oscillation

In the formulation of the energetic shear layer hypothesis it was stated that the separation and reattachment

processes "communicate" over a finite distance by means of "messenger" fluid particles which form the bounding streamline. This suggests that by properly choosing a length and velocity characteristic of this process one may obtain a functional relationship for the frequency of oscillation. That is, frequency is proportional to the ratio of velocity to length.

The obvious choice for the characteristic distance is the distance between the separation and reattachment point which is the length of free shear, x_2 . Referring to Figs. 2, 30 and 42, one may approximate x_2 as a constant equal to the distance between the spike tip and model shoulder. Thus

$$\frac{\ell}{x_2} \simeq \cos\alpha \tag{5.18}$$

where ℓ is the spike length and α the angle formed by the spike and the straight line from the spike tip to body shoulder. This is an approximation that is most valid near the O/S boundary or sufficiently far from the P/O boundary.

The obvious choice for the characteristic velocity would be the dividing streamline velocity, u_j. Unfortunately, it is not possible to make an approximation for this parameter based on experiment. However, as an alternative one may define a time averaged characteristic velocity as

$$\bar{u}_c = \frac{1}{t_{cycle}} \int_0^{t_{cycle}} u_j(t)\, dt \qquad (5.19)$$

Furthermore, since u_j is known to have a maximum value, one may express $u_j(t)$ as a time dependent fraction of this value.

$$\bar{u}_c = \frac{0.587u_2}{t_{cycle}} \int_0^{t_{cycle}} f(t)\, dt \qquad (5.20)$$

Defining the constant of proportionality somewhat arbitrarily

$$F \equiv \frac{1}{t_{cycle}} \int_0^{t_{cycle}} f(t)\, dt$$

one obtains from Eqs. 5.18 and 5.20

$$\frac{S\ell}{D} = 0.587F \left(\frac{u_2}{u_1}\right) \cos\alpha \qquad (5.21)$$

A comparison between the above analysis and experiment is shown in Fig. 61. In this figure the experimental results are represented by the curve fit of the data (Eq. 5.1) and shown as a broken line curve. Against this is plotted Eq. 5.21 for discrete values of F between 0.3 and 0.5. The value of 0.375 shows very good agreement with experiment

for the range $1.0 \lesssim \frac{\ell}{D} \lesssim 2.5$. This provides one piece of evidence supporting the energetic shear layer hypothesis.

5.2.5 Pressure wave amplitude as a function of $\frac{\ell}{D}$

The energetic shear layer hypothesis derives its name from the fact that spike lengths below a certain value create a free shear layer which possesses a $p_{r_{pot}}$ greater than the maximum possible reattachment pressure dictated by the geometry at the model shoulder, p_x. In what follows use will be made of this point to develop a correlation between the pressure amplitude of the oscillation wave and the physical parameters describing the model geometry and flow conditions.

To begin with the mismatch or over pressure at reattachment is assumed proportional to the amplitude of the pressure wave Δp measured at half the radial distance.

In essence this is a fairly mild assumption since the shoulder and face are at the same streamwise position and no requirement is made as to the absolute values of pressure or the phase angle between these positions. For the present the constant of proportionality will be assumed to be unity, thus

$$\Delta p = p_{r_{pot}} - p_x \tag{5.22}$$

Verification of Eq. 5.22 is complicated by the fact that p_x is not analytically soluble. One may, however,

circumvent this obstacle by extending the approximation (see section 5.1.5) that p_x is constant near the O/S boundary to include unstable flow. This is not unreasonable since the angle of the shear layer relative to the body at reattachment varies little during a cycle and basically the same arguments hold as to the behavior of p_x. Since one may not obtain a value of p_x by either analysis or measurement it must be inferred. This is done by measuring Δp for a configuration with oscillation at a known value of $\frac{\ell}{D}$. Note this value of ℓ/D should be as close to the O/S boundary as practically possible in order that the approximation just mentioned holds. Then based on the assumption of a straight shear layer reattaching at the body shoulder and an appropriate separation process, e.g., leading edge, one may evaluate the value of $p_{r_{pot}}$ (Eq. 5.5) at the given $\frac{\ell}{D}$ knowing the free stream conditions. Substituting Δp and $p_{r_{pot}}$ into Eq. 5.22, the value of p_x is obtained.

An interesting point brought out in this analysis was that the value of p_x was agreed upon to within a few percent by three techniques of evaluating $p_{r_{pot}}$ discussed presently. The values for the $\Phi_D = 90°$ model represented 21.5%, 22.6% and 22.8% of the pitot pressure. The $\Phi_D = 70°$ model showed a somewhat larger variation using only two techniques values of p_x at 22% and 25.7% of the pitot pressure respectively.

It is not surprising that for a given body cone angle, Φ_D that the value of p_x is agreed upon. However, the fact that p_x, which is inferred from experiment, seems to be constant for Φ_D greater than the shock detachment angle substantiates the argument that p_x is approximately a constant.

Therefore, once p_x is evaluated, it is necessary to determine $p_{r_{pot}}$ as a function of $\frac{\ell}{D}$ and substitute into Eq. 5.22 with p_x a constant to obtain Δp as a function of $\frac{\ell}{D}$. There are different ways of calculating $p_{r_{pot}}$ as a function of $\frac{\ell}{D}$. They all, however have in common shoulder reattachment. The first method used is the free interaction method described in section 5.1.6. This is shown as the curve labeled I in Fig. 62. Due to the singularity at $x_1 = 0$ the numerical technique used breaks down at $\frac{\ell}{D} = 2.2$. The broken line extending from this point is meant to be used for identification purposes and not as an extrapolation.

The second method is based on the idealized case of leading edge separation. That is, the shear layer is a straight line from the spike tip to the body shoulder. The separation angle is a simple function of $\frac{\ell}{D}$ and hence the free stream conditions down stream of the separation shock are known. The ratio of dividing streamline velocity to the free stream velocity in this region is also known, $z_j = 0.587$ (section 5.1.7) and using Eq. 5.5 $p_{r_{pot}}$ is obtained.

The results of this method are shown in Fig. 62 as curve II.

Finally, in order to investigate the effects of finite spike radii, the separation process was assumed to take place at the cone-cylinder junction of the spike tip. The spike radius, r_a, and cone angle of the spike ($\alpha_s = 15°$) provided a value of x_1. Again the shear layer extended from separation to the model shoulder so that α and hence M_2 and p_2 were readily calculated. The non-dimensional shear length, λ, was evaluated and from this (Eq. 5.8 with λ replacing ξ) z_j was obtained and then $p_{r_{pot}}$ (Eq. 5.5). These results are shown in Fig. 62 as curve III.

Comparing the slopes at the point where p_x was evaluated $\frac{\ell}{D} = 2.25$, curve I is seen to be the steepest. Curve III is also steeper than curve II. This indicates that finite lengths of attached boundary layer enhance the increase of Δp near the O/S boundary. The difference in the three methods is however quite small except very far from the point of evaluation and even then not so different as to be contradictory.

Methods II and III are shown compared against experiment in Fig. 63 and 64. These represent the upper and lower bounds of body cone angle which produced monotonic pressure wave amplitude distributions with $\frac{\ell}{D}$. Agreement is seen to be good between the O/S boundary and $\frac{\ell}{D} \simeq 2$ for

$\Phi_D = 90°$ and $\frac{\ell}{D} = 1.5$ for $\Phi_D = 75°$. This represents approximately the upper 50% of the range of $\frac{\ell}{D}$ producing oscillation in both cases. In the lower half of the oscillation range of ℓ/D the approximations that were involved, such as stationary separation point and constant value of p_x, are violated causing large differences between experiment and this simple analysis. However, the agreement near the O/S boundary demonstrates the proportionality of the overpressure of the energetic shear layer hypothesis to the pressure wave amplitude measured. Although this analysis is not conclusive, it lends to the credence of the energetic shear layer hypothesis.

5.2.6 Mach number effects

At an undisturbed free stream Mach number of 2.21 positive identification of oscillation was made with only one body cone angle, $\Phi_D = 70°$, and then for the limited range $0.80 \lesssim \frac{\ell}{D} \lesssim 1.05$ (section 3.4.1.3). In contrast, oscillation at Mach 6 was observed for $50° \lesssim \Phi_D$ 90° for ranges of $\frac{\ell}{D}$ typically of the order of one. Recalling that one of the necessary conditions for oscillation, as outlined in the energetic shear layer hypothesis, is leading edge separation, it is now possible to offer an explanation for the above mentioned Mach number effect.

Leading edge separation as discussed in section 5.1.7 was seen to occur only for a limited range of Φ_D depending on the undisturbed free stream Mach number and the state of the free shear layer. In particular, the maximum Φ_D which would support leading edge separation was seen to decrease sharply as Mach number decreased below approximately Mach 3. (Figs. 57 and 59). Leading edge separation was observed for the $\Phi_D = 90°$ model even though it is concluded in Figs. 57 and 59 that Φ_D must be less than 65° in order for this to occur. The reason for the seeming discrepancy is given in section 5.1.5 where it is pointed out that shoulder reattachment provides a means of reducing the effective turning angle or body cone angle. At Mach 2.21 oscillation appears only after Φ_D is decreased to 70° which according to Brower's analysis (section 5.1.6) is equivalent to a little more than 45°. This shows that the 20° reduction in actual body cone angle agrees well with that of the effective cone angle providing one final piece of supporting evidence for the energetic shear layer hypothesis.

5.2.7 Oscillation at $\Phi_D \leq 75°$

In sections 3.4.1.4 and 3.4.2.4 it was observed that both the frequency and amplitude of the oscillation pressure wave in the series II tests were affected differently by changes in the spike length for body cone angles $\Phi_D \leq 75°$

than for $\Phi_D > 75°$. At first glance this might be interpreted as a violation of the energetic shear layer hypothesis. However, it should be kept in mind that this hypothesis explains only the existence of the oscillation mechanism and not its dependence on such parameters as body cone angle.

It was observed experimentally that when this divergence in the character of oscillation takes place that the angle between the shear layer and body face, β, is very nearly equal to 45° for all series II results. The exact significance of this is not understood at present, however, this would seem to suggest that there occurs a significant change in the reattachment process for certain conditions. That is, a secondary effect for $\beta > 45°$ may become of primary importance for $\beta < 45°$.

5.3 Pulsation

The mechanism of the pulsation mode is discussed followed by the presentation of a procedure to calculate the time of a pulsation cycle. Results of this procedure are then compared with experiment.

5.3.1 The pulsation driving mechanism

The mechanism which drives the pulsation mode has been recognized for some time to be the intersection of the conical foreshock and the bow shock of the blunt body. Mair (Ref. 26) and Maull (Ref. 27) observed that this

intersection would result in the high pressure behind the bow shock to cause mass flow to the low pressure region behind the conical shock. These qualitative remarks, although enlightening, do not provide a complete understanding of pulsation. Panaras (Ref. 63) made calculations of the resulting flow field of such an intersection using shock hodographs, more commonly known as "heart" diagrams, based on the assumption that this intersection could be considered quasi-steady. He found that for a hypersonic free stream the resulting flow exhibited two important features.

To illustrate these features a heart diagram is presented in Fig. 65 for an undisturbed free stream of Mach 6. Note that for the purpose of this discussion the convention of positive deflection angle, δ, denotes flow away from the body axis. The first important point is that the resulting flow is directed at an angle of little more than 20° towards the axis. The second and possibly more important point is that the flow in region 4 (see sketch at top of Fig. 65) is supersonic. The vertical bars at the shoulder of each heart represent the sonic point. Flow below this point is supersonic and flow above is subsonic. Recalling that the separated region itself is a low speed flow, region 4 is seen to be a supersonic annular flow bounded by two regions of subsonic flow and directed towards the body axis.

Before drawing conclusions it is necessary to discuss the supersonic case. Figure 66 shows that the results of a quasi-steady heart diagram yields results that do not exhibit the features found in the hypersonic case. Specifically, region 4 is subsonic rather than supersonic. Even though the deflection of region 4 is towards the body axis, the absence of the high level of kinetic energy would alter the nature and/or level of the pressure wave. However, experimental findings have shown pulsation to be manifest almost identically in both supersonic and hypersonic undisturbed free streams.

This discrepancy leads one to question the validity of the quasi-steady assumption and in fact, as was pointed out by East and Wilkinson (Ref. 34) time dependent flows characterized by Strouhal numbers of the order of 0.01 or greater are not amenable to quasi-steady analysis. This suggests that a closer look at the time dependent nature of the flow is needed. On examination of Figs. 46c through 46e and 47d through 47f it is observed that the separation point is indeed traveling up the spike towards the tip. This is illustrated in Fig. 67. In other words, the oblique shock is moving forward in the free stream direction and is in effect increasing the undisturbed free stream Mach number.

For the purposes of the present study the concept of a time dependent or "dynamic" heart diagram was used to further investigate the driving mechanism of the pulsation mode. A dynamic heart diagram may be thought of as the calculation of a shock-shock intersection with one shock moving at some constant velocity relative to the other. In Fig. 49 is seen a broad, somewhat hazy region or straight line, also represented in Fig. 50 as the cross hatched region between $\tau = 0$ and $\tau = 0.4$. This line is the path of the foreshock with respect to the body in the x-t plane. The slope of the path in the x-t plane is equal to the velocity which in this case means the velocity of the foreshock is constant as a good approximation. Thus the calculation dynamic heart diagram may be used in the analysis of the pulsation mode.

The calculation of a dynamic heart diagram is analogous to the calculation of a conventional diagram. A fundemantal difference does exist; the Mach number of the foreshock relative to the body ΔM is added to the undisturbed free stream Mach number M_1 to obtain an effective Mach number M_e of the foreshock. M_e is the velocity of the foreshock with respect to the undisturbed free stream.

The value of M_e may be obtained directly from the x-t diagram of Fig. 50 for the hypersonic case under study. Figures 46 and 47 show little variation in the separation

angle α or the shock angle β. Thus an alternative means of determining M_e exists since M_e is a known function of α and β (e.g., Ref. 45). This indirect method of calculating M_e was first used by Mair (Ref. 26). Note the latter method is best suited to moderate to low supersonic flows due to the relative insensitivety of M_e to the inherent inaccuracies of obtaining values of α and β. Both methods were found to agree reasonably well on the value of M_e. It is interesting to note that the foreshock Mach number relative to the body represented 27% and 33% of the undistrubed supersonic and hypersonic freestreams respectively.

After M_e is determined, two halfs of hearts are calculated and plotted for both M_1 and M_e on a single set of pressure-deflection angle axes. This is done in Figs. 68 and 69 with the half heart shown by a solid line representing the M_1 heart and the broken line half heart representing the M_e heart. The initial deflection angle δ, is, of course the separation angle α which is obtained from photographs of the flow. The second broken line half heart to the β is constructed on a pressure axis with its origin at δ_1 as is done for the calculation of the conventional diagram.

Next the vector $\overline{\Delta M}$ is vectorially added to the Mach number M_4 in region 4 relative to the shock. The result is M_4 relative to the body as shown at the bottom

of Fig. 67. The deflection behind the moving foreshock relative to the body is then used to "correct" the second broken line half heart shown by the solid lines capped with arrow heads. These lines continue to $\delta_4 = \pm 180°$ at which point the respective values of pitot pressure are achieved. Because the bow shock is stationary with respect to the body during the time being considered the M_1 half heart is left unchanged. Thus the intersection between the M_1 half heart and the arrow capped line denote the conditions in regions 3 and 4 respectively.

The results shown in Figs. 68 and 69 indicate that the resulting flow fields of both the supersonic and hypersonic cases exhibit a supersonic region 4 directed towards the body axis. This demonstrates the cause for the similarity of pulsation in these two speed regimes. That is, the basis of the driving mechanism of pulsation is the efficient compression of a supersonic stream (region 4) towards the body axis in the vicinity of the face. This in turn creates a region of high pressure gas supplying the impetus for the subsequent rapid expansion of the foreshock.

Also brought out with the use of the dynamic "heart" diagram analysis is the importance of the movement of the separation point especially at moderate supersonic Mach numbers. In effect, this increment to the undisturbed free stream Mach number is responsible for the existence

of a supersonic annular region bounded by two subsonic regions. This velocity increment reduces the deflection towards the models axis which increases the Mach number in region 4. Since the static pressure is nearly a constant behind strong conical shocks this is equivalent to an increase in the total pressure in region 4. At Mach 2.21 this increases the total pressure by a factor of more than two while at Mach 6 the increase is more than a factor of 4, a significant increase.

Experimental evidence of the existence of a supersonic annular region is seen in Figs. 3b, 46d, 46c and 34c. These figures show region 4 as a light region or line directed towards the body axis. Further evidence of the existence of a supersonic annular region was obtained using a sublimation technique, a technique more generally used in steady flows to detect regions of high shear and or heat transfer. Figure 70 shows results obtained by Loll (Ref. 64) which reveals a dark circle at a radius of $\frac{D}{4}$ indicated by arrows. This is the region of high shear and/or heat transfer such as would most probably result from the high kinetic energy flow emanating from the shock-shock intersection directed towards the model face. This region was seen to coincide more or less with an extension of the line originating at the shock-shock intersection as determined from photographs.

Thus, one may conclude that the shock-shock intersection is time dependent rather than quasi-steady resulting in a supersonic flow providing the driving mechanism behind the pulsation mode at both supersonic and hypersonic speeds. Also the dynamic nature of this flow enhances the efficiency of this process in terms of the total pressure in region 4.

5.3.2 A model of pulsation

In the preceeding section a discussion was given on how the strong shock - weak shock intersection caused an reversal of mass towards the body axis. This gas will subsequently expand into the foreshock region as shown in Figs. 46e through 46g and Figs. 47f through 47i. As a result of the expansion the shock-shock intersection will be displaced in the direction of the body shoulder and eventually beyond (Figs. 46h - 47i). Once this occurs there no longer exists a means to reverse mass into the foreshock region and therefore this region collapses.

One may construct a simple physical model of pulsation mode based on the above observations and the conical shock relations, which depicts the general features of the instability. This is accomplished by first dividing the cycle into two parts similar to the approach taken in the analysis of oscillation. One portion, Δt_1 is defined as the time during which mass is added to the foreshock region.

The other portion, Δt_2, is the time during the collapse of the inflated foreshock. The sum of these time increments represents the time for one complete cycle.

The calculation of the first time increment, Δt_1, is based on a tabulation of mass and the knowledge of mass influx. In order to carry out this calculation a few simplifying assumptions based on experiment are made. A right circular cylindric control volume is constructed with its cross section equal to that of the body and its height equal to that of the spike length (Fig. 71a). For the present the cone body angle, Φ_D, will be taken to be 90° since the difference in the control volume for $60° \leq \Phi_D \leq 90°$ is negligible. Thus the mass at the beginning of the cycle may be calculated knowing the free stream conditions, the separation angle which represents the effective cone angle, and the shock stand-off distance, x_s. This is represented in Fig. 71b. However, since the temperature in volume 2b is almost equal to the free stream total temperature and the pressure equal to the cone static, the density ρ_{2b} is less than the free stream static density ρ_1 while the density in the shock layer, ρ_{2a} is greater than ρ_1. Thus the average density in region 2 will not differ greatly from ρ_1. Additionally the fact that the conical volume is relatively small compared to the entire control volume allows one to simplify the mass tabulation by neglecting

the deviations in the conical region from free stream conditions. (Fig. 70c). This point was verified numberically by studying a range of separation angles in the neighborhood of those measured experimentally.

The expression for the initial mass, m_i, may therefore be written as

$$m_i = [\rho_3 x_s + \rho_1 (\ell - x_s)] \frac{\pi D^2}{4} \tag{5.23}$$

Next the mass at the end of the time increment Δt_1 is calculated based on two more simplifications. First the foreshock is assumed to have expanded in such a manner as to occupy the entire control volume at the end of Δt_1 as represented in Fig. 71d. This is justified by experiment as seen in Fig. 46h.

Secondly, the mass in the entire control volume is initially considered to be of uniform density which in reality is not the case. Due to the highly complex nature of the flow at the time in question a reference density, ρ_{3ref}, will be used. The expression for the mass at the end of Δt_1 is given as

$$m_f = \rho_{3ref} \ell \frac{\pi D^2}{4} \tag{5.24}$$

There are three possibilities readily available for the value ρ_{3ref}. These are the stagnation, static, and sonic conditions behind a normal shock in a known free

stream. The first may be ruled out as unrealistic due to the dynamic nature of the flow. As will be seen the sonic value will yield results that agree best with the details of one particular experiment, but that the static value seems to show a more general overall agreement.

In order to obtain a value of the mass influx during Δt_1, the concept of a capture stream tube is introduced. This tube is formed by the locus of streamlines which stagnate on the body face. The flow inside this tube will be reversed into the foreshock region, hence the term capture stream tube. The diameter of this tube will be nearly coincidental with the shock-shock intersection due to the high kinetic energy flow directed towards the model axis, as explained in the previous section. This is shown schematically in Figs. 72a and 72b. The limiting diameter of the capture stream tube will be that of the model itself. In fact, as illustrated in Fig. 46e and 47f the shock-shock intersection takes place almost directly above the shoulder throughout Δt_1. Therefore, although the capture area will vary slightly as the shock-shock intersection displaces laterally as described in section 5.3.1 the area of the capture stream tube will be taken equal to that of the body for convenience. This is not a bad approximation since the shock-shock intersection is at the shoulder for the most part of its existence. Thus, the mass influx may be approximated as

$$\dot{m} = \rho_1 u_1 \frac{\pi D^2}{4} \tag{5.25}$$

Mass flux is defined as

$$\dot{m} = \frac{\Delta m}{\Delta t} \tag{5.26}$$

where Δt is Δt_1.

Combining Eqs. 5.23 through 5.26, one obtains an expression for the time increment required to fill the foreshock to its expanded configuration.

$$\Delta t_1 = \frac{\frac{\rho_3}{\rho_1}\left[\left(\frac{\rho_{3_{ref}}}{\rho_3}\ell - x_s\right) - (\ell - x_s)\right]}{u_1} \tag{5.27}$$

Before continuing it should be pointed out that the use of a stream tube capture area leading to Eq. 5.27 is a convenient simplification based on experiment. This approach neglects some detail and time dependence of this portion of the problem. For instance, Fig. 72a shows all the mass added to the foreshock region to be reversed near the face. A short time later a small portion of normal shock is created at the tip (Fig. 46f) as illustrated schematically in Fig. 72c. This shows that the central core of the stream tube will be added to the foreshock region directly after passing through the normal shock while the remaining mass passing through an annular conical shock will continue to be reversed near the face. Figure

72d depicts the mass addition near the end of the time increment under discussion. At this point all the mass is added at the tip after passing through the normal shock. In all cases the capture area remains of constant diameter equal to approximately that of the model.

The calculation of the second time increment, Δt_2, is based on a time dependent calculation of the isentropic expansion of the foreshock. For this purpose the cylindrical shock envelope achieved in the previous step develops according to the normal shock relation. The cylindrical portion expands in the radial direction and the portion normal to the spike displaces in the streamwise direction. That is, the shock velocity and direction are determined by the static pressure ratio across it. This is done by determining the Mach number in front of and behind the shock. These are found from the following relations

$$M_1 = \left\{ \frac{6\frac{p_3}{p_1} + 1}{7} \right\}^{\frac{1}{2}} \tag{5.28}$$

and

$$M_3 = \left(\frac{M_1^2 + 5}{7M_1^2 - 1} \right)^{\frac{1}{2}} \tag{5.29}$$

where the subscripts 1 and 3 refer to the regions before and after a normal shock respectively (Fig. 73a).

The velocities are obtained by multiplying each Mach number, M, by the appropriate speed of sound, a. For a perfect gas

$$a = \sqrt{\gamma RT} \tag{5.30}$$

and the static temperature, T, is obtained from an isentropic expansion from the total conditions, thus,

$$T = \frac{T_0}{1 + \frac{\gamma - 1}{2} M^2} \tag{5.31}$$

Recalling that the compression by a shock is an adiabatic process, one may write

$$u_i = \frac{M_i \sqrt{\gamma R T_0}}{\sqrt{1 + \frac{\gamma - 1}{2} M_i^2}} \tag{5.32}$$

where i = 1, 3.

In order to obtain the velocity relative to the body, account must be taken of the free stream velocity. In the radial or lateral direction the free stream velocity is by definition zero, and the shock velocity in the lateral direction, $u_{s\ell}$, relative to the model is given by Eq. 5.32 in conjunction with Eq. 5.28 with the index equal to 1 as illustrated in Fig. 73b. Thus, $u_{s\ell}$ is seen to be a function only of the static pressure ratio. In the streamwise direction, u_1 is non zero and the shock velocity will be

the difference between this value and that required to sustain the static pressure ratio. Thus,

$$u_s = u_1 - u_{s\ell} \tag{5.33}$$

It was, however, observed experimentally that the portion of the shock normal to the free stream direction remained stationary for a finite period of time before the actual collapse began. This is due, of course, to the fact that at the end of the foreshock expansion a considerable part of the mass in this region has a velocity vector in directions other than that of the free stream, in fact, opposed to it. Therefore, a certain time period is required to overcome this momentum. As a first order estimate this is taken to be the time for an acoustic wave to propagate radially from the spike to the shock surface

$$t_c = \frac{D}{2\sqrt{\gamma R T_3^*}} \tag{5.34}$$

Apart from this small deviation the shock collapse is a continuous process.

Thus, the volume of the foreshock will change during the collapse period. By using a sufficiently small time differential, t, one may model this using the following numerical technique:

$$D_c(t_{i+1}) = D_c(t_i) + 2u_{s\ell}(t_i)\,\delta t \qquad t_i \geq t_0$$

$$\ell_s(t_{i+1}) = \ell_s(t_i) - u_s(t_i)\,\delta t \qquad t_i \geq t_c \tag{5.35}$$

where D_c is the diameter of the cylindrical portion of the expanding shock and ℓ_s is the streamwise location of the normal portion of the expanding shock. The initial conditions at $t = t_0$ are simply those at the end of the foreshock expansion or

$$\begin{aligned} D_c(t_0) &= D \\ \ell_s(t_0) &= \ell \qquad\qquad t_0 \leq t \leq t_c \\ \rho_3(t_0) &= \rho_{3_{ref}} \end{aligned} \tag{5.36}$$

The volume of the foreshock is

$$V = \frac{\pi}{4} D_c^2\, \ell_s \tag{5.39}$$

Based on the shock velocities, the free stream vlocity and their respective directions one may determine the amount of mass added during a given time interval, δt. This is expressed simply as

$$m_{in} = \rho_1 \left[\frac{\pi}{4} D_c\,(u_1 - u_s) + \pi D_c\, \ell_s u_{s\ell}\right]\delta t \tag{5.38}$$

The first term in the parenthesis is due to mass addition

through the normal shock and the second term comes from mass entrained by the lateral expansion. The mass escapes from the collapsing foreshock through an annular area formed by the body and the cylindrical shock. This area is taken to be planar and normal to the free stream direction. At the beginning of a cycle the mass flow will be choked or sonic due to the large pressure ratio across the exit plane.

Upon examining the effective angle between the cylindrical shock and the free stream due to the radial velocity of the former, one may show by vector addition that there is formed an annular region of supersonic flow. This point may be verified at least qualitatively, by referring to Fig. 48c which shows the flow in the foreshock region to be uniform except for an inverted conical region at the spike tip which is the subsonic flow which has crossed the normal shock in this region. The lack of large disturbances indicates the flow will pass downstream more or less unoffected except that flow which will encounter the model face. Therefore, it will be assumed for the purposes of this procedure that the mass crosses the exit area such that

$$m_{out} = \rho_3^* u_3^* \frac{\pi}{4} (D_C^2 - D^2)\, \delta t \qquad \text{for } M_3 < 1$$

and (5.39)

$$m_{out} = \rho_3 u_3 \frac{\pi}{4} (D_C^2 - D^2)\, \delta t \qquad \text{for } M_3 \geq 1$$

The mass at any time t_{i+1} may be obtained from the mass calculated in the previous time interval.

$$m(t_{i+1}) = m(t_i) + m_{in} - m_{out} \tag{5.40}$$

From which it is a simple matter to calculate the density

$$\rho_3(t_{i+1}) = \frac{m(t_{i+1})}{V(t_{i+1})} \tag{5.41}$$

This assumes that the entire mass is moving at the same velocity and there exist no density gradients. This is very nearly the case as seen in Fig. 46b. The relatively even photographic intensity and lack of shocks or density gradients which would otherwise be shown as dark lines bear this point out.

The pressure, as was stated, is determined assuming an isentropic expansion:

$$p_3(t_{i+1}) = K\, \rho(t_{i+1})^{\gamma} \tag{5.42}$$

where

$$K = p_3(t_0)\, \rho_3(t_0)^{-\gamma}$$

This pressure is then used in the pressure ratio to determine the shock displacement during the following time step. This process is continued until the shock normal to the free stream has reached the shock stand-off distance,

$$\ell_s = x_s \tag{5.43}$$

This results in a shock envelope equivalent to that at the start of the first time interval. Note that Fig. 50 shows the shock merger to take place below the shock stand-off distance which means Eq. 5.43 is slightly in error. This is, however, expected to be small and can be neglected in light or foregoing approximations.

Before proceeding to a comparison of the results of such a technique with experiment, it is useful to examine some details of the numerical results. In Fig. 74 are shown the results of Δt_2 calculated with $\rho_{3_{ref}}$ taken as both static and sonic. There is seen to be little difference in the final result, but on examination of the results of Δt_1, the sonic reference agrees much better with experiment than does the static. Also illustrated in Fig. 74 is the fact that the shock collapse velocity attains only a fraction of the free stream velocity. In fact, the terminal value was experimentally evaluated to be 55% of the free stream velocity and the numerical results give a value of 50%. The cause for this relatively low velocity is that the mass flux out of the collapsing shock region is choked resulting in the static pressure in this region remaining approximately 10 times that of the free stream.

Also in the way of qualitative agreement is the maximum radial diameter of the shock which from experiment

was seen to be roughly twice the body diameter (Figs. 46 and 47). From the analysis the diameter is likewise twice the body diameter about one third the way through the collapse. In both theory and experiment the shock continues to expand, but in experiment the diameter becomes a function of the streamwise position and further comparison is not possible.

In Fig. 75 are presented values of frequency in terms of the Strouhal number from the above described model and the curve fits obtained from experiment. Notice that the two theoretical curves are labeled with symbols ∞ and * representing $\rho_{3_{ref}}$ taken as the static and sonic values respectively. Note also that the comparison is made over a limited range of $\frac{\ell}{D}$'s. This is due to the fact that the model is valid only when the foreshock expands in the prescribed manner. This was observed to coincide with $\frac{\ell}{D}$'s roughly twice the shock stand-off distance. Although the agreement between experiment and the model are less than excellent, it is important and encouraging when one recalls that there are no empirical inputs that there is an order of magnitude agreement. At the larger values of $\frac{\ell}{D}$'s, near the P/O boundary, there is even what may be considered engineering accuracy. This, however, depends on the $\rho_{3_{ref}}$ one chooses. Overall it appears that the static value gives best agreement, but it should be kept in mind that the sonic value agreed best with the detailed

experiment. It is seen that the trend of increasing frequency with decreasing spike length is agreed upon but again not in a precise manner. It appears that an under-prediction of Δt_1 based on an overestimated capture area or an under-prediction of Δt_2 caused by neglecting momentum at the beginning of the cycle result in Strouhal number considerably above experiment. Either of these points could be corrected with empirical inputs.

6. CONCLUSIONS

The phenomenon of unstable axisymmetric separation on spiked cone has been shown experimentally to be comprised of two basic modes, oscillation and pulsation, in agreement with the existing literature. As the spike length is decreased from a sufficiently large value ($\frac{\ell}{D} \simeq 3$) on a relatively large angle cone ($\Phi_D > 75°$) in a hypersonic flow, the separated flow passes smoothly from the stable regime to the oscillation mode. Oscillation is distinguished by the regular variation of the foreshock envelope between a convex and a concave shape. Further decreasing the spike length results in an abrupt change in the pulsation mode. The actual value of $\frac{\ell}{D}$ at which this event takes place, $\ell^{\times}/D$, exhibited a hysteresis effect, i.e., $\ell^{\times}/D$ depended on the regime from which it was approached.

The pulsation mode is manifest as the excursion between two radically different shock envelopes. One envelope consists of a conical foreshock emanating from the spike tip and intersecting the bow shock caused by the blunt body. The other extreme envelope is a single bow shock which passes through the spike tip. The process of transformation is not, however, a simple movement of the bow shock but a periodic expansion and collapse of the foreshock. In contrast the oscillation shock envelope simply "flexes" between its extremes.

Pressure measurements made on the face of spiked cones were recorded as wave forms which were analyzed in terms of the time averaged frequency, f, and amplitude, Δp. The Strouhal number, $S = \frac{fD}{u_1}$, of oscillation at hypersonic speeds ($\Phi_D > 75°$) was found to vary inversely with $\frac{\ell}{D}$ (Eq. 3.1) and to be independent of body cone angle, Φ_D, and Reynolds number, Re_D. Oscillation was identified for the first time at a moderate supersonic Mach number M = 2.21. These results indicated that S is also indpendent of Mach number. The amplitude, Δp, was found to be not only a function of $\frac{\ell}{D}$ but Φ_D and Re_D as well. The maximum value of Δp in the oscillation mode was of the order of one tenth the pitot pressure.

The pulsation Strouhal number was also found to be independent of Φ_D, Re_D, and M while decreasing linearly with $\frac{\ell}{D}$ (Eq. 3.2). Again Δp was a function of $\frac{\ell}{D}$, Φ_D and Re_D, but independent of M. The maximum value of Δp was of the order of the pitot pressure or ten times larger than that of the oscillation mode. The above findings agreed well with the limited data available for comparison.

The non dimensional spike length at which the onset of oscillation occurs, $\frac{\ell^*}{D}$, was found to be a function of Φ_D in hypersonic flow. The value of $\frac{\ell^*}{D}$ decreased as Φ_D decreased similar to previous investigations which had extrapolated this trend to $\frac{\ell^*}{D} = 0$ at Φ_D equal to the shock detachment angle. However, in the present study where much

more sensitive instrumentation has been used, oscillation was documented at a Φ_D less than the shock detachment angle. An examination of oscillation data showed the two necessary conditions for this mode of unstable flow are leading edge separation and shoulder reattachment. With these findings and a review of the calculation of large separated regions, an original hypothesis of the mechanism of oscillation was developed.

The energetic shear layer hypothesis, as it is called, is based on the conclusion that the separation creates a free shear layer which supplies a potential pressure of the bounding streamline at reattachment that cannot be supported by a shoulder reattaching flow. Due to an experimentally observed phase lag between the separation and reattachment processes there results a time dependent mass flux in and out of the foreshock region. Since one of the necessary conditions for oscillation was experimentally observed to be shoulder reattachment and since this type of reattachment has not yet been satisfactorily treated theoretically, calculations for the present of such things as stability boundaries are not possible. However, the viscous nature of the oscillation mechanism is clear and one may indirectly verify the validity of the hypothesis.

Verification was accomplished by making use of the energetic shear layer hypothesis to explain the experimental findings outlined above. For example, the oscillation shock

envelope history was recreated and the functional relation of S and $\frac{\ell}{D}$ was shown using this hypothesis. Further evidence was obtained by demonstrating the proportionality of the shear layer overpressure and Δp measured for spike lengths near the stability boundary. Also, it was shown that leading edge separation is created by ranges of Φ_D at supersonic Mach numbers smaller than the ranges hypersonic Mach numbers which offers an explanation for the limited range of geometric parameters which provoke oscillation at moderate supersonic Mach numbers. Finally, a tentative explanation, based on the balance of shear layer pressure and momentum, is given to account for the difference in the behaviour of the oscillation pressure wave for $\Phi_D > 75°$. The internal consistency of the above analyses and favorable comparison with experiment show that the energetic shear layer hypothesis is a sound physical model.

A detailed study of the pulsation shock envelope has verified to the conclusion of previous research that the strong shock - weak shock intersection is the mechanism which causes the mass influx to the expansion of the foreshock. A simple model was developed assuming that the collapse of the foreshock to be an isentropic process. Predicted frequencies show satisfactory agreement with the hypersonic experiments, but less favorable comparison with the supersonic experiments.

The dramatic difference in the two basic modes of unstable axisymmetric separated flow obviously is due to the difference in the nature of the driving mechanism. The mechanism behind oscillation is viscous in nature while that of pulsation is inviscid. As one might expect, the shock-shock intersection is more efficient than the shear layer in terms of mass reversal which explains why Δp is larger for pulsation than oscillation. On the other hand, characteristic velocities of both modes were found to be approximately one half that of the free stream and characteristic lengths of the order of the body diameter. Hence, the frequencies of these modes are of the same order of magnitude.

It should also be noted that although the driving mechanism of oscillation is viscous in nature, the frequency of oscillation was found to be independent of Re_D. This is because the characteristic, or dividing streamline, non-dimensional velocity achieves its maximum value with leading edge separation which is also a constant for laminar flow, independent of Reynolds and Mach number. Turbulent flow behaves similarly with the maximum non-dimensional dividing streamline velocity also independent of Reynolds number but dependent on Mach number. However, it was shown that, at least for free stream Mach numbers less than about 7, the increase in the dividing streamline velocity due to a transition to turbulent flow is relatively small. Thus, since the characteristic body dimension, D, is constant, the

frequency can be expected to be nearly independent of both Re_D and the state of the shear layer.

7. EPILOGUE

In the introduction examples were given of bodies encountered in practical applications which produce instabilities similar to those of the spiked blunt body. It is therefore appropriate to compare the results of flow field measurements over one of these more practical bodies with those of the present study in order to assess its usefulness.

The flow over an idealized ablation shape (Fig. 76) was studied at realistic reentry Mach and Reynolds numbers. This body shape was derived from experimental (Refs. 65 and 66) and theoretical (Refs. 67 through 70) investigations of ablating nose shapes during typical reentry profiles. The concave portion of the forebody was generated by an ellipse with the major axis perpendicular to the model axis. Four ported pressure taps were located along a single meridian of the forebody and instrumented with Kulite pressure sensors type XTEL-190-100. It was experimentally determined that these sensor and mounting configurations had a flat response to 13 kHz. Output was recorded on Tektronix 502A oscilloscopes. Further details are given in Ref. 24.

The tests were conducted in the von Karman Institute Longshot Free Piston Hypersonic Tunnel at a nominal free stream Mach number of 15 and Reynolds numbers based on body diameter of 4×10^{6} and 2×10^{6}. For details of the tunnel operation see Refs. 71 and 72.

A typical result of the high speed film technique described in section 2.4.3 is shown in Fig. 77; the time between frames is approximately 100 microseconds. The frame marked with the letter P indicates the time of peak tunnel reservoir conditions. Fig. 77 demonstrates clearly that the flow is unstable. Beginning with the second frame after the peak one observes a nearly conical shock created by the model nose which intersects the bow wave. In the next two frames the foreshock expands to a spherical shape until the bow shock is displaced beyond the body shoulder. The following frame shows the expanded foreshock to have commenced its collapse towards the model face, and in the next frame the original shock envelope is reestablished. This process is seen to repeat itself in a regular manner. Within the resolution of this film technique the cycle history is the same as that of the pulsation mode as discussed in section 4.2.1. Measurement of pressure made at station near the model shoulder, station 4 as denoted in Fig. 76, showed the Strouhal number and amplitude as a fraction of the pitot pressure to be 0.17 and 0.4 respectively.

In order to make comparison between these experimental results and those of the spiked cones it is necessary to arrive at values of the equivalent geometric parameters, $\frac{\ell}{D}$ and Φ_D, for the ablation model. The spike length, ℓ, was taken as the distance measured parallel to the body axis

from the point where the forebody forms a 90° angle with the free stream. The body diameter, D was measured at the model shoulder with a resulting value of $\frac{\ell}{D}$ just less than 0.5 for the model tested. The quantity Φ_D was taken to be 90° since this was the body angle in the region of the shoulder. Referring to Fig. 18 one sees that these geometric parameters correspond to those which produced the pulsation mode on the spike cone. Based on these geometric parameters the results of the study of spiked cones predict a Strouhal number of 0.21 (Fig. 35) and an amplitude of approximately 30% of the pitot pressure (Fig. 39). These values show reasonably good agreement with those measured as mentioned above.

Keeping in mind that not only the shape of the ablation model was significantly different from a spiked cone, but the conditions at which it was tested were also beyond the range of the present sutdy, the agreement between results is acceptable as an engineering guideline. One may now conclude that the results of the idealized case of the spiked blunt body are useful as a first order estimate of the pressure wave parameters of unstable flow over more practical shapes.

REFERENCES

REFERENCES

1. OSWATITSCH, K.: Der Druckruckgewinn bei Geschossen mit Ruckstossantrieb bei hohen Uberschallgeschwindigkeiten. Bericht Nr 1005, Forsch. & Entwickl. Heereswaffenamtes (Gottingen), 1944, also NACA TM 1140.

2. HUNCZAK, H.R. & KREMZER, E.J.: Characteristics of perforated diffusers at free stream Mach number 1.90. NACA RM E50B02, 1950.

3. FERRI, A. & NUCCI, L.M.: The origin of aerodynamic instability of supersonic inlets at subcritical conditions. NACA RM L50K30, 1951.

4. STERBENTZ, W.H. & EVVARD, J.C.: Criterions for prediction and control of ram-jet flow pulsations. NACA TN 3506, August 1955.

5. TRIMPI, R.L.: An analysis of buzzing in supersonic ram jets by a modified one dimensional non-stationary wave theory. NACA TN 3695, January 1962.

6. TRIMPI, R.L.: A theory for stability and buzz pulsation amplitude in ram jets and an experimental investigation including scale effects. NACA TR 1265, July 1953.

7. MOECKEL, W.E. & EVANS, P.J. Jr: Preliminary investigations of use of conical flow separation for efficient supersonic diffusion. NACA RM E51J08, December 1951.

8. EGGERS, A.J. & ALLEN, M.J.: A study of the motion and aerodynamic heating of ballistic missiles entering the earth's atmosphere at high supersonic speeds. NACA TR 1281, 1958.

9. EGGERS, A.J., DENNIS, D.H., RESNIKOFF, M.M.: Bodies of revolution for minimum drag at high supersonic airspeeds. NACA RM A51K27, 1952.

10. JONES, J.J.: Flow separation from rods ahead of blunt noses at Mach number 2.72. NACA RM L52E05a, July 1952.

11. BEASTALL, D. & TURNER, J.: The effect of a spike protruding in front of a bluff body at supersonic speeds. ARC R&M 3007, 1957.

12. HUNT, G.K.: Supersonic wind tunnel study of reducing the drag of a bluff body at incidence by means of a spike. RAE Report Aero 2606, May 1958.

13. CHAPMAN, D.R.: A theoretical analysis of heat transfer in regions of separated flow. NACA TN 3792, 1956.

14. STALDER, J.R. & NIELSEN, H.V.: Heat transfer from a hemisphere cylinder equipped with flow separation spikes. NACA TN 3287, 1954.

15. BOGDONOFF, S.M. & VAS, I.E.: Preliminary investigations of spiked bodies at hypersonic speeds. Princeton U., Report 412, 1958, also J. Aero/Space Science, Volume 26, No. 2, 1959.

16. CRAWFORD, D.H.: Investigation of the flow over a spiked-nose hemisphere-cylinder at a Mach number of 6.8. NASA TN D 118, 1959.

17. HOLDEN, M.S.: Experimental studies of separates flows at hypersonic speeds. Part I - Separated flows over axisymmetric spiked bodies. AIAA J., Volume 4, No. 4, 1966.

18. ALBUM, H.H.: Spiked blunt bodies in supersonic flow. AFOSR TR 307, 1961.

19. WYBORNY, W.: Der Einfluss eines ausgelenkten Zentralstifes auf die aerodynamischen Beiwerte rotationssymmetrischer Hyperschallflugkorper. DLR FB 69-37, 1969.

20. ROBERTS, B.G.: An experimental study of the drag of rigid models representing two parachute designs at M = 1.40 and 2.19. RAE TN Aero 2734, 1960.

21. MAYNARD, J.D.: Aerodynamic characteristics of parachutes at Mach numbers from 1.6 to 3.0. NASA TN D 752, 1961.

22. JONES, R.A., BUSHNELL, D.M., HUNT, J.L.: Experimental flow field and heat transfer investigation of several tension shell configurations at a Mach number of 8. NASA TN D 3800, 1967.

23. MINGES, M.L.: Ablation phenomenology (a review). High Temperatures-High Presses, Volume 1, 1969.

24. KENWORTHY, M.A. & RICHARDS, B.E.: A study of the unsteady flow over concave conic models at Mach 15 and 20. AFML TR 138, 1976.

25. ABBETT, M.J. COOPER, L., DAHM. T.J., JACKSON, M.D.: Flow characteristics about concave conic forebodies at high Mach numbers. AIAA P 75-153, 1975.

26. MAIR, W.A.: Experiments on separation of boundary layer on probes in front of blunt bodies in a supersonic stream. Philosophical Magazine, Series 7, Volume 43, No. 342, July 1952.

27. MAULL, D.J.: Hypersonic flow over axially symmetric spiked bodies. J. Fluid Mechanics, Volume 8, 1960.

28. WOOD, C.J.: Hypersonic flow over spiked cones. J. Fluid Mechanics, Volume 12, Part 4, 1961.

29. ROBINSON, M.L., ROBERTS, B.G. & SAYER, A.M.: An examination of the flow instability associated with spiked bluff body configurations. WRE HSA TN 101, 1964.

30. KABELITZ, H.P.: Zur Stabilitat geschlossener Greznschichtablosegebiete an konischen Drehkorpern bei Hyperschallstromung. DLR FB 71-77, 1971.

31. KORDULLA, W.: Calibration of the hypersonic blowdown wind tunnel H-3. VKI PR 70-264, 1970.

32. BERGH, H. & TIJDEMAN, H.: Theoretical and experimental results for the dynamic response of pressure measuring systems. NLR TR F 238, 1965.

33. SCHULTZ, D.L. & JONES, T.V.: Heat transfer measurements in short duration hypersonic facilities. AGARD AG 165, 1973.

34. EAST, R.A. & WILKINSON, P.P.: A study of the oscillating separated flow ahead of a forward facing step oscillating traversely to a hypersonic free stream. AASU Rep. 263, 1966.

35. LIEPMANN, H.W. & ROSHKO, A.: Element of Gasdynamics. J. Wiley & Sons, Inc., 1957, page 105.

36. GADD, G.E., HOLDER, D.W., REGAN, J.D.: An experimental investigation of the interaction between shock waves and boundary layers. Proc. Roy. Soc. London, Ser. A., Volume 226, 1954.

37. SCHUH, H.: On determining turbulent boundary layer separation in incompressible and compressible flows. J. Aero. Sc., Volume 22, 1955.

38. CHAPMAN, C.R., KUEHN, D.M., LARSON, H.K.: Investigation of separated flows in supersonic and subsonic streams with emphasis on the effect of transition. NACA TR 1356, 1958.

39. STERRETT, J.R. & HOLLOWAY, P.F.: On the effects of transition on parameters within a separation region at hypersonic speeds with emphasis on heat transfer. ASME Symposium on fully separated flows, New York, 1964.

40. GADD, G.E.: A theoretical investigation of laminar separation in supersonic flow. J. Aero. Science, Volume 24, 1957.

41. HAKKINEN, R.J., GERBER, I., TRILLING, L., ABARBANEL, S.S.: The interaction of an oblique shock with a laminar boundary layer. NASA Memo 2-18-59W, 1959.

42. MICHEL, R.: Conditions de decollement de la couche limite a grande altitude aux vitesses hypersoniques. WGL Jahrbuch, 1961.

43. STERRETT, J.R. & EMERY, J.C.: Experimental separation studies for two dimensional wedges and curved surfaces at M = 4.8 to 6.2. NASA TN D 1014, 1962.

44. ERDOS, J. & PALLONE, A.: Shock boundary layer interaction and flow separation. Proc. 1962 Heat Transfer and Fluid Mechanics Institute, Stanford U. Press, 1962.

45. Equations, tables and charts for compressible flow. NACA TR 1135.

46. NEEDHAM, D.A.: Laminar separation in hypersonic flow. Doctoral Thesis, U. London, 1965.

47. BURGGRAF, O.R.: Inviscid reattachment of a separated shear layer. Proc. 3rd Int. Conf. on Numerical Methods in Fluid Mechanics, Volume II, 1972.

48. NASH, J.F.: An analysis of two dimensional turbulent base flow including the effects of the approaching boundary layer. NPL Aero R. 1036, ARC 24,000, 1962.

49. HOLDER, D.W. & GADD, G.E.: The interaction between shock waves and boundary layers and its relation to base pressure in supersonic flows. Symp. on Boundary Layer Effects in Aerodynamics, NPL, 1955.

50. SIRIEIX, M.: Pression de culot et pression de melange turbulent en ecoulement supersonique plan. ONERA RA 78, 1960.

51. COOKE, J.C.: Separated supersonic flow. RAE TN Aero 2879, 1963.

52. CHAPMAN, D.R.: Laminar mixing of a compressible fluid. NACA TR 958, 1950.

53. LOCK, R.C.: The velocity distribution in the laminar boundary layer between parallel streams. Qu. J. Mech. and Appl. Math., Volume IV, 1951.

54. NASH, J.F.: Laminar mixing of a non uniform stream with a fluid at rest. ARC CP 613, 1962.

55. MERRITT, G.E.: Hypersonic laminar flow over cavities and steps. Ph.D. Thesis, U. Southampton, 1964.

56. APPELS, C.: Compressible turbulent boundary layer separation. D. Sc. Thesis, Katholieke U. Leuven, 1975.

57. DENISON, M.R. & BAUM, E.: Compressible free shear layer with finite initial thickness. IAS Paper 62-125, 1962.

58. MANGLER, W.: Zusammenhang zwischen eben und rotationssymmetrischen Grenzschichten in kompressiblen Flussigkeit. ZAMM, Volume 28, No. 4, 1948.

59. PROBSTEIN, R.F. & ELLIOT, D.: The transverse curvature effect in compressible axially symmetric laminar boundary layer flow. J. Aero. Sc., Volume 23, 1956.

60. DOLLING, D.S.: Ph.D. Thesis presented at the University of London, Imperial College, 1976.

61. BROWER, W.B. Jr: Leading edge separation of laminar boundary layers in supersonic flow. J.A.S. 1951.

62. KORST, H.H., PAGE, R.H., CHILDS, M.E.: Compressible two dimensional jet mixing at constant pressure. U. Illinois, ME TN 392-1, 1954.

63. PANARAS, A.G.: The high speed unsteady separation around concave bodies can be explained by an inviscid flow mechanism. These Annexe, U. Libre de Bruxelles, 1976.

64. LOLL, V.: Unsteady supersonic flow around a spiked blunt body. VKI PR 74-4, 1974.

65. MILLER, I.M. & SUTTON, K.: An experimental study of oxidation of graphite in high temperature supersonic and hypersonic environments. NASA TN D 3444, 1966.

66. DERBRIDGE, T., WOOL, M., BAKER, D.: Pant series D wind tunnel test report. Aerotherm Project Report 7044, 1973.

67. THYSON, N., NEUBRINGER, J., PALLONE, A., CHEN, K.K.: Nose tip shape change prediction during atmosphere reentry. AIAA Paper 70-827, 1970.

68. WELSH, W.E. Jr: Shape and surface roughness effects on turbulent nosetip ablation. AIAA J. Volume 8, No. 11, 1970.

69. CHIN, J.H.: Shape change and conduction for nose tip at angles of attack. AIAA J., Volume 13, No. 5, 1975.

70. GRABOW, R.M. & WHITE, C.O.: Surface roughness effects on nosetip ablation characteristics. AIAA J. Volume 13, N° 5, 1975.

71. RICHARDS, B.E. & ENKENHUS, K.R.: The longshot free piston hypersonic tunnel. VKI TN 49, 1968.

72. RICHARDS, B.E. & ENKENHUS, K.R.: Hypersonic testing in the VKI longshot free piston tunnel. AIAA Paper 69-333, April 1969.

73. KIRK, F.N.: An approximate theory of base pressure in two dimensional flow at supersonic speeds. RAE TN Aero 2377, 1959.

74. YOUNG, A.D. & KIRKBY, S.: The profile drag of biconvex and double wedge wing section at supersonic speeds. Symp. on Boundary Layer Effects in Aerodynamics, N.P.L. 1955.

75. NASH, J.F.: The effect of an initial boundary layer on the development of a turbulent free shear layer. NPL Rep. 1019, ARC 23,847, 1962.

76. MOECKEL, W.E.: Flow separation ahead of blunt bodies at supersonic speeds. NACA TN 2418, 1951.

77. LIGHTHILL, M.J. & GLAUERT, M.B.: The axisymmetric boundary layer on a thin cylinder. Symp. on B.L. effects in Aero, NPL, 1955.

APPENDICES

APPENDIX A - EXPERIMENTAL RESULTS

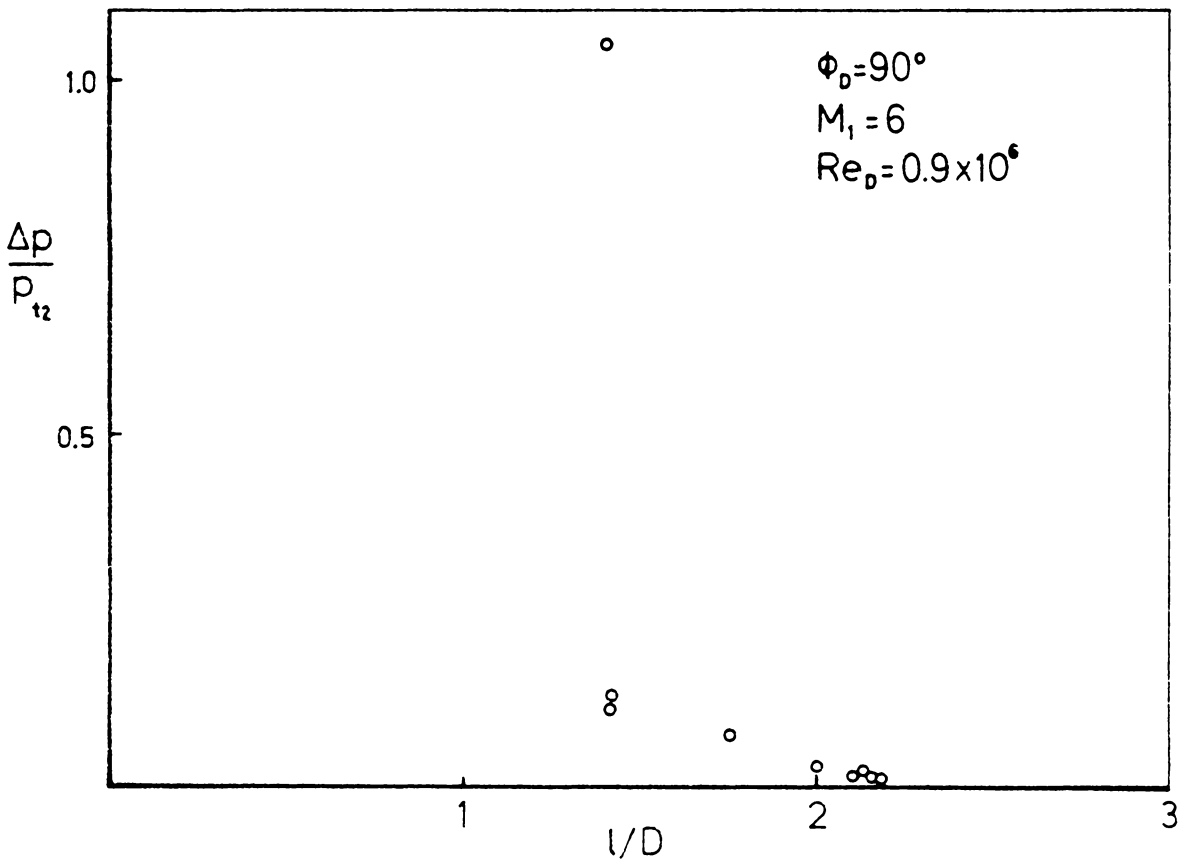

Figure A-1. High Reynolds Number Hypersonic (Series I) Pressure Amplitude Distribution

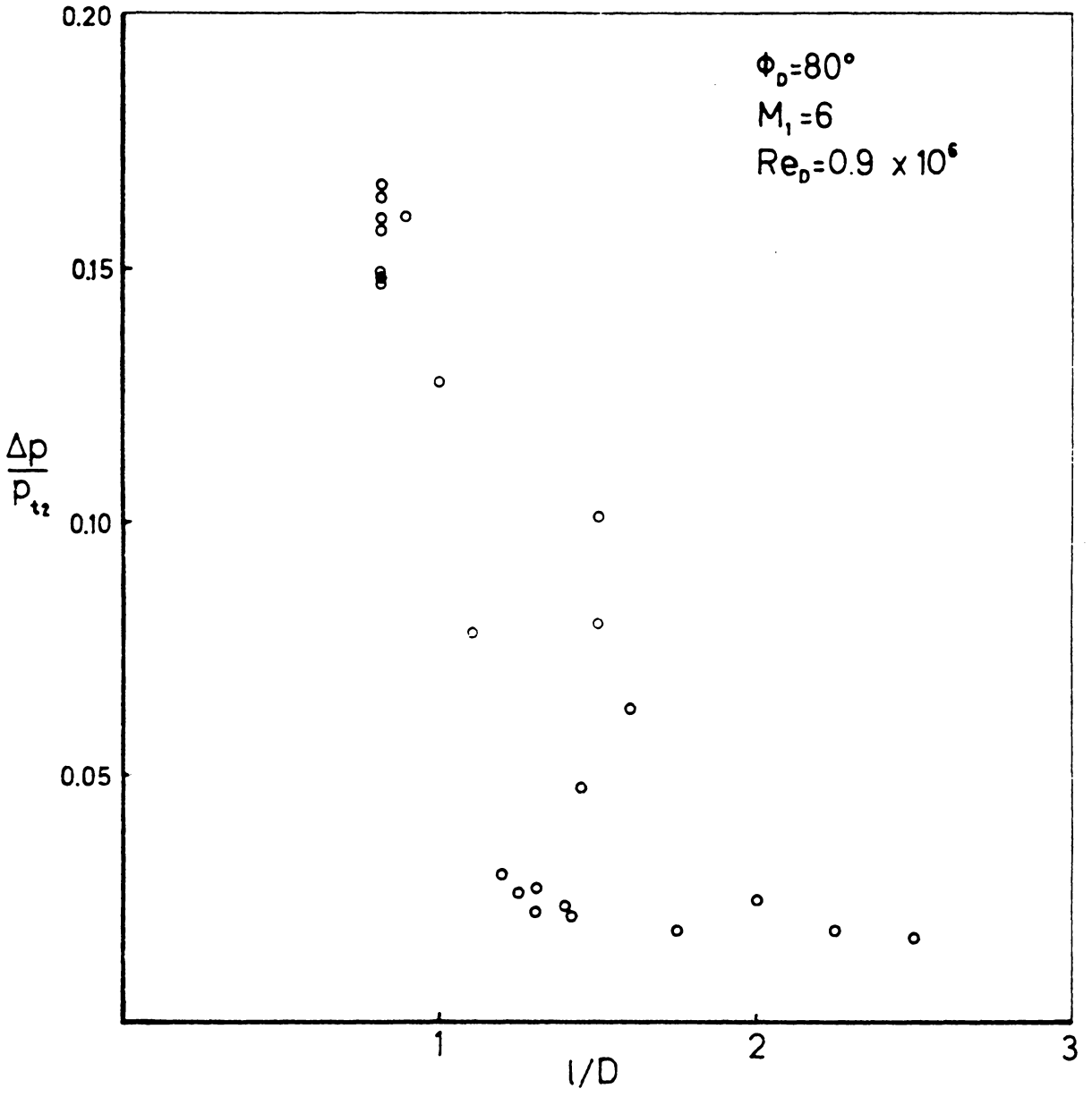

Figure A-1 (continued)

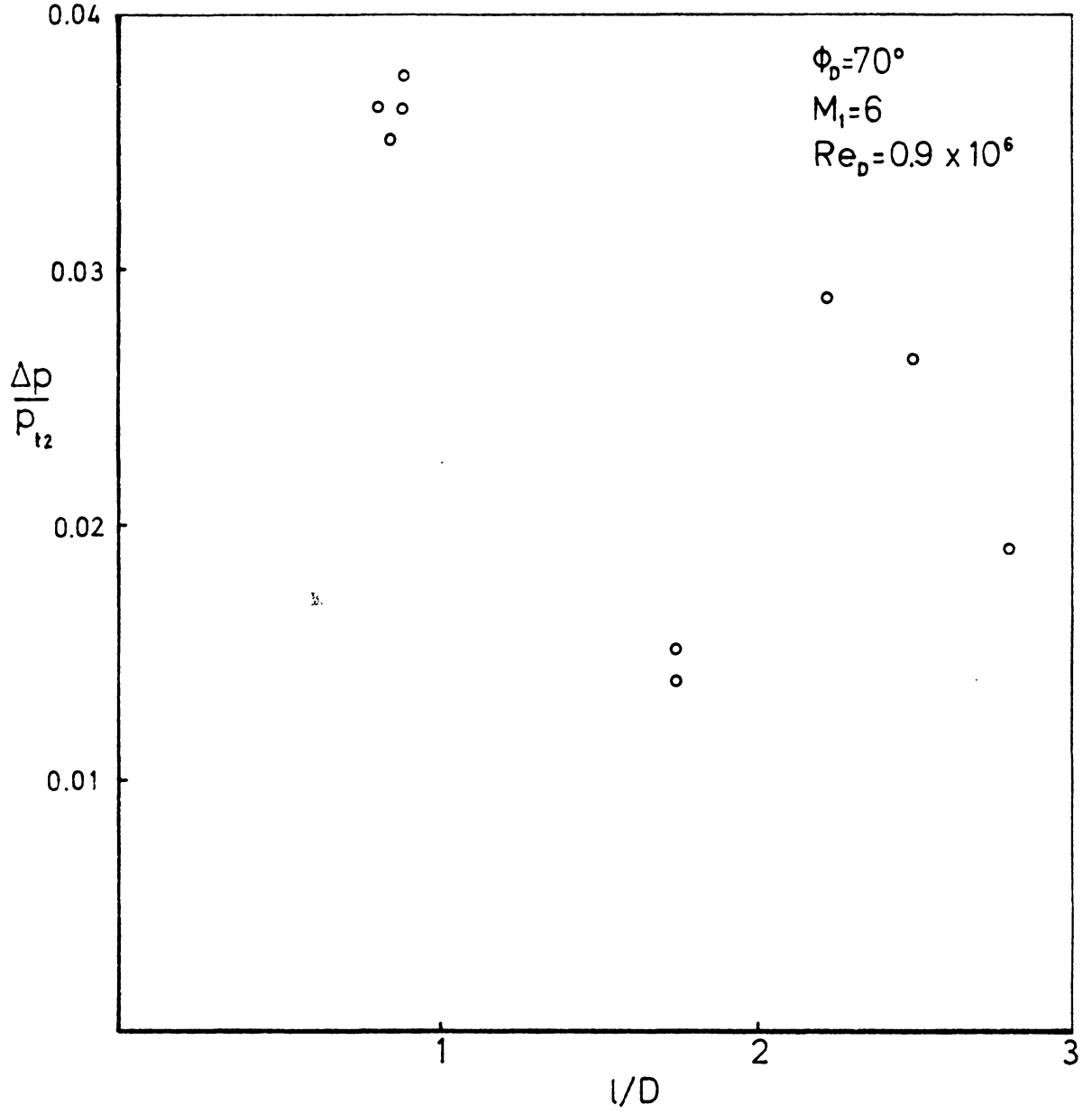

Figure A-1 (continued)

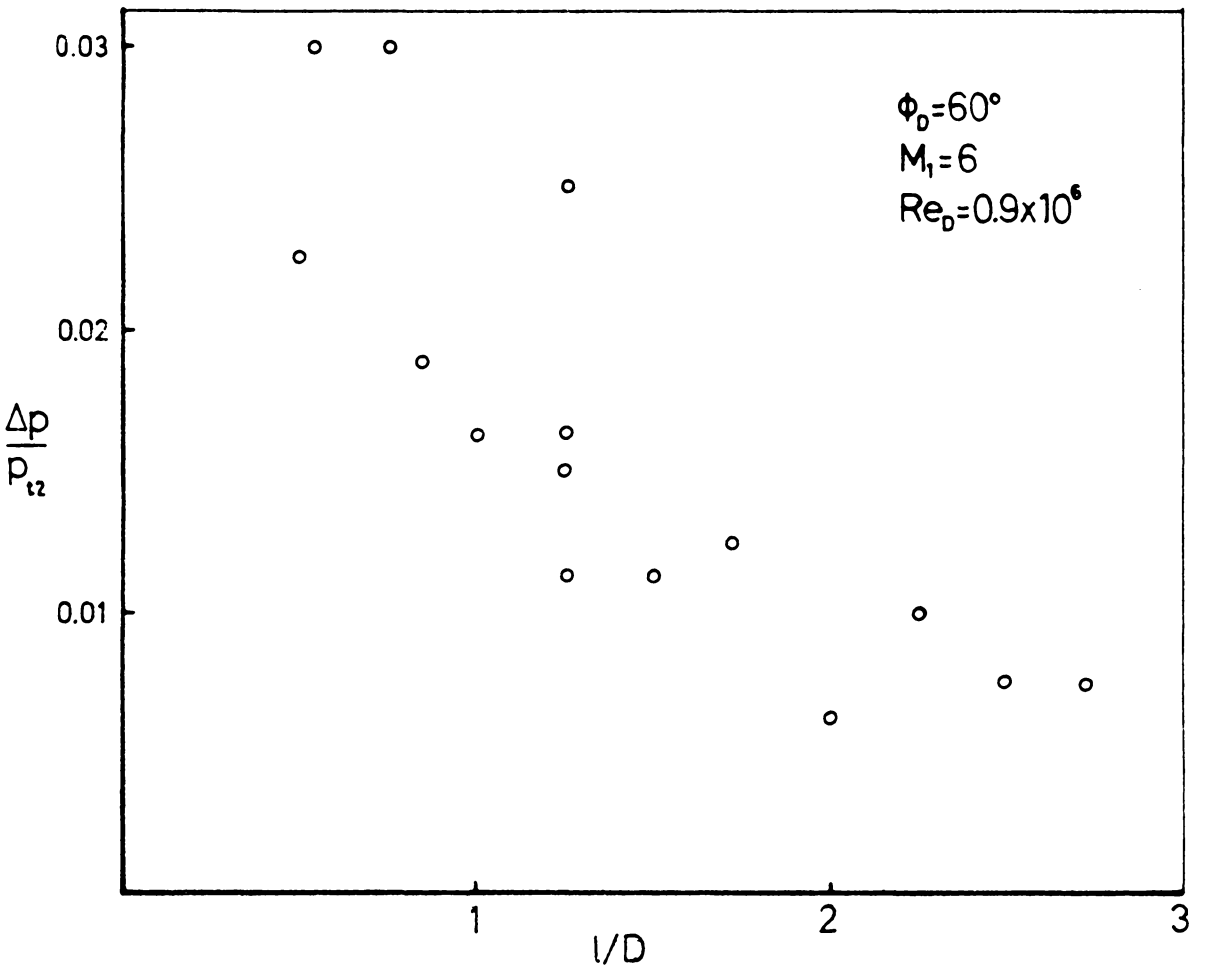

Figure A-1 (continued)

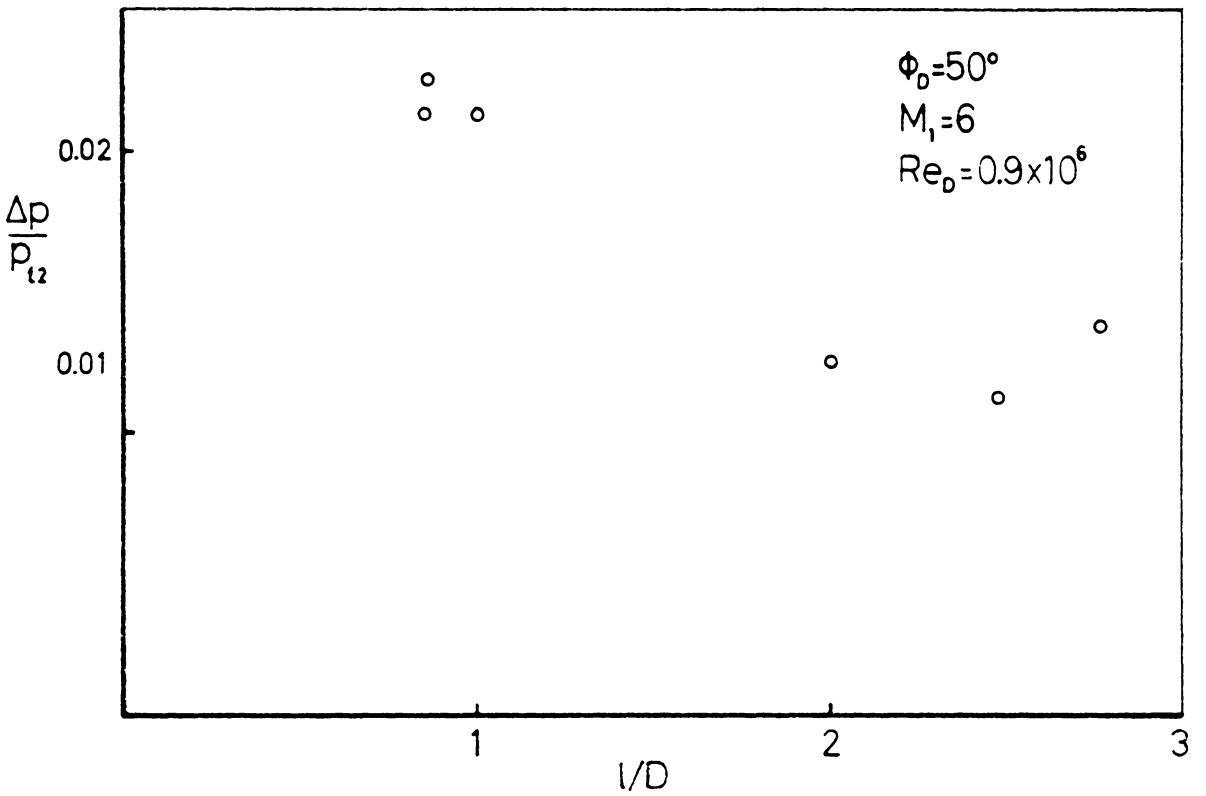

Figure A-1 (continued)

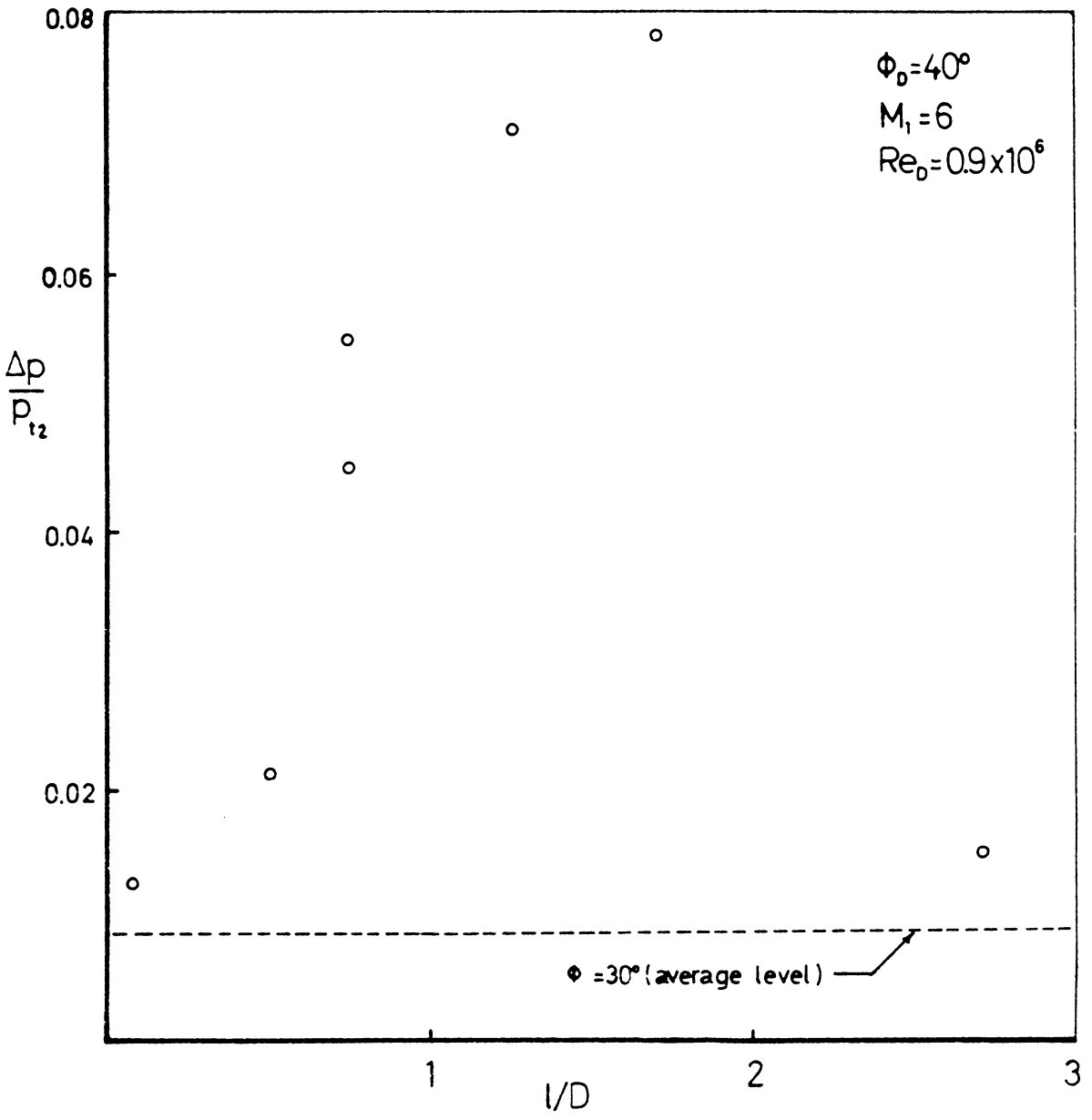

Figure A-1 (continued)

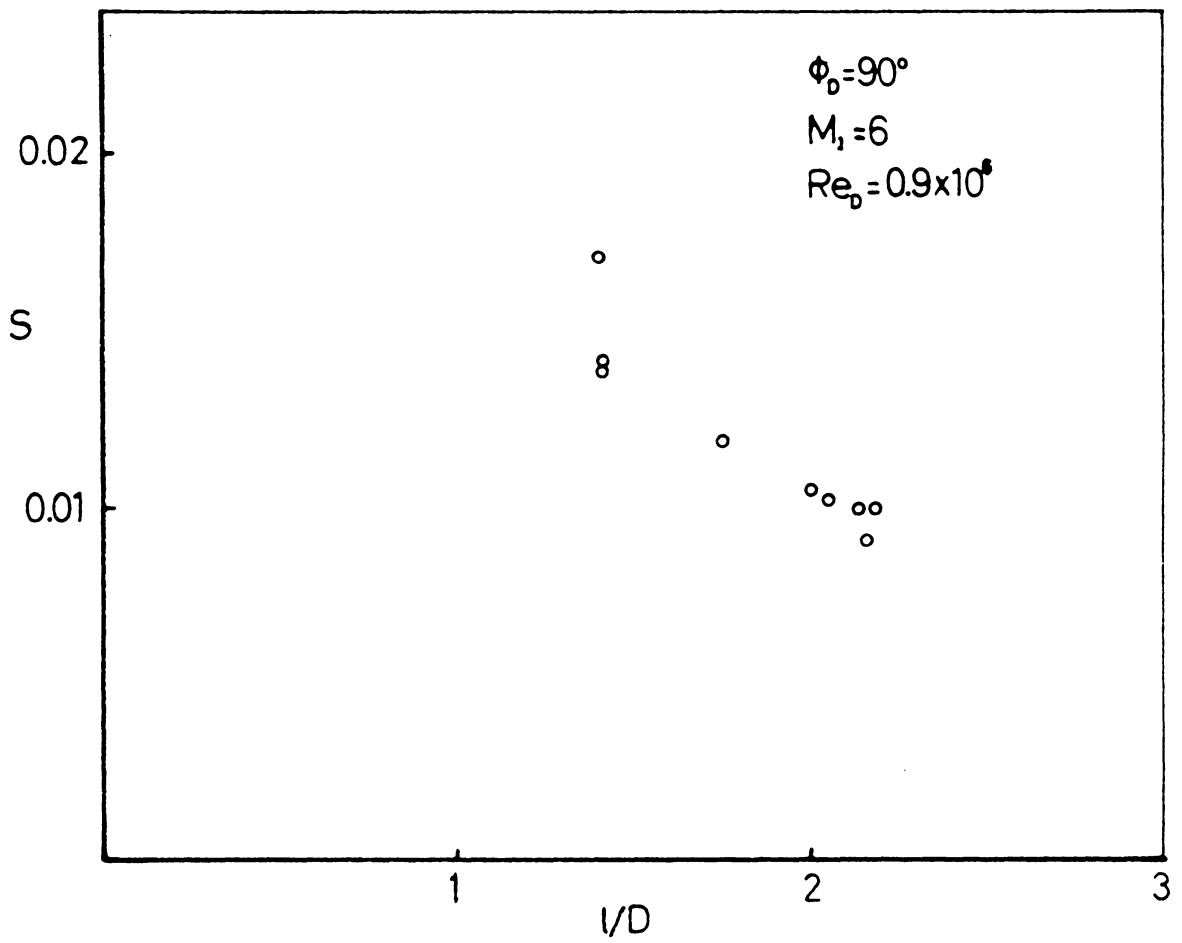

Figure A-2. High Reynolds Number Hypersonic (Series I) Frequency Distribution

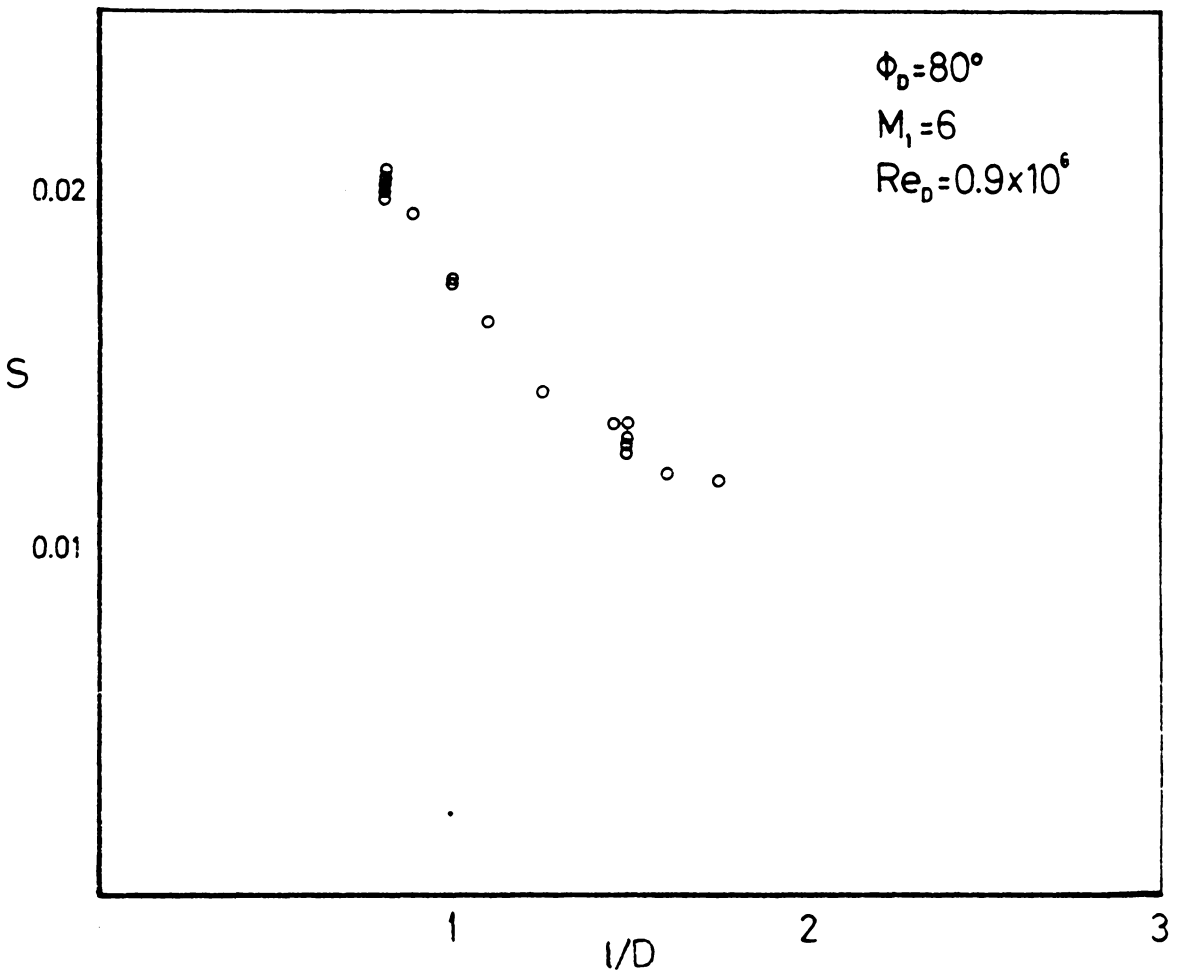

Figure A-2 (continued)

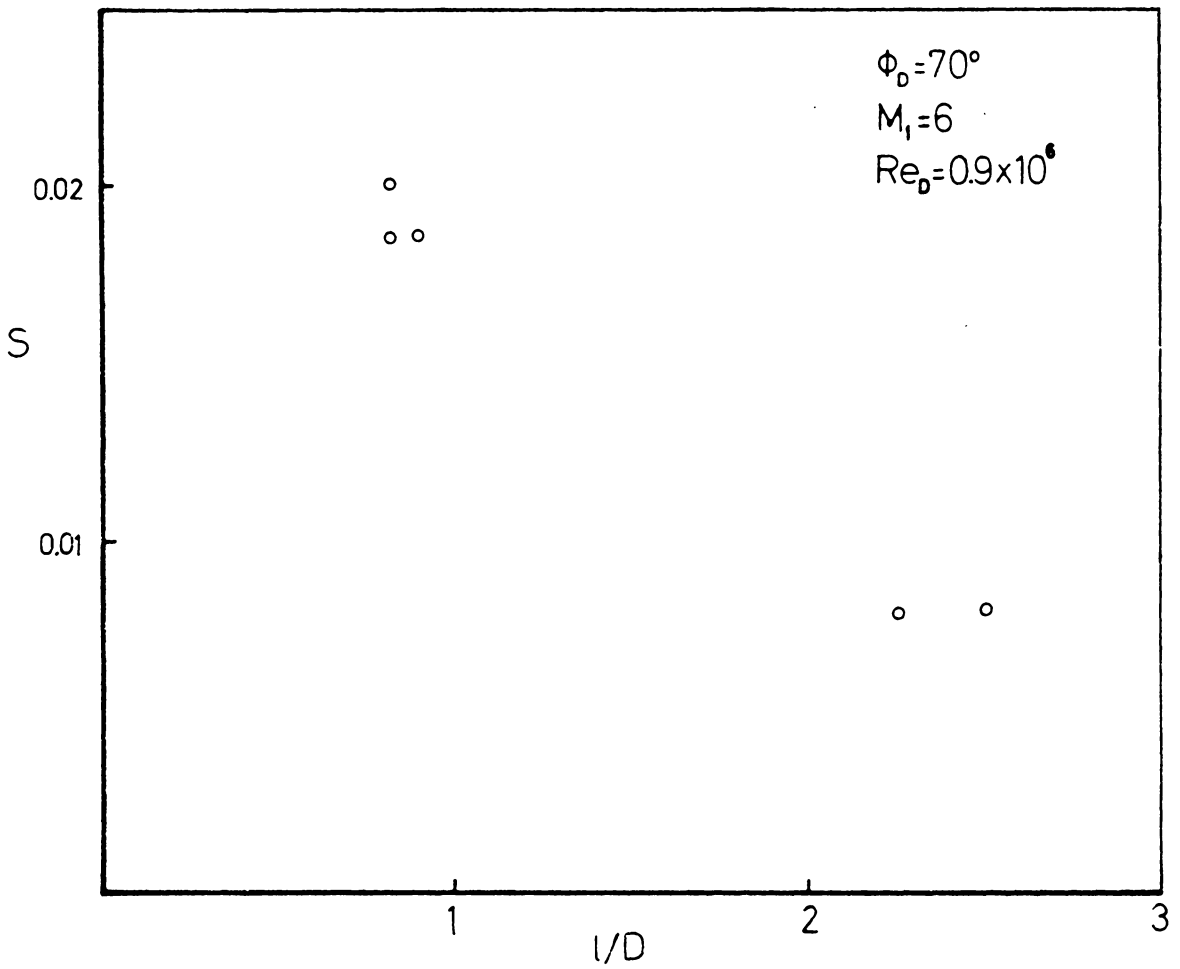

Figure A-2 (continued)

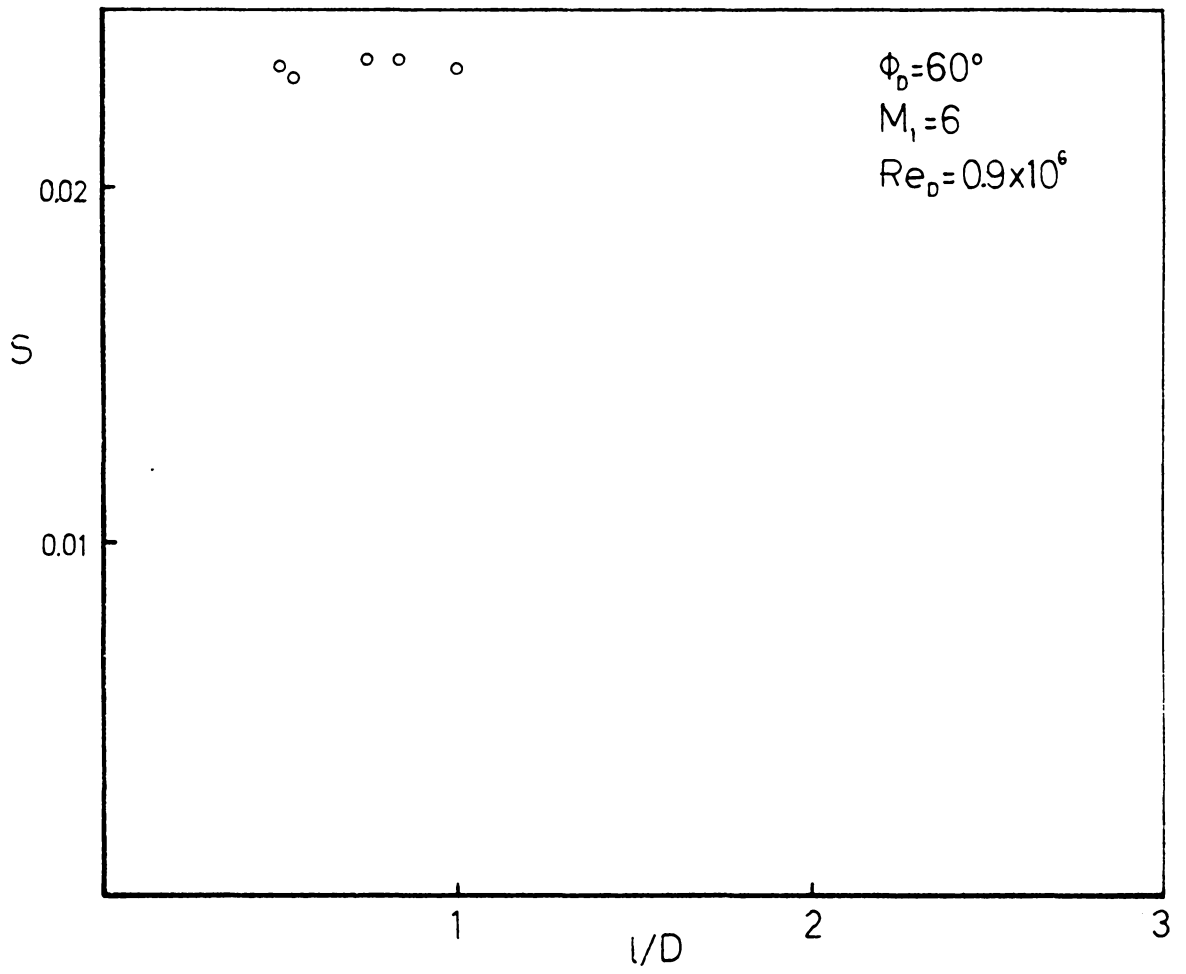

Figure A-2 (continued)

The frequency data for the $\Phi_D = 30°$ and $\Phi_D = 40°$ (Series I) model are not presented due to the high degree of irregularity in all data obtained for these models. On the whole the Strouhal number was of the same order of magnitude as that exhibited by the turbulence in the shear layer.

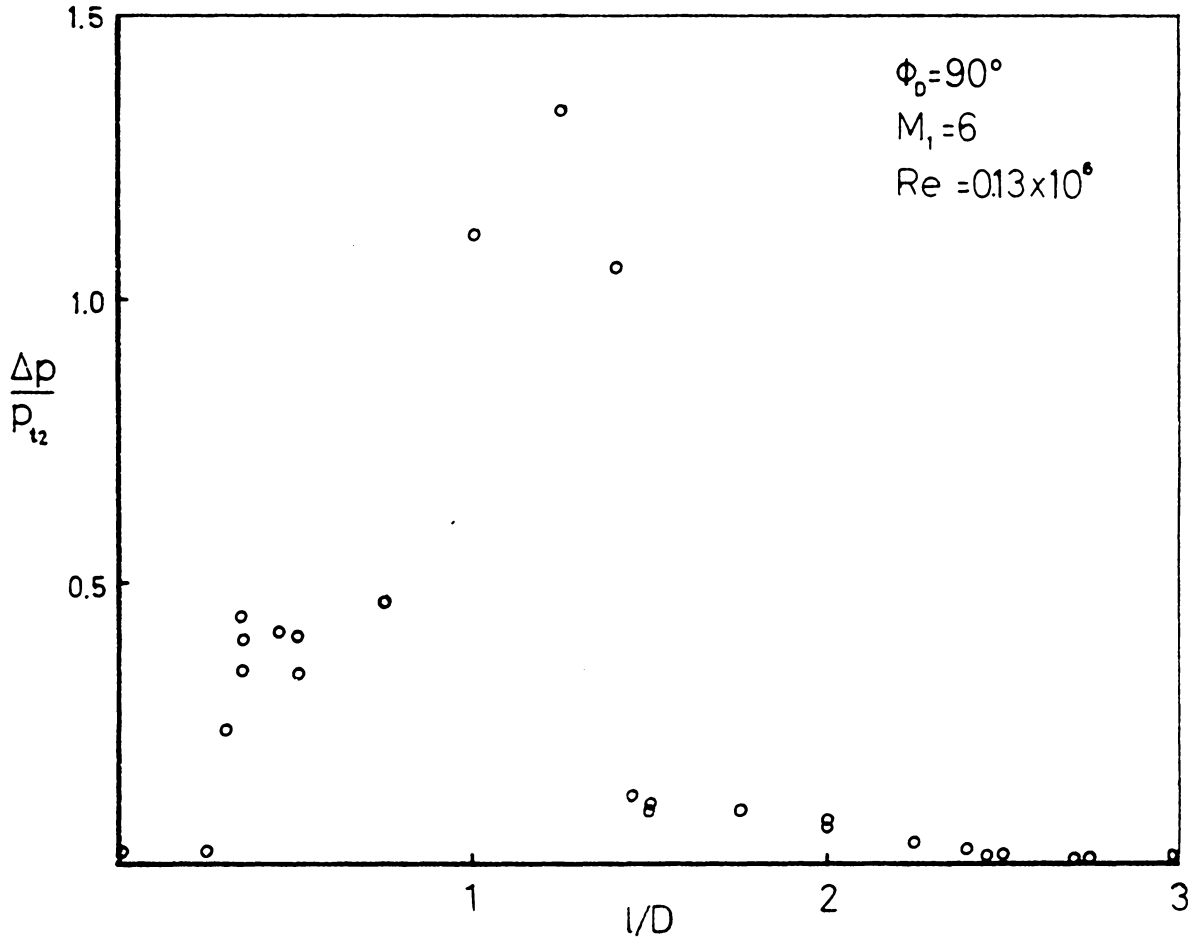

Figure A-3. Low Reynolds Number Hypersonic (Series II) Pressure Amplitude Distribution

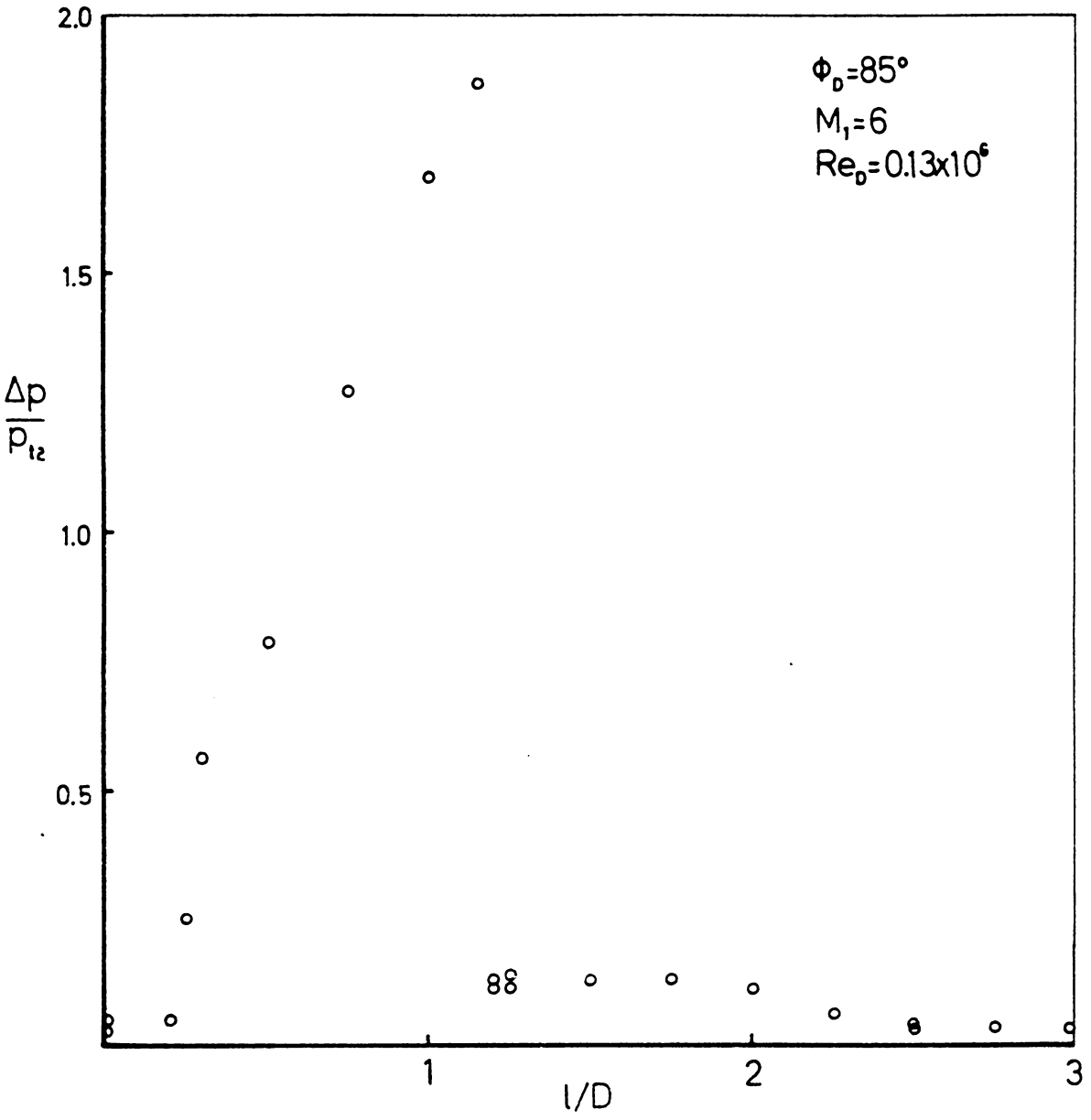

Figure A-3 (continued)

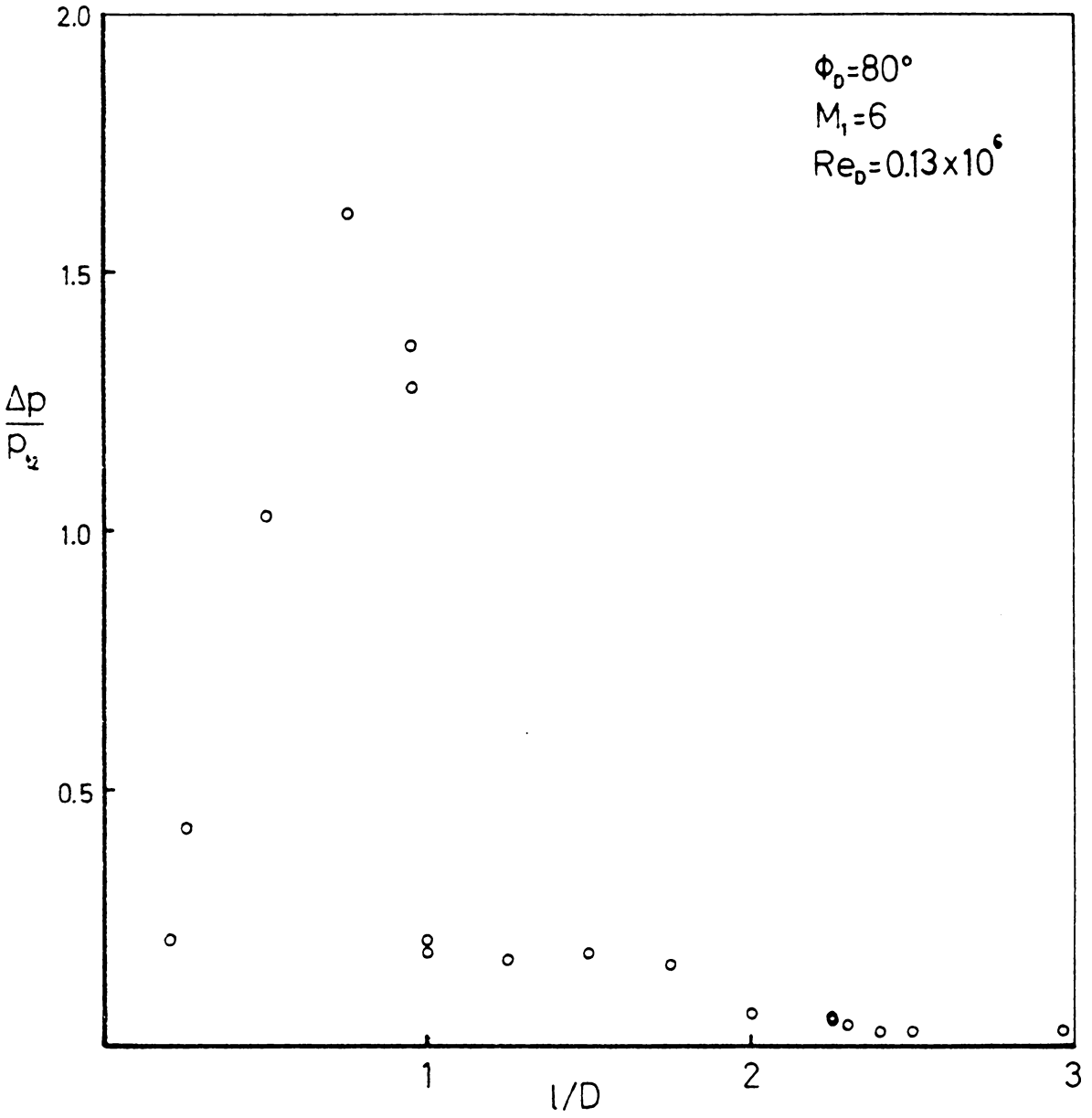

Figure A-3 (continued)

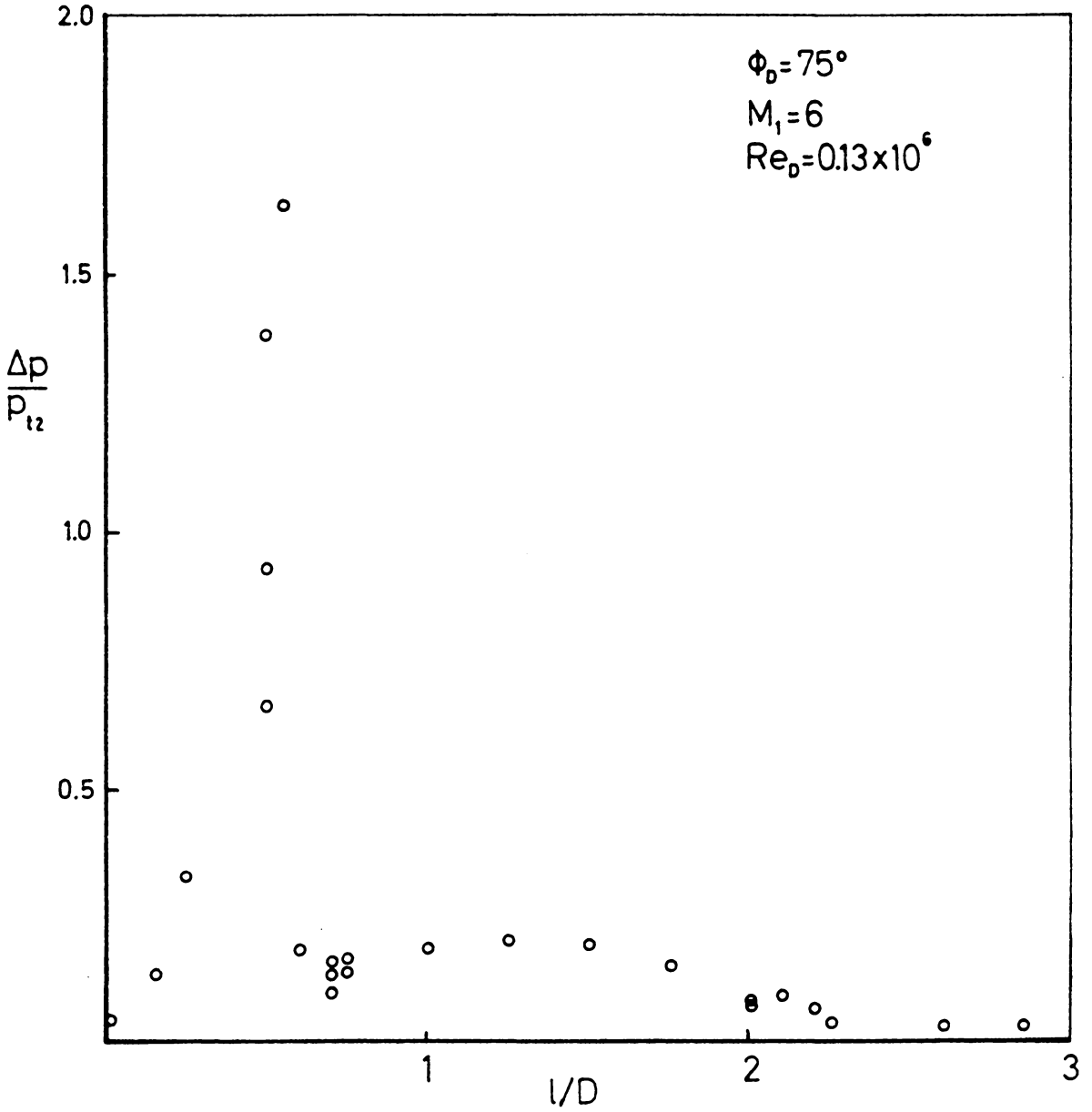

Figure A-3 (continued)

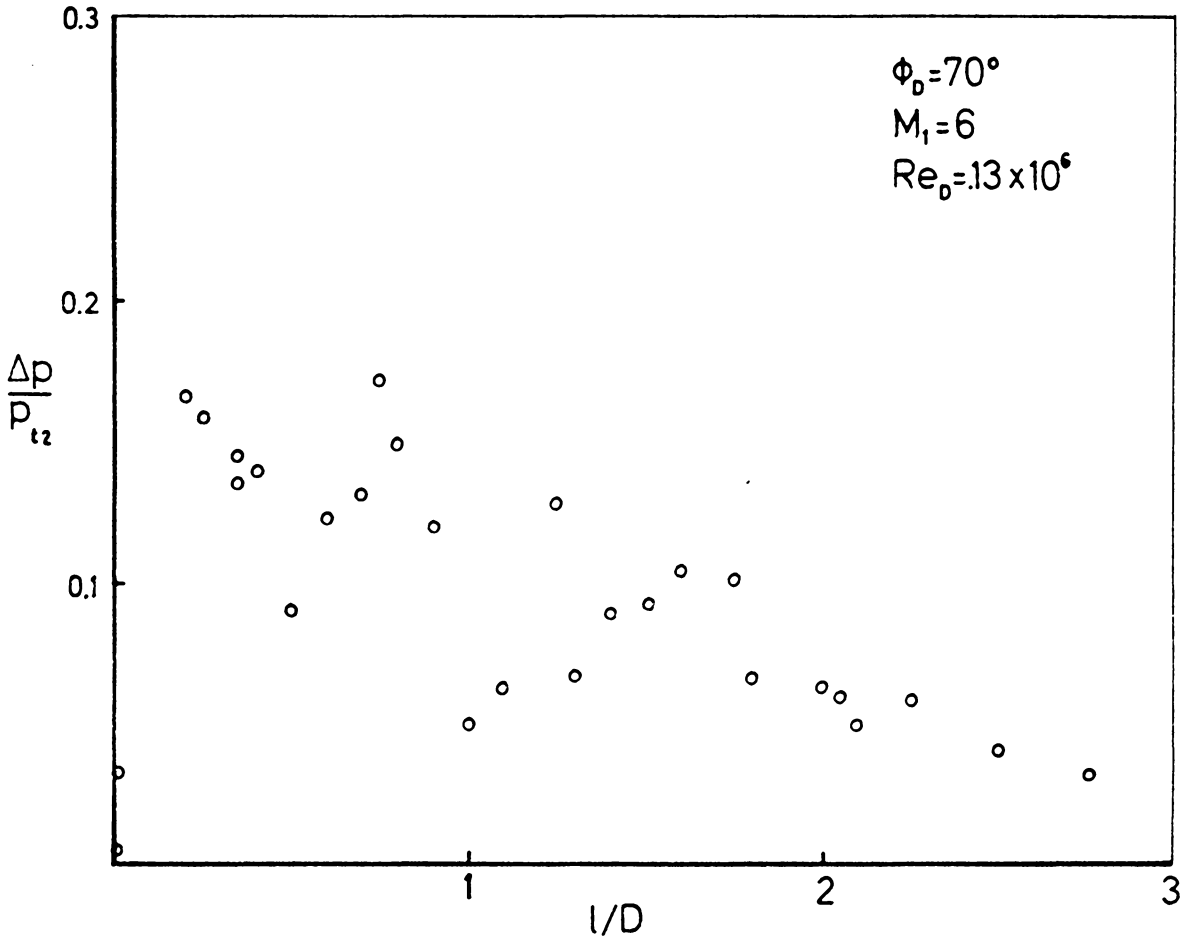

Figure A-3 (continued)

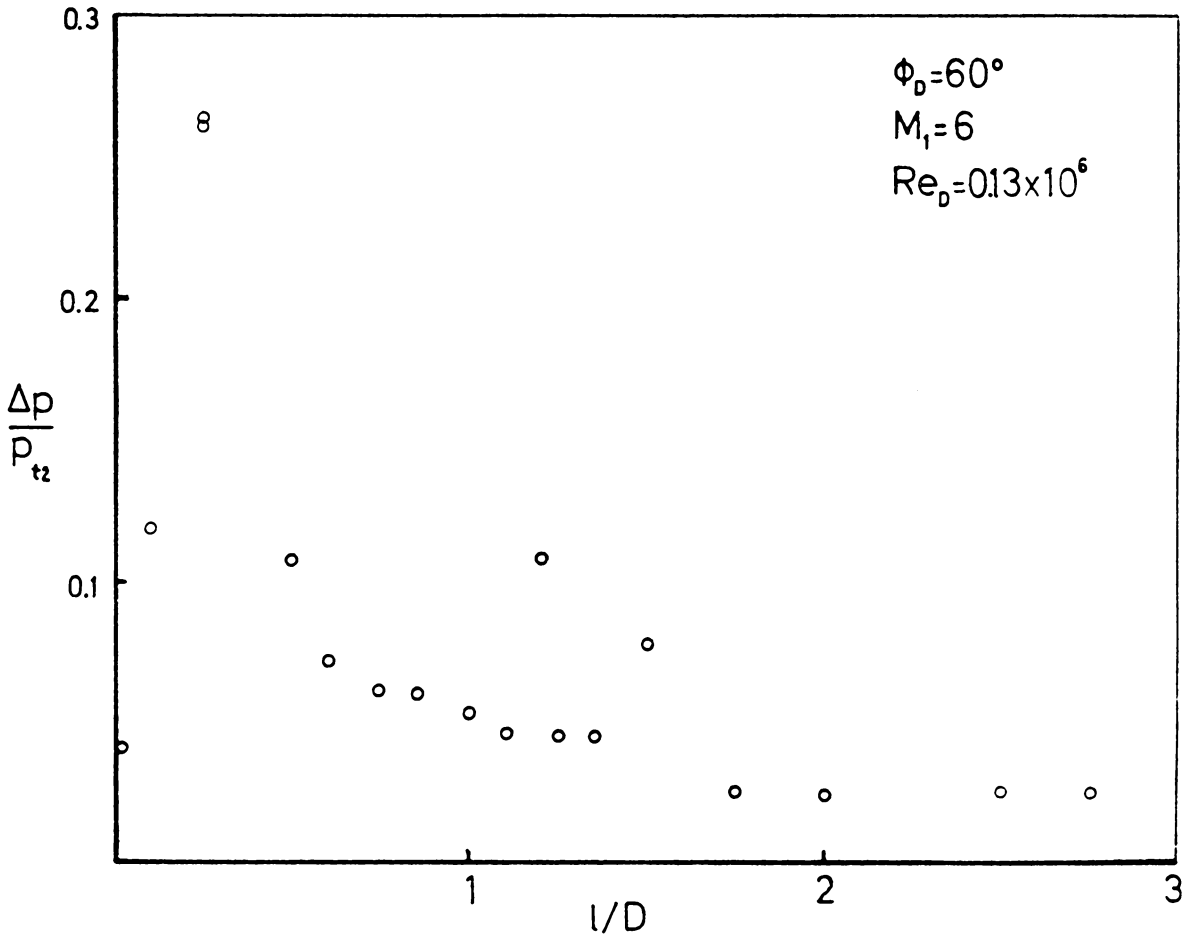

Figure A-3 (continued)

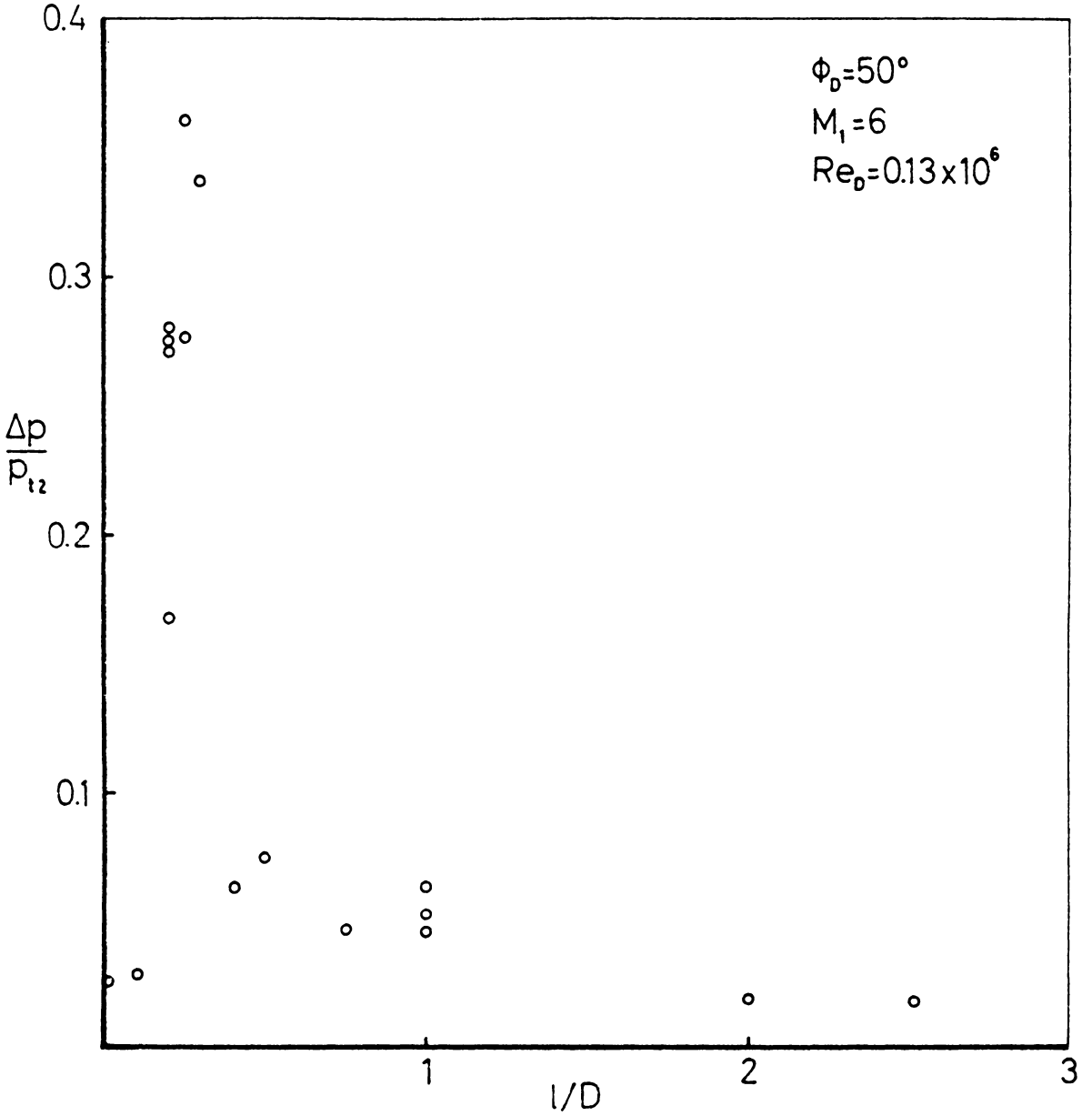

Figure A-3 (continued)

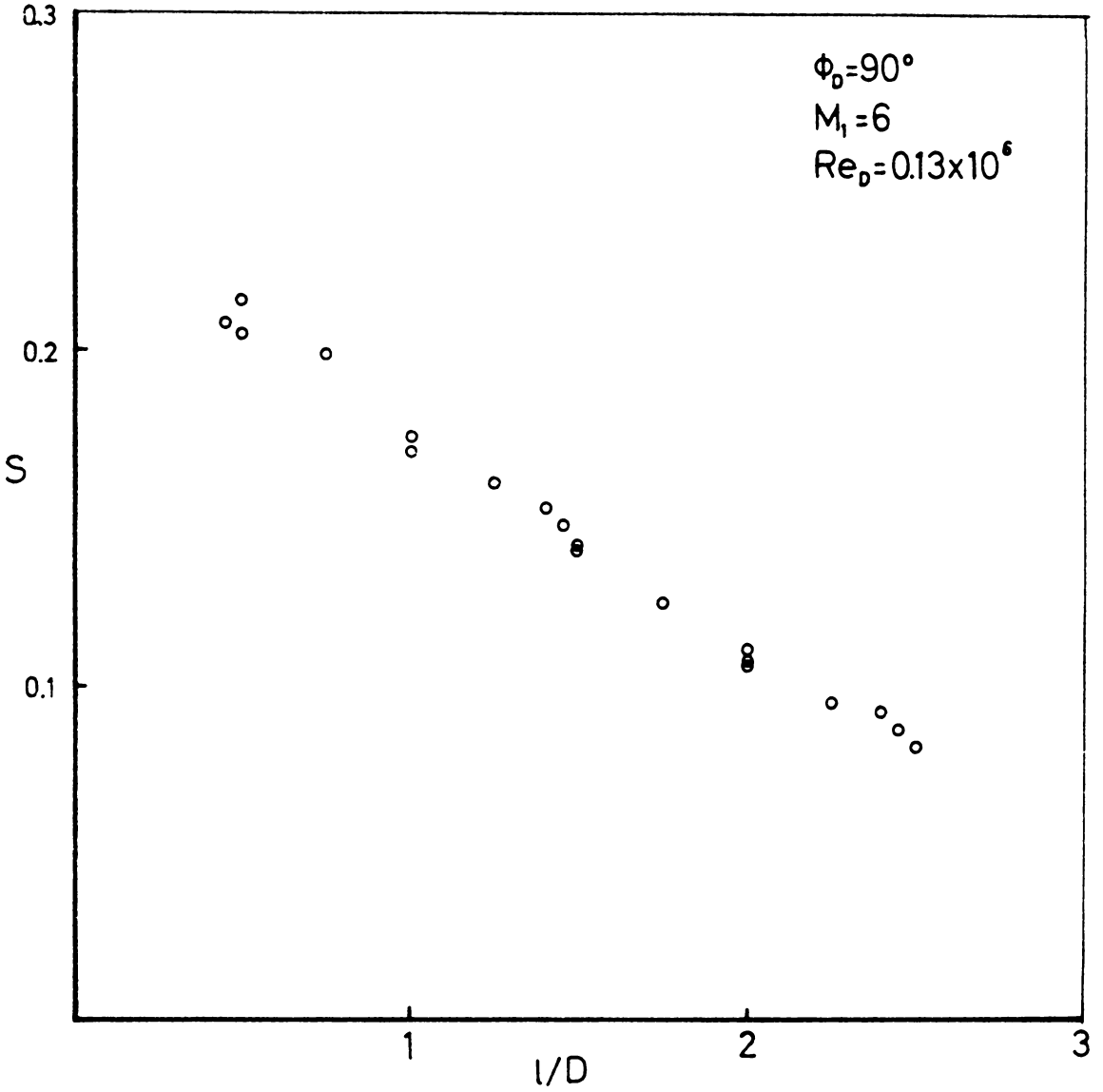

Figure A-4. Low Reynolds Number Hypersonic (Series II) Frequency Distribution

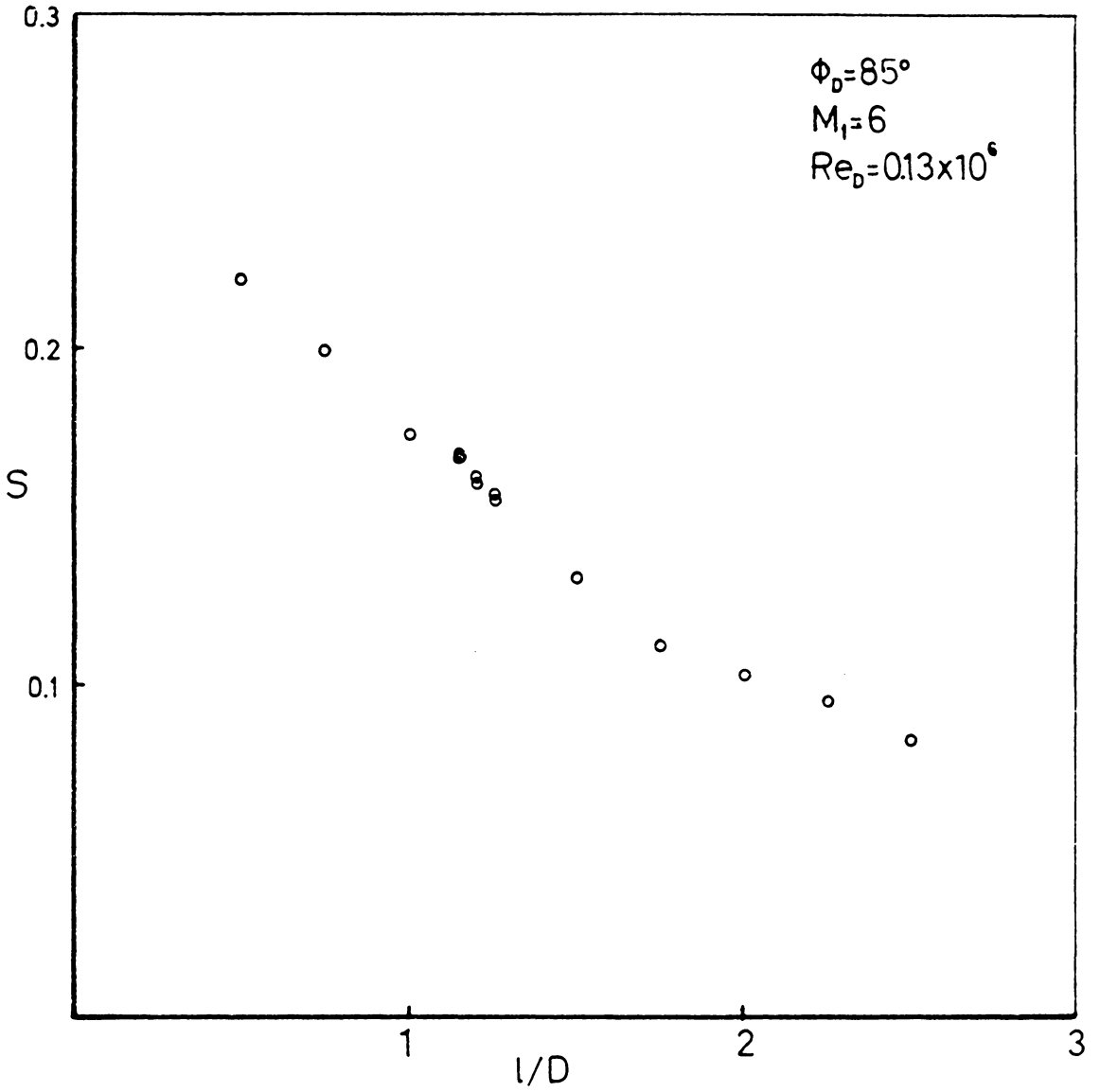

Figure A-4 (continued)

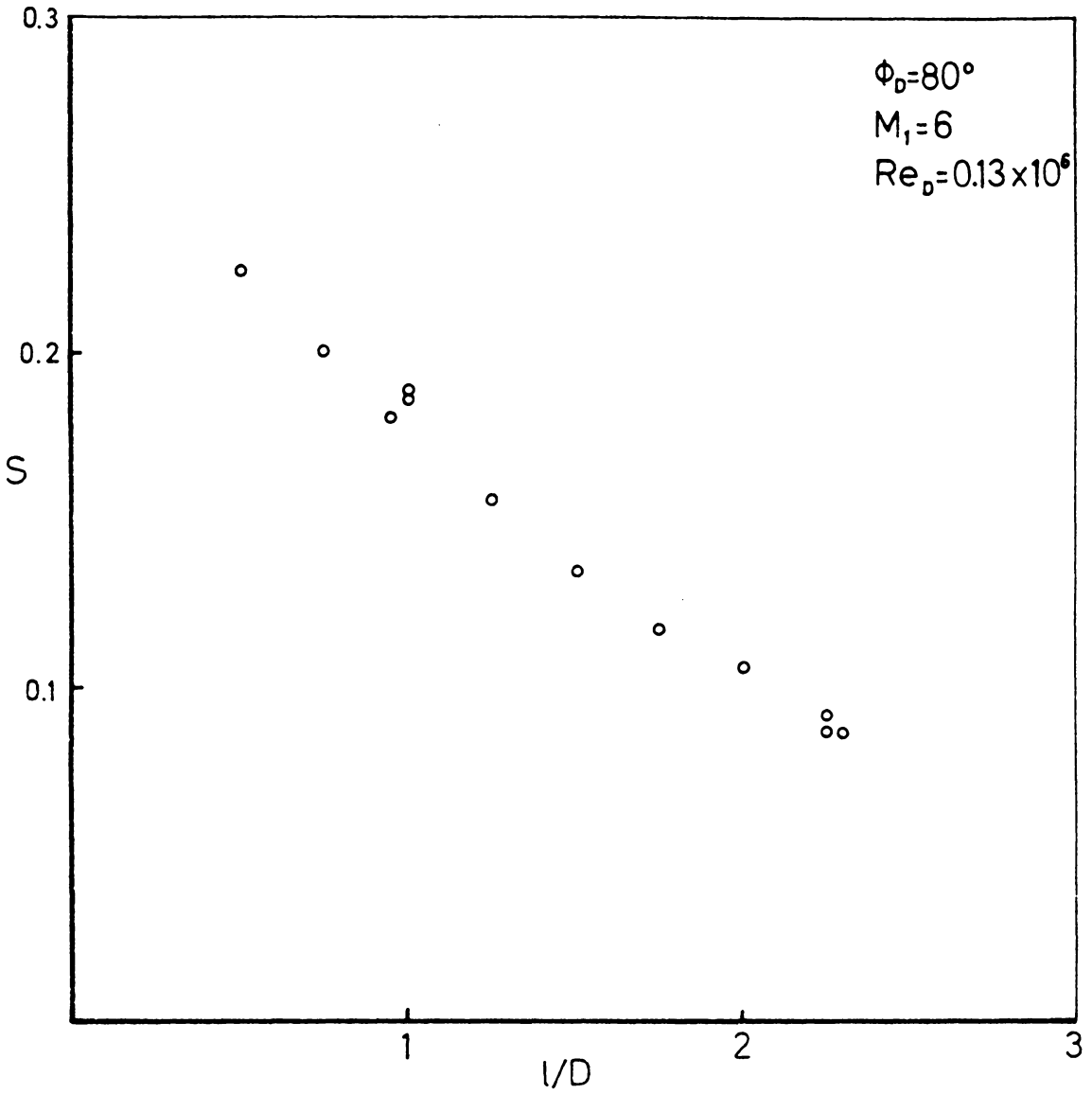

Figure A-4 (continued)

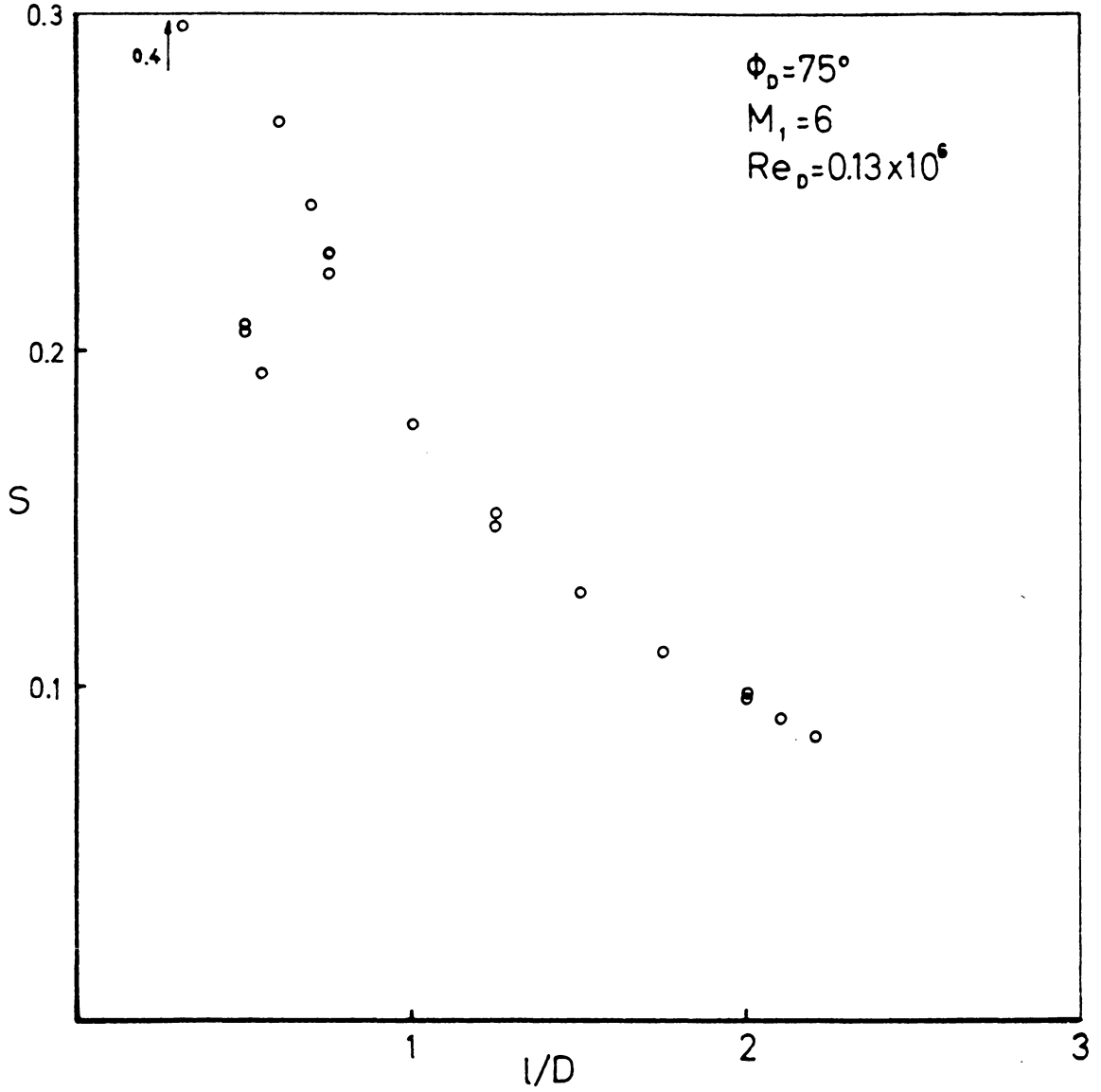

Figure A-4 (continued)

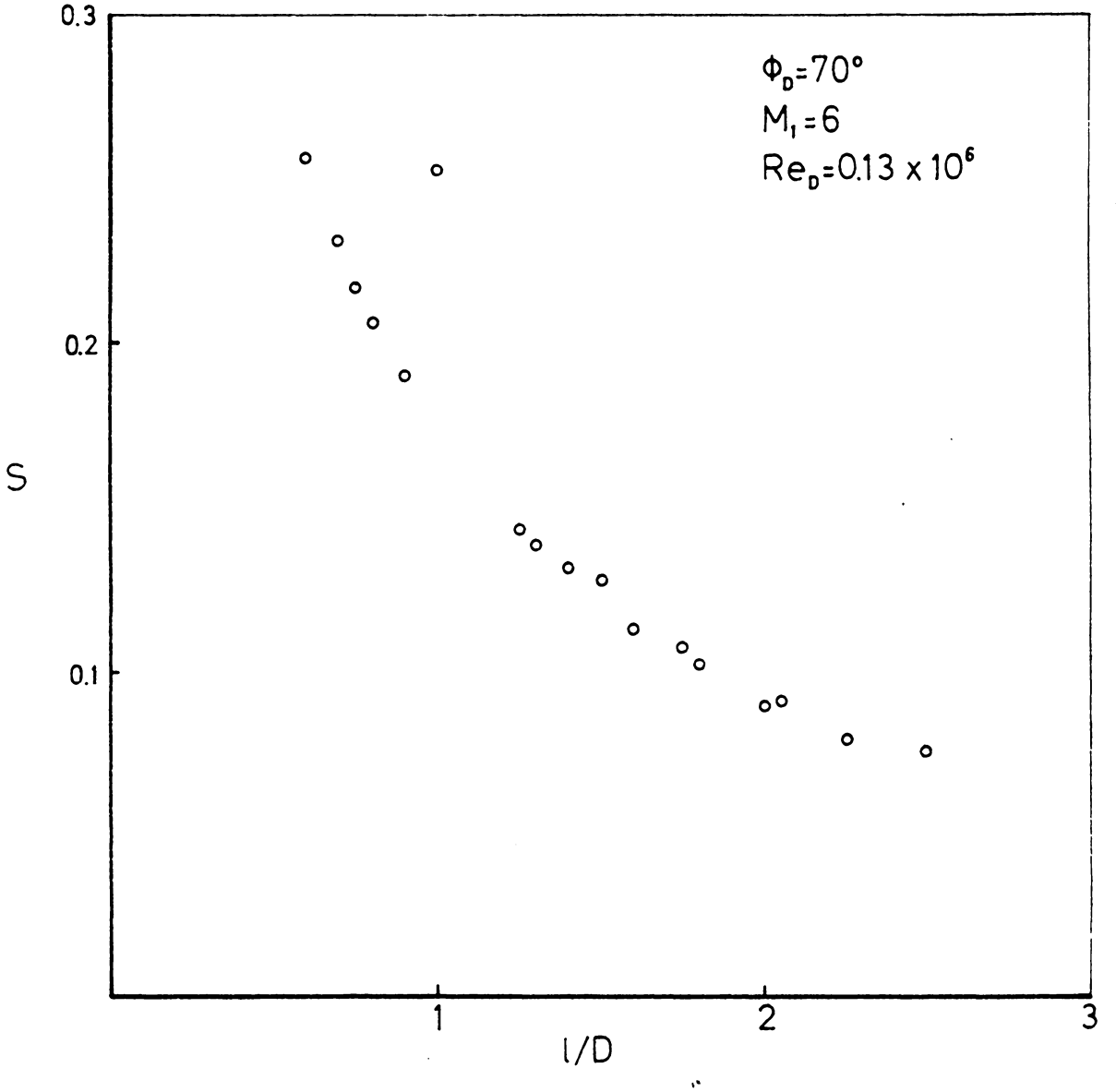

Figure A-4 (continued)

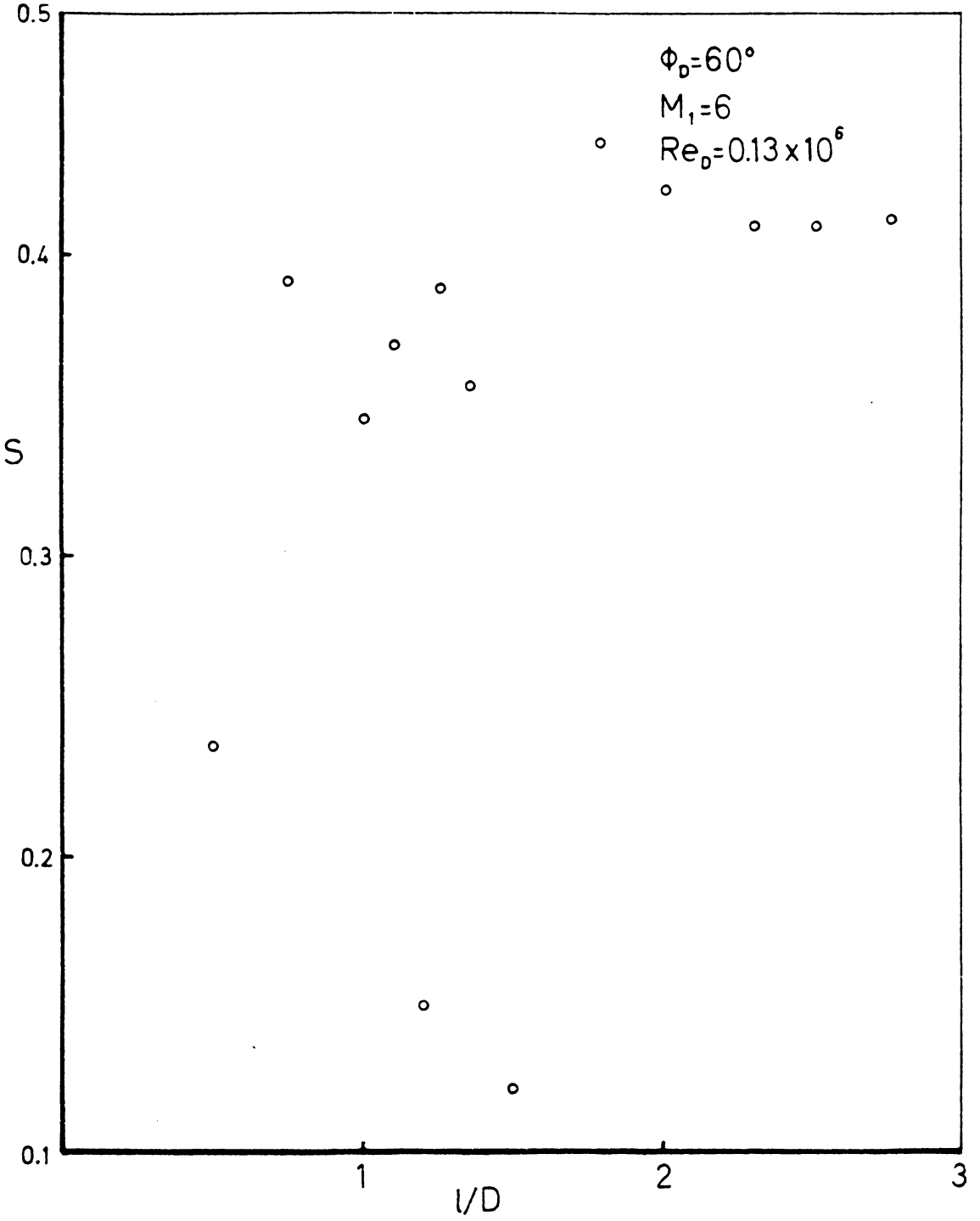

Figure A-4 (continued)

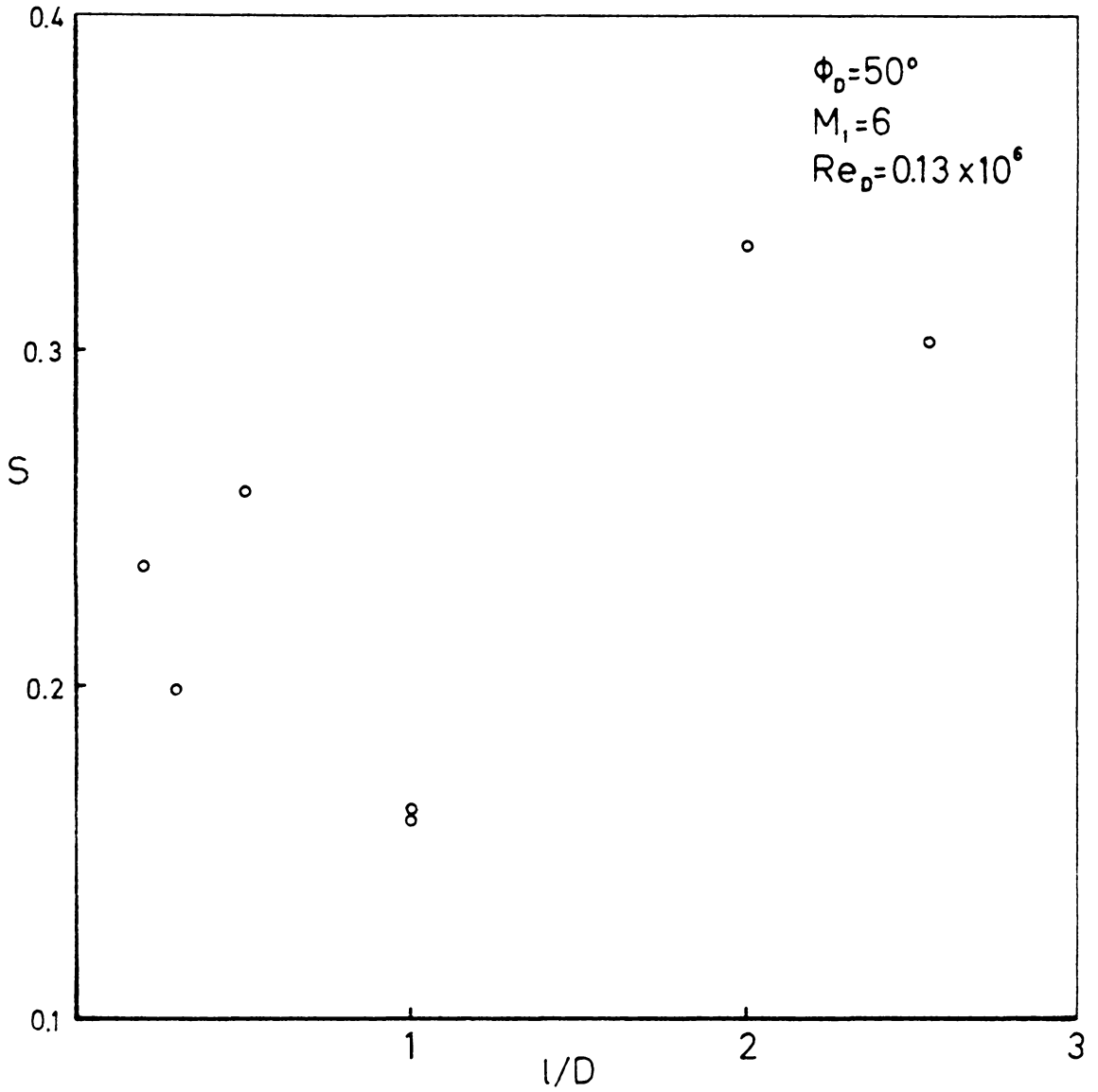

Figure A-4 (continued)

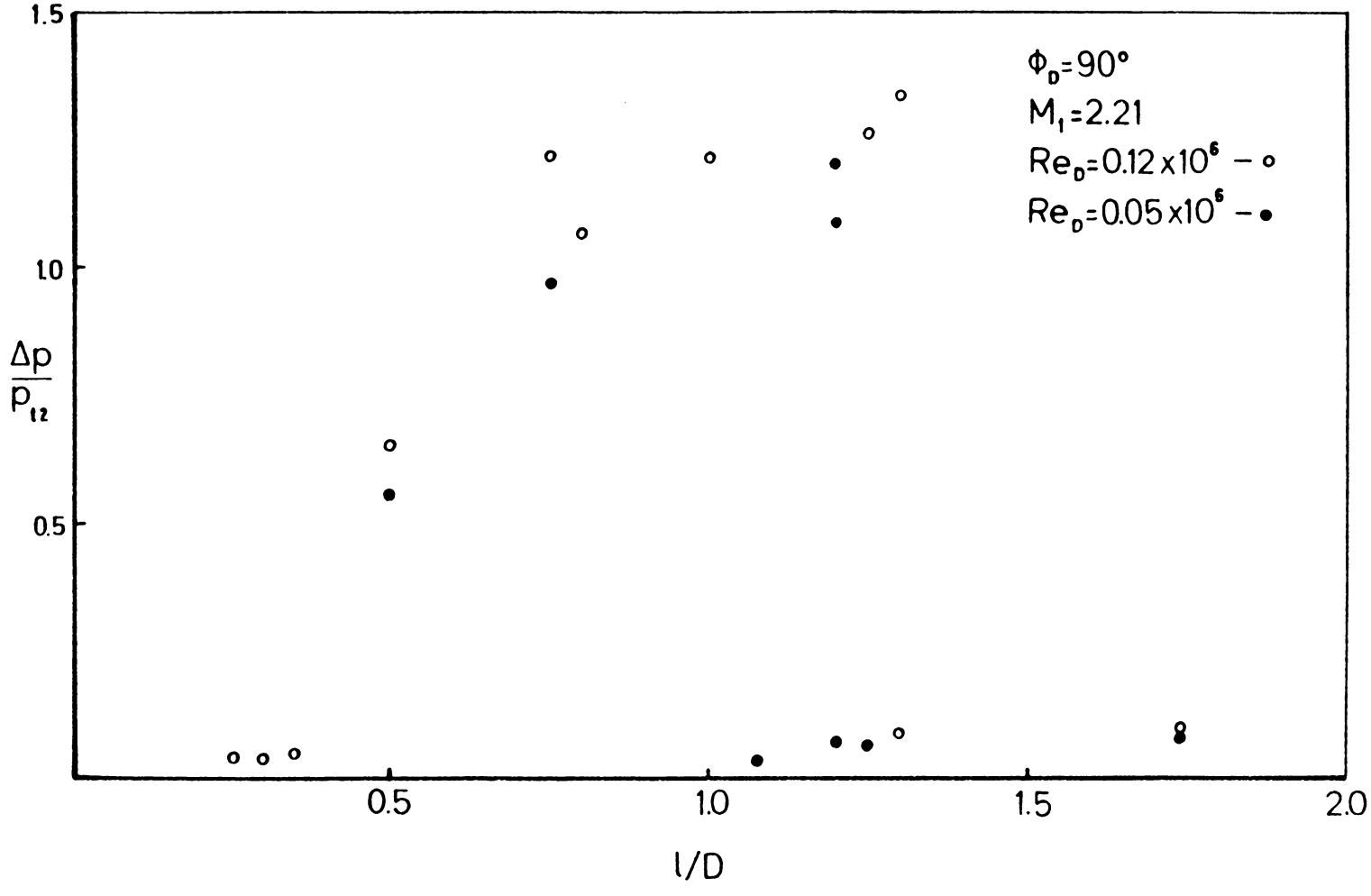

Figure A-5. Supersonic (Series III) Pressure Amplitude Distribution

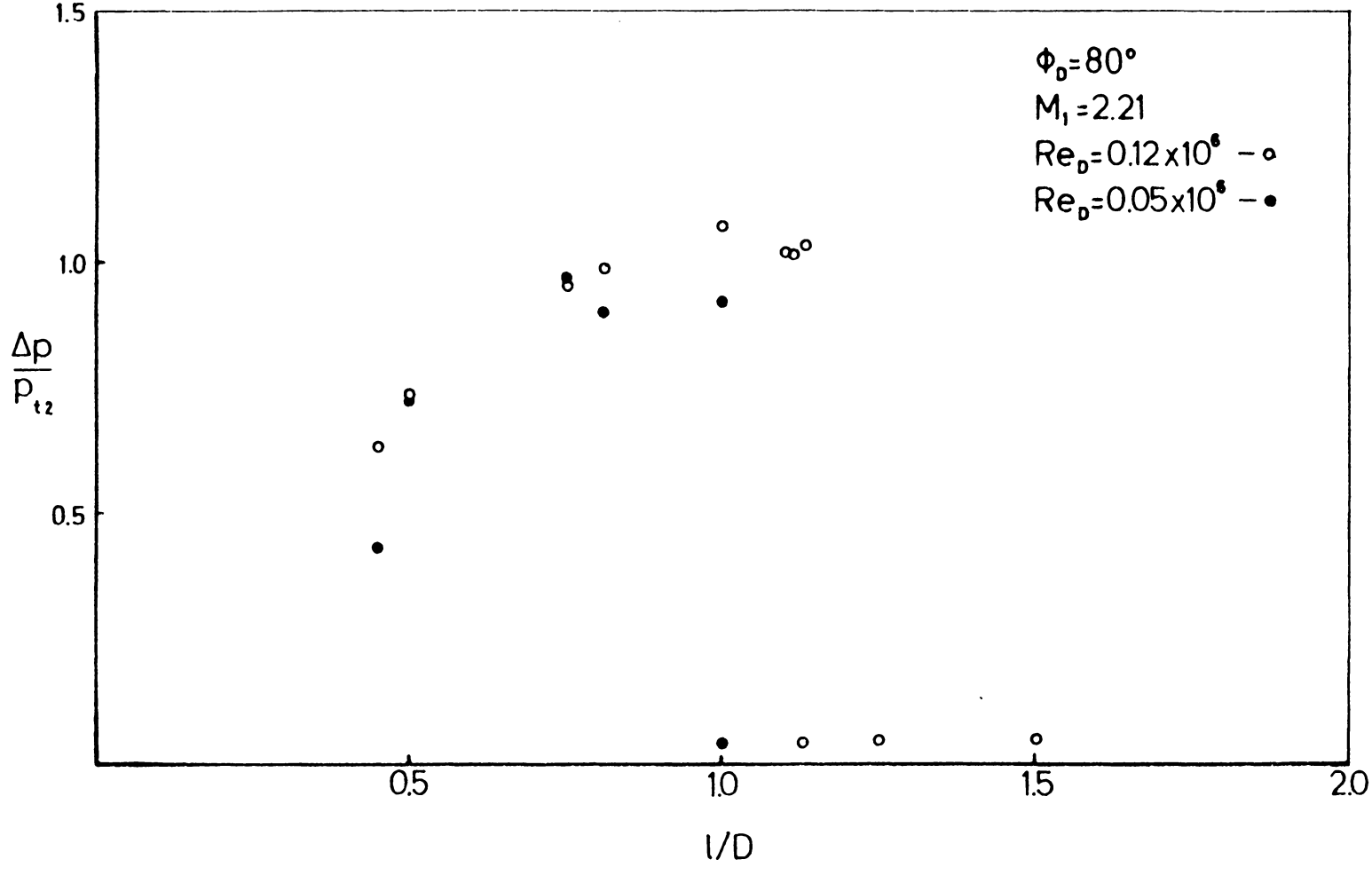

Figure A-5 (continued)

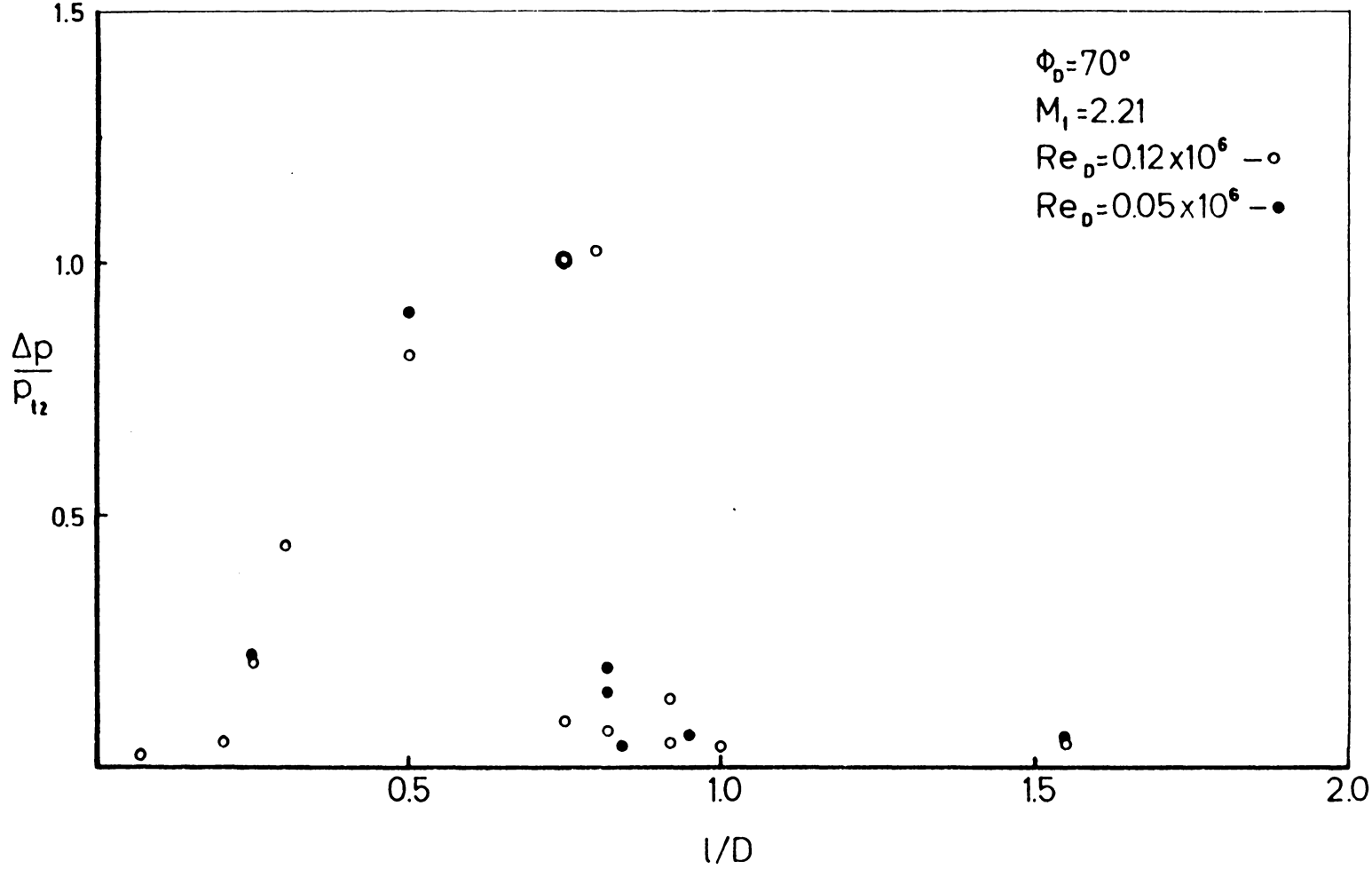

Figure A-5 (continued)

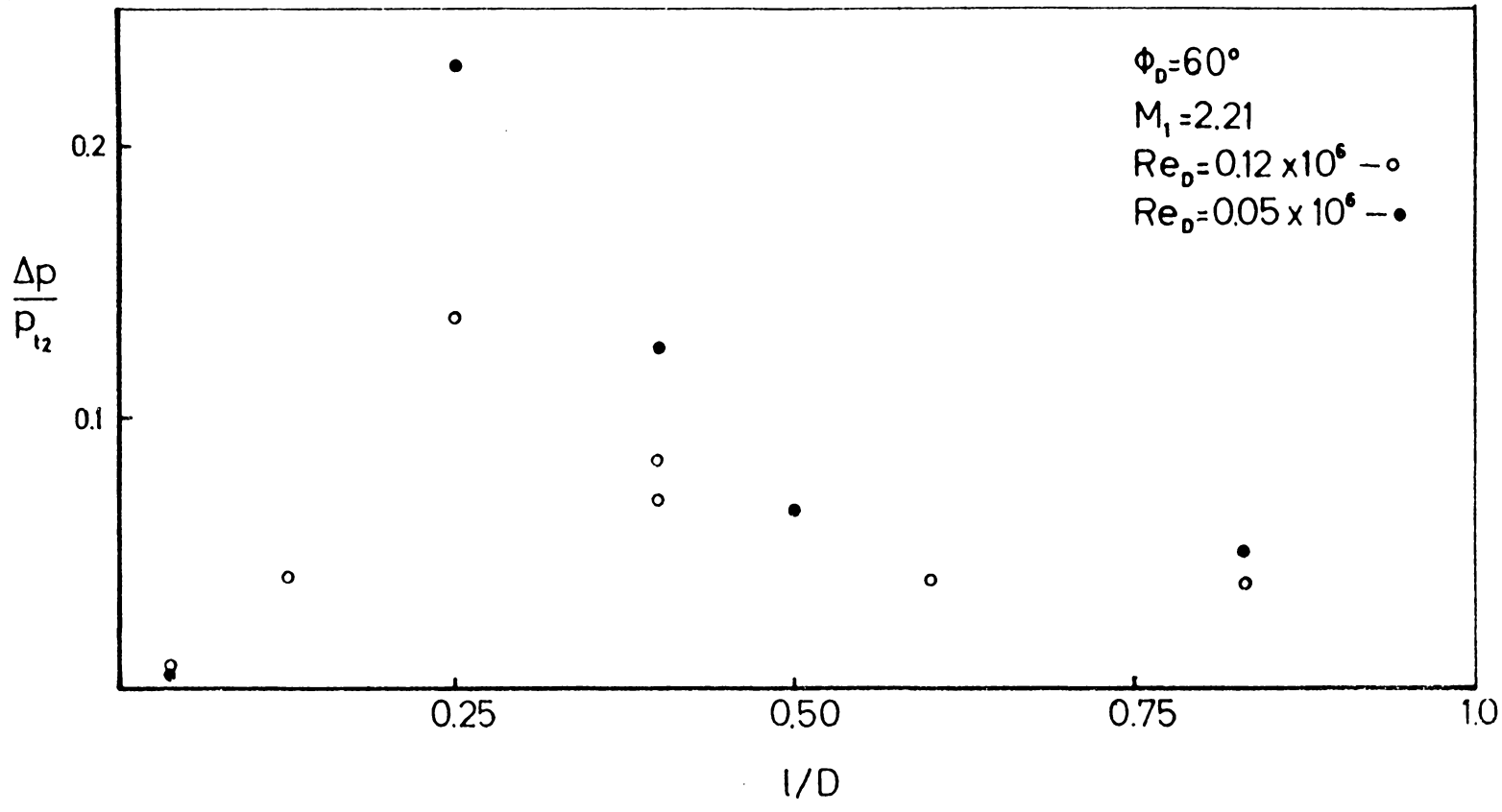

Figure A-5 (continued)

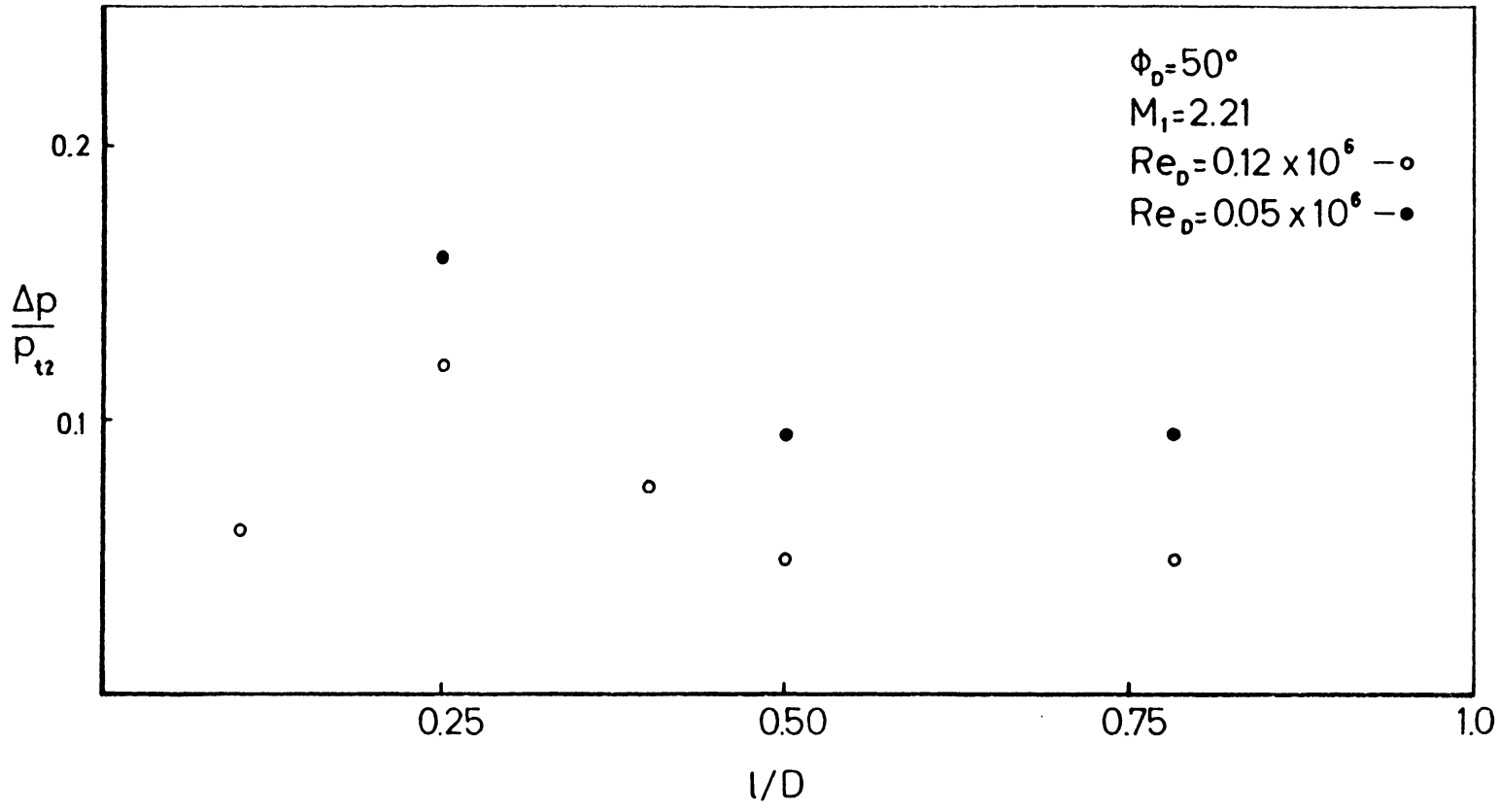

Figure A-5 (continued)

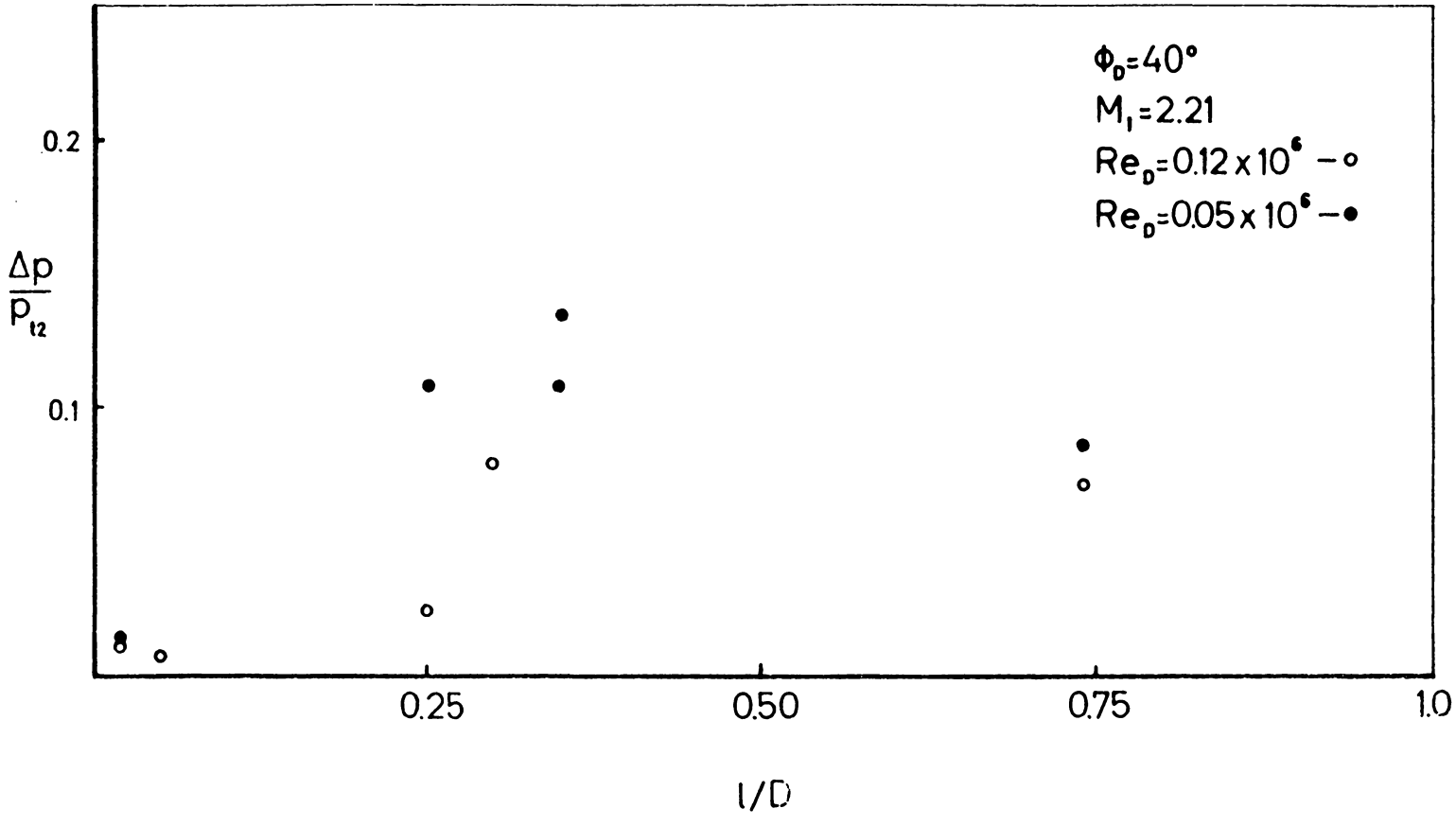

Figure A-5 (continued)

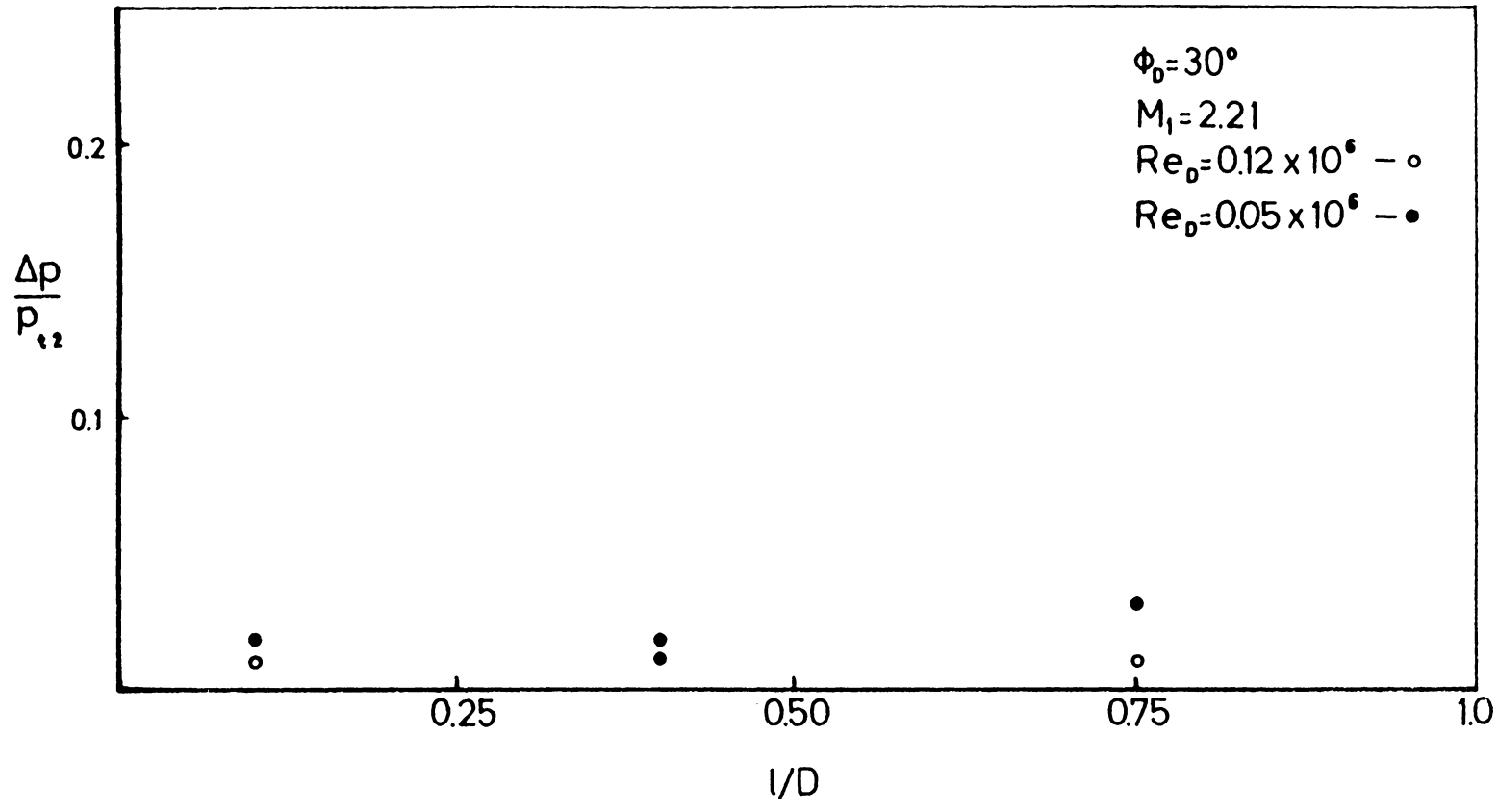

Figure A-5 (continued)

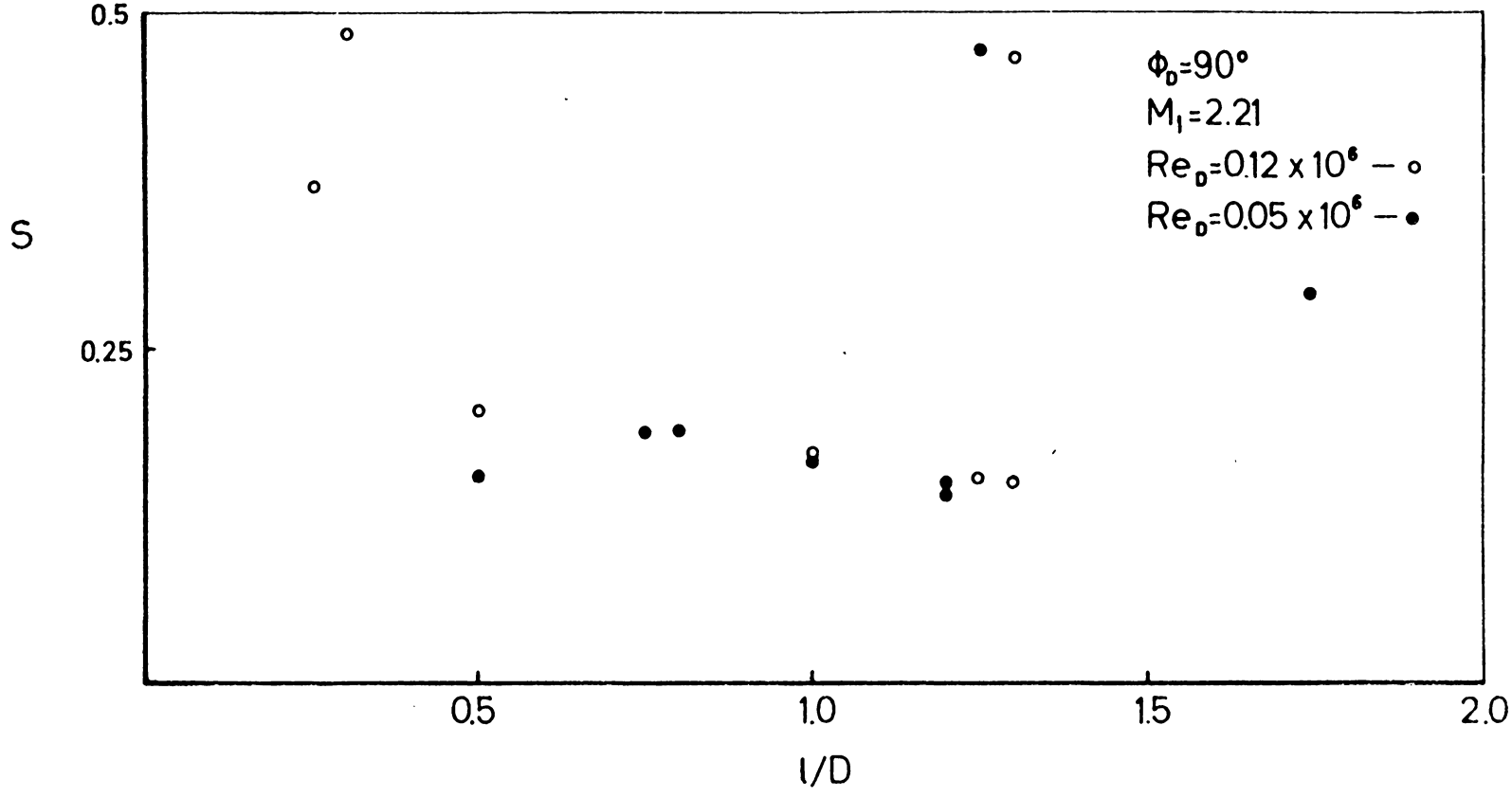

Figure A-6. Supersonic (Series III) Frequency Distribution

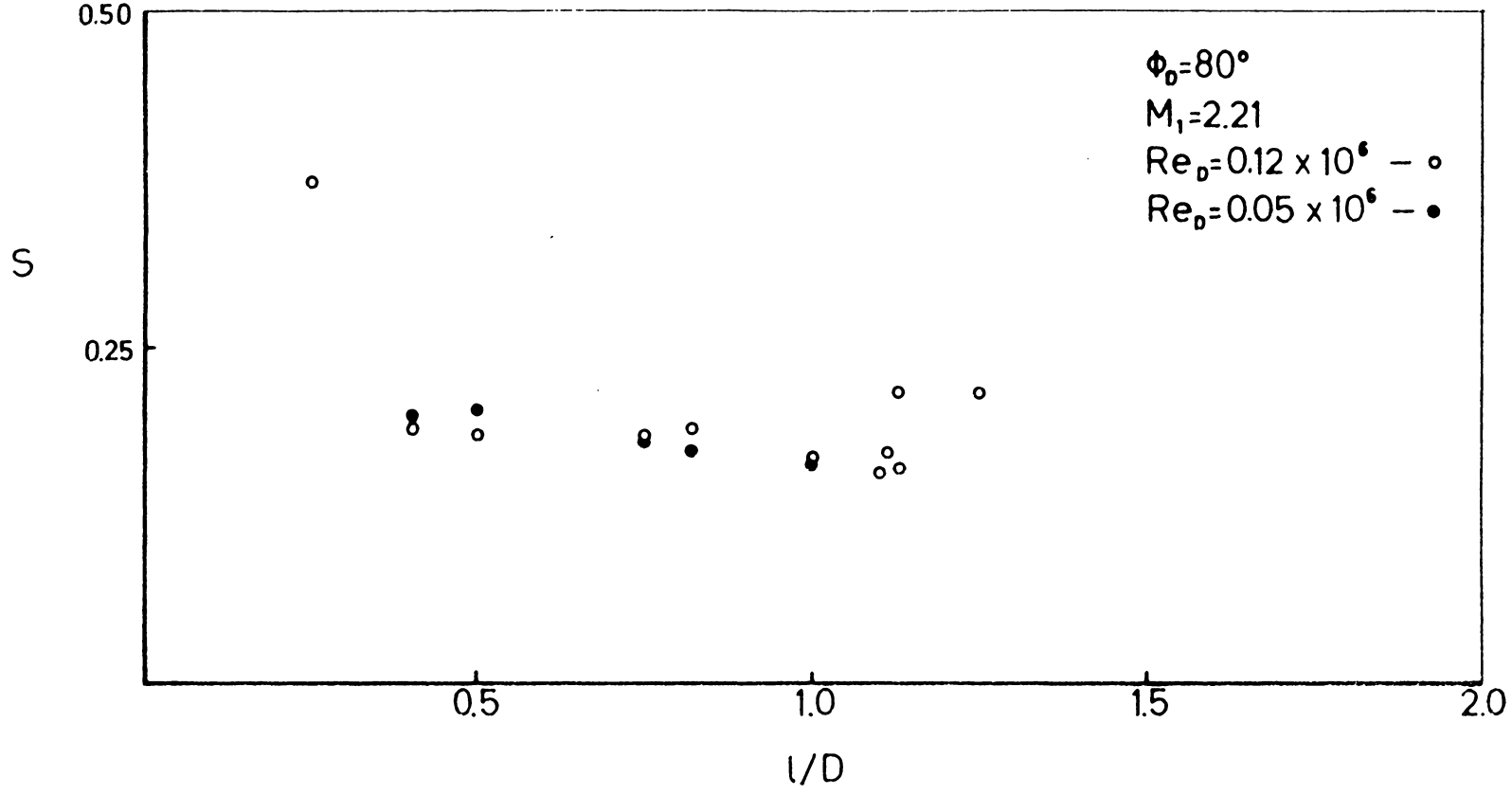

Figure A-6 (continued)

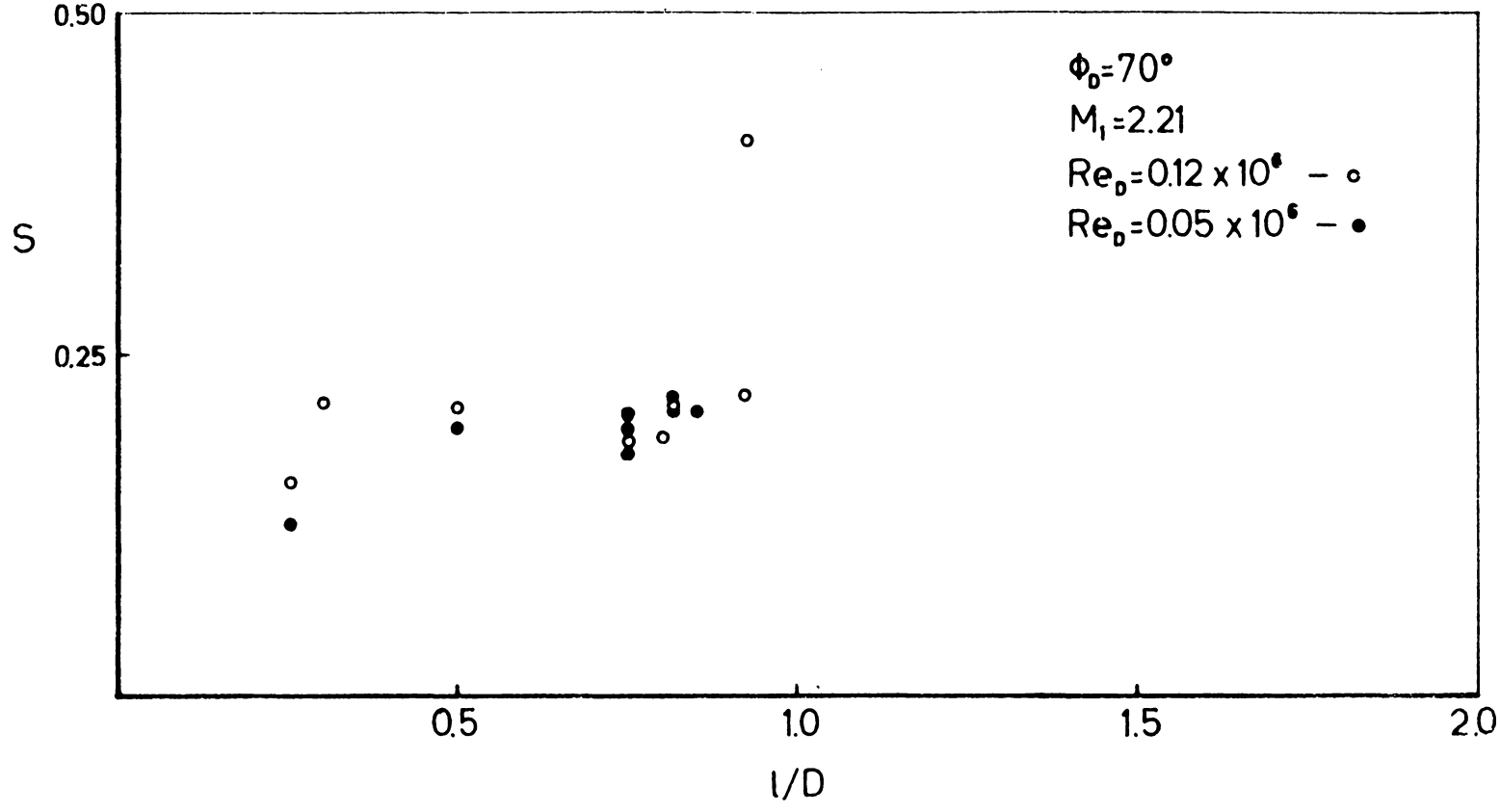

Figure A-6 (continued)

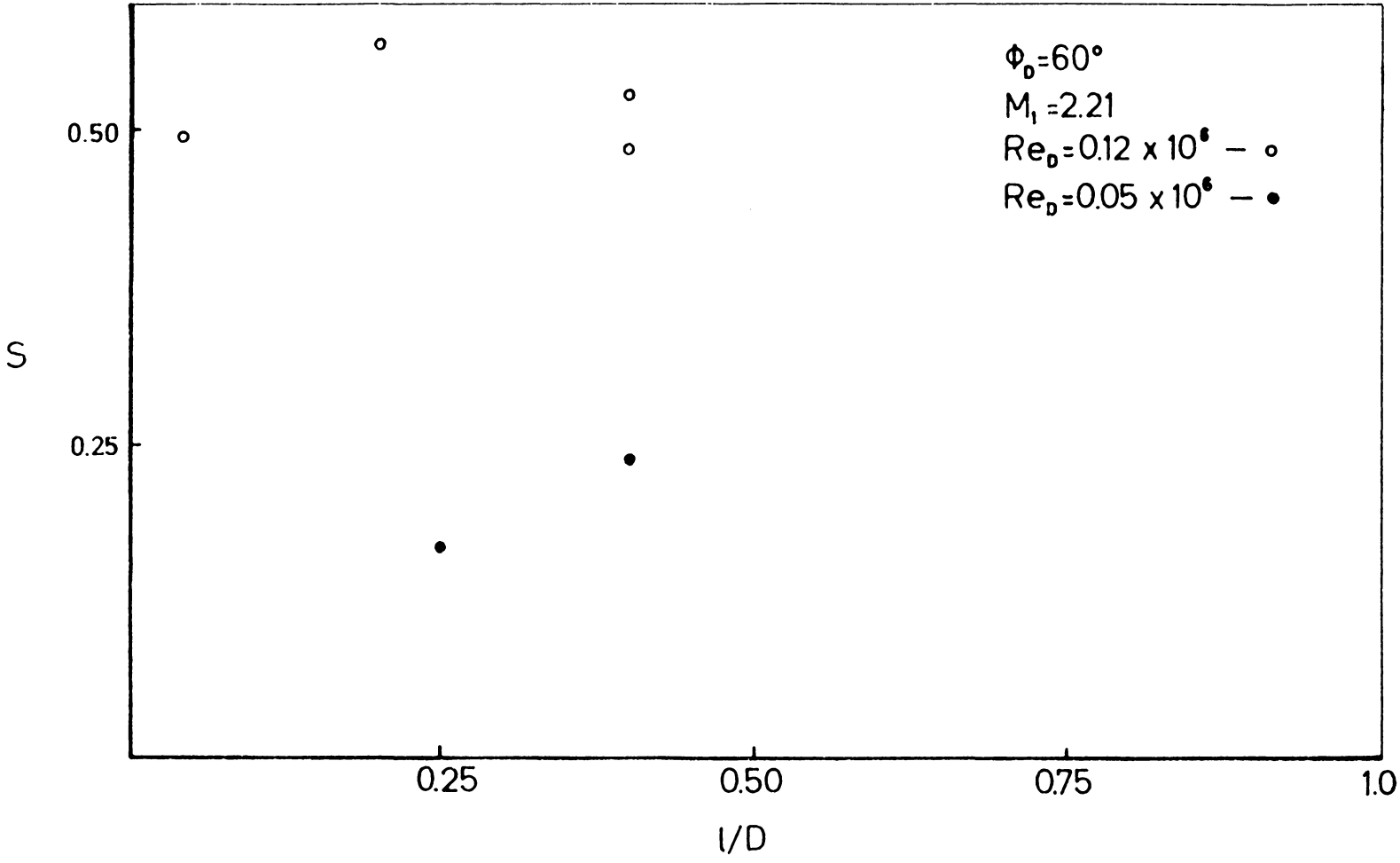

Figure A-6 (continued)

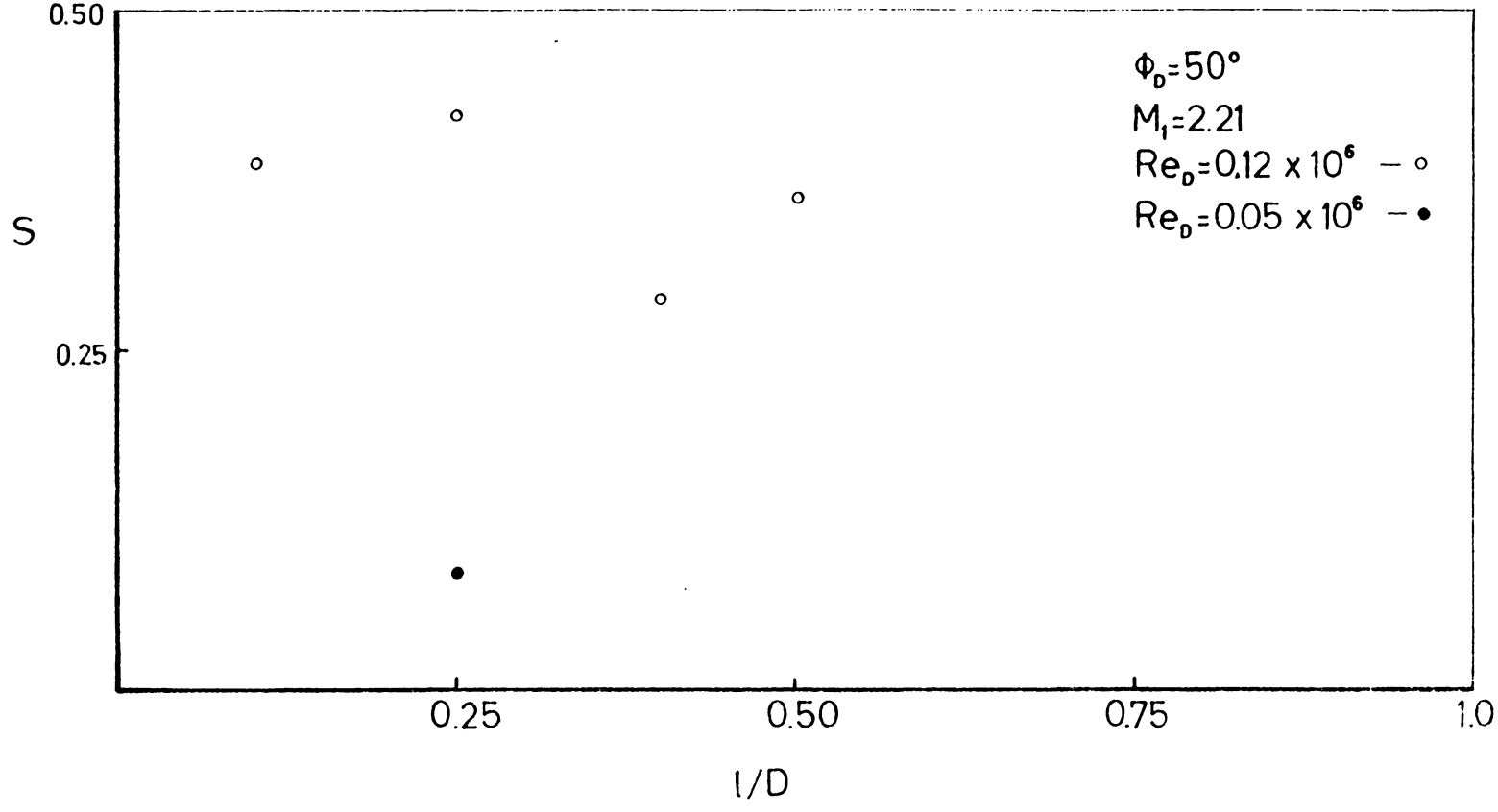

Figure A-6 (continued)

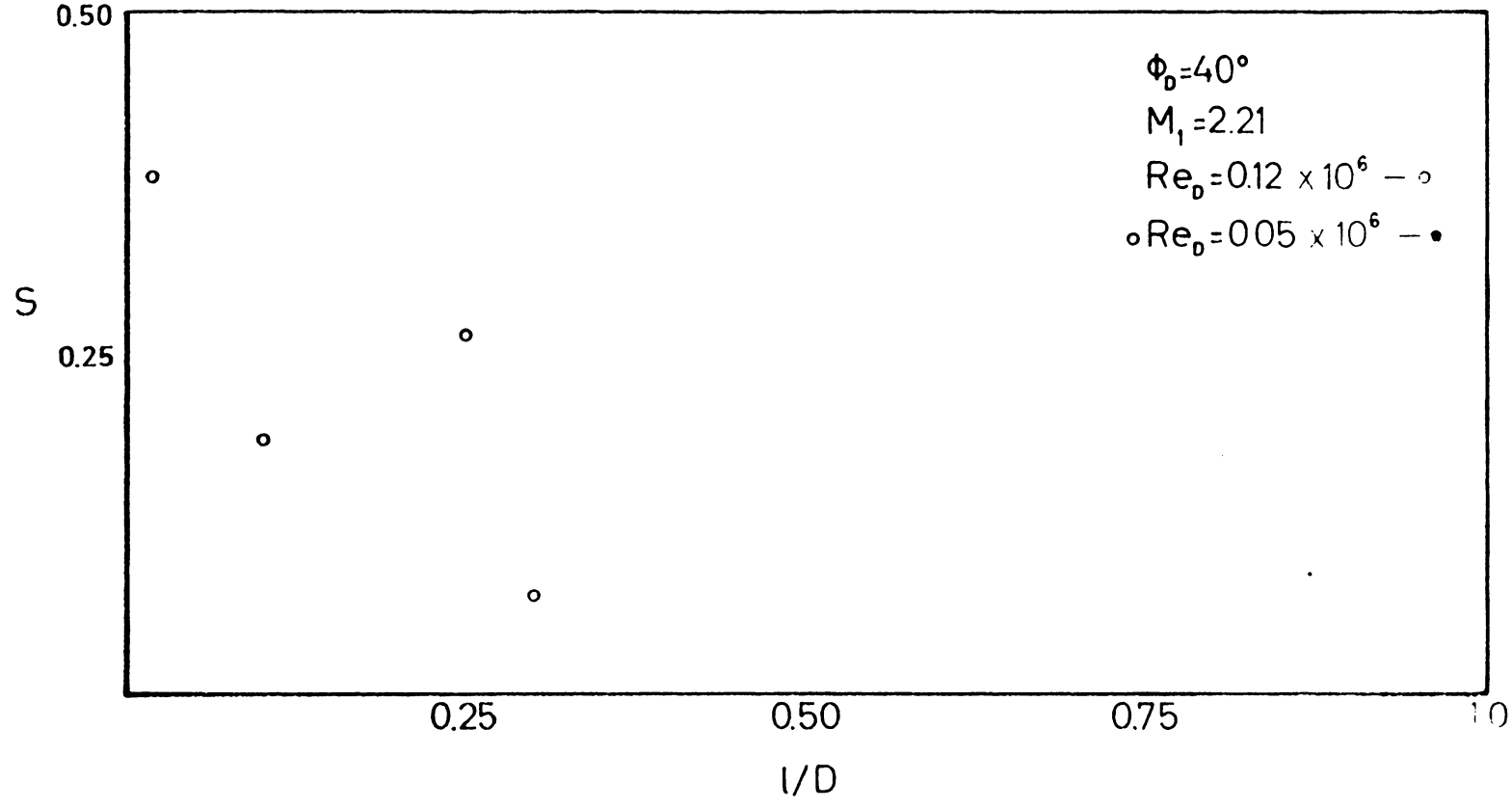

Figure A-6 (continued)

APPENDIX B - THE MOMENTUM THICKNESS RATIO

In the analysis of the laminar compressible shear layer by Cooke (Ref. 51) and also that of Appendix C, the ratio of momentum thicknesses across the separation point, θ_2/θ_1, is used to obtain the initial shear layer width, W, knowing the boundary layer thickness at separation, δ_1, i.e.,

$$W = n\,\delta_1 \qquad \text{where } n \equiv \frac{\theta_2}{\theta_1} \tag{B-1}$$

The subscripts 1 and 2 denote conditions before and after separation respectively.

A number of expressions for n have been developed for the two dimensional case, e.g. Kirk (Ref. 73), Young and Kirkby (Ref. 74) and Nash (Ref. 75). References 73 and 74 were developed for small expansions but are readily adapted to small compression by a simple change in sign. Parametric studies made with these expressions by Cooke (Ref. 51) and Appels (Ref. 55) have shown n to be approximately unity for small separation angles.

Moeckel (Ref. 76) has also developed expressions for n in compression both for the two dimensional and axisymmetric case. The axisymmetric expression is

$$n = \left\{ \frac{1 + H_1^2 + \left(\frac{u_2}{u_1}\right)\cos\alpha}{Q} \right\}^{1/2} \tag{B-2}$$

$$Q \equiv \frac{q_2}{q_1} \cos\alpha$$

where the shape factor, H_1, is the ratio of boundary layer displacement thickness, δ_1^*, and momentum thickness, θ_1, u the velocity, α the separation angle and q the dynamic pressure. Again subscripts 1 and 2 refer to conditions before and after separation respectively.

In Fig. 78 is plotted n versus α for different values of H_1. For two dimensional flow H_1 varies from 2.5 for a Blasius profile to 4 at the separation of an adiabatic Cohen-Reshotko flow. For $H_1 = 4$, the value of n is within 10% of unity for separation angles below 20°. Thus, as was found in the two dimensional case, one may approximate n as unity.

APPENDIX C - AN AXISYMMETRIC LAMINAR COMPRESSIBLE MIXING LAYER THEORY

For reasons given in section 5.1.3.3 an axisymmetric laminar compressible mixing layer theory is developed following Lock (Ref. 53) and Cooke (Ref. 51).

A set of orthogonal coordinates is defined such that x is parallel to the flow and y perpendicular to it. This means x is inclined to the undisturbed free stream by the separation angle, α. Therefore the radial distance, r, measured perpendicular to the axis of symmetry is given by

$$r = x \sin\alpha + y \cos\alpha \qquad \text{(C-1)}$$

The dividing streamline is defined as y = 0.

The equations of mass and momentum with the usual boundary layer assumptions for axisymmetric flow are introduced as follows:

$$\frac{\partial(\rho u r)}{\partial x} + \frac{\partial(\rho v r)}{\partial y} = 0 \qquad \text{(C-2)}$$

$$\rho u \frac{\partial u}{\partial x} + \rho v \frac{\partial v}{\partial y} = - \frac{\partial p}{\partial x} + \frac{1}{r} \frac{\partial}{\partial y} \left(r u \frac{\partial u}{\partial y} \right) \qquad \text{(C-3)}$$

Use is made of the Dorodnitzyn type transformation

$$X = Cx \qquad \text{and} \qquad Y = \int \frac{\rho}{\rho_\infty} \, dy \qquad \text{(C-4)}$$

to transform Eqs. C-2 and C-3 to the incompressible plane providing the viscosity-temperature law

$$\frac{\mu}{\mu_{ref}} = C \left(\frac{T}{T_{ref}}\right) \tag{C-5}$$

is valid, where C is Chapman's constant. The value of C is readily evaluated from knowledge of conditions at the edge of both sides of the shear layer. Therefore, one may write

$$C_2 = \frac{\rho\mu}{\rho_2 u_2} \tag{C-6}$$

since $\frac{\partial p}{\partial y}$ is negligible across shear flow, where the subscript 2 indicates the free stream conditions downstream of the separation shock.

Next the condition of zero streamwise pressure gradient is imposed since it has been ascertained that the mixing process of large separated regions takes place for the most part under this condition (section 5.1.3). This eliminates the pressure term in Eq. C-3.

The transformation of Eqs. C-2 and C-3 then yield

$$\frac{\partial(ur)}{\partial X} + \frac{\partial(\bar{v}r)}{\partial Y} = 0 \tag{C-7}$$

and

$$u \frac{\partial u}{\partial X} + \bar{v} \frac{\partial u}{\partial Y} = \frac{\mu}{r} \frac{\partial}{\partial Y} \left(r \frac{\partial u}{\partial Y}\right) \tag{C-8}$$

where

$$\bar{v} \equiv [u \frac{\partial Y}{\partial X} + v (\frac{\rho}{\rho_\infty})]/C_2 .$$

The definition of $\bar{v}$ is a result of the stretching of the y-coordinate requiring the velocity in this direction to be "stretched".

Equation C-7 is multiplied by u and Eq. C-8 by r, added and then integrated with respect to Y to obtain

$$\int_0^\delta \frac{\partial (ru^2)}{dX} dY + u_2 \bar{v}_2 r_2 = - \nu_2 r_0 \frac{\partial u}{\partial Y} \Bigg|_0 \qquad \text{(C-9)}$$

where δ is the edge of the viscous flow region and "o" the dividing streamline. Note that $\bar{v}$ on the dividing streamline vanishes and likewise $\frac{\partial u}{\partial Y}$ at the edge of the shear flow vanishes.

Making use of Leibnitz' theorem for differentiation of an integral and evaluating the normal velocity component at the shear layer edge from Eq. C-7, one obtains

$$\frac{d}{dX} \int_0^\delta ru(u_2 - u)\, dY = \nu_2 r \frac{\partial u}{\partial Y} \Bigg|_0 \qquad \text{(C-10)}$$

Next the shear layer profile is assumed to be self-similar throughout its length and a suitable profile is chosen. Following Cooke (Ref. 51) the profile chosen is sinusoidal. Thus, the velocity profile for the flow above the dividing streamline is:

$$\frac{u_u}{u_2} \equiv z_u = z_j + (1-z_j) \sin \frac{\pi \eta_u}{2} \qquad \text{(C-11)}$$

$$\text{where } \eta_u = \frac{Y}{\delta_u}$$

and the flow below the dividing streamline is

$$\frac{u_\ell}{u_2} \equiv z_\ell = z_j - z_j \sin \frac{\pi \eta_\ell}{2} \qquad \text{(C-12)}$$

$$\text{where } \eta_\ell = \frac{-Y}{\delta_\ell}$$

In these expressions and developments that follow z_j is a non-dimensional dividing streamline velocity based on the velocity at the outer edge of the shear layer, u_2 (velocity velow the shear layer is zero). The shear layer width, W, is divided into the width above the streamline, δ_u, and that below, δ_ℓ.

Substituting Eq. C-11 and C-12 into the momentum equation (Eq. C-10) one obtains

$$\frac{d}{dX} \delta_u \int_0^1 r_u z_u (1-z_u) \, d\eta_u = \frac{\nu_2}{u_2} r_0 \left. \frac{\partial u}{\partial Y_u} \right|_0 \qquad \text{(C-13)}$$

and

$$-\frac{d}{dX} \delta_\ell \int_1^0 (r_\ell z_\ell^2) \, d\eta_\ell = \frac{\nu_2}{u_2} r_0 \left. \frac{\partial z_\ell}{Y} \right|_0 \qquad \text{(C-14)}$$

One may now invoke the condition of continuity of shear stress across the dividing streamline.

$$\frac{\partial z_u}{\partial Y_u} = \frac{\partial z_\ell}{\partial Y_\ell} \qquad \text{at } Y = 0 \tag{C-15}$$

Making use of the velocity profiles, Eqs. C-11 and C-12, one obtains the following relations of thicknesses

$$\delta_u = W(1-z_j) \qquad \text{and} \qquad \delta_\ell = Wz_j \tag{C-16}$$

The continuity of shear stress also allows one to combine Eqs. C-13 and C-14 after which the result is integrated to yield

$$\delta_u \int_0^1 r_u(z_u - z_u^2)\, d\eta_u - \delta_\ell \int_0^1 r_\ell z_\ell^2\, d\eta_\ell = \text{const.} \tag{C-17}$$

The radial distance from the axis of symmetry is r_j therefore,

$$r_u = r_0 + \delta_u \eta_u \cos\alpha \tag{C-18}$$

and

$$r_\ell = r_0 - \delta_\ell \eta_\ell \cos\alpha \quad . \tag{C-19}$$

Substitution of Eqs. C-13, C-14, C-18 and C-19 into Eq. C-17 and integration yields

$$\delta_u r_0 (a+dz_j-ez_j^2) + \delta_c r(-ez_j^2) + \delta_u^2 (f+\ell z_j - kz_j^2)\cos\alpha -$$

$$\delta_\ell^2 (-kz_j^2)\cos\alpha = \text{const.} \qquad \text{(C-20)}$$

where

$$a = \frac{2}{\pi} - \frac{1}{2}, \quad d = 2 - \frac{6}{\pi}, \quad e = \frac{3}{2} - \frac{4}{\pi}, \quad f = \frac{3}{\pi^2} - \frac{1}{4},$$

$$\ell = 1 - \frac{10}{\pi^2} \quad \text{and} \quad k = \frac{3}{4} - \frac{7}{\pi^2}.$$

Further substitution into the above results using Eq. C-16 yields

$$Wr_0 (a+bz_j-cz_j^2) + W^2\cos\alpha (f+gz_j-hz_j^2+iz_j^3) = \text{const.} \qquad \text{(C-21)}$$

where

$$b = d - a, \quad c = d + e, \quad g = \ell - 2f, \quad h = 2\ell - f - k,$$

$$i = \ell + 2k$$

The initial conditions are

$$W = \delta_2, \quad r_0 = r_a \quad \text{and} \quad z_j = 0 \qquad \text{(C-22)}$$

That is, at separation the dividing streamline velocity is zero and the initial shear width is equal to the boundary layer thickness just downstream of separation, δ_2. Also at

separation the radial distance to the dividing streamline is equal to the spike radius, r_a. Note that the expression for the radial distance to the dividing streamline, r_0, is written as

$$r_0 = r_a + X \sin\alpha \tag{C-23}$$

Thus, the constant of Eq. C-21 may be written as

$$\text{constant} = a\delta_2 r_a + f\delta_2^2 \cos\alpha \tag{C-24}$$

Next Eq. C-14 is evaluated making use of Eq. C-12. The result is

$$\frac{d}{dX}\left[Wz_j^3(er_0 - k\delta_\ell \cos\alpha)\right] = r_0 \frac{\nu_2 \pi}{2Wu_2} \tag{C-25}$$

or

$$\frac{d}{dX}\left[Wz_j^3(er - kz_j W\cos\alpha)\right] = r_0 \frac{\nu_2 \pi}{2Wu_2} \tag{C-26}$$

Now available is a system of three equations, Eqs. C-21, C-23 and C-26, with the three unknown r_0, W, and z_j as functions of X. Unfortunately, these will not admit an analytic solution such as was obtained by Cooke. As a consequence one must either apply a numerical technique or make approximations to the equations by omitting higher order terms. In light of the promising results obtained with the Mangler transformation (section 5.1.3.2) and in

view of the application which will be made of these results, it is felt expedient that an approximation of the equations be used.

If the condition $W/r_0 < 1$ is met, Eq. C-21 may be approximated as

$$Wr_0(a+bz_j-cz_j^2) = a\delta_2 r_a \qquad \text{(C-27)}$$

It should be noted here that the restriction at separation on the ratio δ_2/r_a need not be strict since the constant "a" is more than twice as large as "f". Nonetheless, care must be exercised using the present development that $\delta_2/r_a <$ 0.25 as an approximate limit.

The differentiation of Eq. C-25 is carried out yielding

$$(er_0-k\delta_\ell\cos\alpha)\frac{d}{dX}(Wz_j^3) + Wz_j^3\left(e\frac{dr_0}{dX}-k\cos\alpha\frac{d\delta_\ell}{dX}\right) = \qquad \text{(C-28)}$$

$$r_0\frac{\nu_{2\pi}}{2Wu_2} \quad .$$

Next to ascertain the relative importance of terms one may reasonably assume that $\delta_\ell \sim X^n$ where $0 < n < 1$. From boundary layer n could be restricted to a smaller range, but this will not be necessary. Therefore

$$\frac{d\delta_\ell}{dX} = \frac{n\delta_\ell}{X} \qquad \text{(C-29)}$$

From Eq. C-23 the derivative of r_0 is

$$\frac{dr_0}{dX} = \sin\alpha \sim \frac{r_0}{X} \tag{C-30}$$

Thus on applying the restriction $W/r_0 < 1$ Eq. C-28 is reduced to approximately

$$e \frac{d}{dX} (Wz_j^3 r) = r_0 \frac{\nu_2 \pi}{2Wu_2} \tag{C-31}$$

Equation C-27 may be rewritten as

$$a + bz_j - cz_j^2 = \frac{a\delta_2 r_a}{Wr_0} = c(A-z_j)(B+z_j) \tag{C-32}$$

and then substituted into Eq. C-31 to obtain

$$\frac{d}{dX}\left[\frac{z_j^3}{(A-z_j)(B+z_j)}\right] = \left(\frac{r_0}{r_a}\right)^2 \left(\frac{\nu_2}{u_2\delta_2^2}\right)\left(\frac{\pi c^2}{2a^2 e}\right) (A-z_j)(B+z_j) \tag{C-33}$$

At this point it is necessary to evaluate δ_2. Because a finite spike radius is being dealt with and relatively short lengths of boundary layer are being considered, the boundary develops as a Blasius boundary layer would on a flat plate (see Lighthill and Glauert, Ref. 77). Therefore,

$$\delta_1 = K\left(C_1 \frac{\nu_1 x_1}{u_1}\right)^{1/2} \tag{C-34}$$

where K is a constant which depends on the definition of δ, i.e., whether δ is taken as $u/u_1 = 0.99$ or 0.999. Cooke's

value of K = 4.795 will be used here to align with his results given later. The boundary layer thickness downstream of separation is now obtained by assuming the velocity profile has remained similar (see Hakkinen, Greber, Trilling and Abarbanel, Refs. 41). Thus the ratio of displacement thickness to momentum thickness are equal and one may write

$$\delta_2 = n\delta_1 \qquad \text{where } n \equiv \frac{\theta_2}{\theta_1} \tag{C-35}$$

A discussion of n is given in Appendix B.

Next the following definitions are made

$$D \equiv K^2 \frac{2a^2 e}{\pi c^2} \left(\frac{C_2}{C_1}\right) \tag{C-36}$$

and

$$\lambda \equiv \left(\frac{\sin^2\alpha}{3}\right)\left(\frac{x_2}{x_1}\right)^3 \left(\frac{u_1 \nu_2}{u_2 \nu_1 n^2}\right) \left(\frac{x_1}{r_a}\right)^2 \tag{C-37}$$

Note that in the definition of D appears the ratio of Chapman's constants, C_2/C_1. This is included here for completeness but as explained in section 5.1.3, this ratio can be approximated as unity.

On substituting the results and definitions of Eqs. C-34, C-35, C-36 and C-37 into Eq. C-33, one obtains

$$D \frac{d}{d\lambda}\left[\frac{z_j^3}{(A-z_j)(B+z_j)}\right] = (A-z_j)(B+z_j) \tag{C-38}$$

The solution of which is

$$\lambda = \frac{D}{(A+B)^3}\left[3AB\ln\left(\frac{A-z_j}{B+z_j}\right) - \frac{B^3(A+B)}{2(B+z_j)^2} + \frac{A^3(A+B)}{2(A-z_j)^2} - \right. \tag{C-39}$$

$$\left. \frac{B^3}{(B+z_j)} + \frac{A^3}{(A-z_j)} + E\right]$$

The constant E is determined by the condition that at $\lambda = 0$, $z_j = 0$. Thus, one obtains

$$A = 0.5873$$

$$B = 0.7388$$

$$\frac{D}{(A+B)^3} = 0.2675$$

$$E = 0.5782$$

FIGURES

a) AXISYMMETRIC DIFFUSER INLET

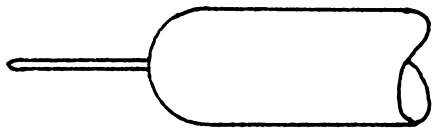

b) SPIKED HEMISPHERE

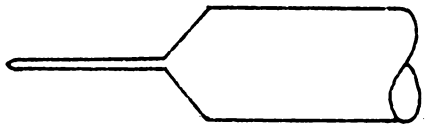

c) SPIKED CONE

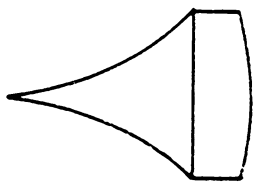

d) TENSION SHELL

FIG. 1 THE FAMILY OF SPIKED BLUNT BODIES

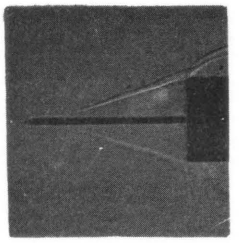

a

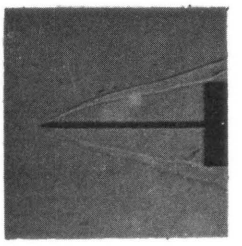

b

$\Phi_D = 90°$ $l/D = 2$

Fig. 2 The Oscillation Shock Envelope; $M_f = 6$, $Re_D = 0.13 \times 10^6$

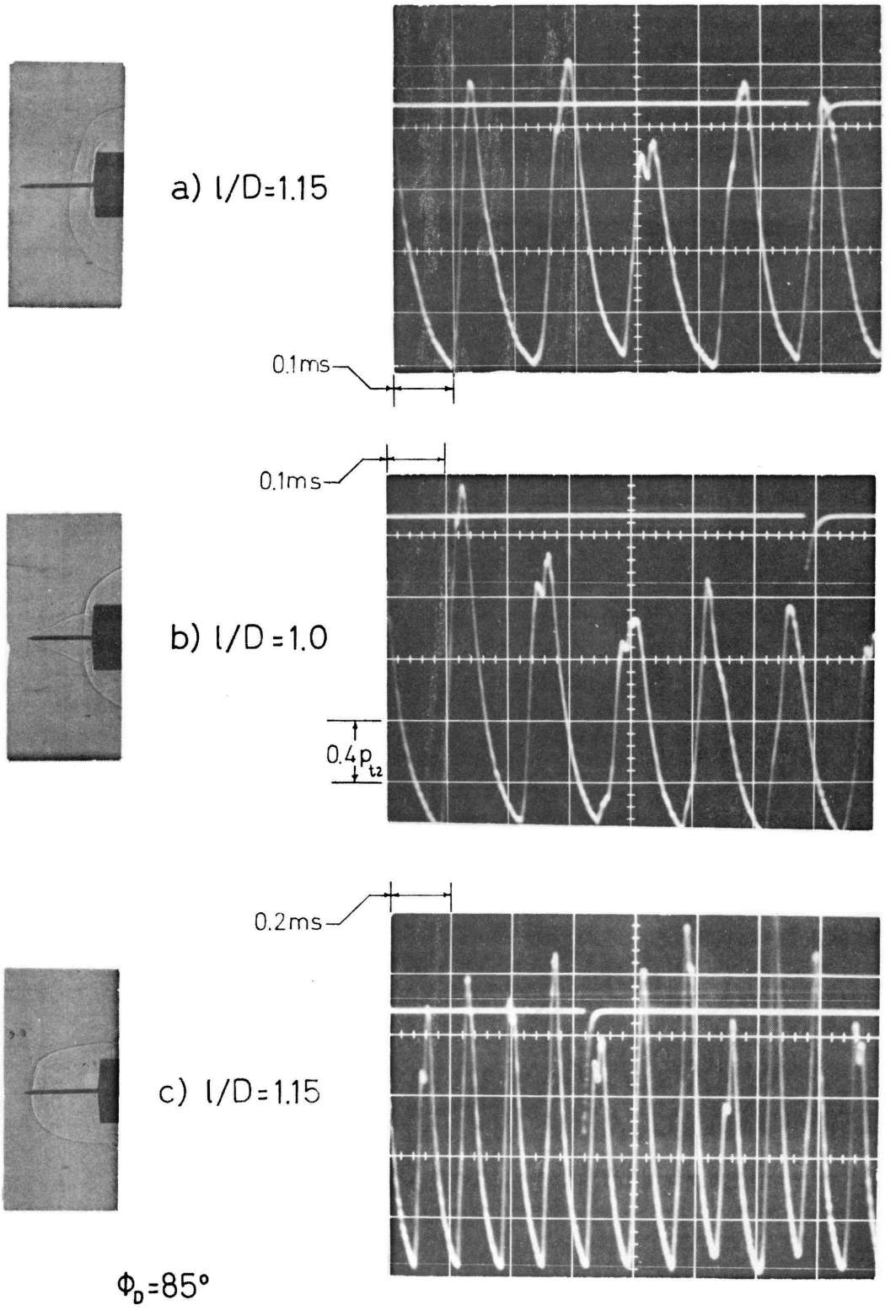

Fig. 3 The Pulsation Shock Envelope; $M_1=6$, $Re_D=0.13\times10^6$

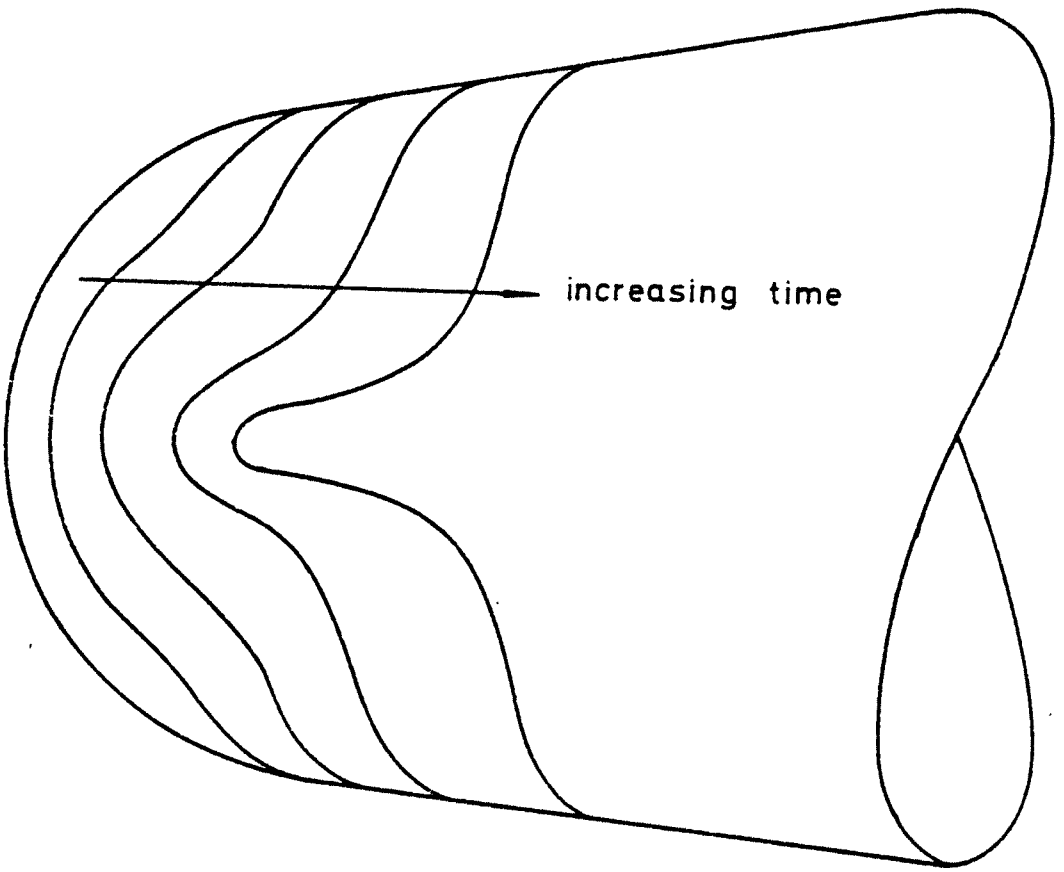

FIG. 4 HISTORY OF A TYPICAL RE-ENTRY ABLATION NOSE

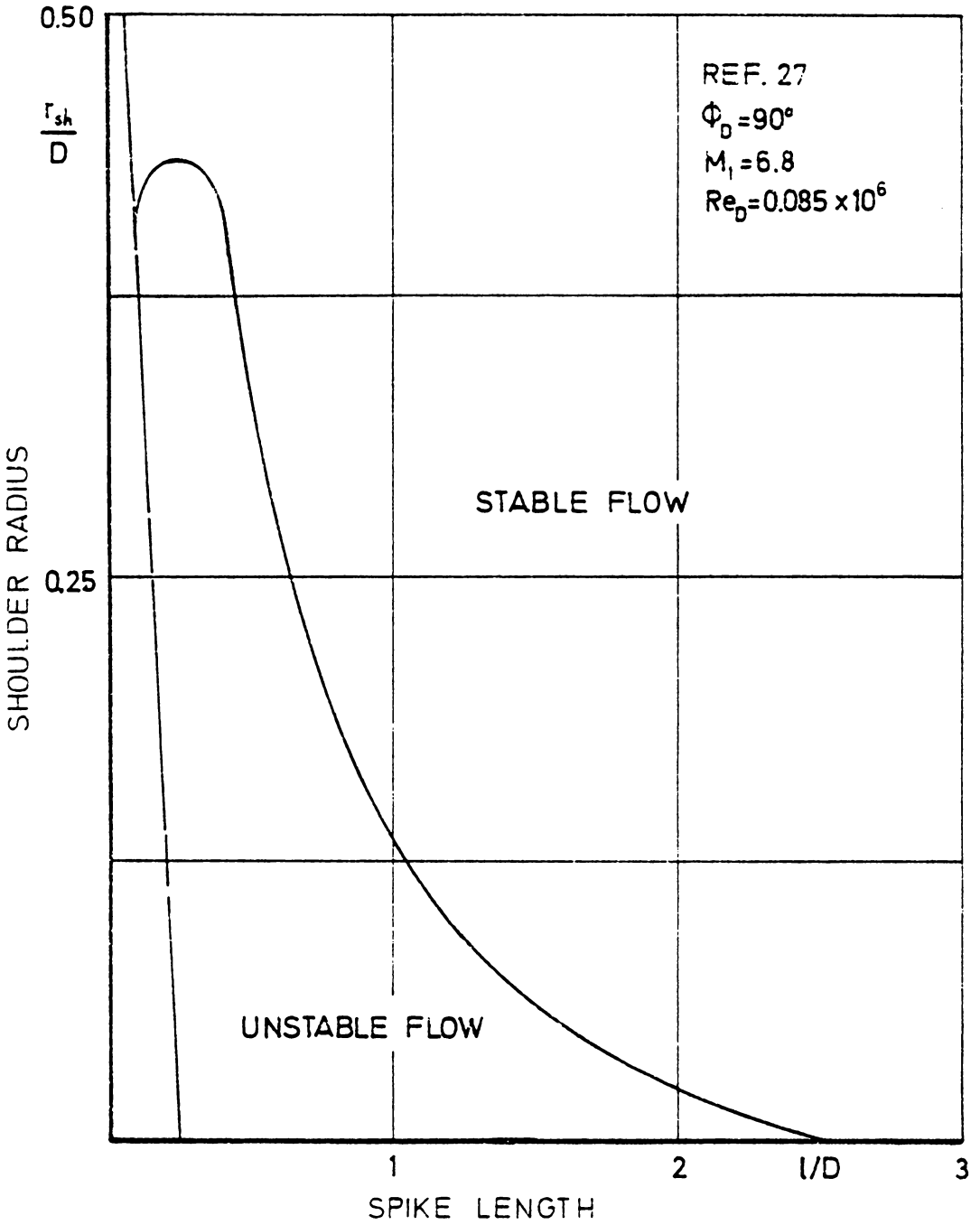

FIG. 5 THE EFFECT OF BODY SHOULDER RADIUS ON UNSTABLE FLOW

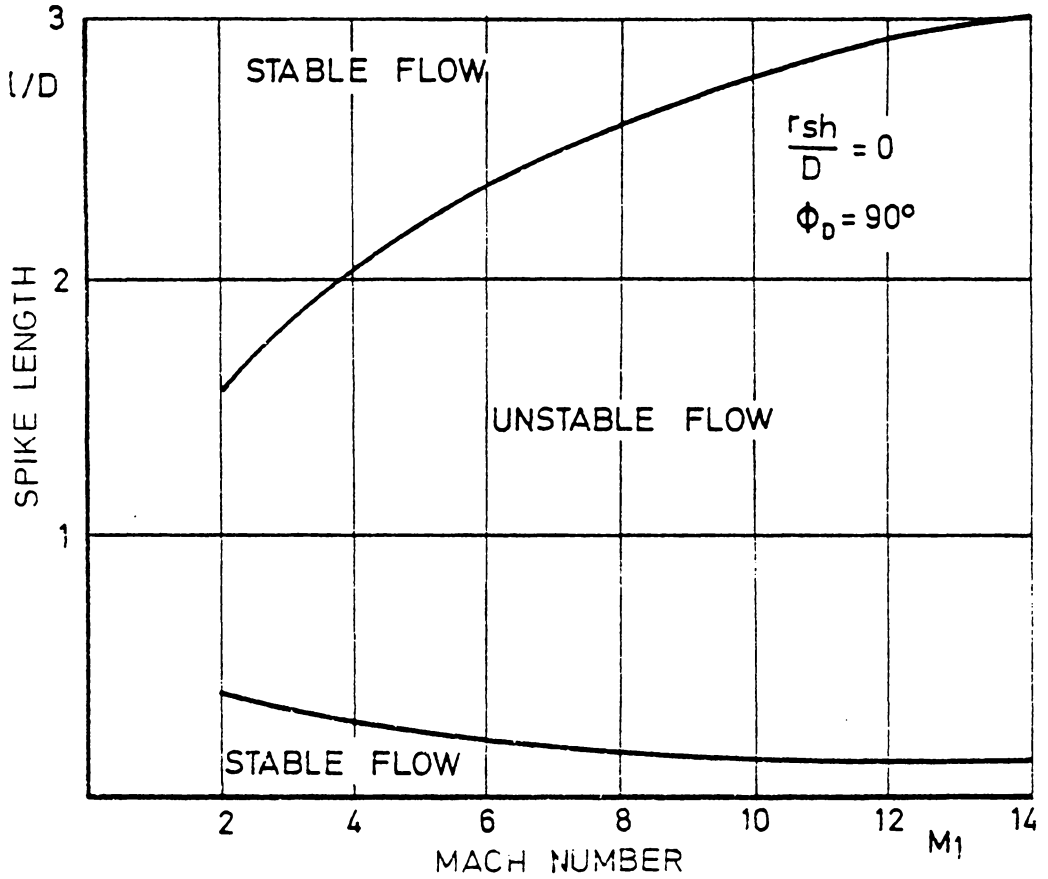

FIG. 6 THE RANGE OF UNSTABLE FLOW AS A FUNCTION OF MACH NUMBER AFTER MAULL (REF 27)

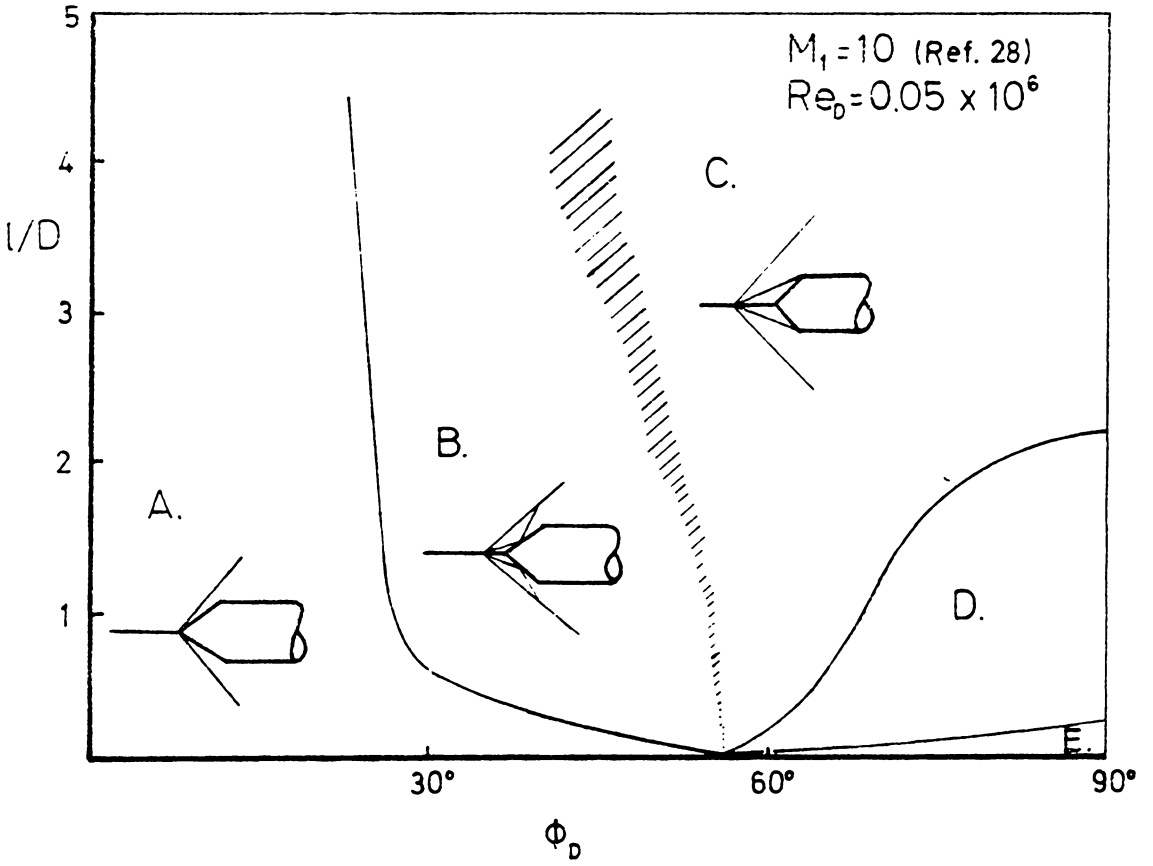

A. Unseparated Flow

B. Separated Flow

C. Shoulder Reattaching Flow

D. Unstable Flow

E. Stable Flow ($l < x_s$)

Fig. 7 Flow Regions for Spiked Cones after Wood

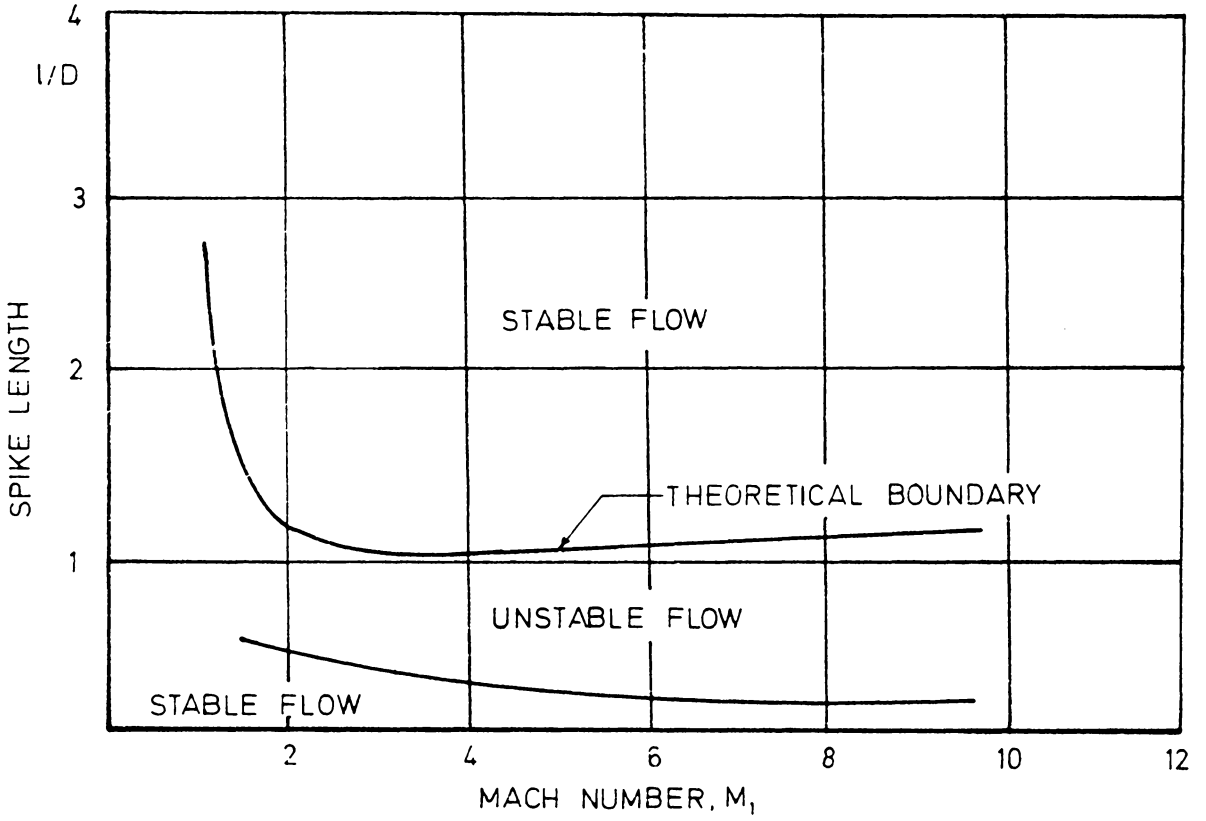

FIG. 8 THE RANGE OF UNSTABLE FLOW AS A FUNCTION OF MACH NUMBER AFTER ROBINSON ET AL (REF 29)

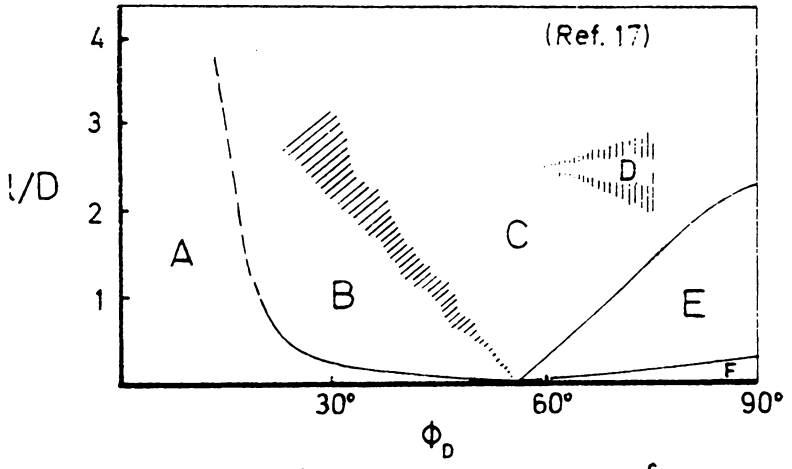

$M_1 = 10$; $Re_D = 0.27 \times 10^6$

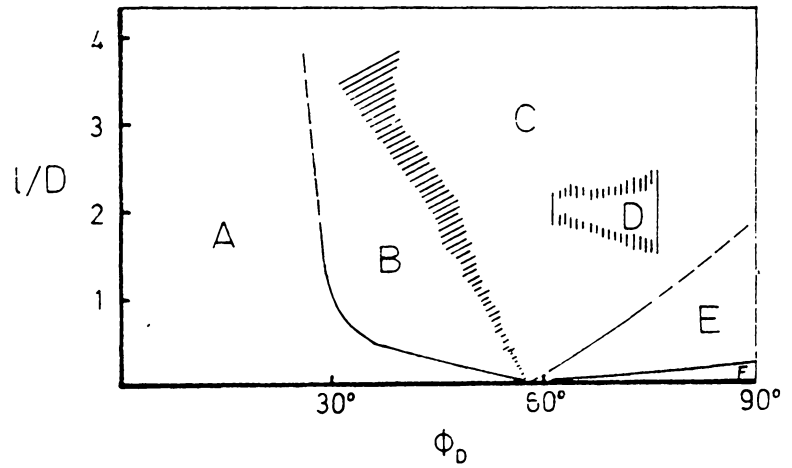

$M_1 = 15$; $Re_D = 0.27 \times 10^6$

A. Unseparated Flow
B. Face Reattaching Flow
C. Shoulder Reattaching Flow
D. Oscillation - Type "D"
E. Oscillation - Type "E"
F. Stable Flow ($l < x_s$)

Fig.9 Flow Regions for Spiked Cones after Holden

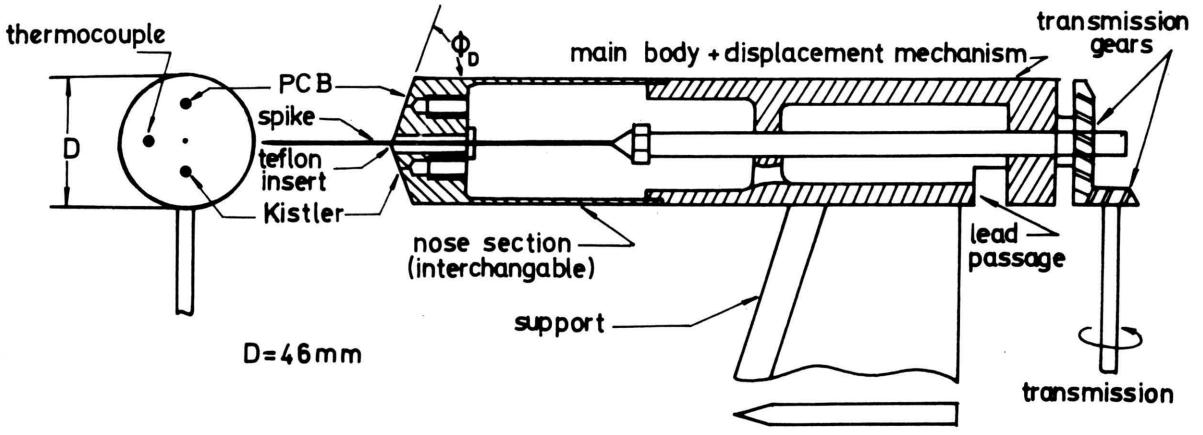

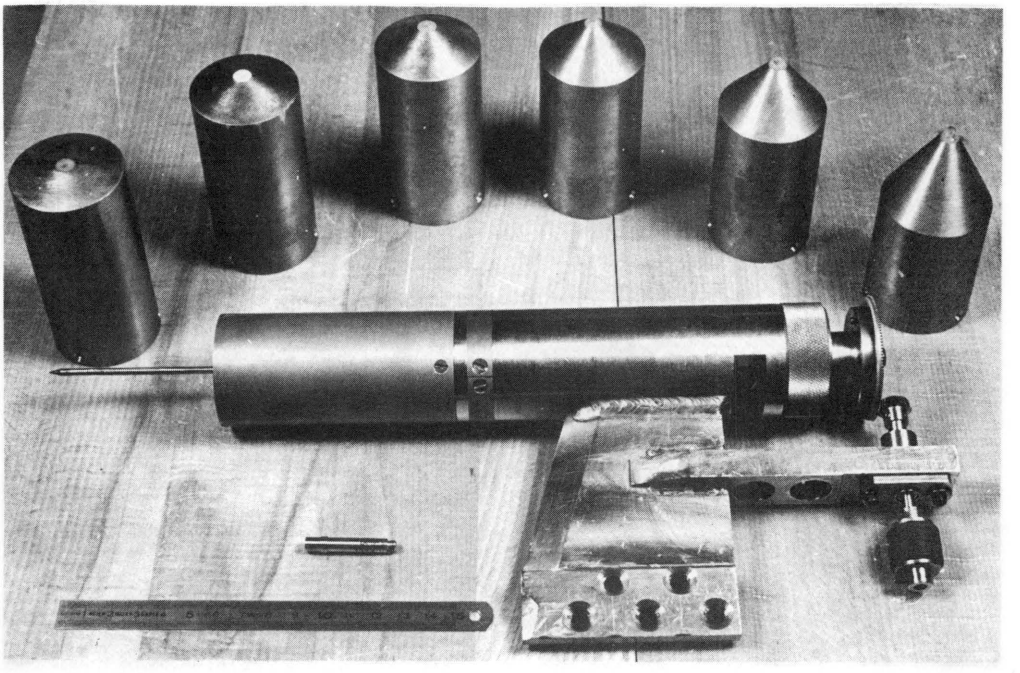

FIG. 10 THE LARGE MODEL

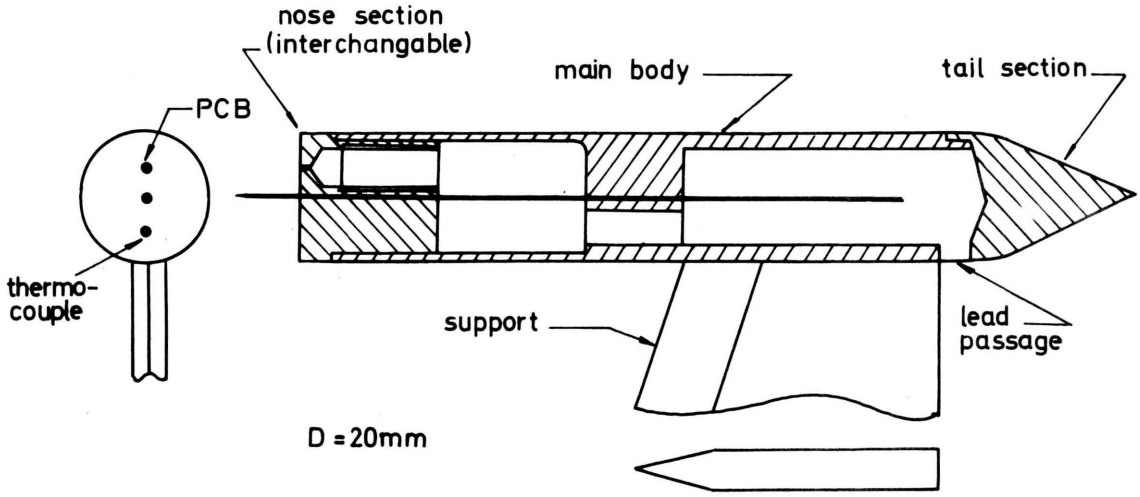

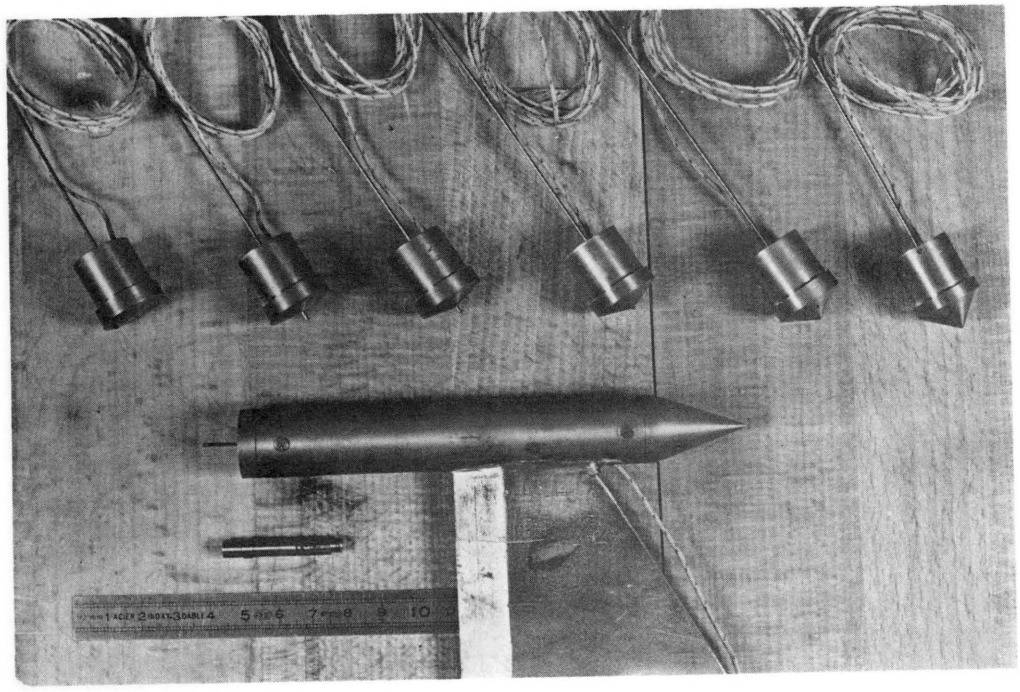

FIG. 11 THE SMALL MODEL

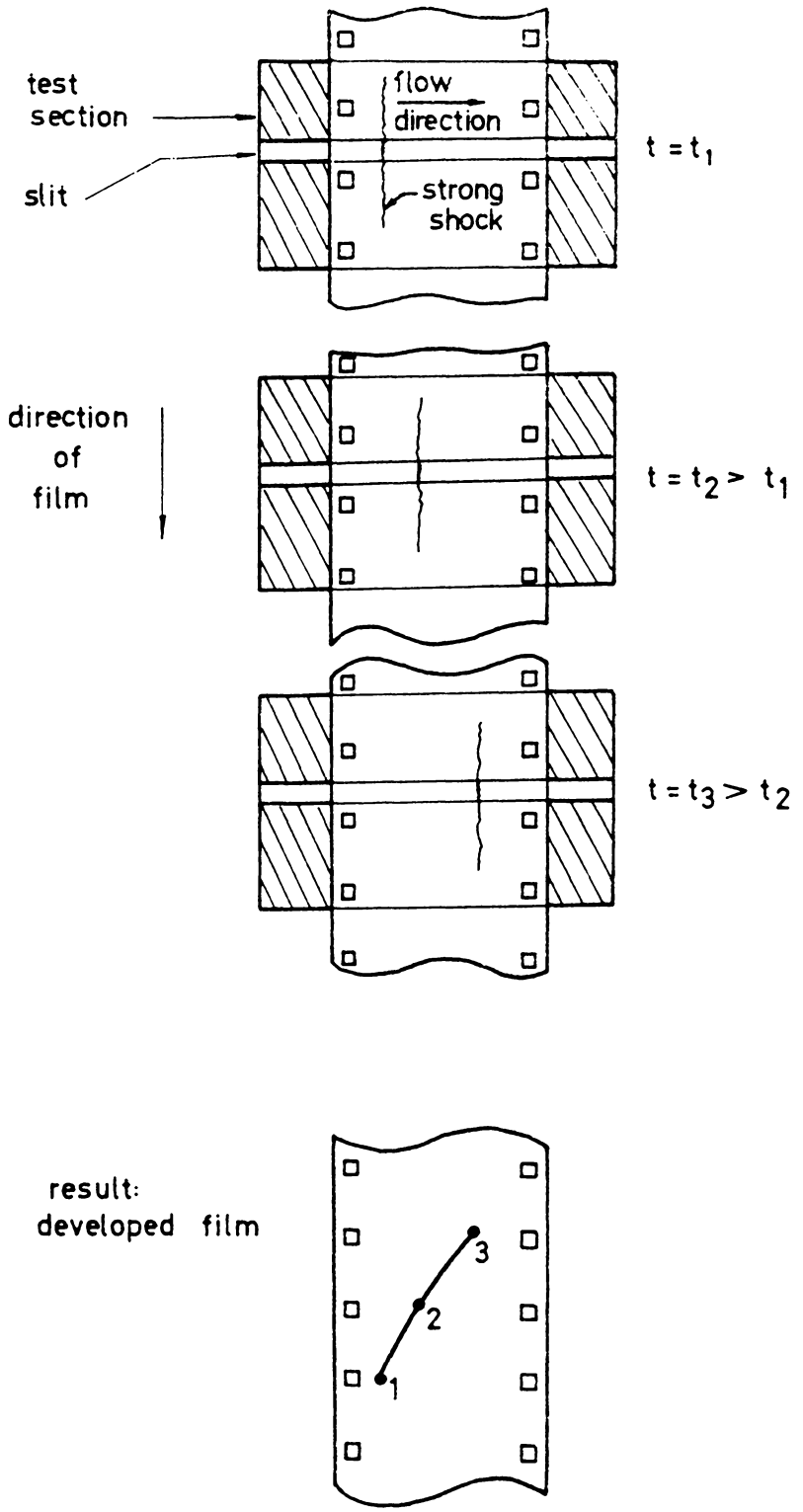

FIG. 12 THE HIGH SPEED CINE STREAK TECHNIQUE

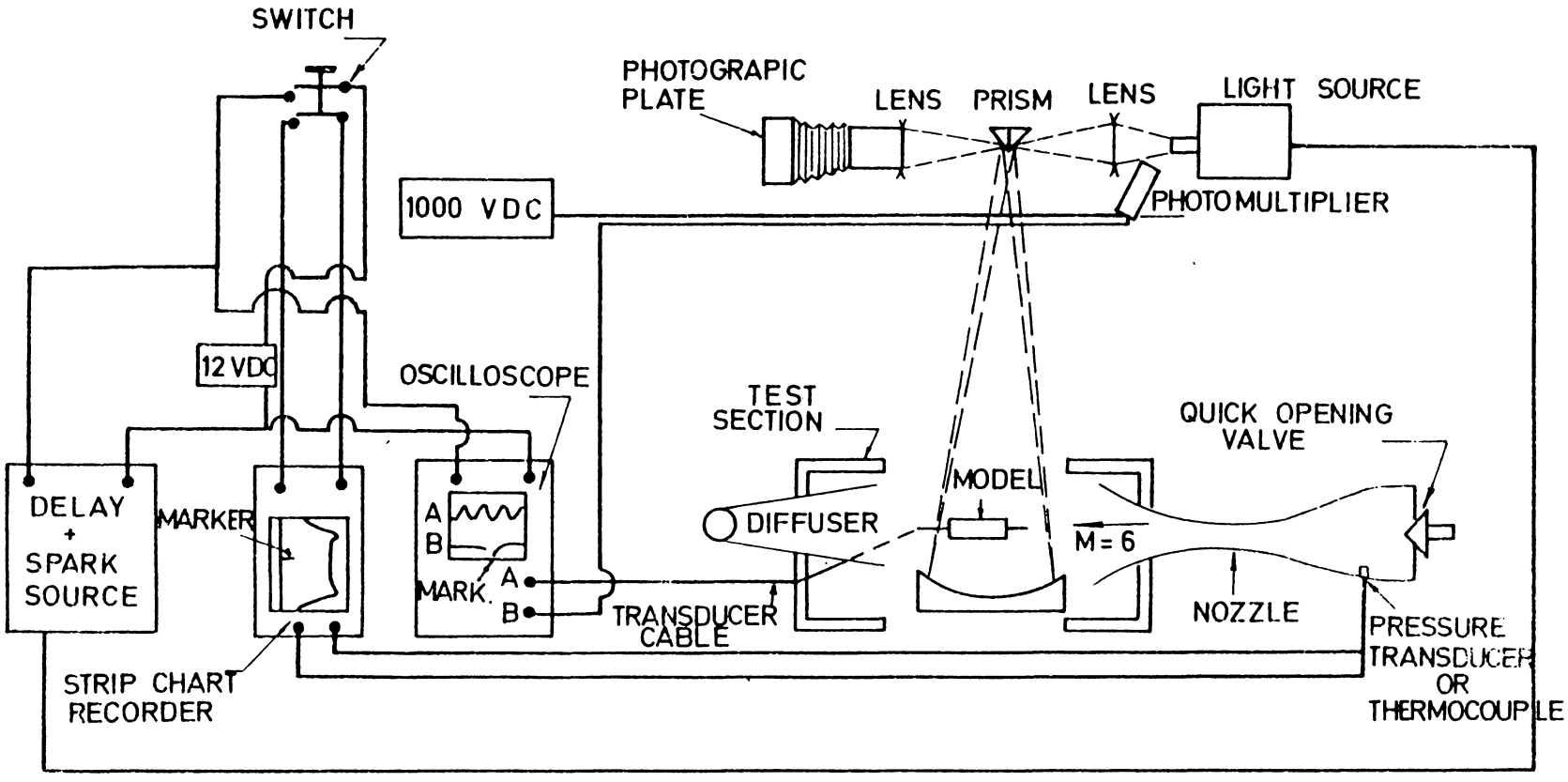

FIG. 13 THE SYNCHRONIZATION SYSTEM

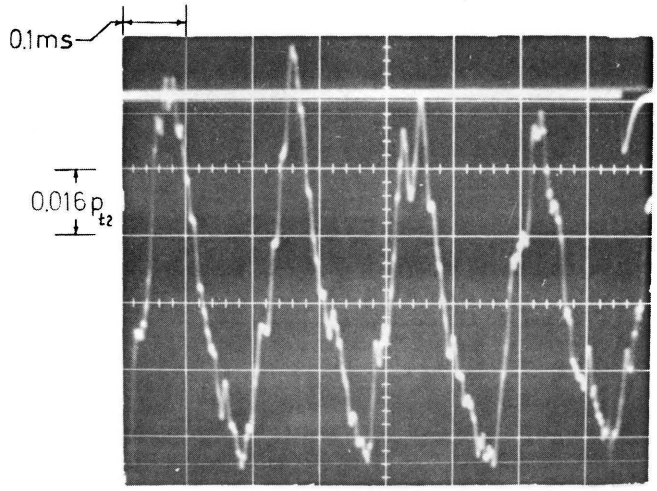

a) Φ_D=90° l/D=1.75 M_1=6 Re_D=0.13 x 10^6

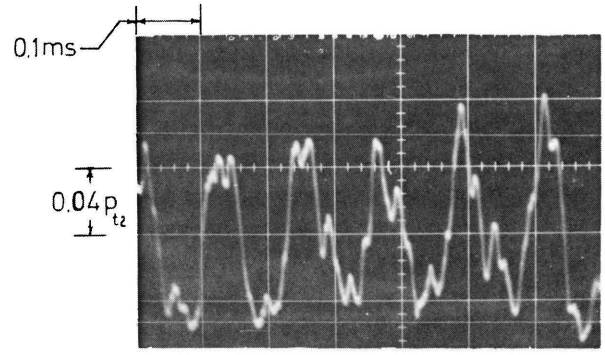

b) Φ_D=70° l/D=0.9 M_1=6 Re_D=0.13 x 10^6

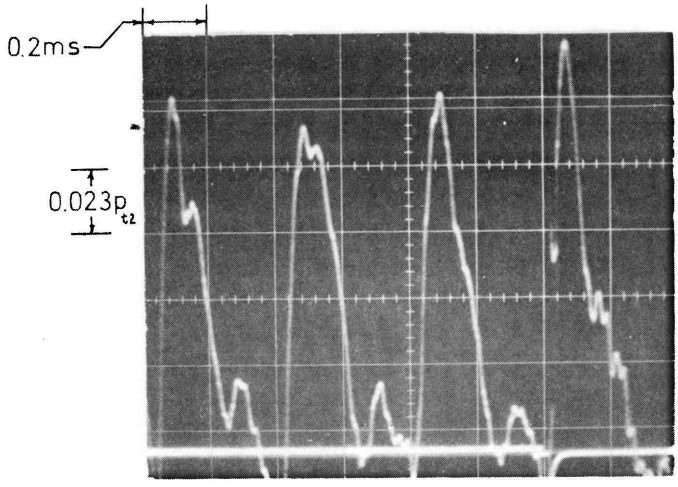

c) Φ_D=70° l/D=0.92 M_1=2.21 Re_D=0.12 x 10^6

Fig. 14 Samples of the Oscillation Pressure Wave

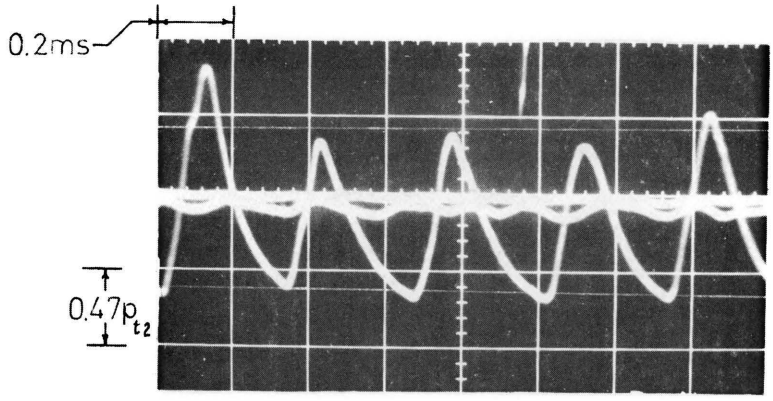

a) $\Phi_D = 90°$ $l/D = 1.4$ $Re_D = 0.9 \times 10^6$

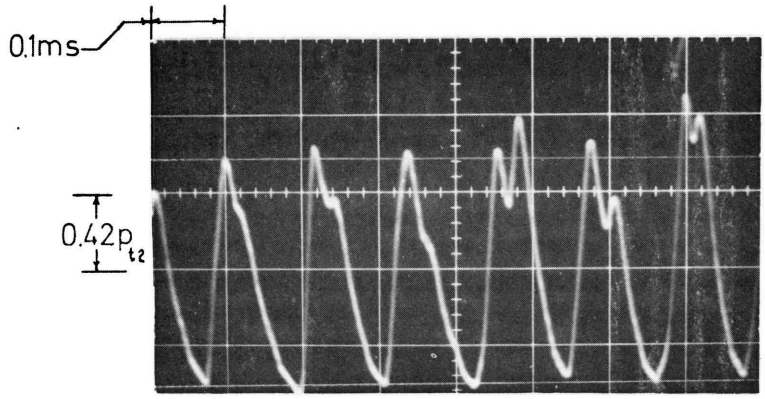

b) $\Phi_D = 85°$ $l/D = 0.75$ $Re_D = 0.13 \times 10^6$

Fig. 15 Samples of the Pulsation Pressure Wave at $M_1 = 6$

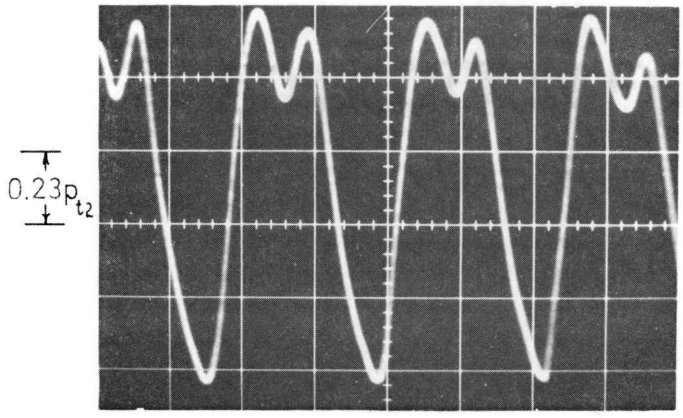

a) $Re_D = 0.12 \times 10^6$

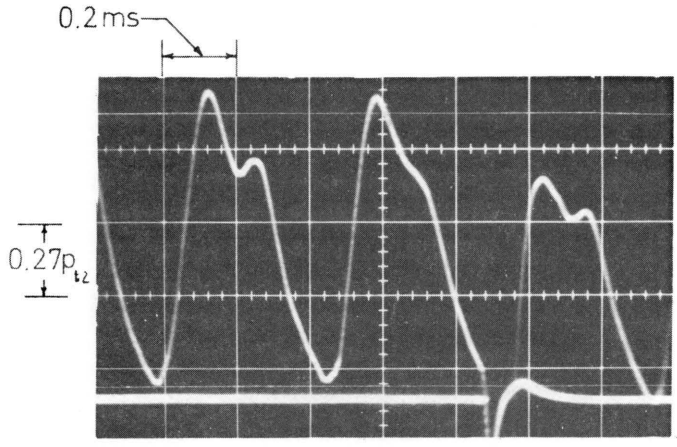

b) $Re_D = 0.05 \times 10^6$

$\Phi_D = 90°$ $l/D = 0.8$

Fig. 16 Samples of the Pulsation Pressure Wave at $M_1 = 2.21$

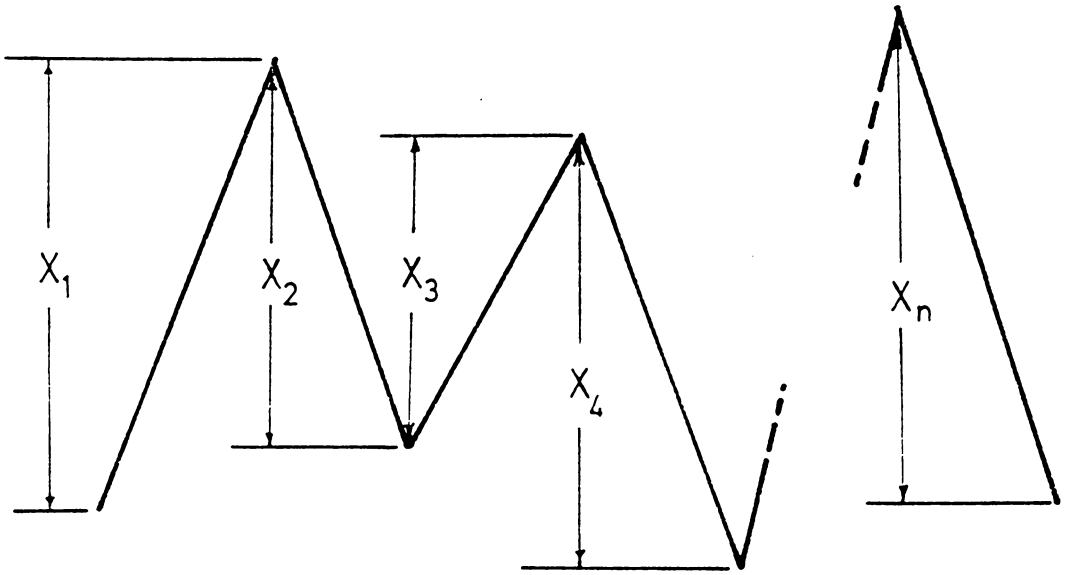

SCHEMATIC WAVE FORM

$$\bar{X} = \frac{1}{n} \sum_{i=1}^{n} X_i$$

$$\sigma = \sqrt{\frac{1}{n} \sum_{i=1}^{n} (X_i - \bar{X})^2}$$

FIG. 17 THE METHOD OF DATA REDUCTION

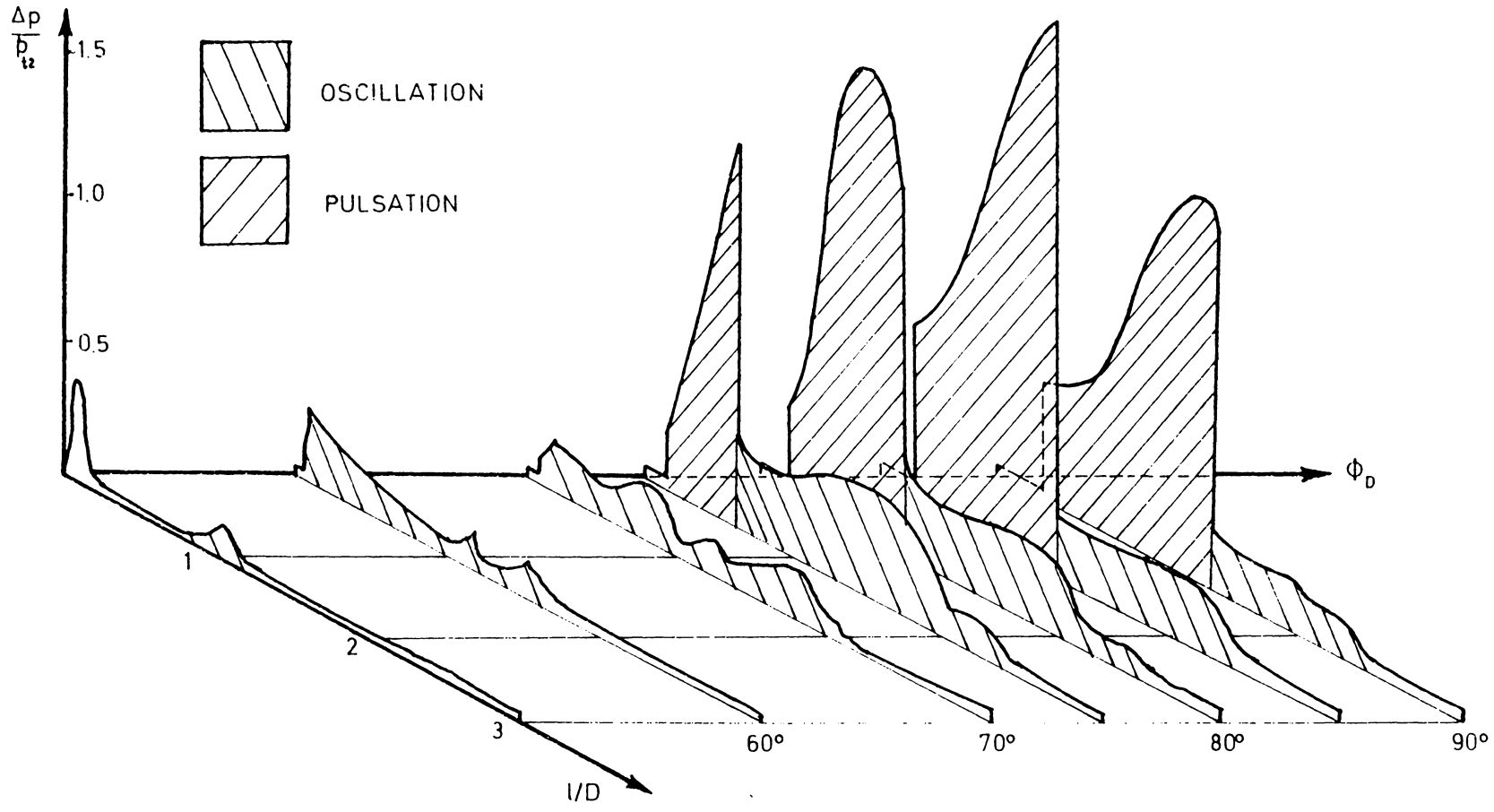

FIG. 18 SERIES II PRESSURE WAVE AMPLITUDE

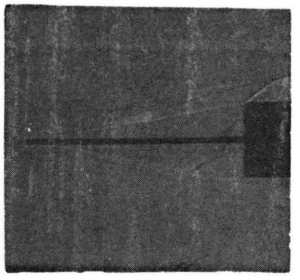

$\Phi_D = 90°$ $M_1 = 6$ $Re_D = 0.13 \times 10^6$

a) l/D = 3.00

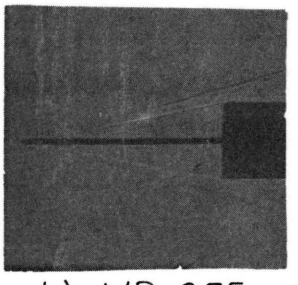

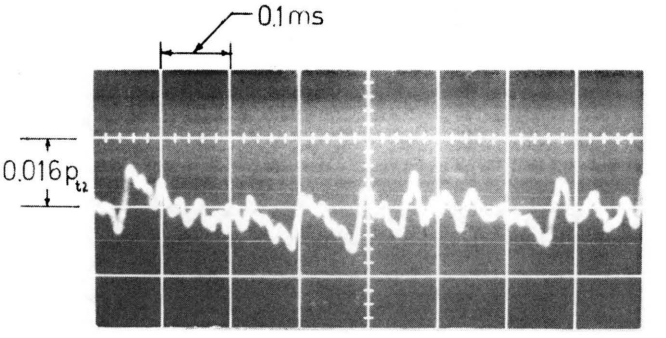

b) l/D = 2.75

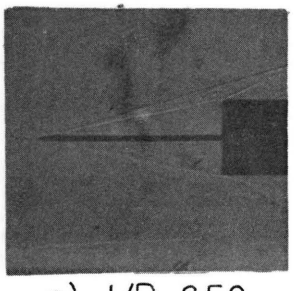

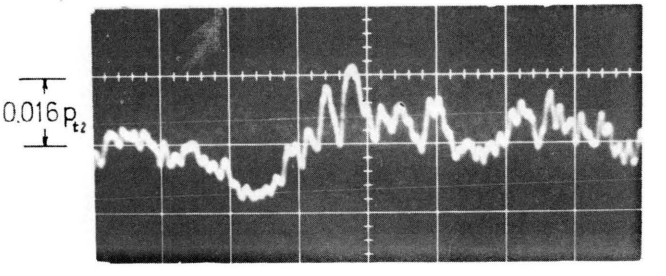

c) l/D = 2.50

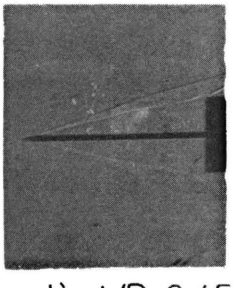

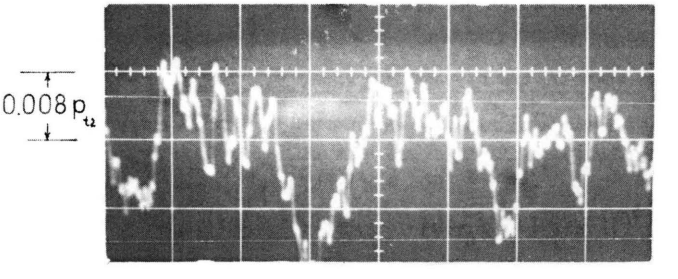

d) l/D = 2.45

Fig. 19 Experimental Results near the O/S Boundary

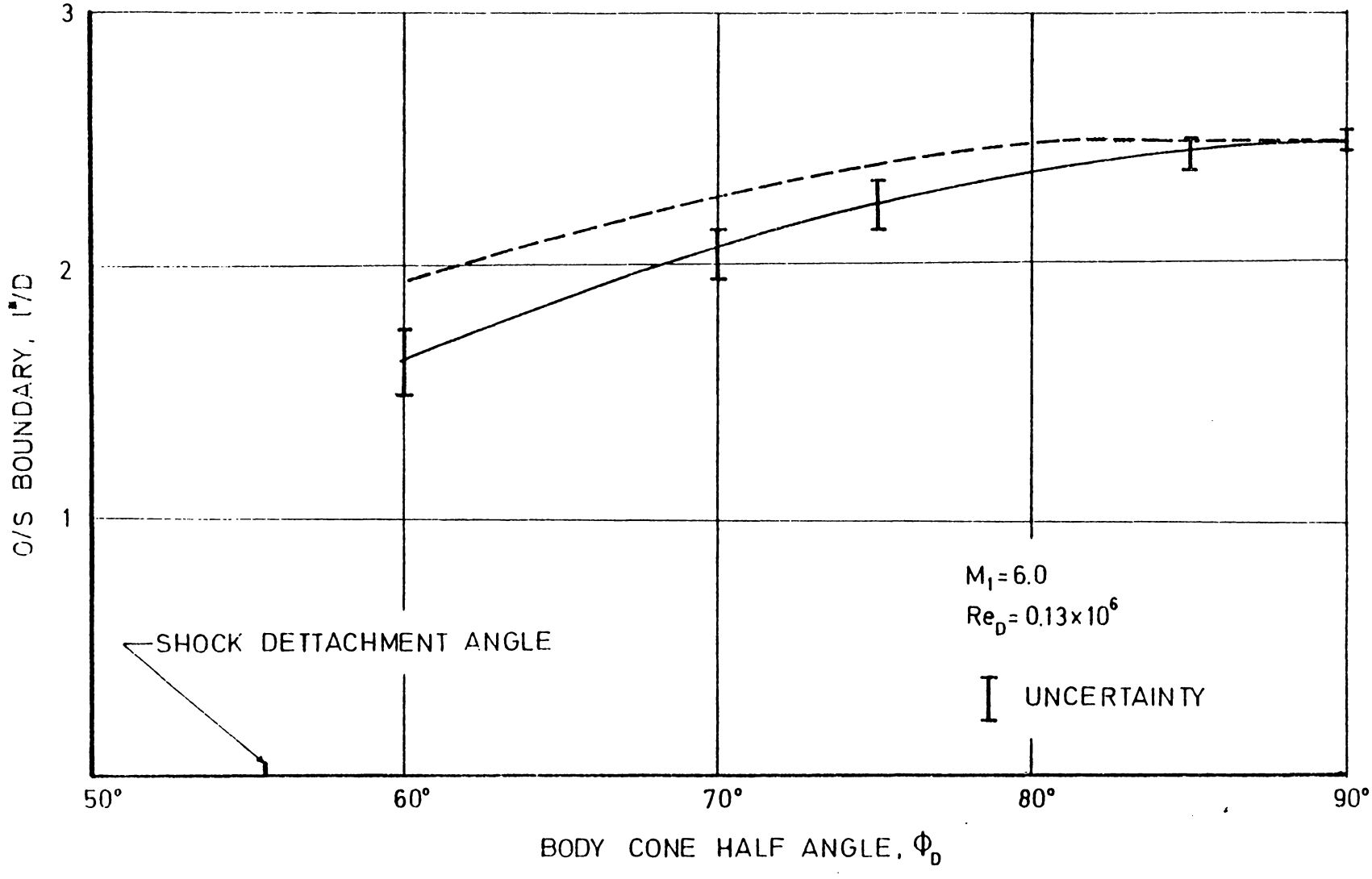

FIG. 20 THE O/S BOUNDARY

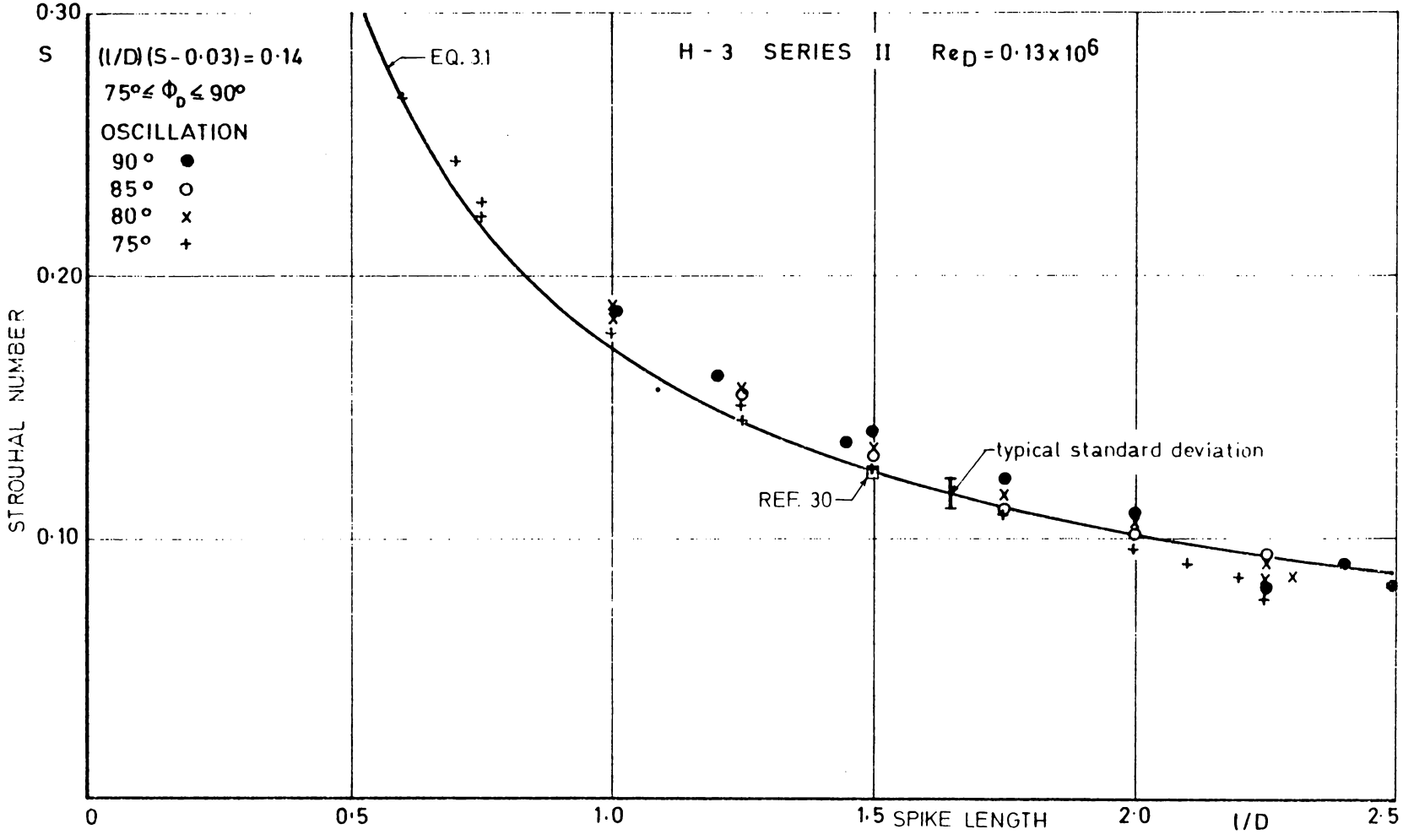

FIG. 21 THE EFFECT OF MODEL ON THE FREQUENCY OF OSCILLATION, M = 6.0, $Re_D = 0{\cdot}13 \times 10^6$

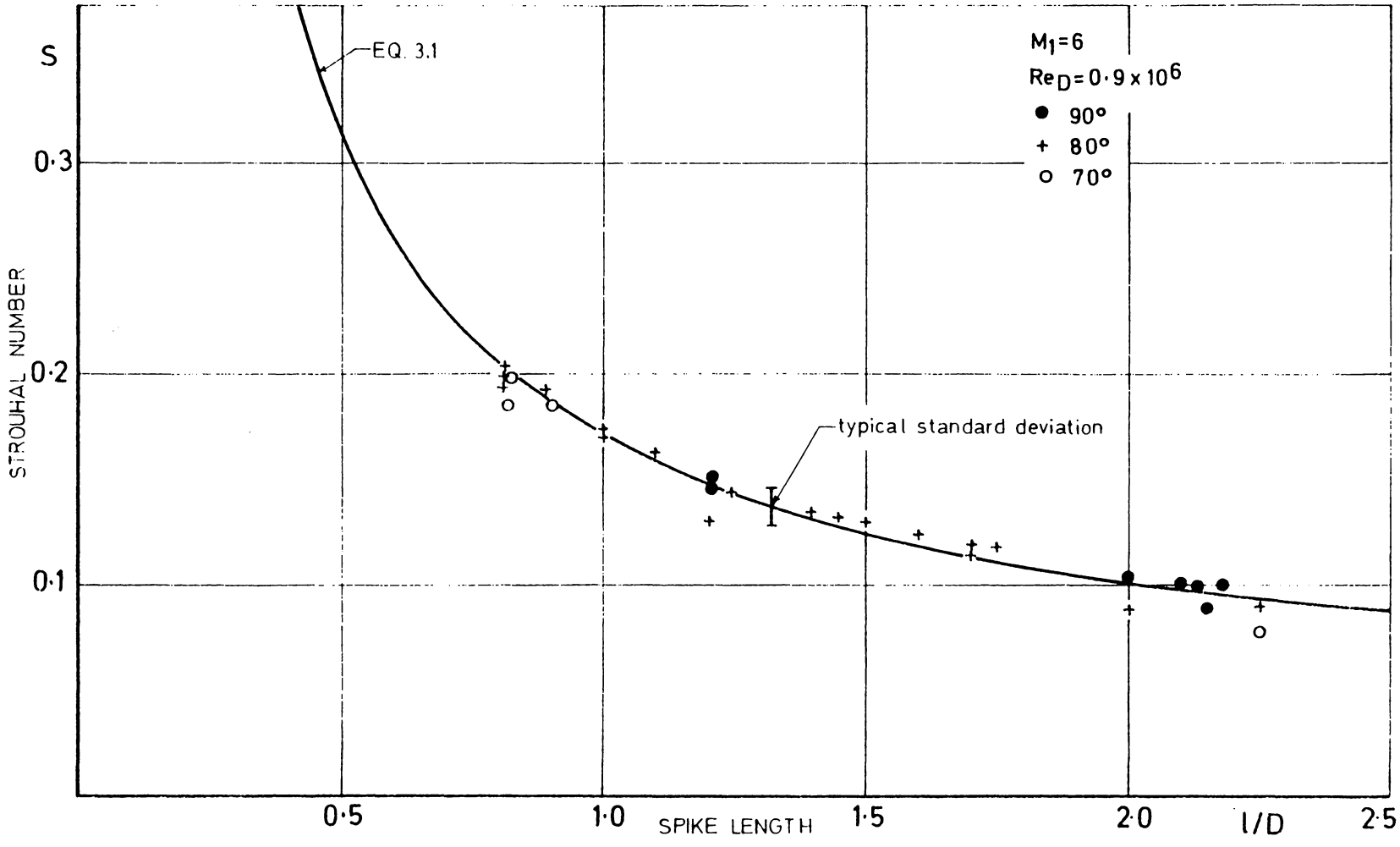

FIG. 22 THE EFFECT OF MODEL GEOMETRY ON THE FREQUENCY OF OSCILLATION, $M=6.0, Re_D = 0·9 \times 10^6$

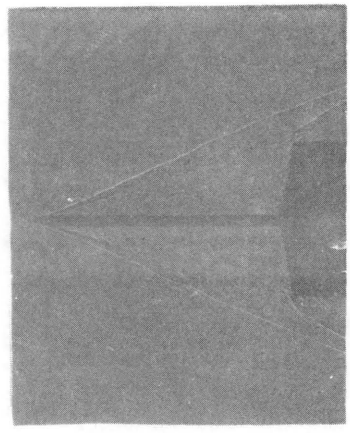

a) $\phi_D = 80°$ $\ell/D = 1.60$

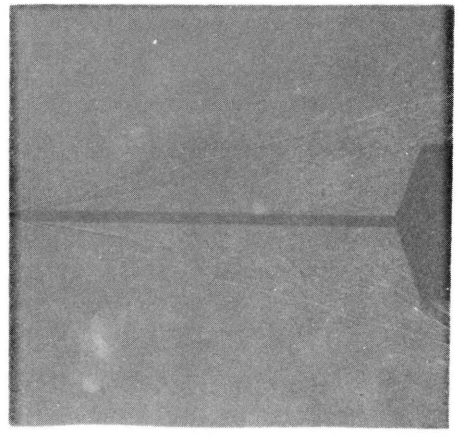

b) $\phi_D = 70°$ $\ell/D = 2.50°$

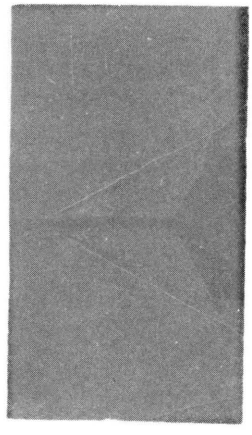

c) $\phi_D = 60°$ $\ell/D = 0.84$

FIG. 23 SERIES I SHEAR LAYER – TRANSITION

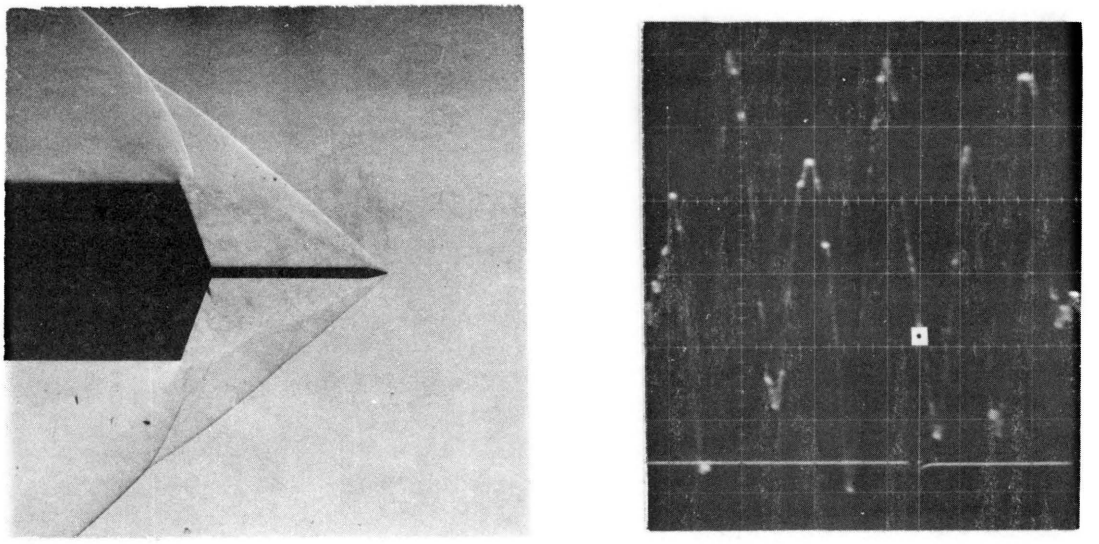

a

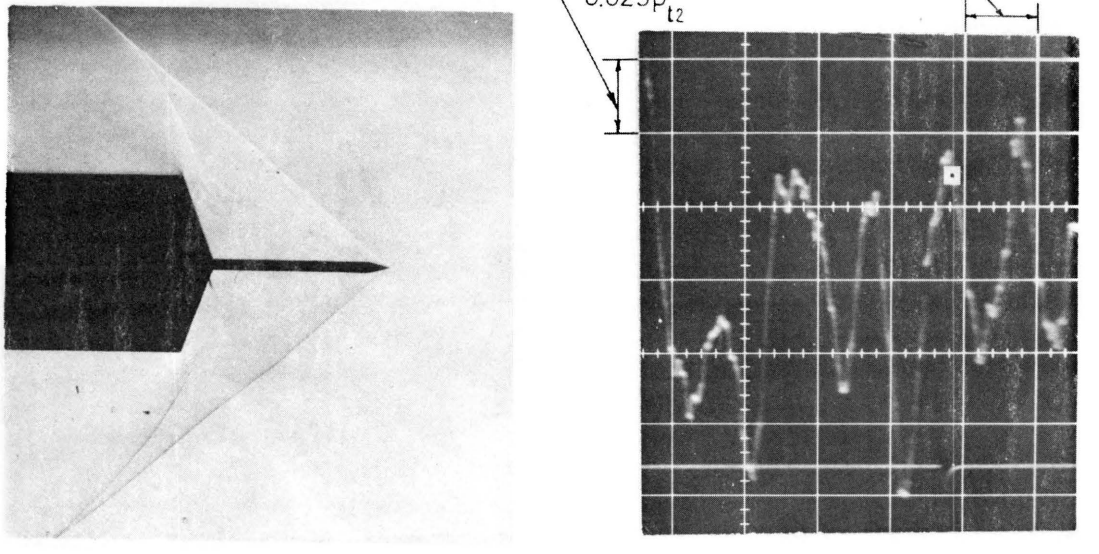

b

$\Phi_D = 70°$ $l/D = 1$

Fig. **24** The Oscillation Shock Envelope; $M_1 = 2.21$, $Re_D = 0.12 \times 10^6$

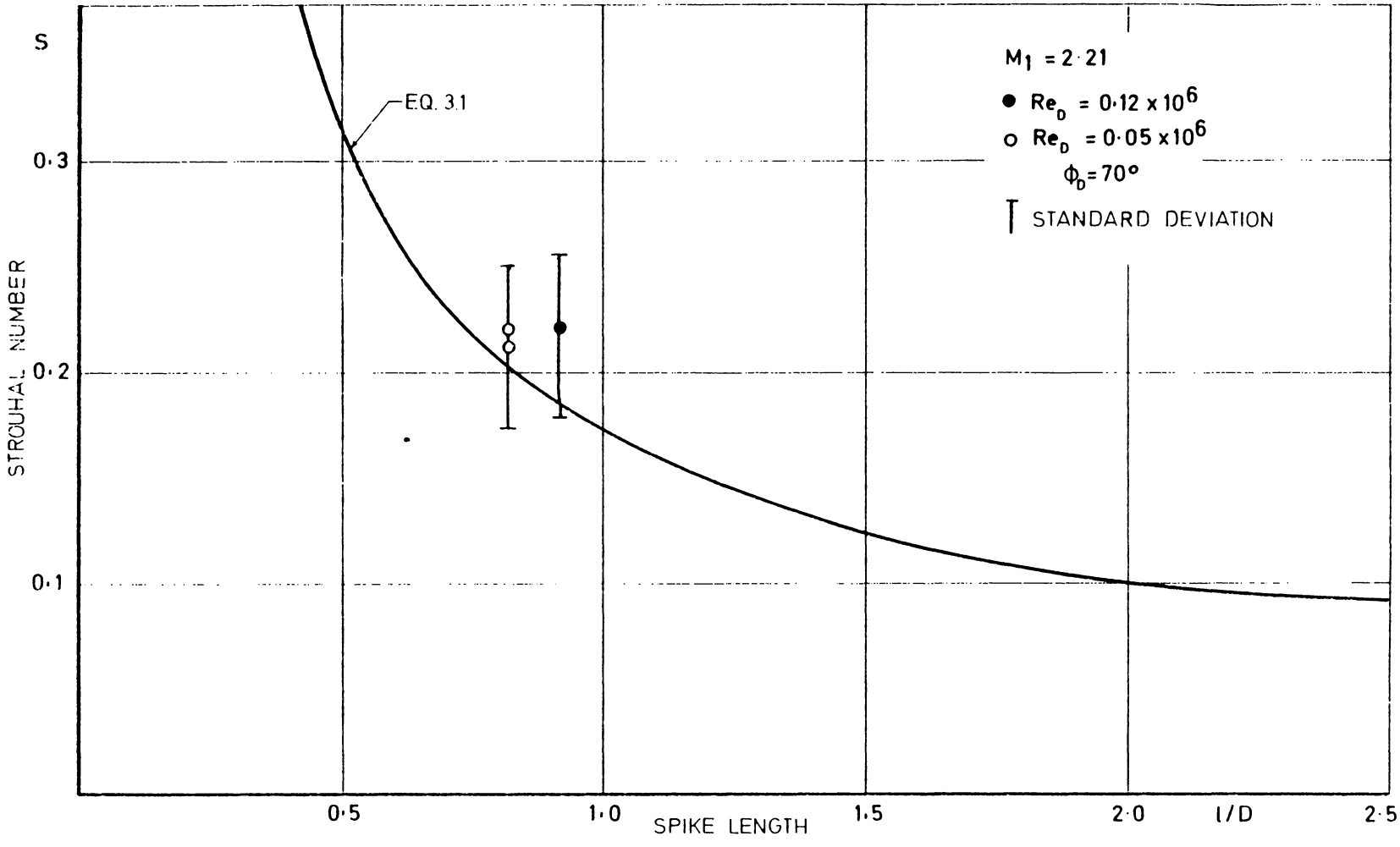

FIG. 25 THE EFFECT OF MODEL GEOMETRY ON THE FREQUENCY OF OSCILLATION, M = 2·21

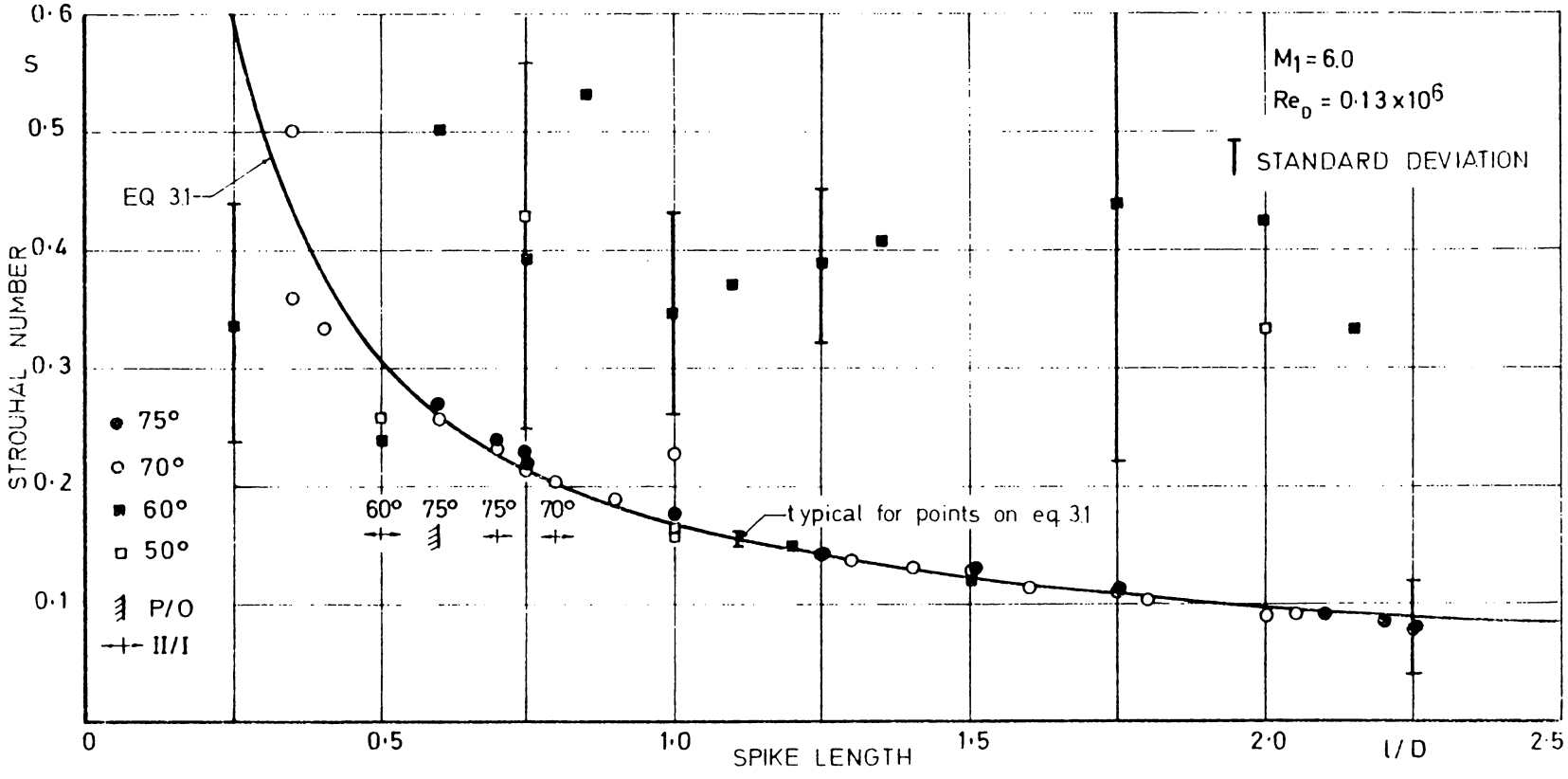

FIG. 26 THE EFFECT OF MODEL GEOMETRY ON THE FREQUENCY OF OSCILLATION BELOW $\Phi_0 = 75°$

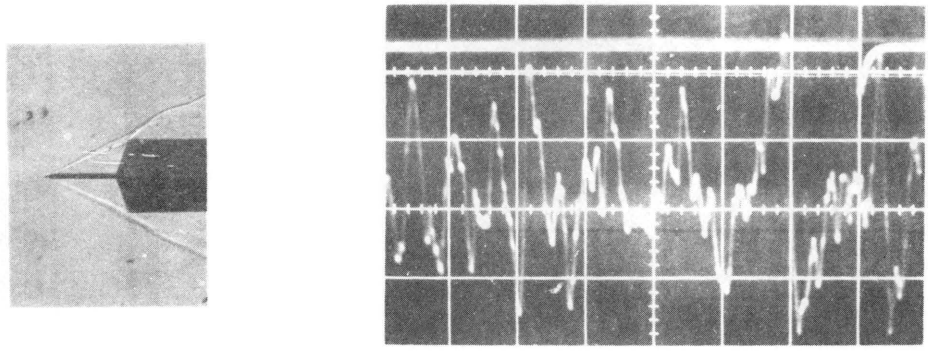

a) l/D = 1.0

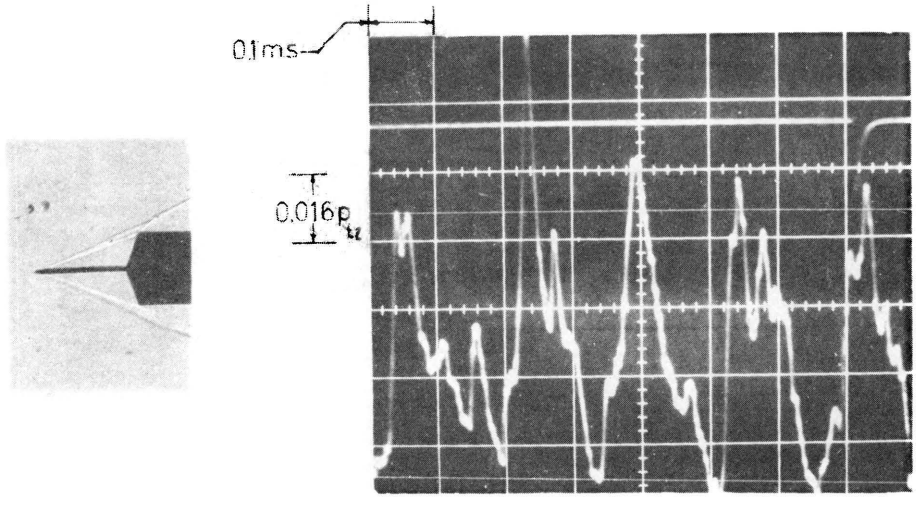

b) l/D = 1.3

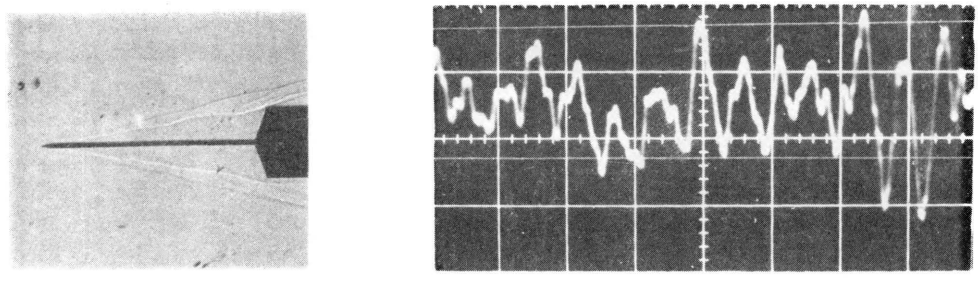

c) l/D = 3.0

Fig. 27 Experimental Results; Φ_D=70°, M_1=6, Re_D=0.13 x 10^6

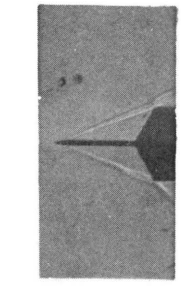

a) l/D=1.10

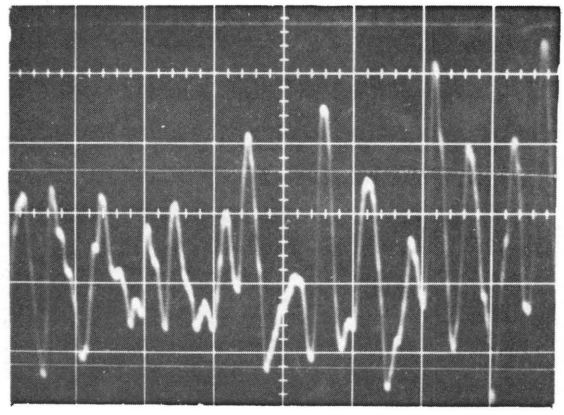

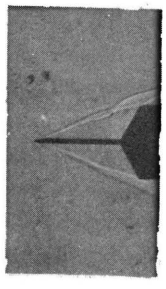

b) l/D=1.20

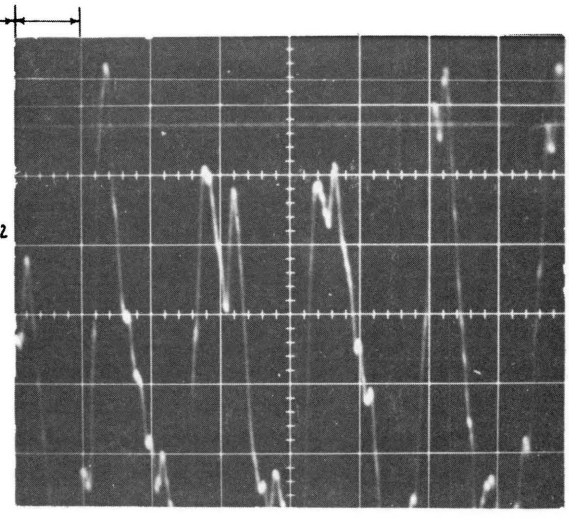

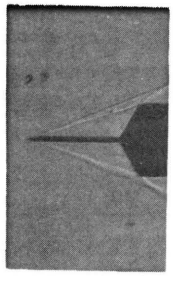

c) l/D=1.25

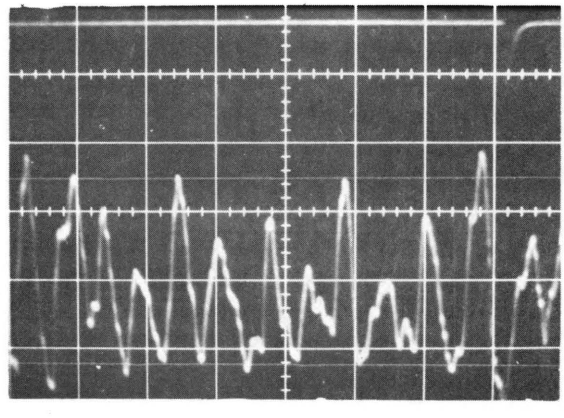

Fig. 28 Experimental Results; $\Phi_D=60°$, $M_1=6$, $Re_D=0.13\times10^6$

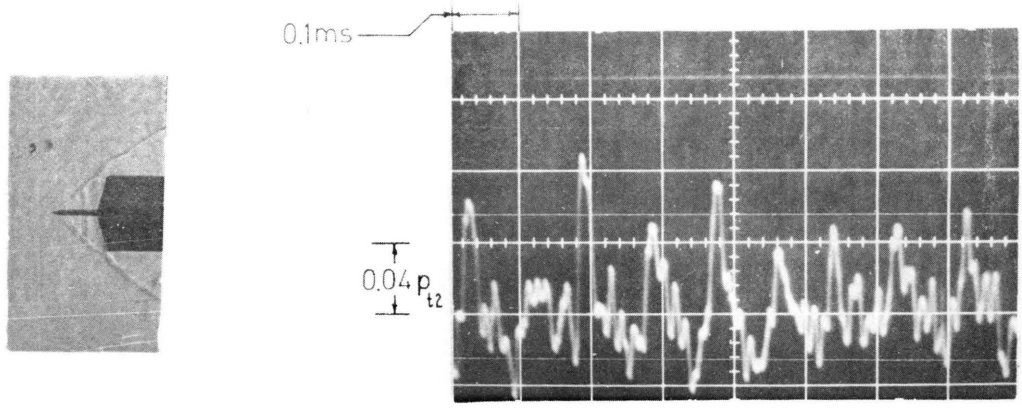

a) Oscillation-Secondary Form (l/D=0.6)

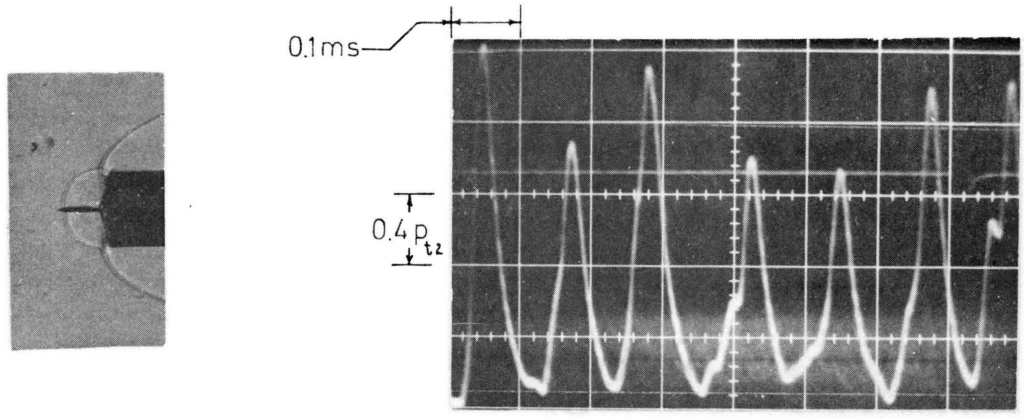

b) Pulsation (l/D=0.55)

Φ_D=75° M_1=6 Re_D=0.13 x 10^6

Fig. 29 A Comparison of the Secondary Form of Oscillation with Pulsation

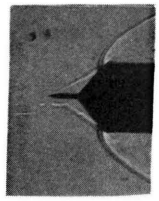

a) $\ell/D = 0.40$

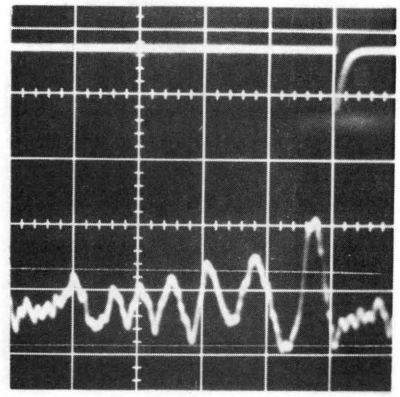

b) $\ell/D = 1.0$

0.1 ms

$0.042 P_{t2}$

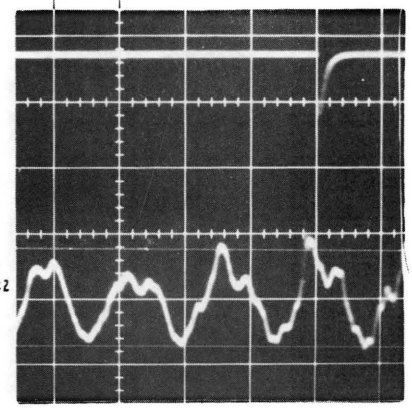

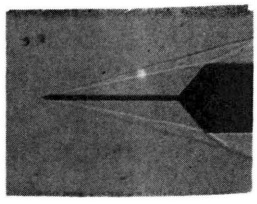

c) $\ell/D = 2.0$

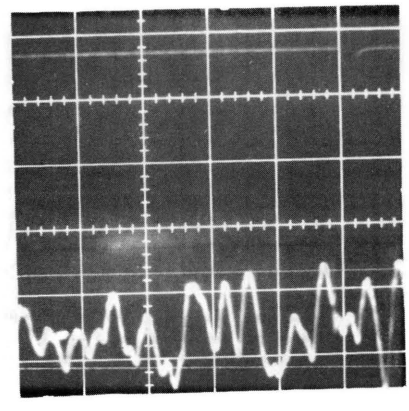

FIG. 30 EXPERIMENTAL RESULTS; $\phi_D = 50°$, $M_\infty = 6.0$, $Re_D = 0.13 \times 10^6$

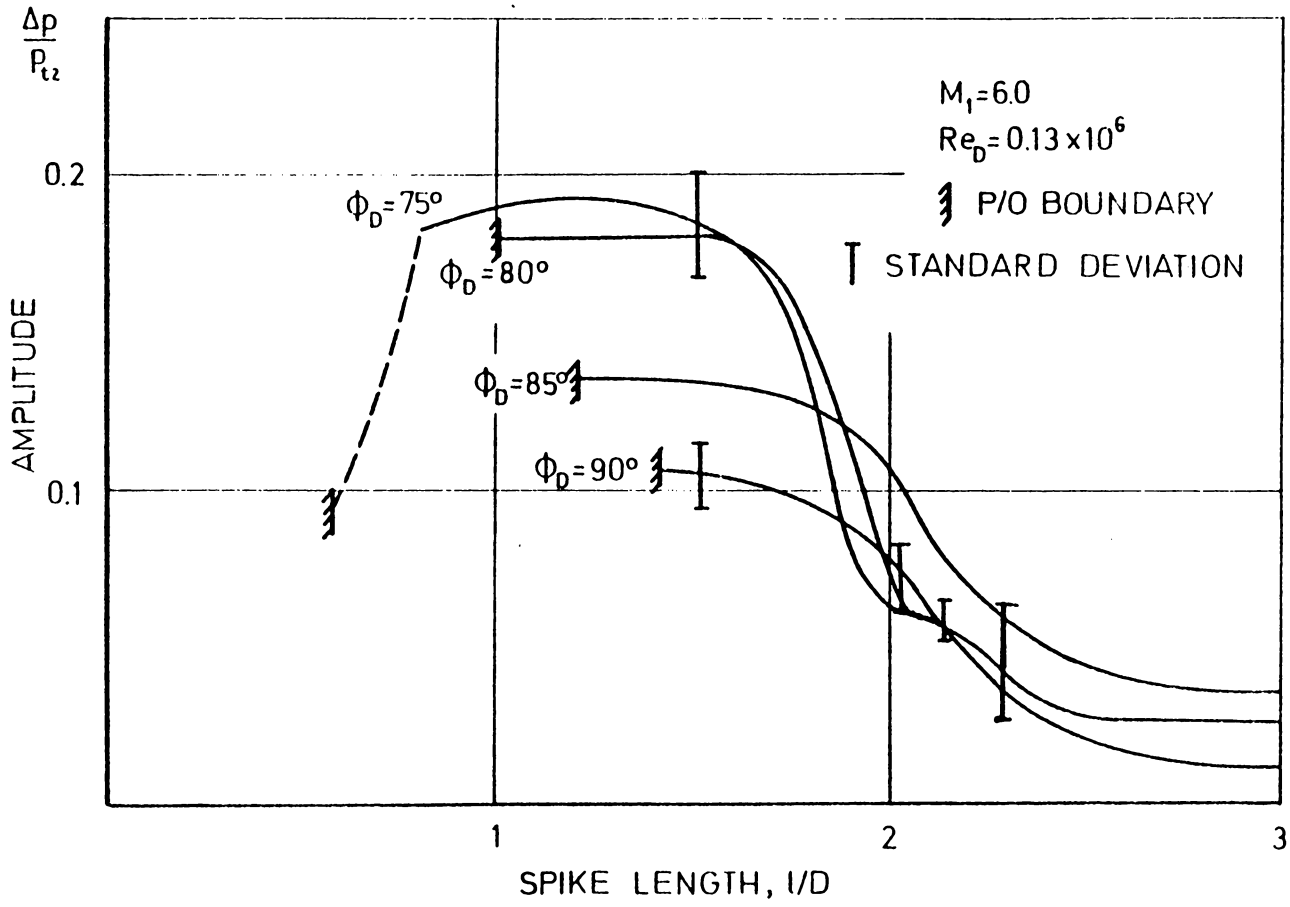

FIG. 31 THE EFFCT OF MODEL GEOMETRY ON THE OSCILLATION PRESSURE WAVE AMPLITUDE

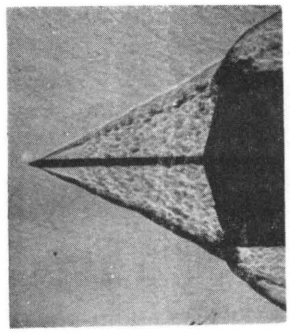

a

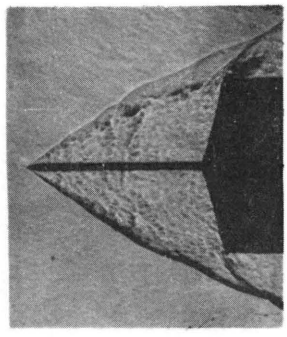

b

$\Phi_D = 75°$ $l/D = 1$

Fig. 32 The Oscillation Shock Envelope from Schlierens; $M_1 = 6$, $Re_D = 0.9 \times 10^6$

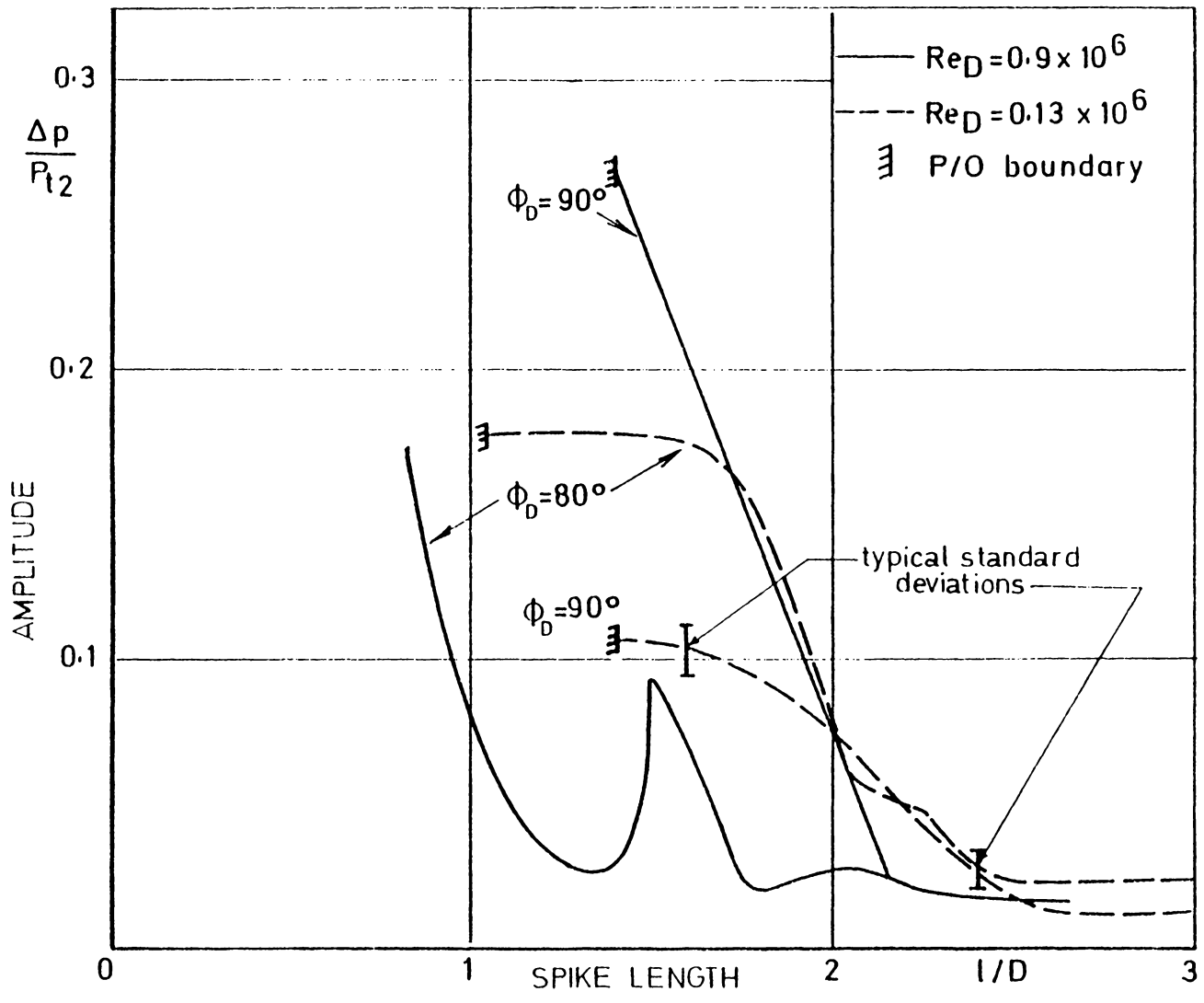

FIG. 33 THE REYNOLDS NUMBER EFFECT ON THE OSCILLATION PRESSURE WAVE AMPLITUDE AT HYPERSONIC SPEEDS

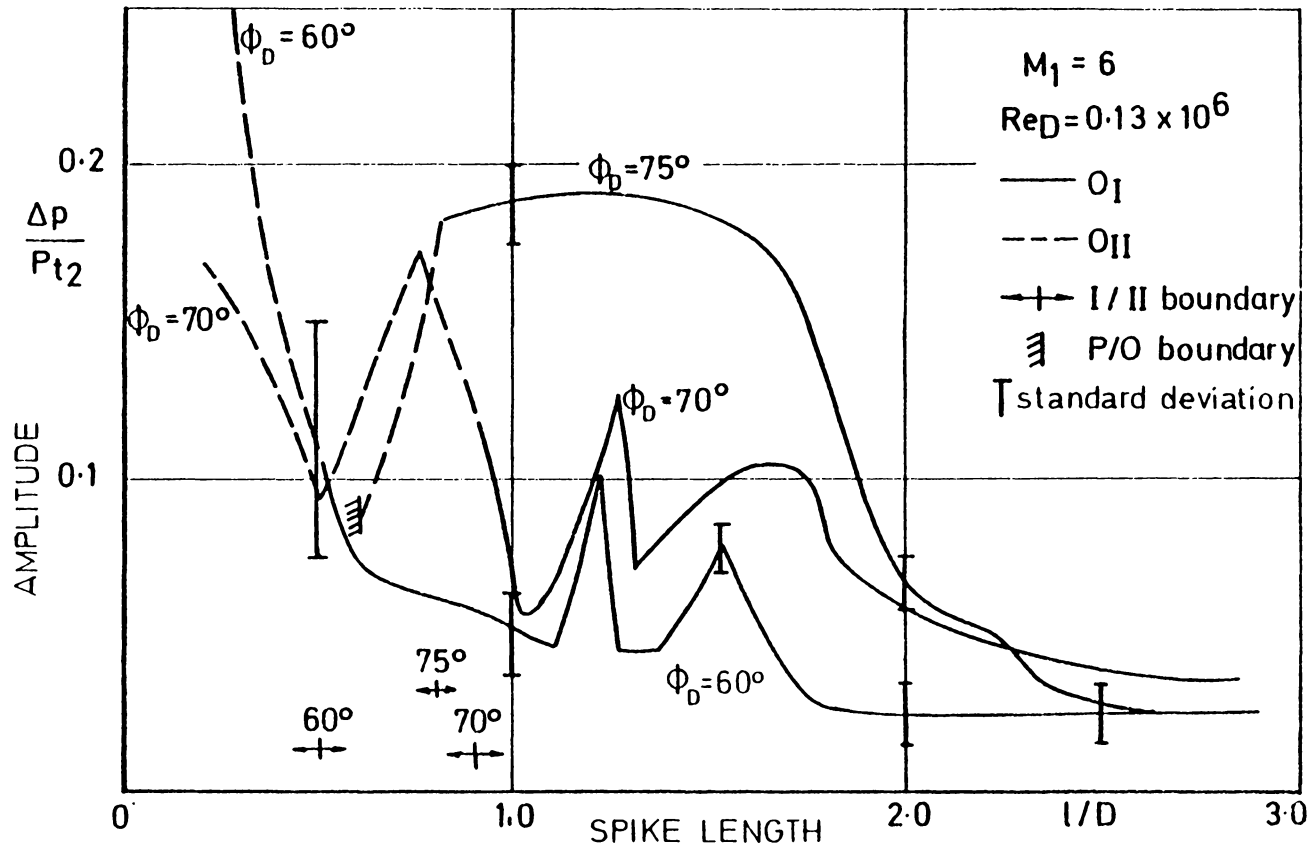

FIG. 34 THE EFFECT OF MODEL GEOMETERY ON THE OSCILLATION PRESSURE WAVE AMPLITUDE, $\Phi_D \leq 75°$

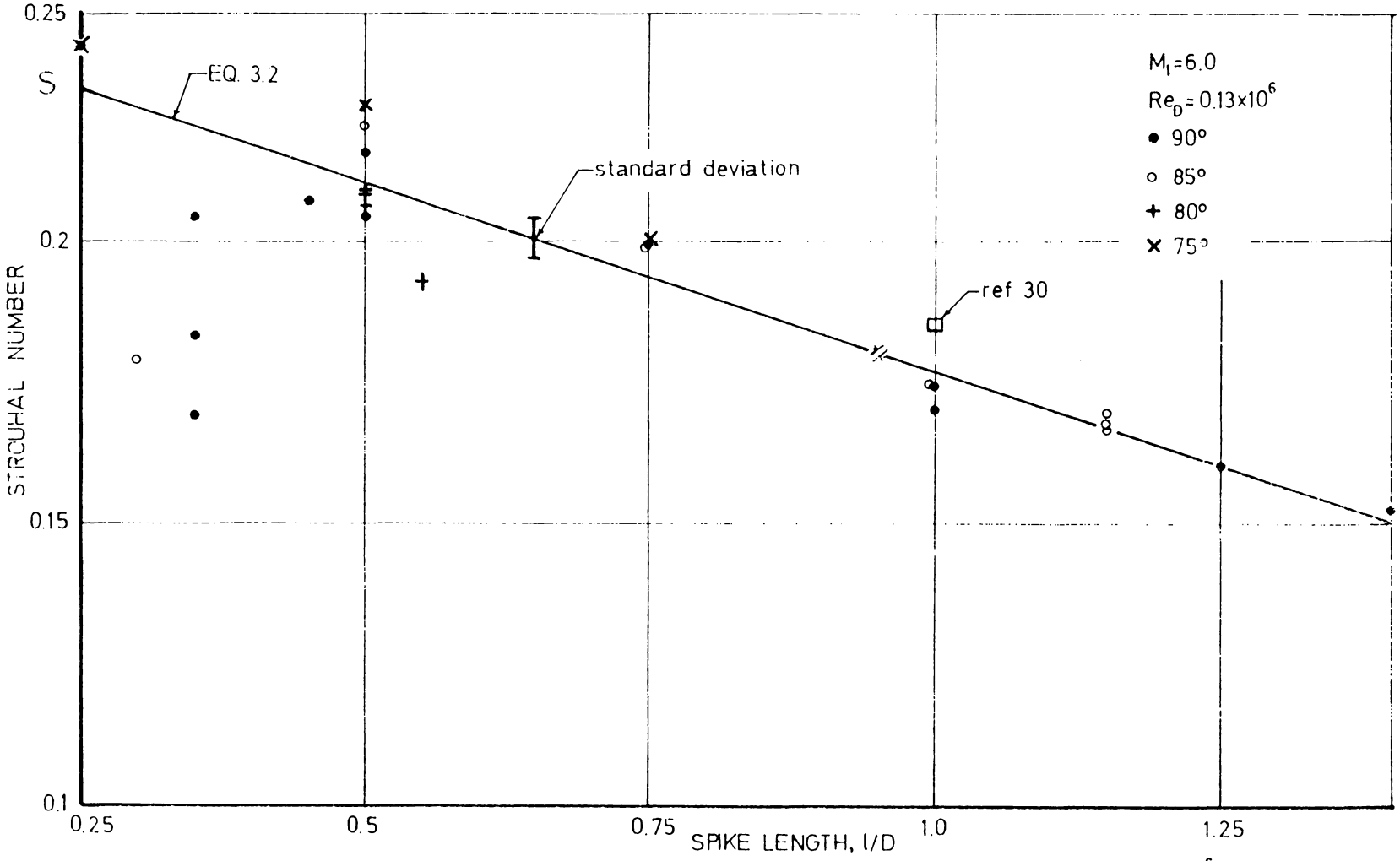

FIG. 35 THE EFFECT OF MODEL GEOMETRY ON THE FREQUENCY OF PULSATION; M_1=6.0, Re_D = 0.13x10^6

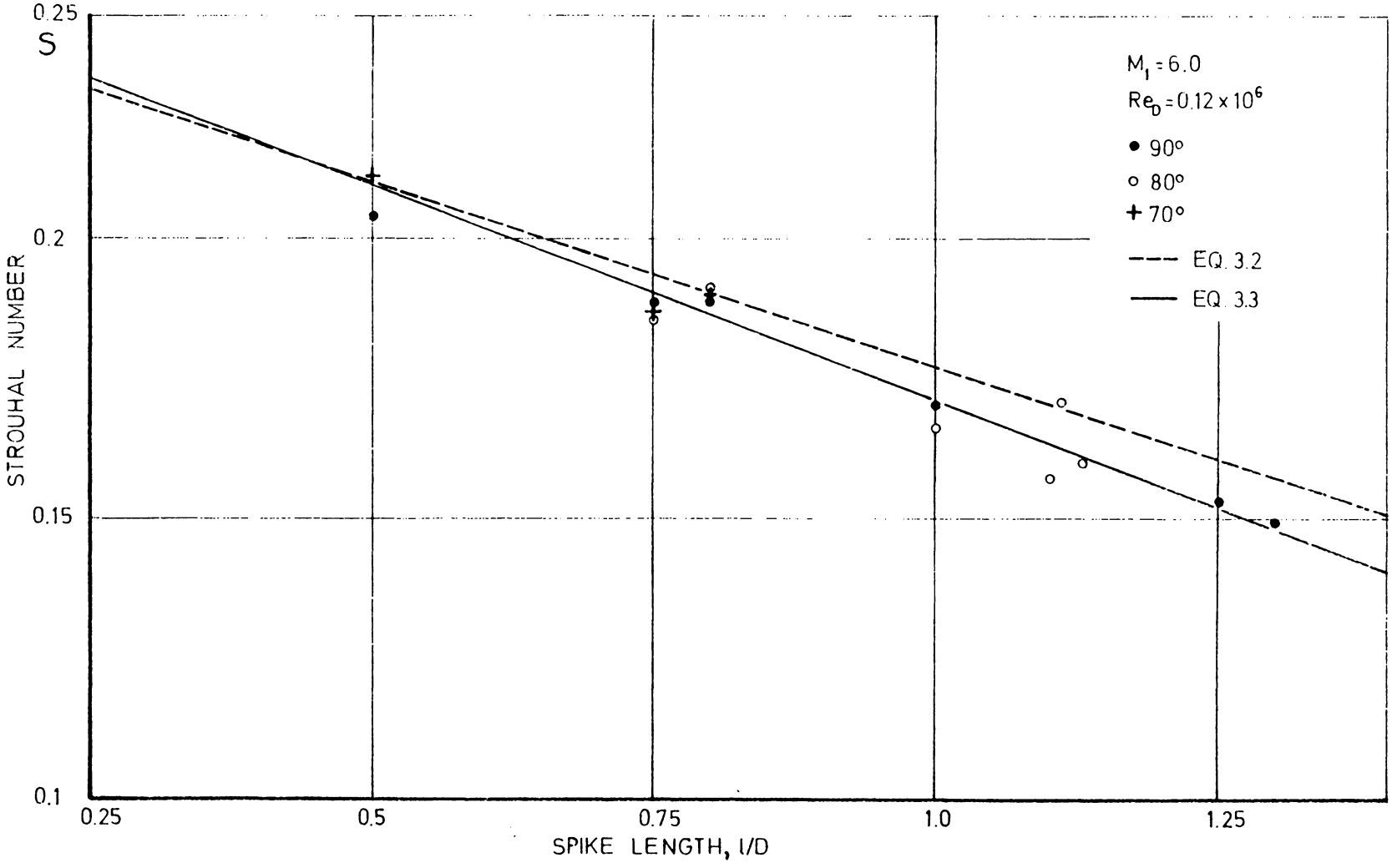

FIG. 36 THE EFFET OF MODEL GEOMETRY ON THE FREQUENCY OF PULSATION; $M_1 = 2.21$, $Re_D = 0.12 \times 10^6$

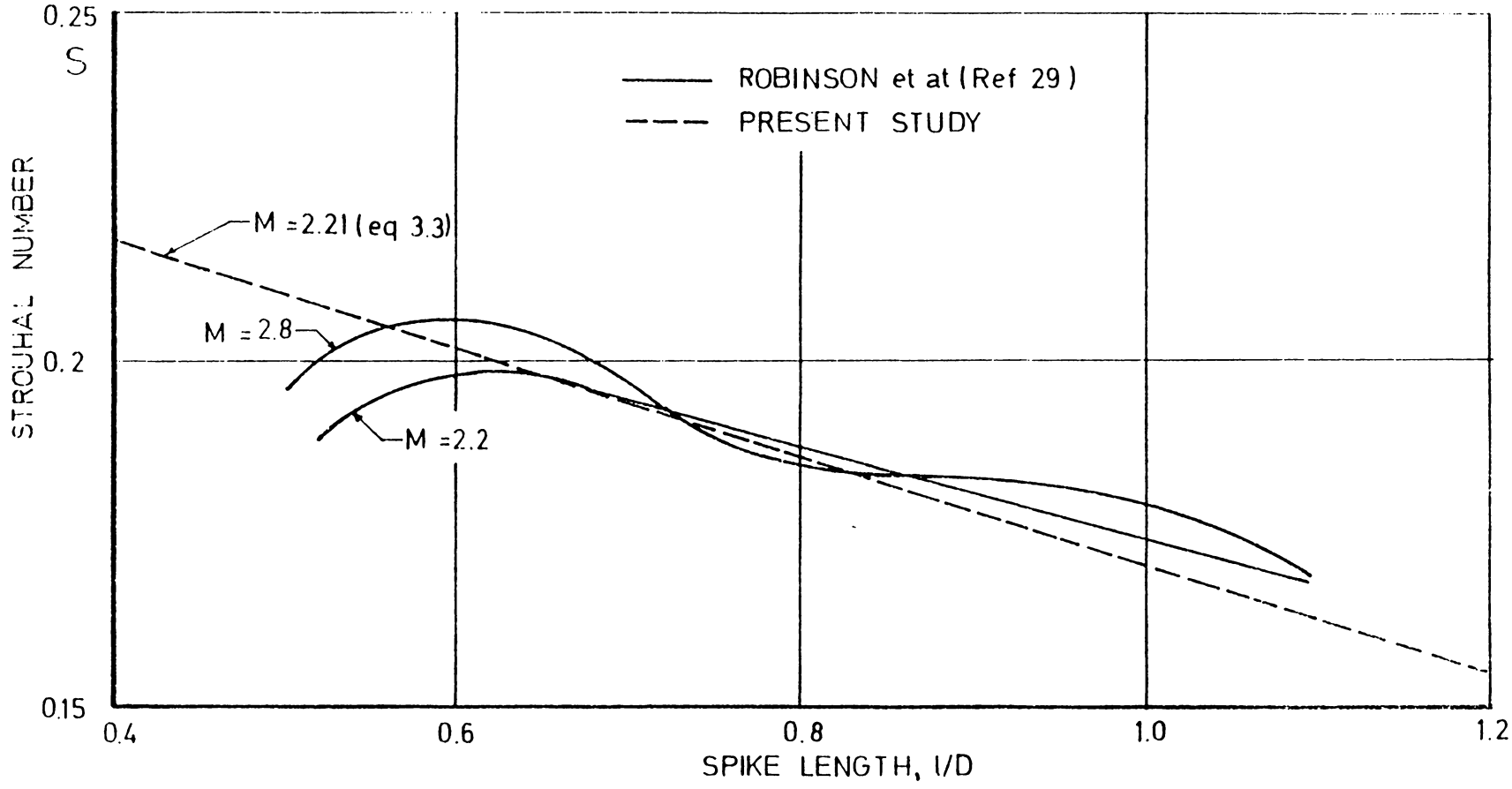

FIG. 37 COMPARISON OF THE PRESENT STUDY WITH ROBINSON et al

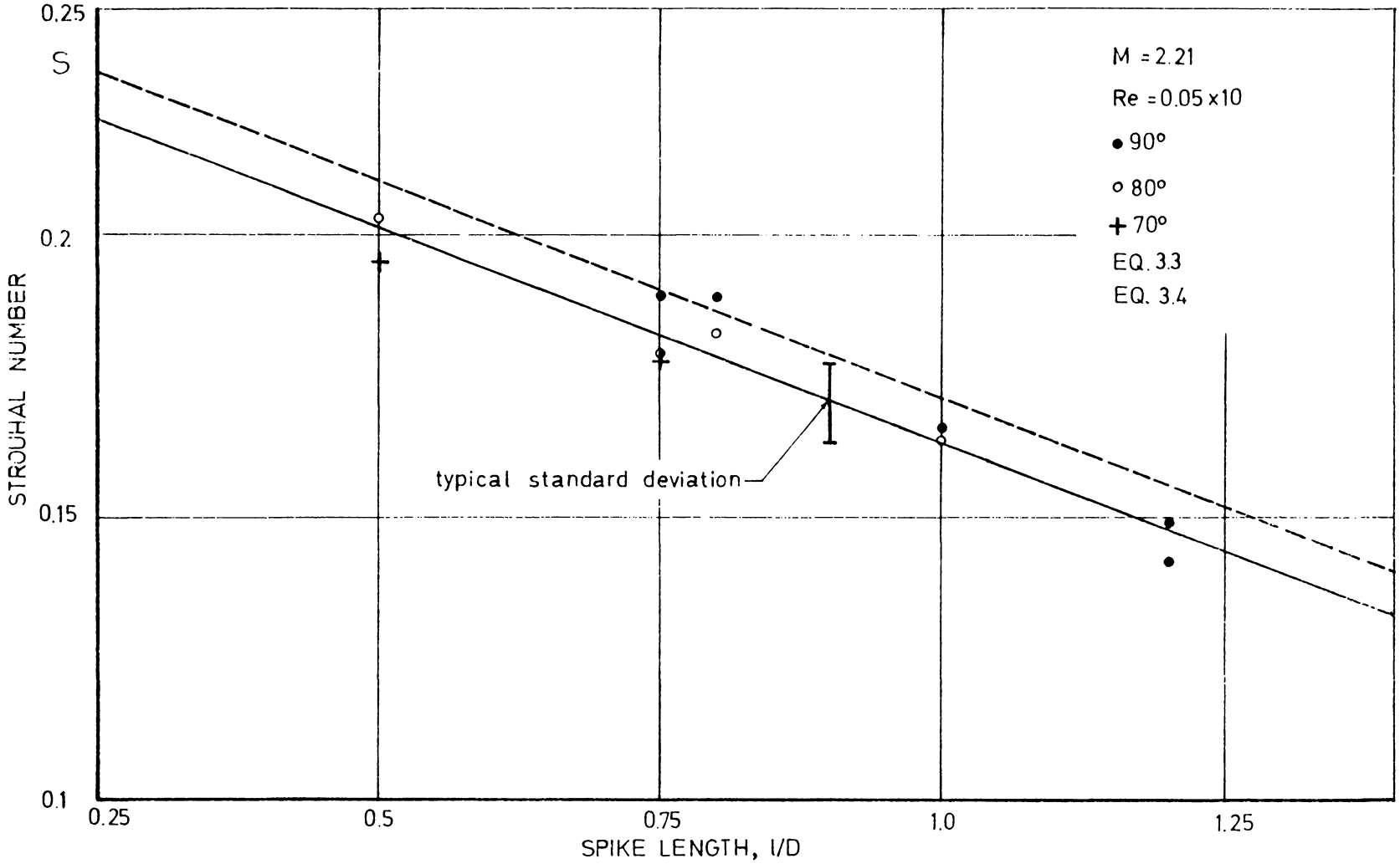

FIG. 38 THE EFFECT OF MODEL GEOMETRY ON THE FREQUENCY OF PULSATION $M_1 = 2.21$ $Re_D = 0.05 \times 10^6$

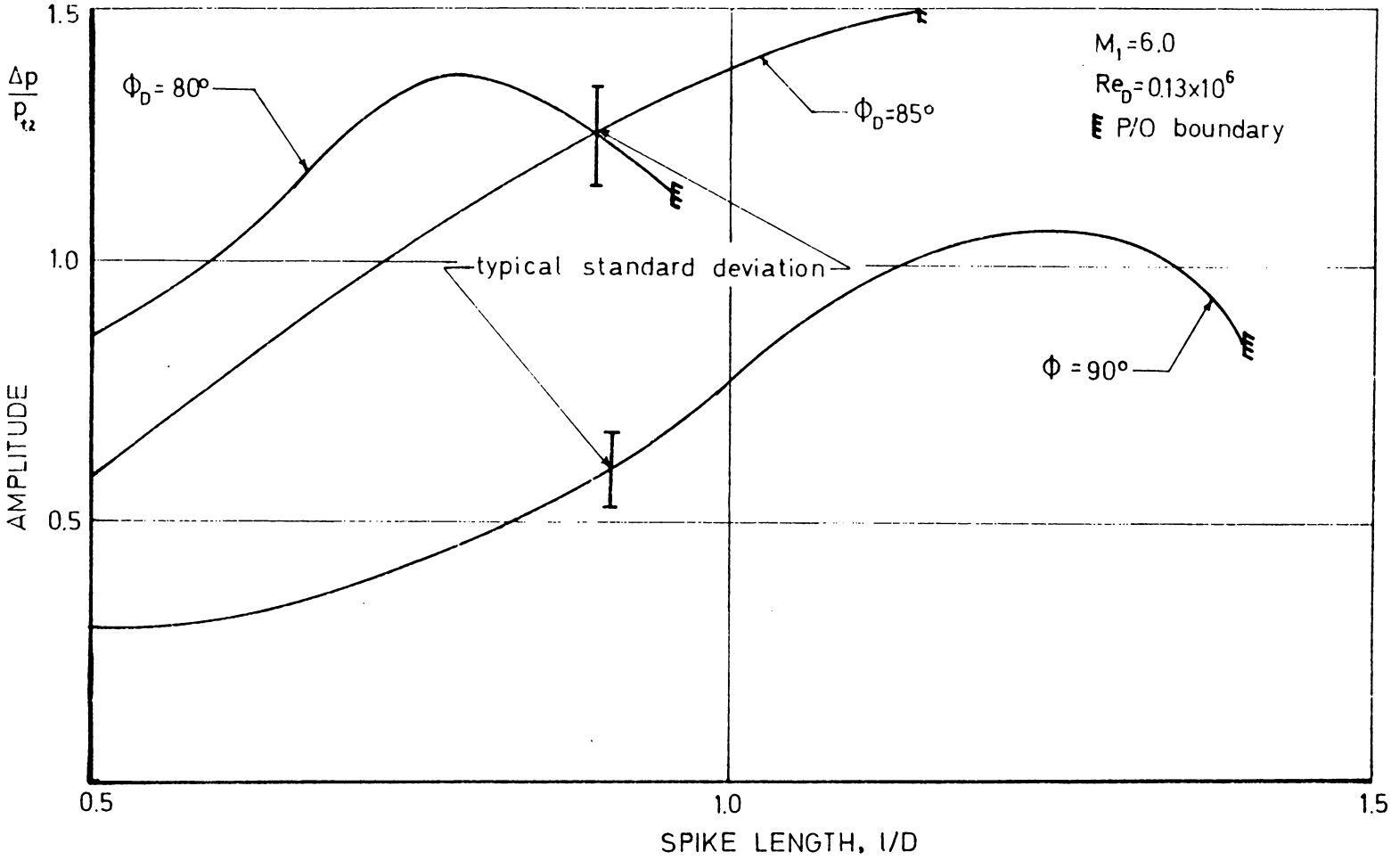

FIG. 39 THE EFFECT OF MODEL GEOMETRY ON THE PULSATION PRESSURE WAVE AMPLITUDE; M_1=6.0, Re_D=0.13x10^6

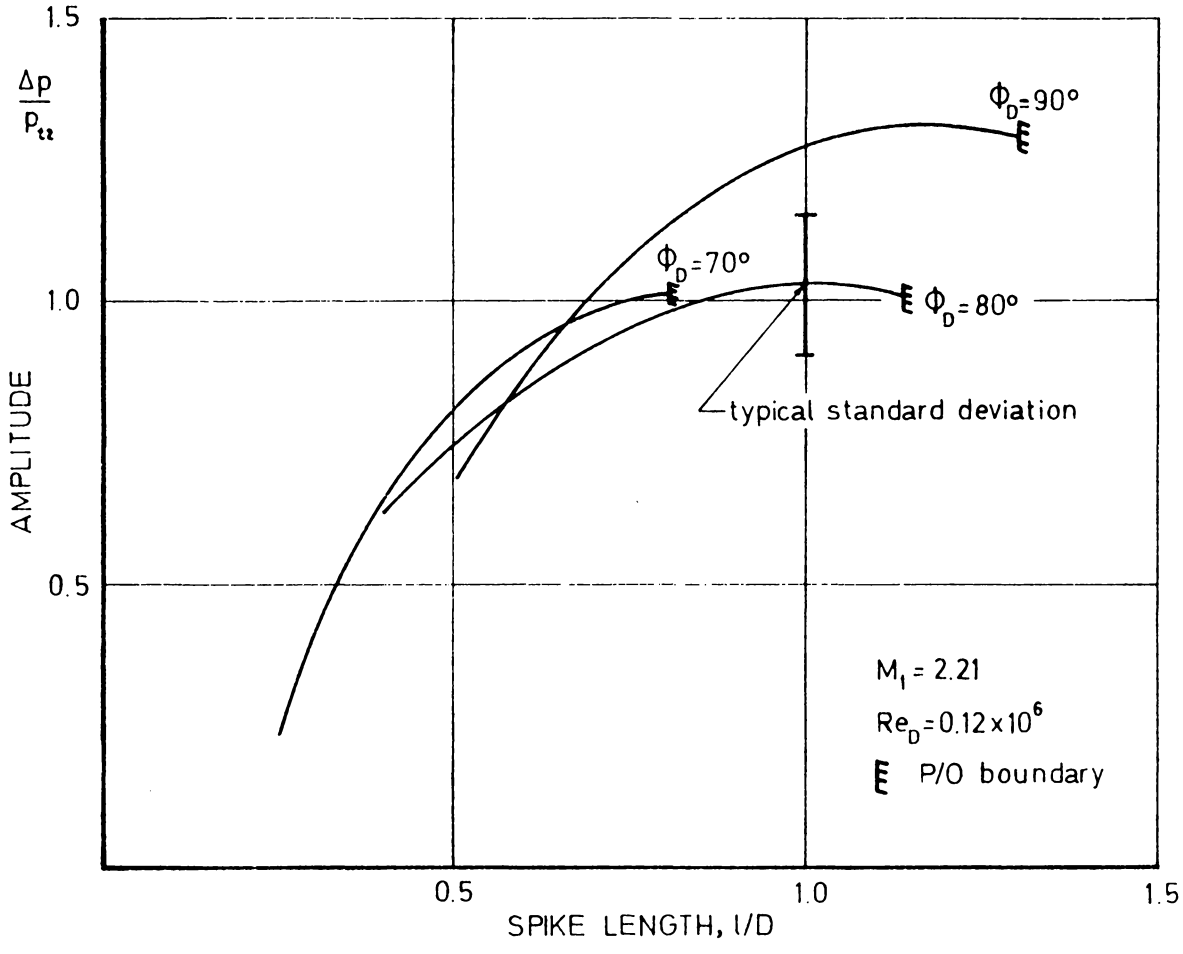

FIG. 40 THE EFFECT OF MODEL GEOMETRY ON THE PULSATION PRESSURE WAVE AMPLITUDE; M_1=2.21, Re_D=0.12x10^6

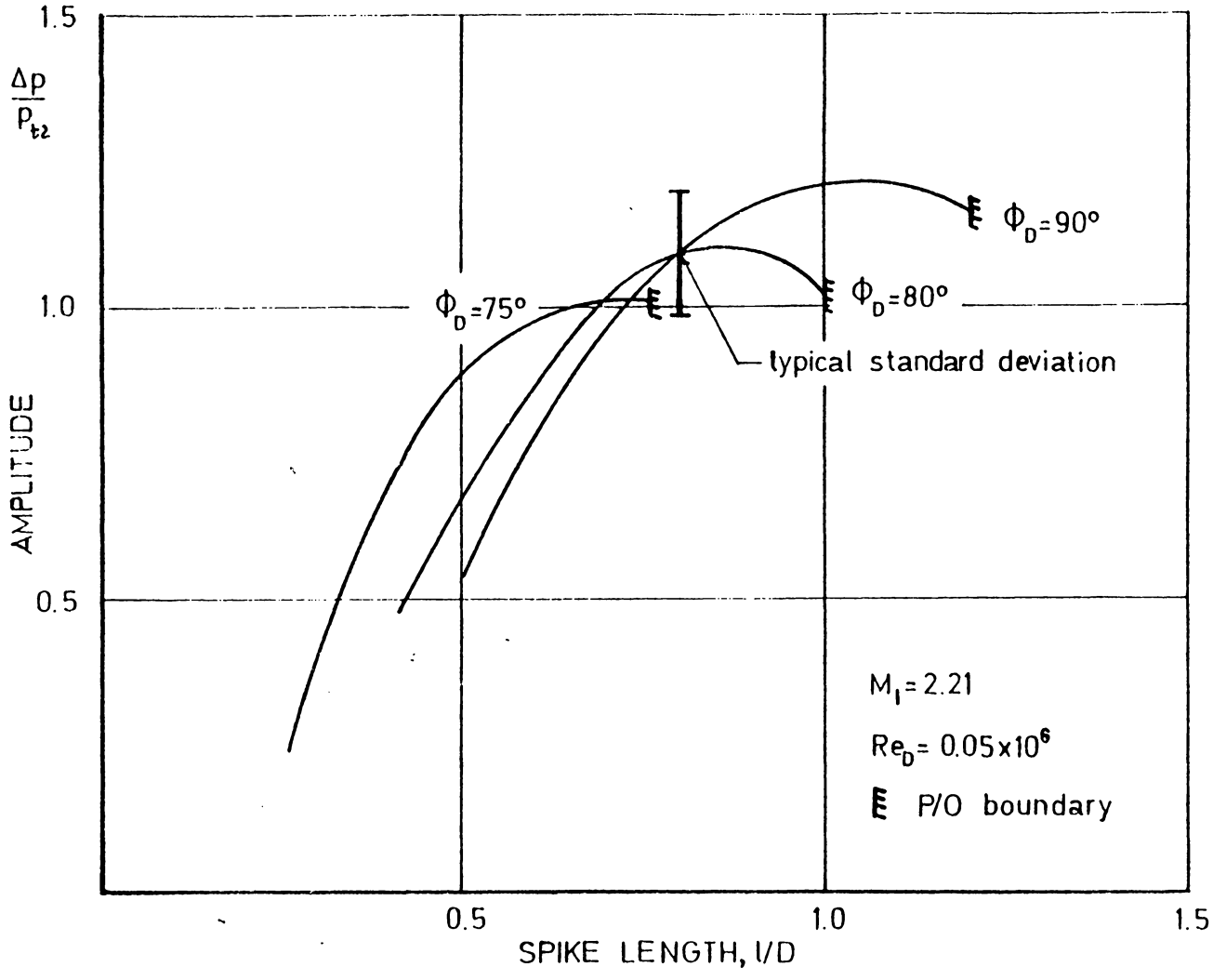

FIG. 41 THE EFFCT OF MODEL GEOMETRY ON THE PULSATION PRESSURE WAVE, M_1=2.21, Re_D=0.05x10^6

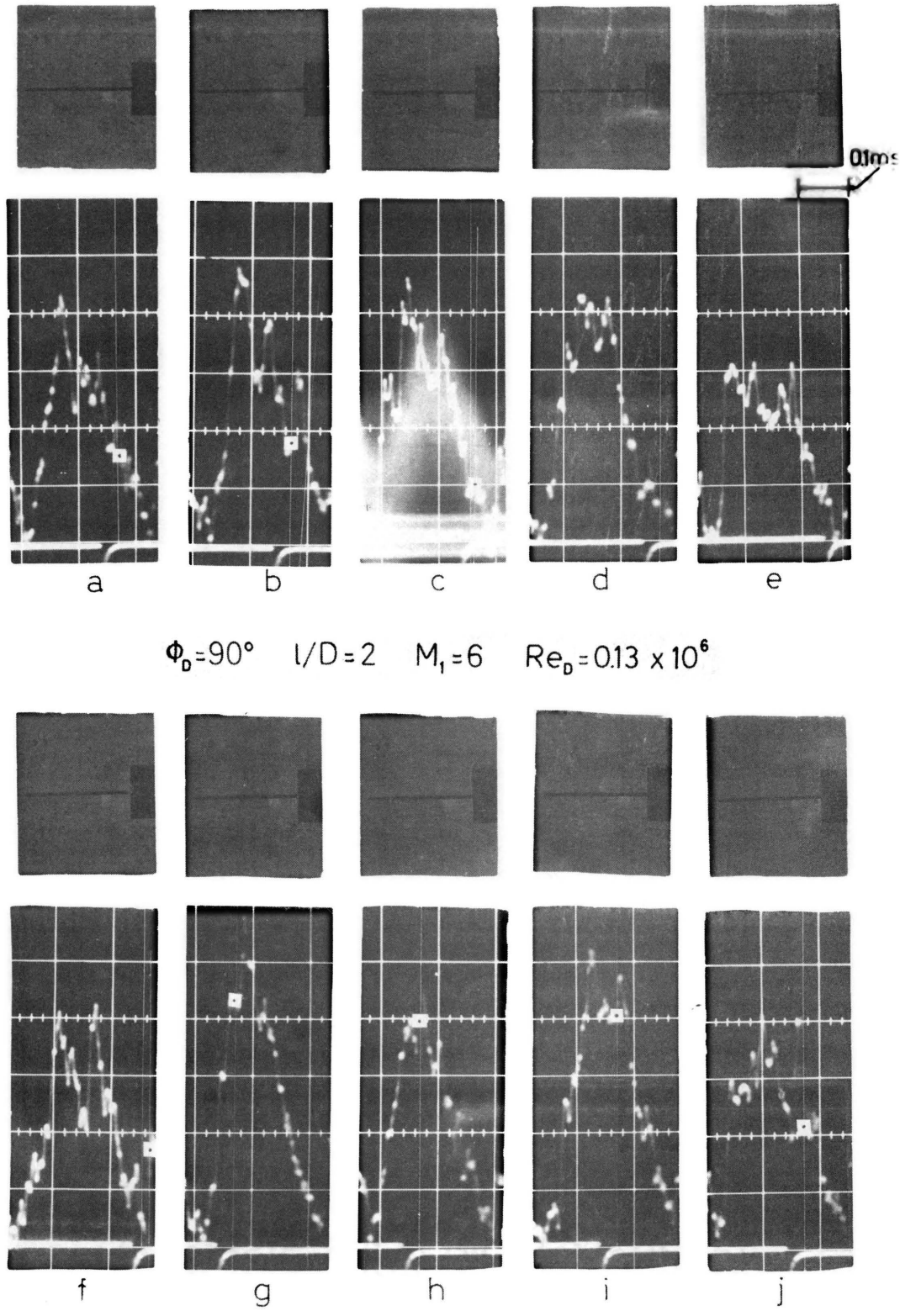

Fig. 42 The History of an Oscillation Cycle

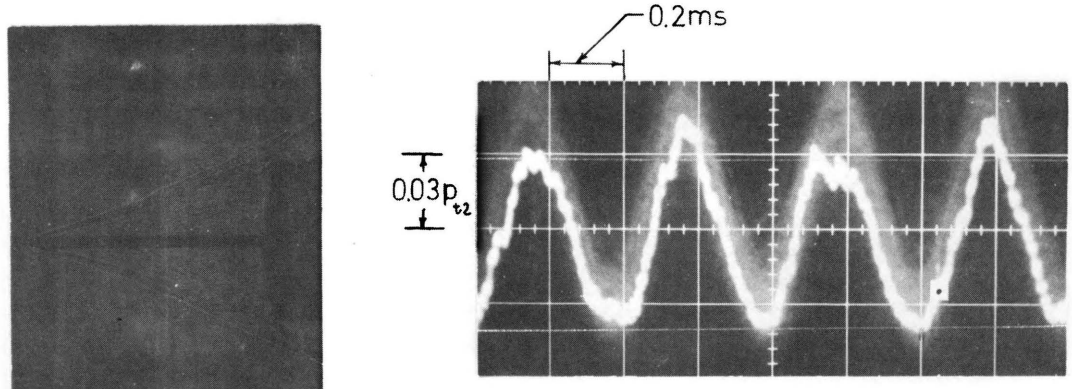

a

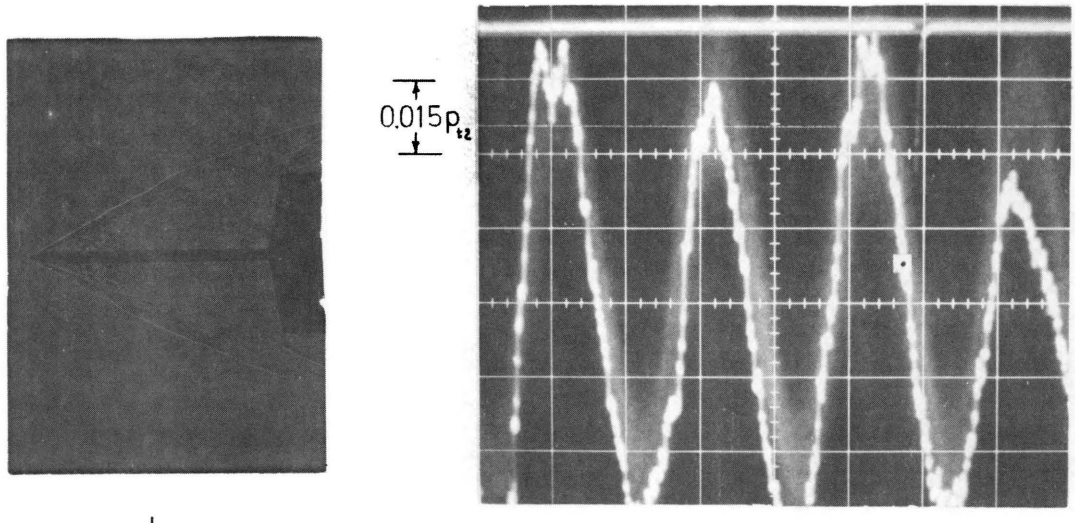

b

$\Phi_D = 80°$ $l/D = 1.5$

Fig. 43 The Oscillation Shock Envelope from Shadowgraphs; $M_1 = 6$, $Re_D = 0.9 \times 10^6$

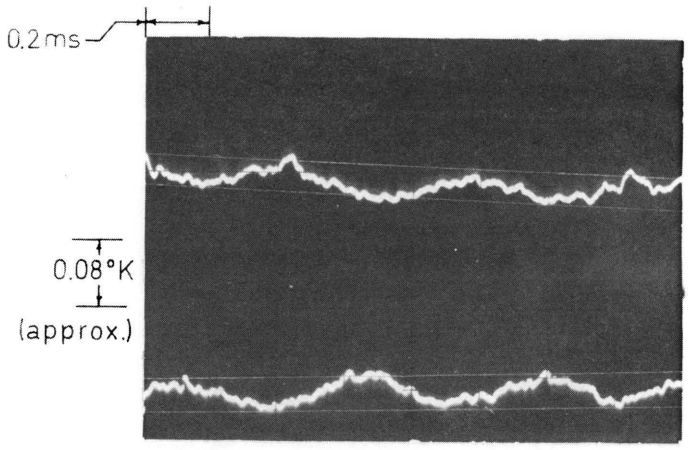

a) Thin Film Traces:
top - x/l = 0.9
bottom - x/l = 0.1

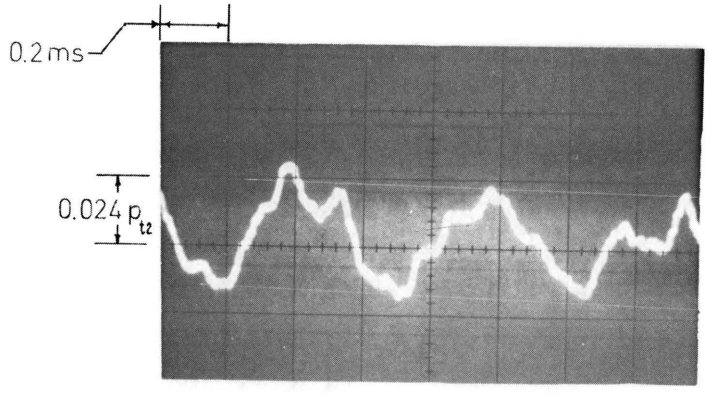

b) Pressure Wave: x/l = 1

Fig. 44 Measurements in the Streamwise Direction

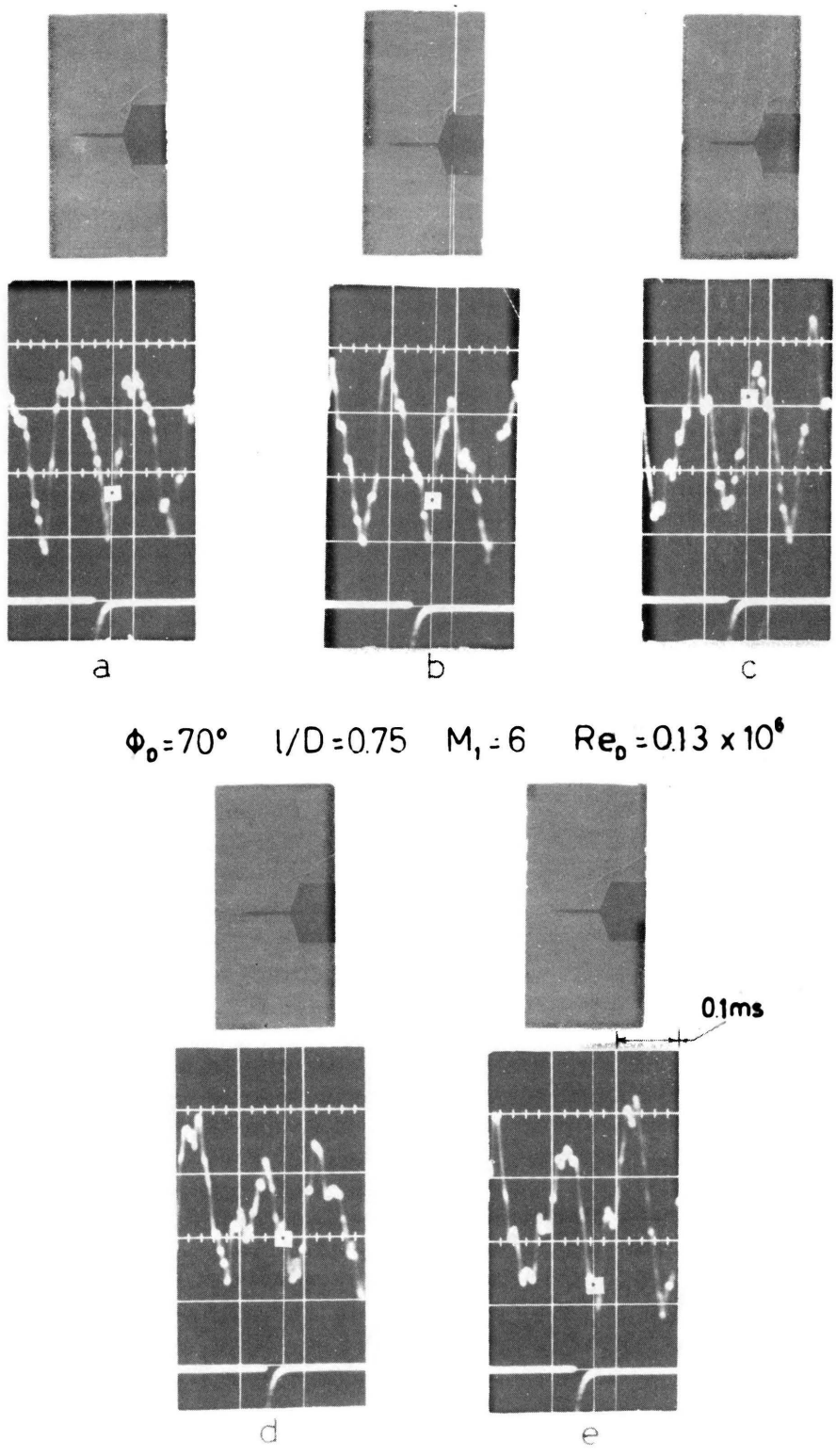

Fig. **45** The History of an Oscillation-Secondary Form Cycle

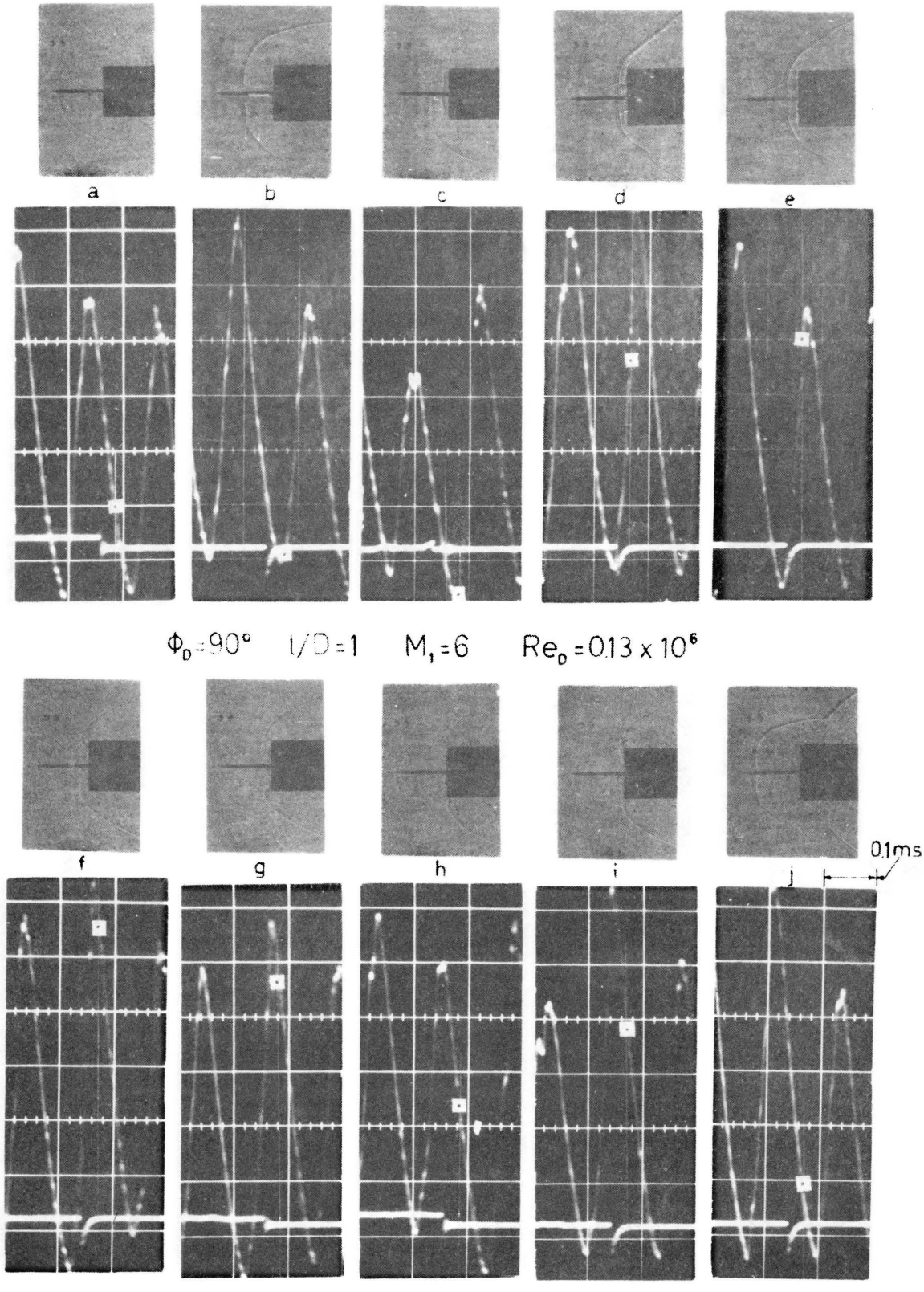

Fig. 46 The History of a Pulsation Cycle at M=6

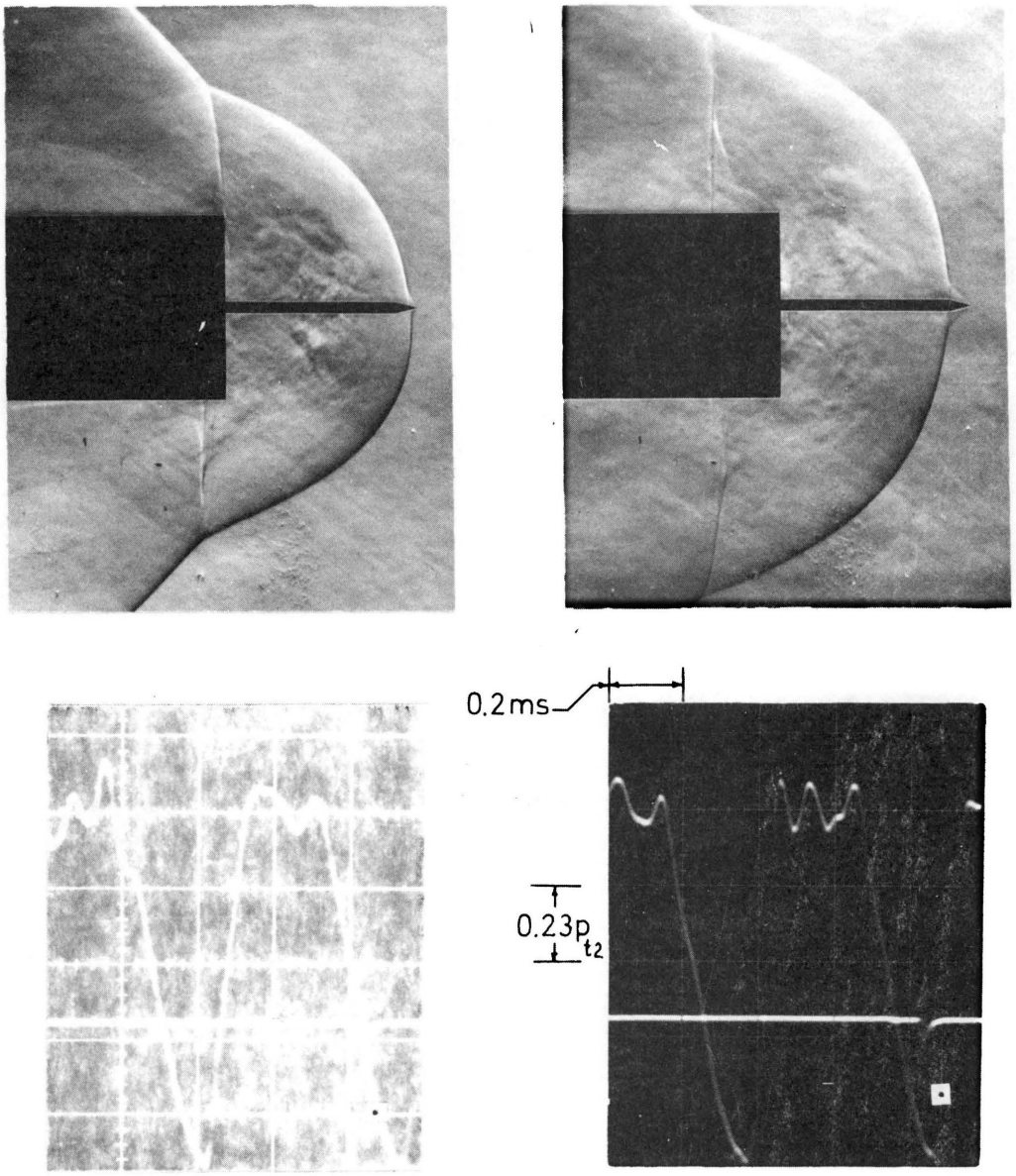

Fig. 47 The History of a Pulsation Cycle at M=2.21

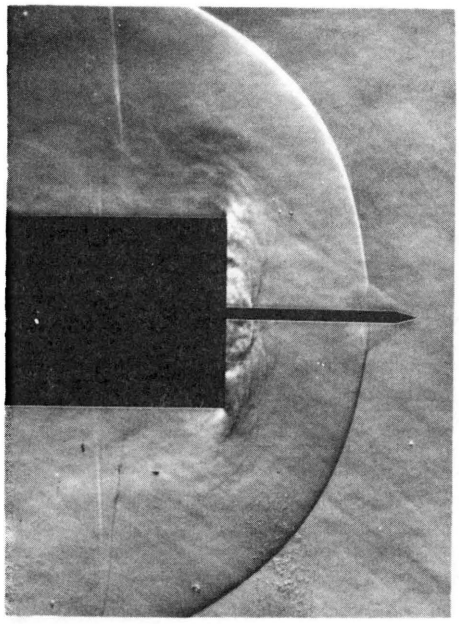

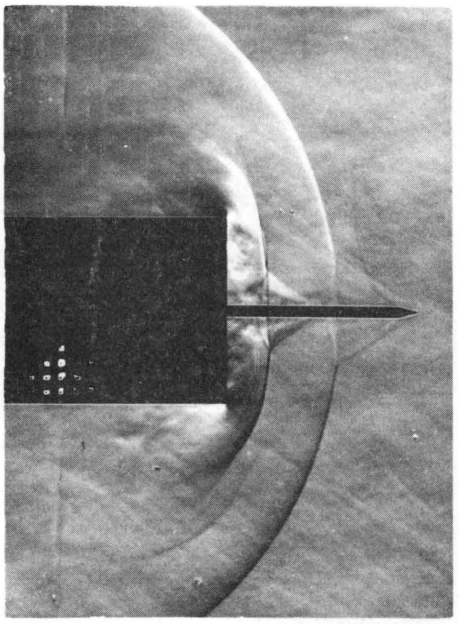

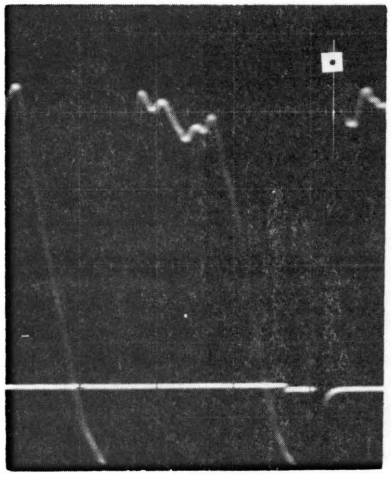

c

d

Fig. 47 (continued)

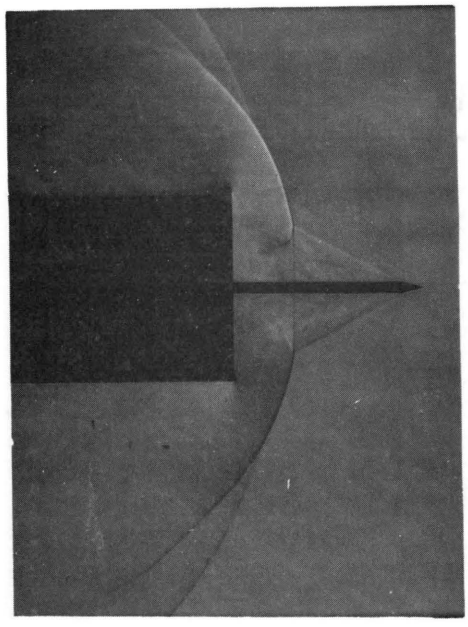

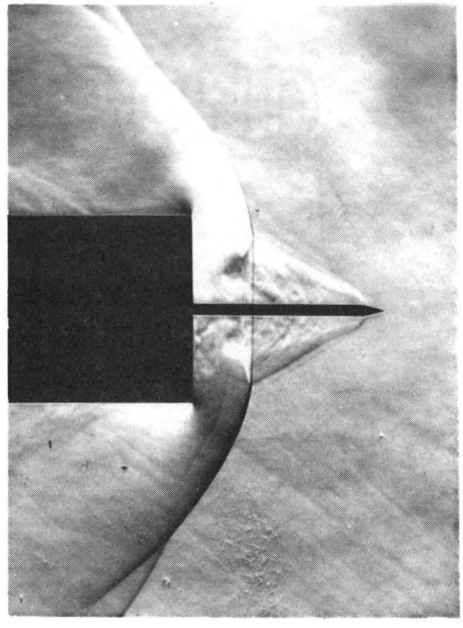

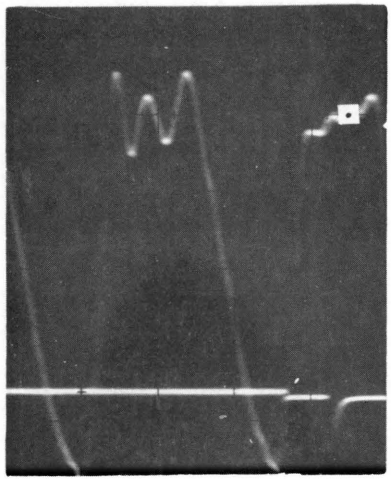

e

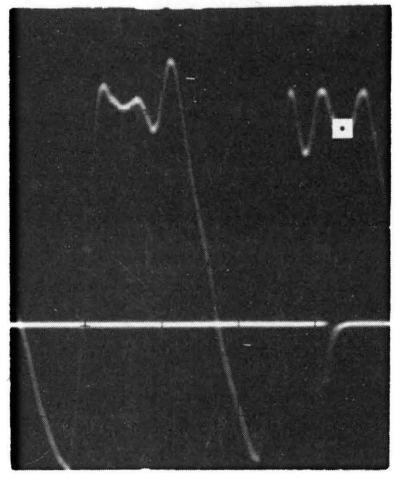

f

Fig. 47 (continued)

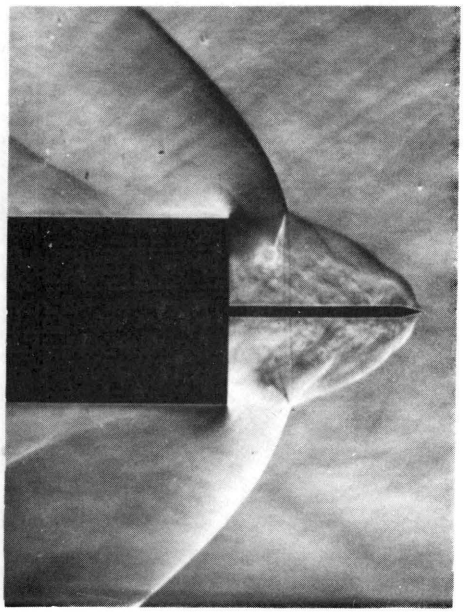

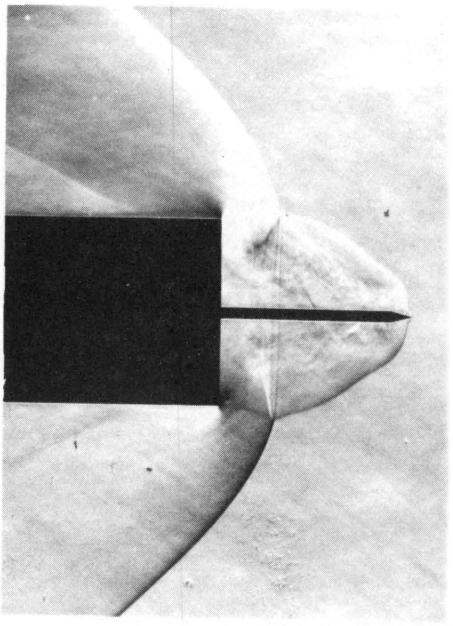

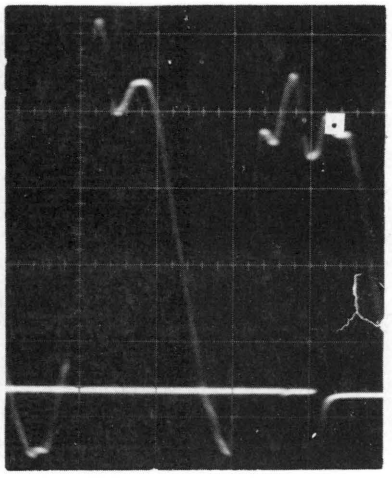

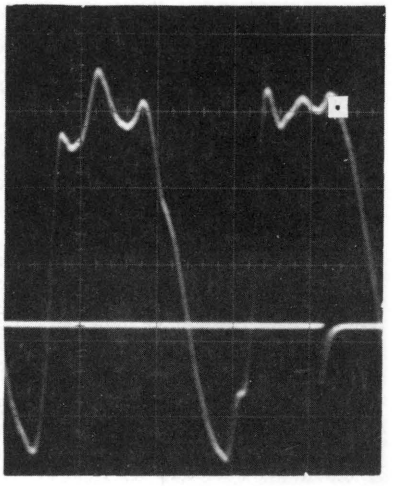

g

h

Fig. 47 (continued)

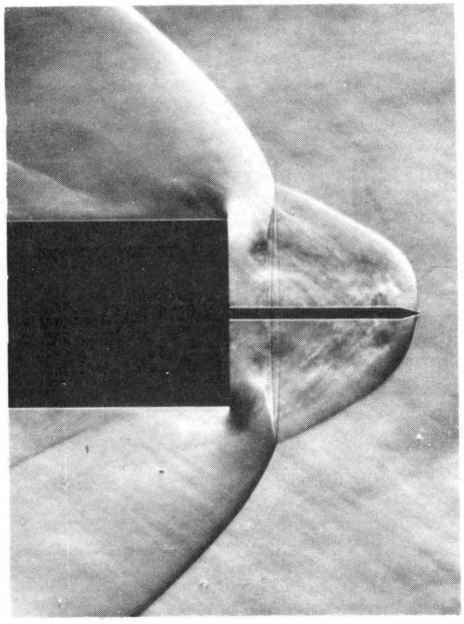

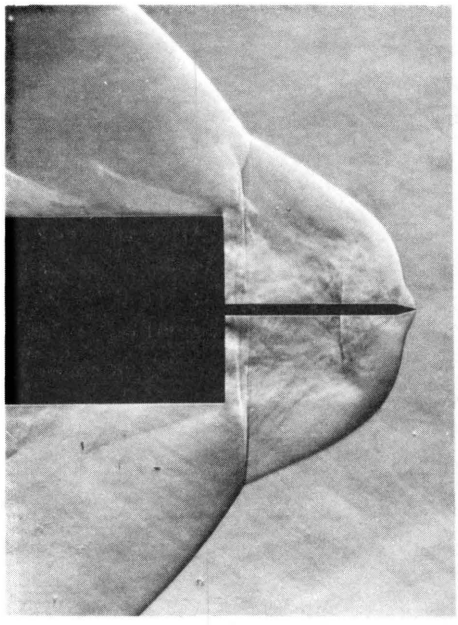

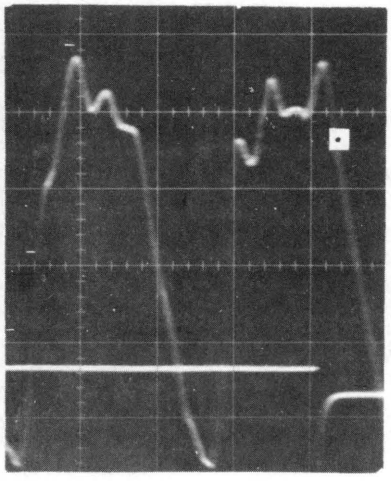

i

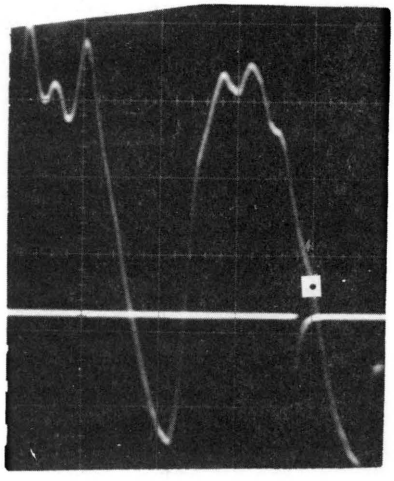

j

Fig. 47 (concluded)

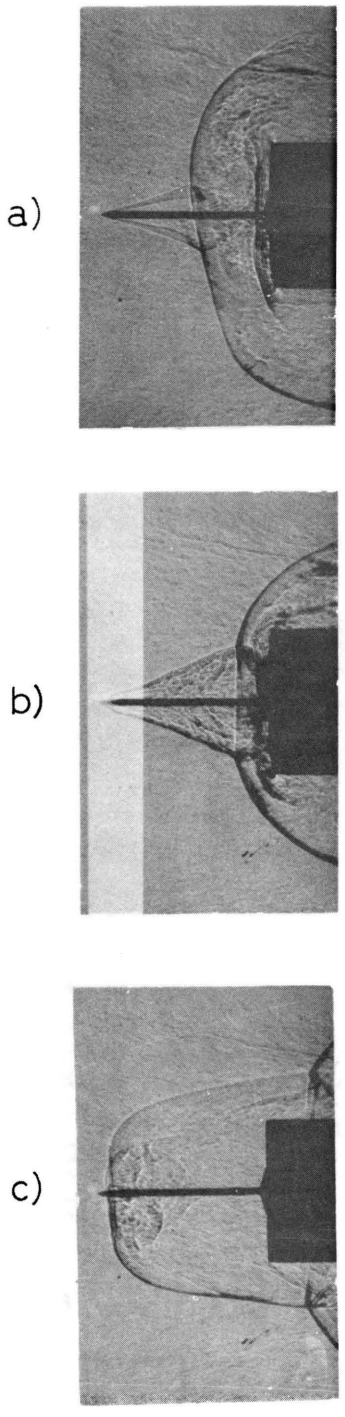

Fig. 48 The Pulsation Shock Envelope; M_1=6, Re_D=0.9x10^6

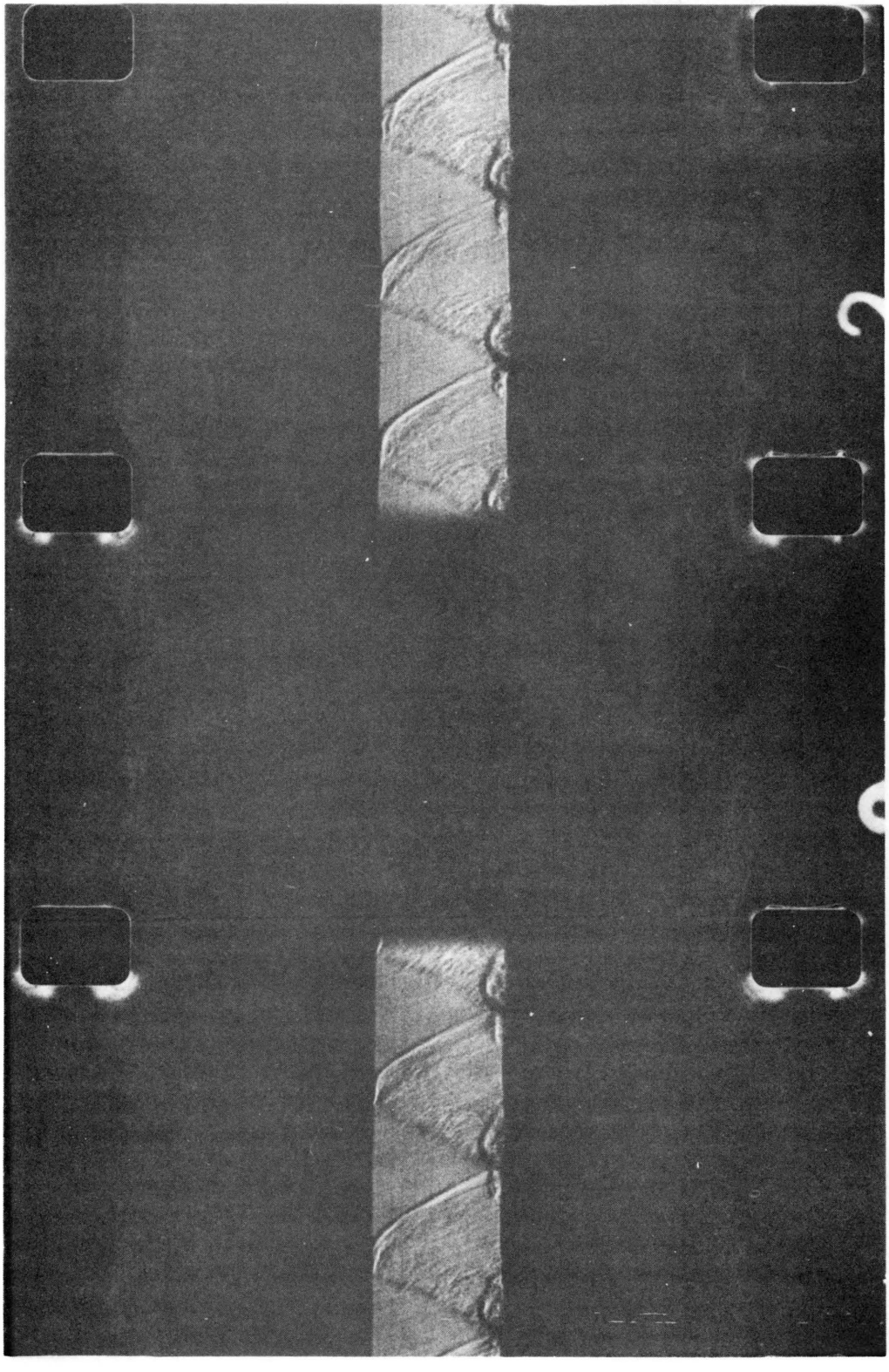

Fig. 49 High Speed Ciné Streak Test Results

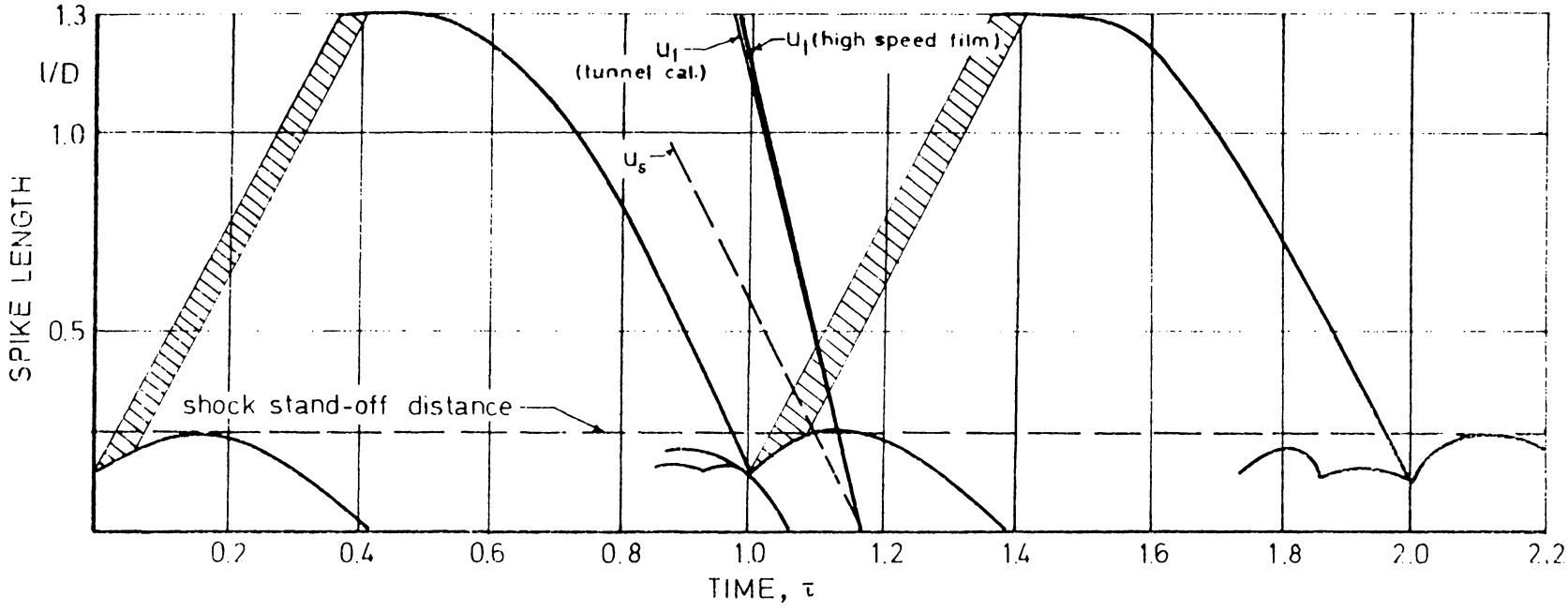

FIG. 50 REDUCED RESULTS FROM A HIGHSPEED CINE TEST

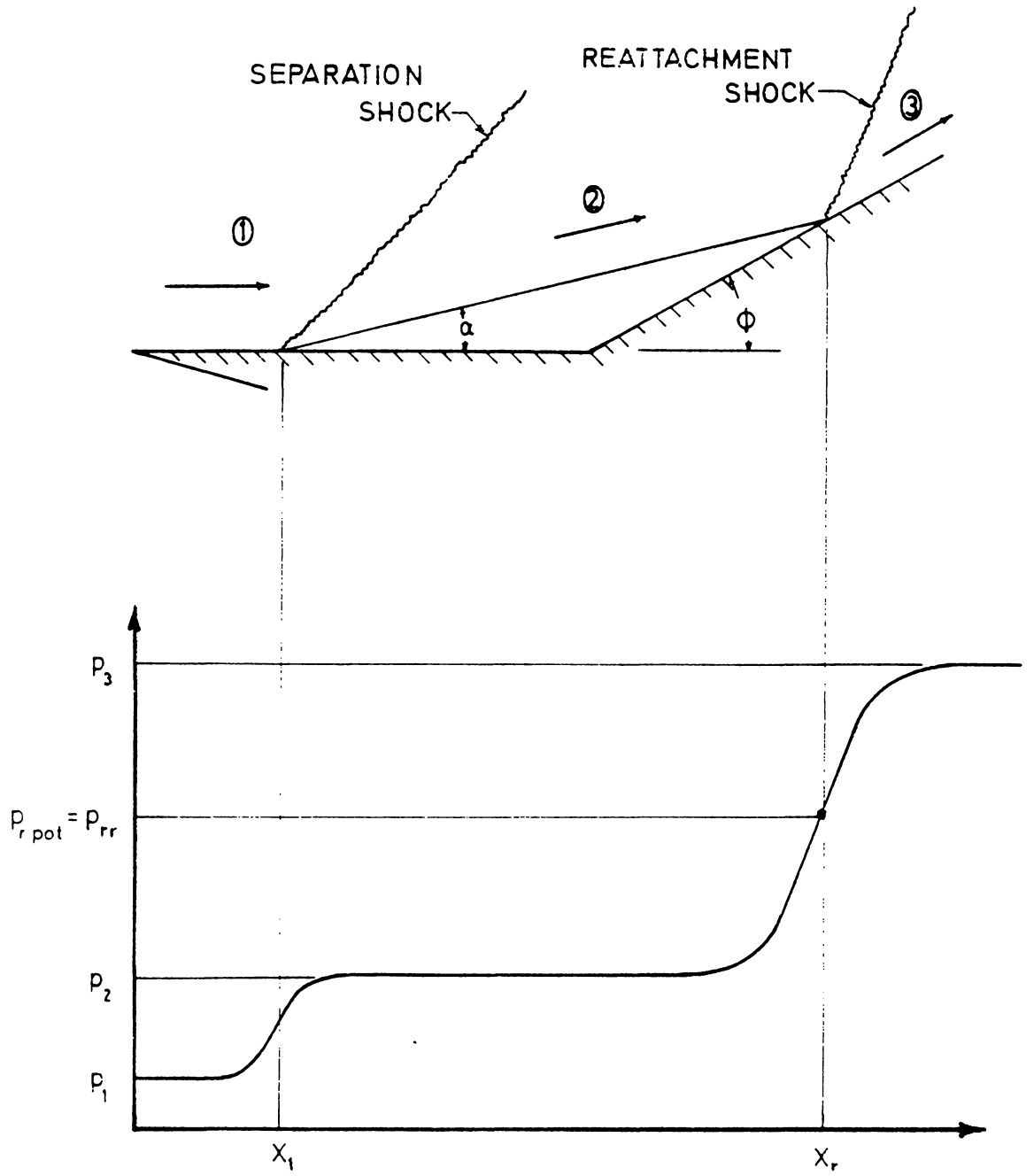

FIG. 51 SCHEMATIC OF SEPARATION

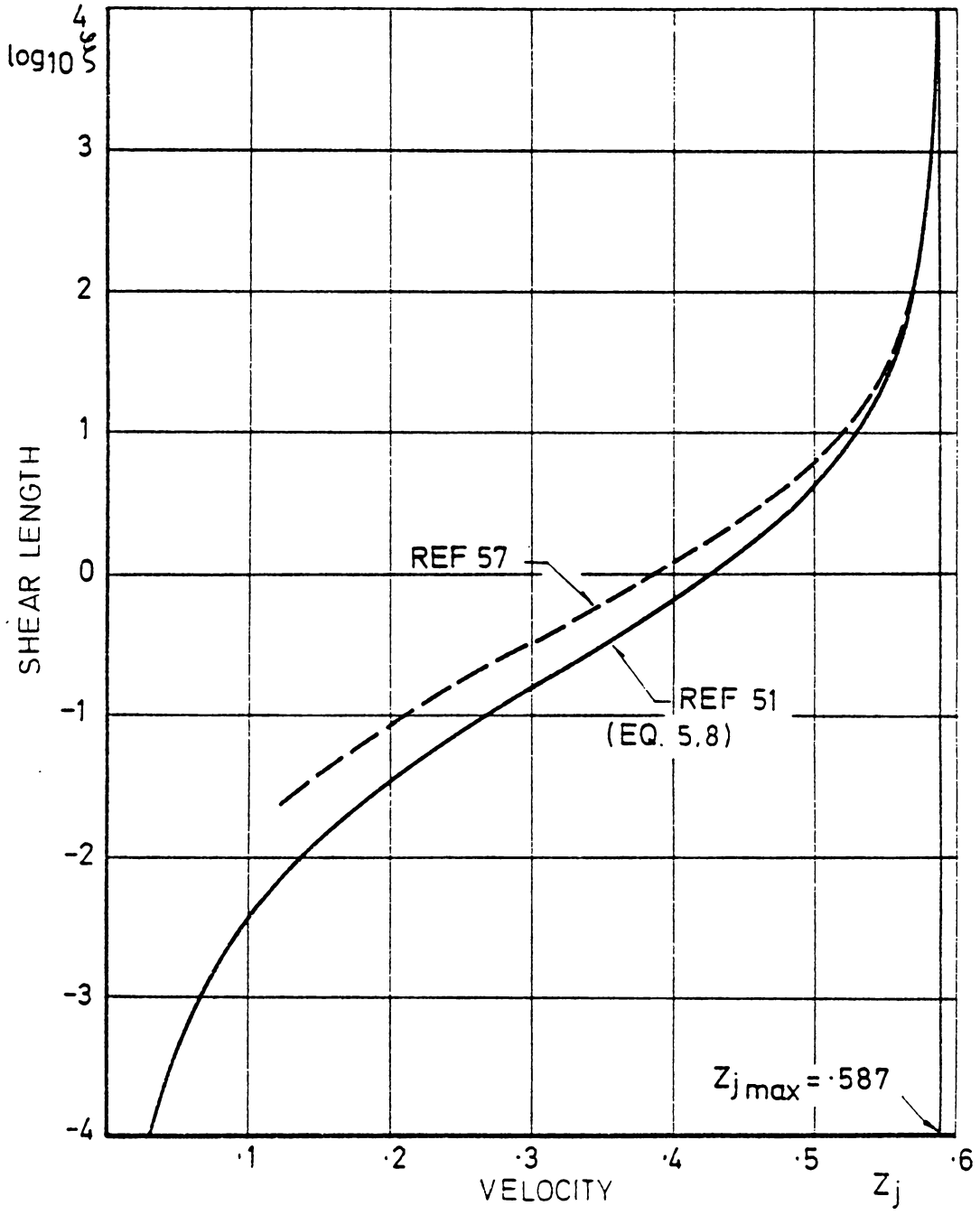

FIG. 52 THE LAMINAR DIVIDING STREAMLINE VELOCITY DISTRIBUTION

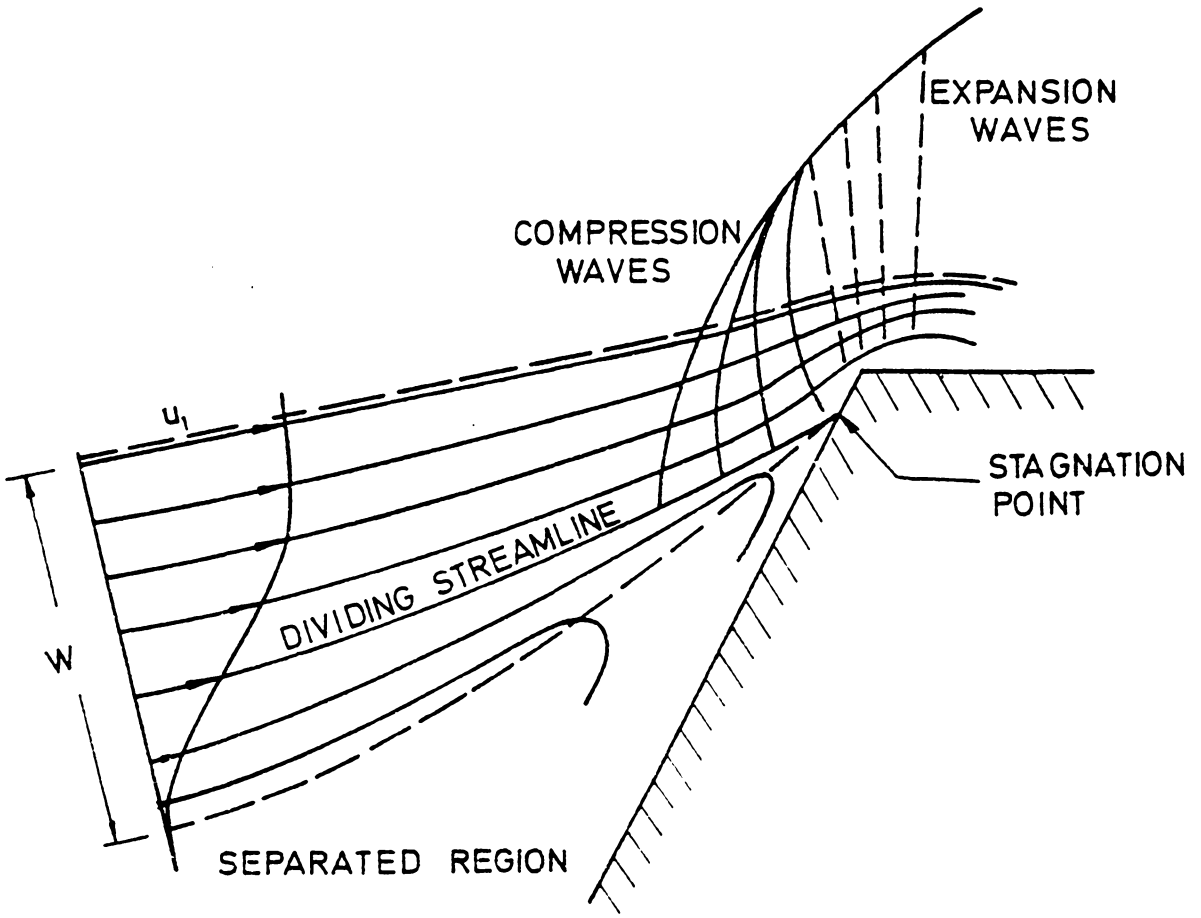

FIG. 53 SHOULDER REATTACHMENT AFTER WOOD (REF. 28)

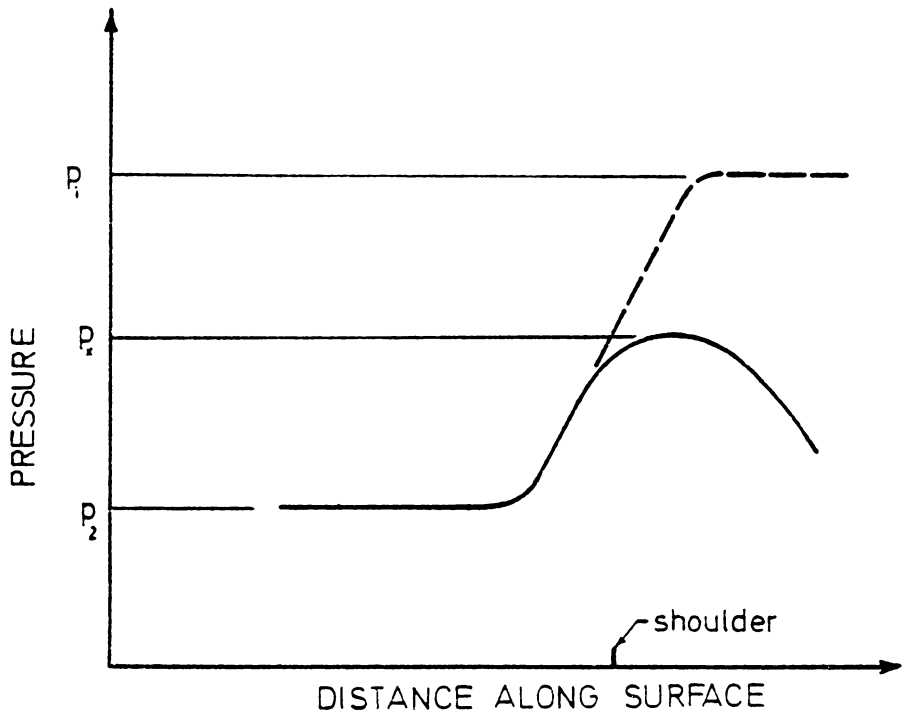

FIG.54 SHOULDER REATTACHMENT PRESSURE DISTRIBUTION

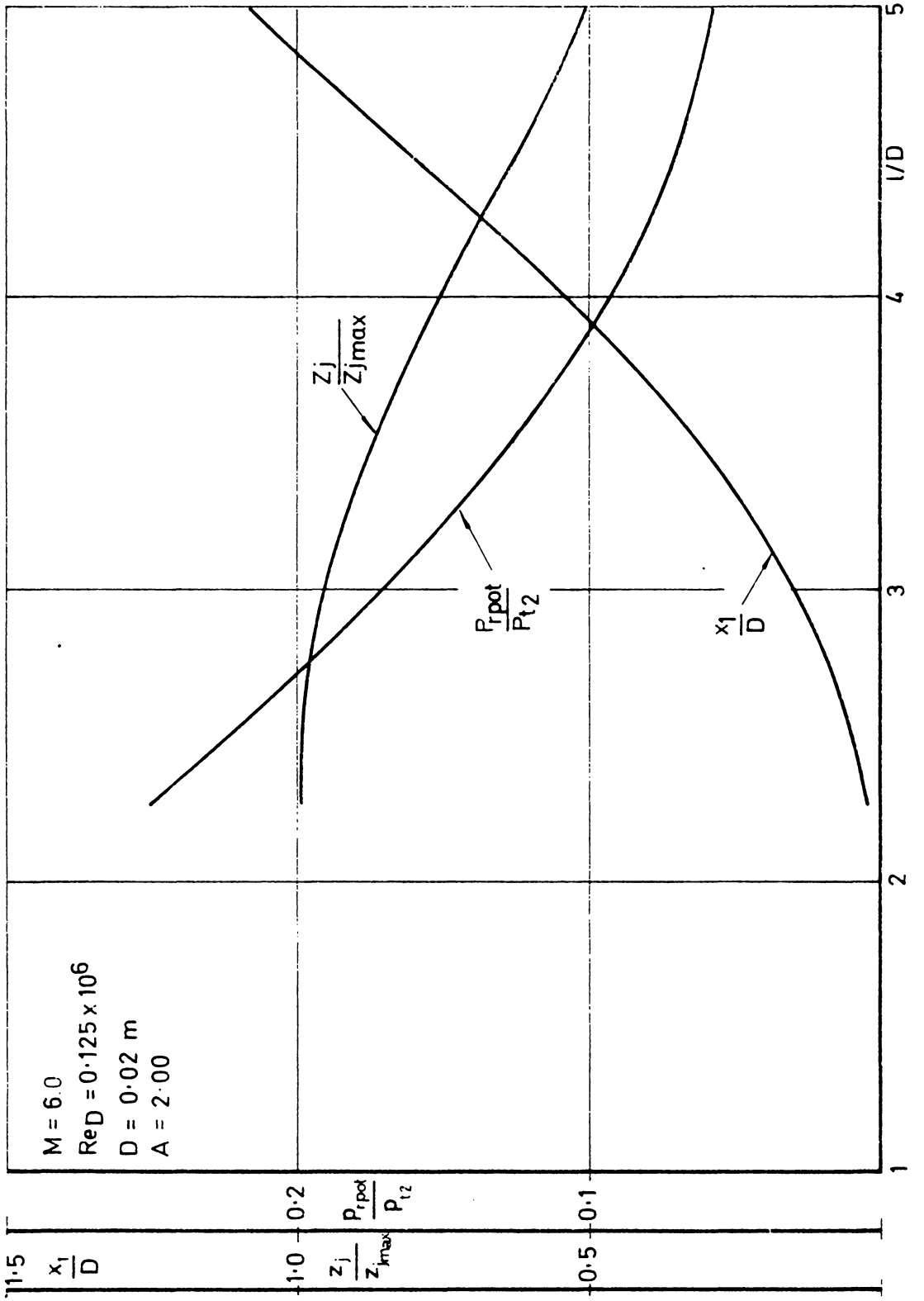

FIG.55 FREE INTERACTION CALCULATION; $M_1=6$, $Re_D=0.125\times10^6$

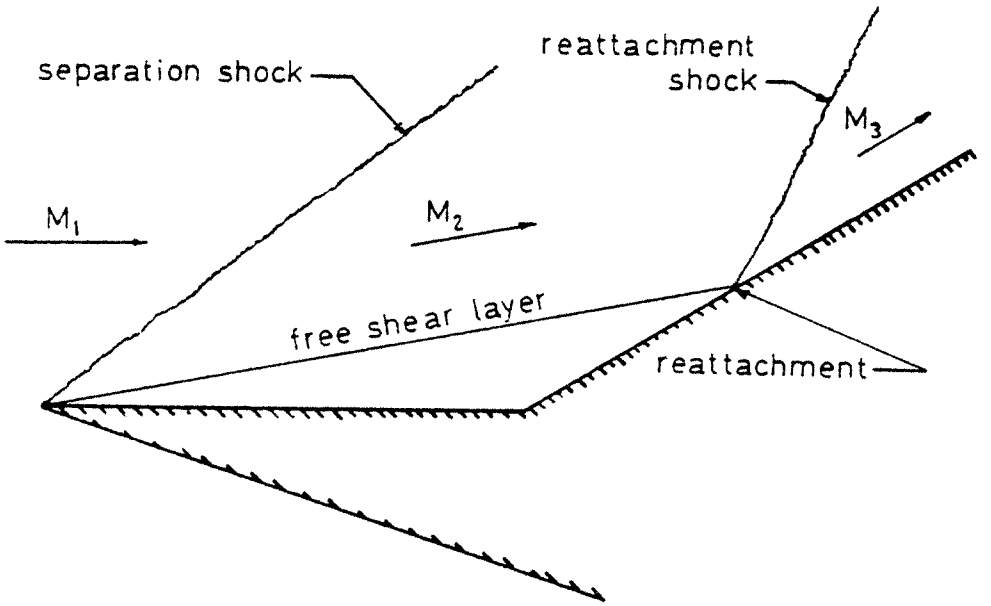

FIG. 56 SCHEMATIC OF LEADING EDGE SEPARATION

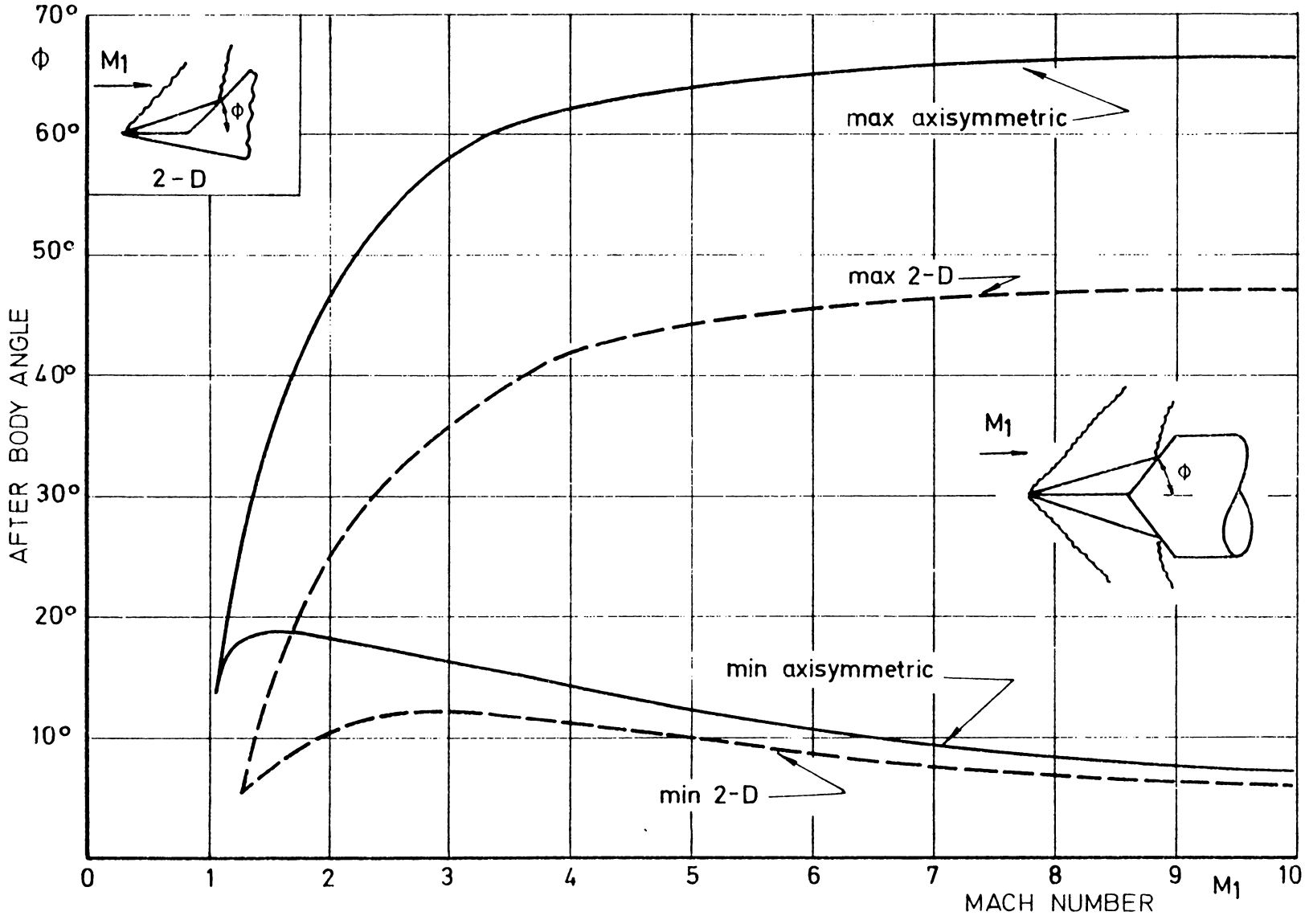

FIG. 57 LIMIT OF LEADING EDGE SEPARATION (LAMINAR)

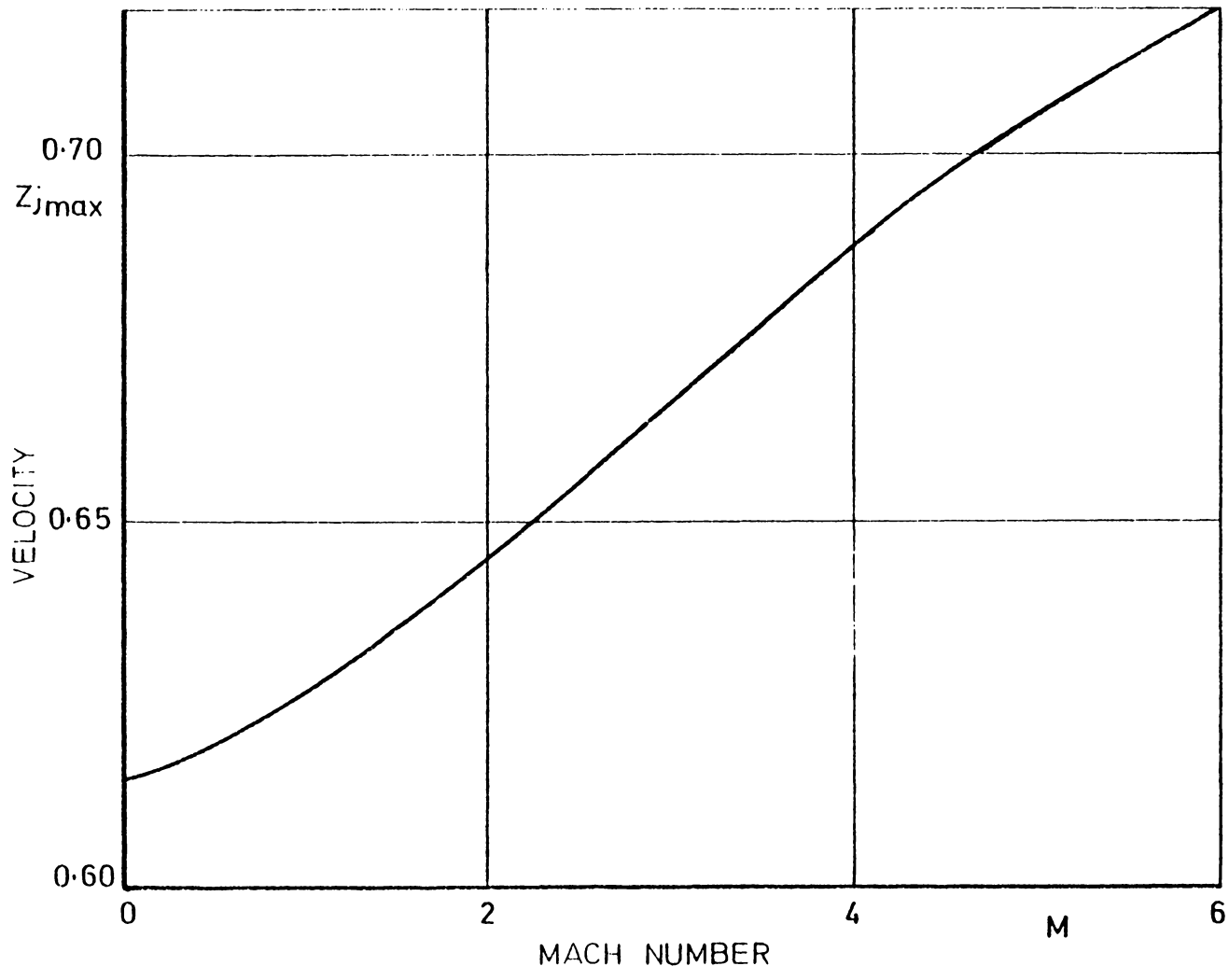

FIG. 58 THE MAXIMUM DIVIDING STREAMLINE VELOCITY IN TURBULENT FLOW

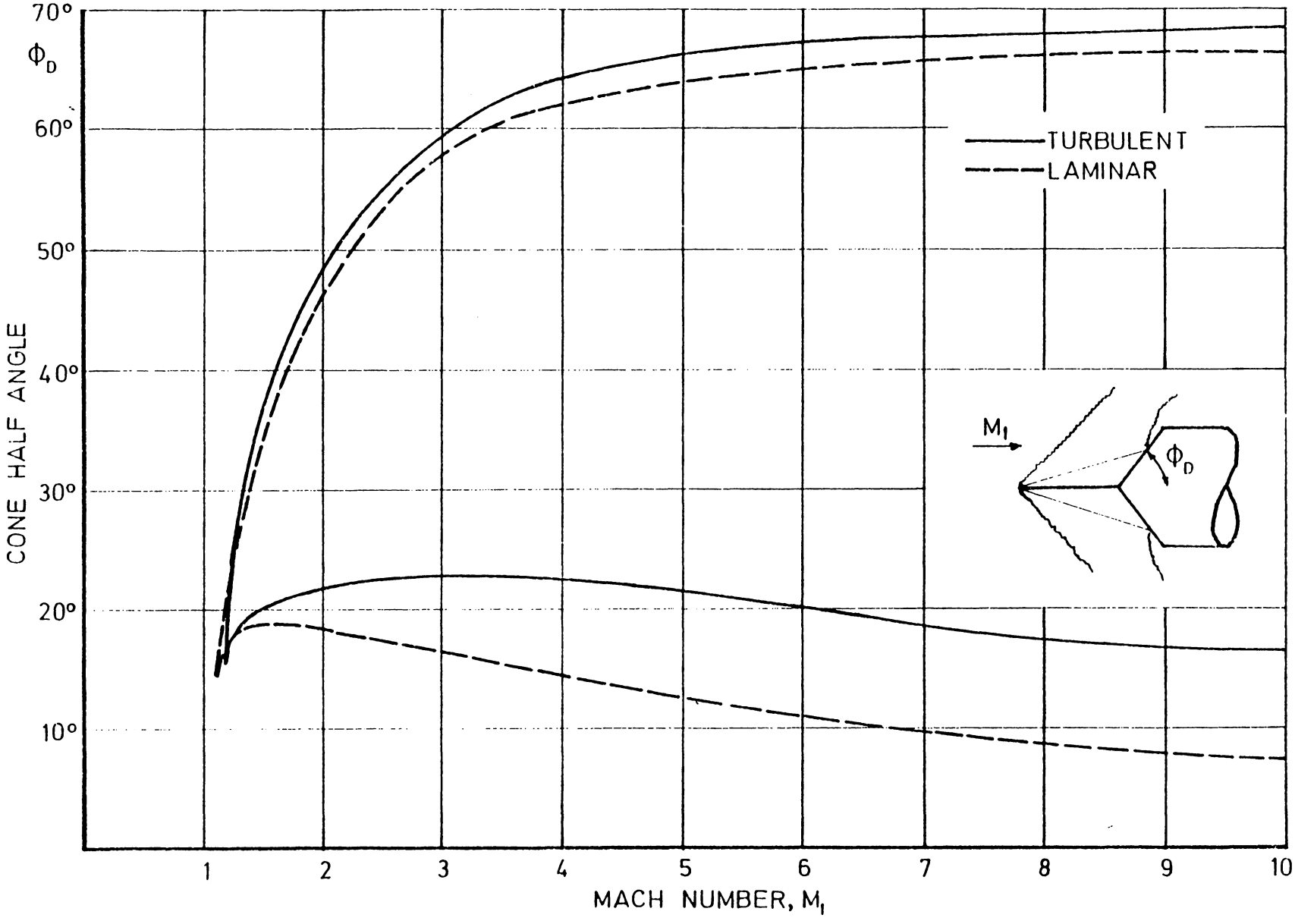

FIG.59 LIMIT OF AXISYSMMETRIC LEADING EDGE SEPARATION

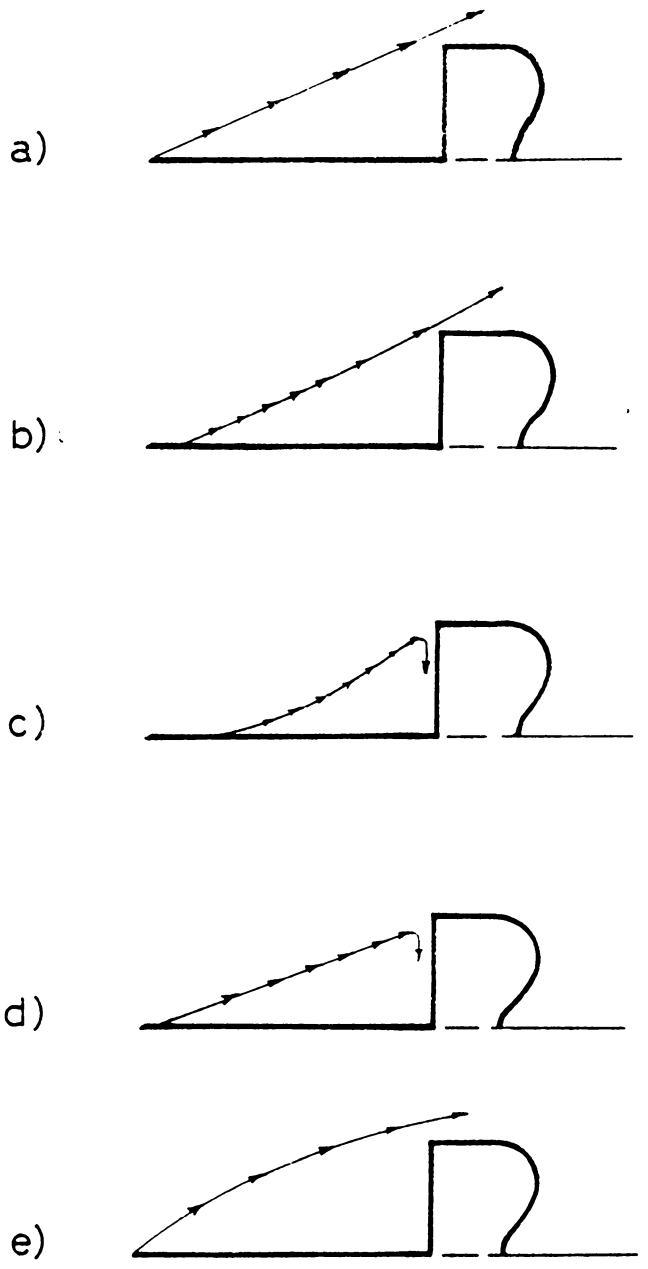

FIG.60 THE BOUNDING STREAMLINE HISTORY FROM THE ENERGETIC SHEAR LAYER HYPOTHESIS

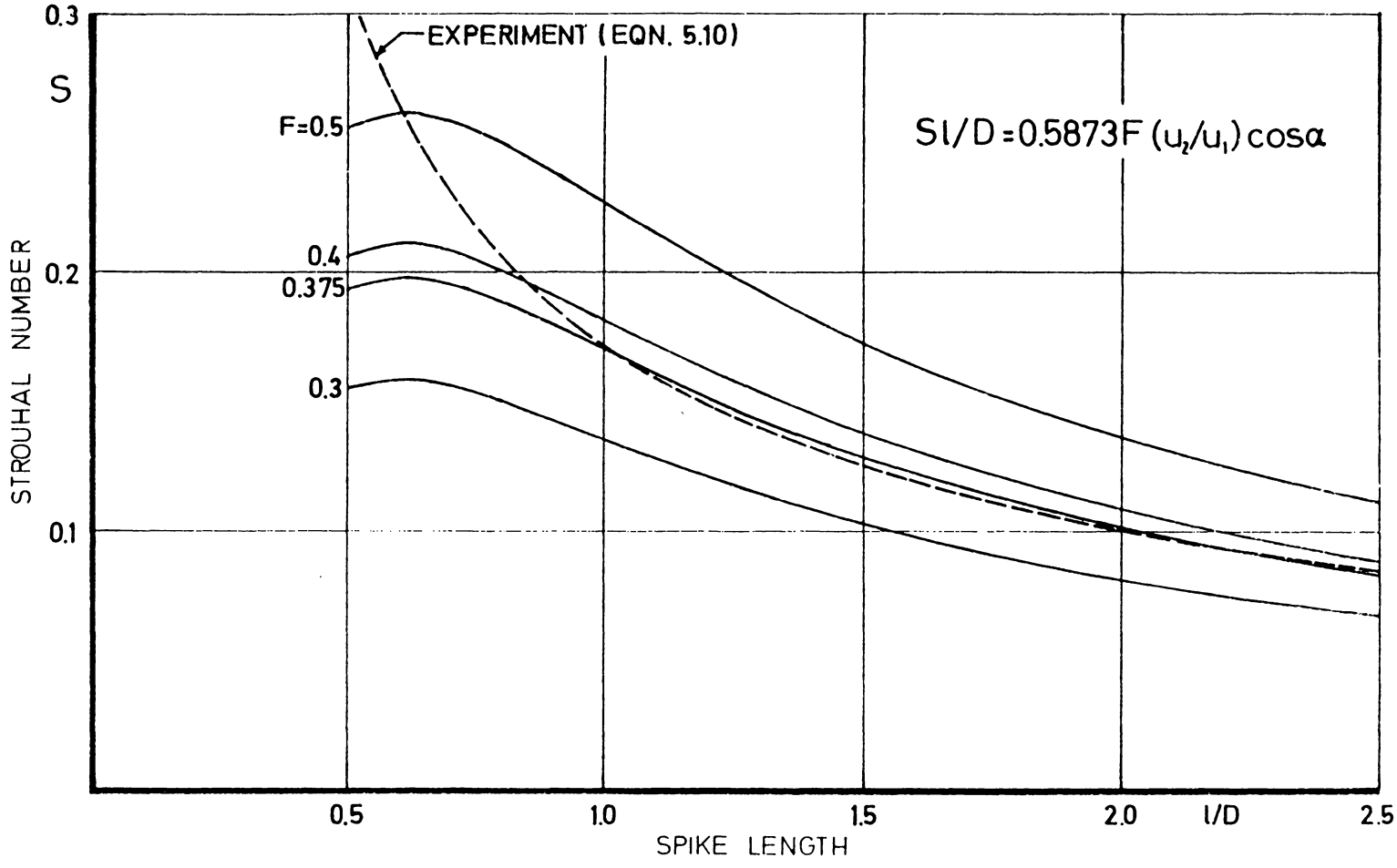

FIG. 61 A COMPARISON OF THEORETICAL AND EXPERIMENTAL FREQUENCY OF OSCILLATION

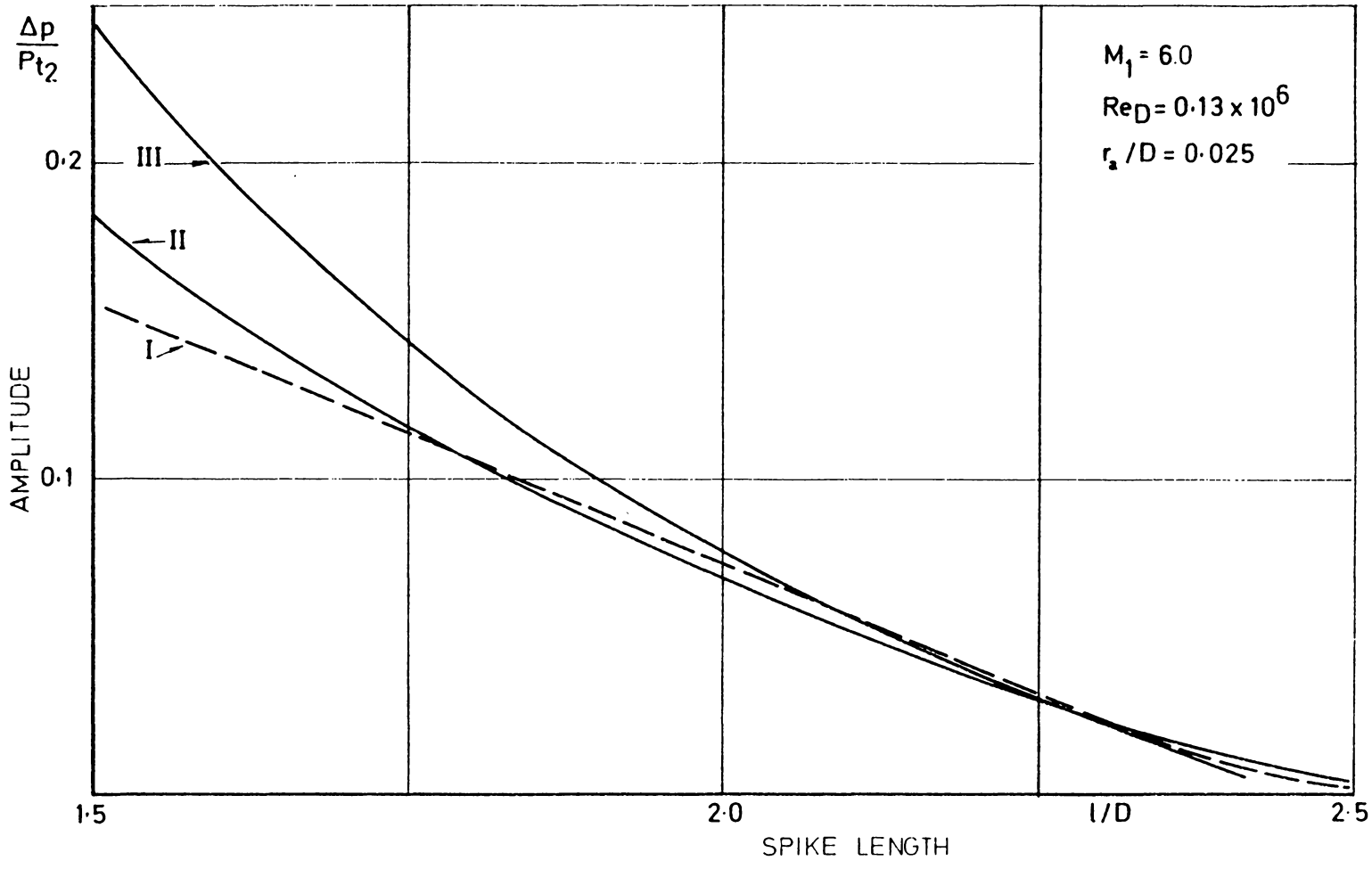

FIG. 62 A COMPARISON OF THREE METHODS OF CALCULATING THE EFFECT OF SPIKE LENGTH ON THE OSCILLATION PRESSURE WAVE AMPLITUDE

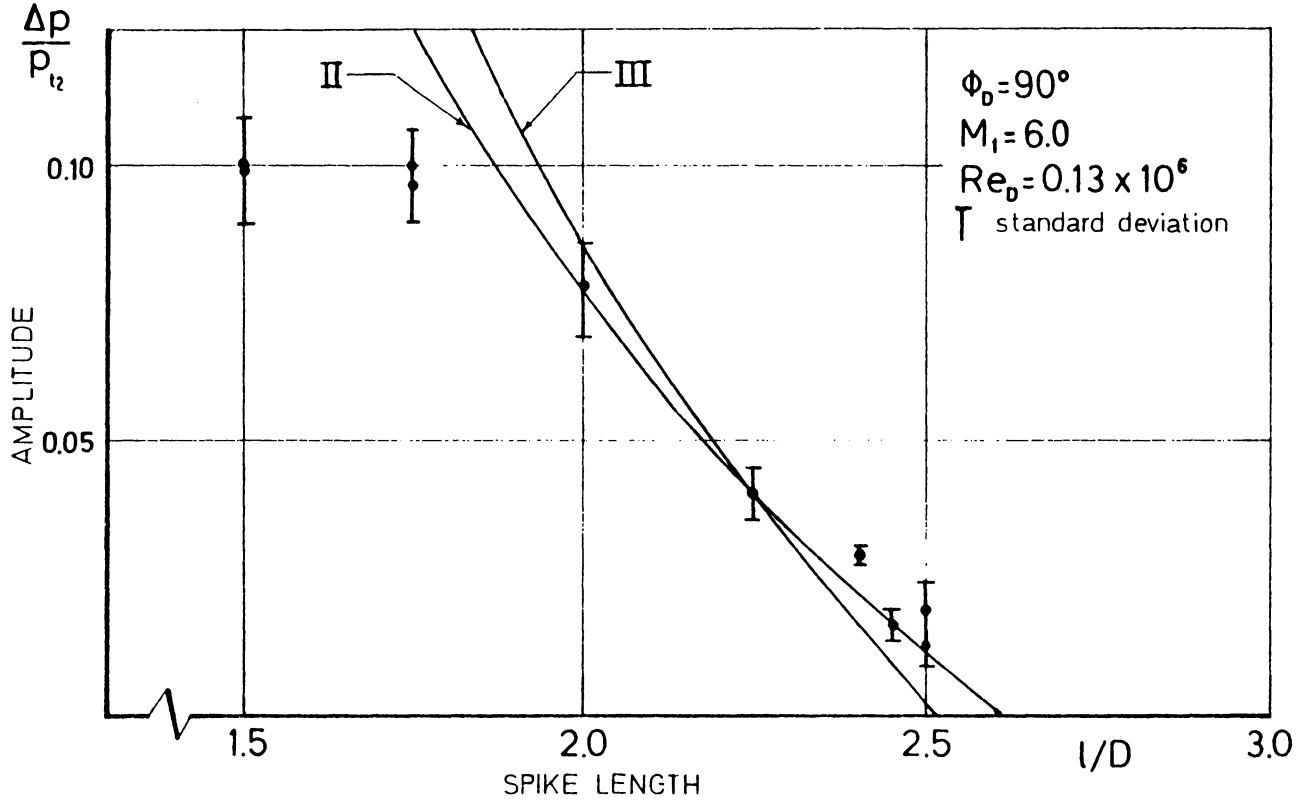

FIG. 63 A COMPARISON OF SHEAR LAYER OVERPRESSURE AND MEASURED PRESSURE WAVE AMPLITUDE, $\Phi_D = 90°$

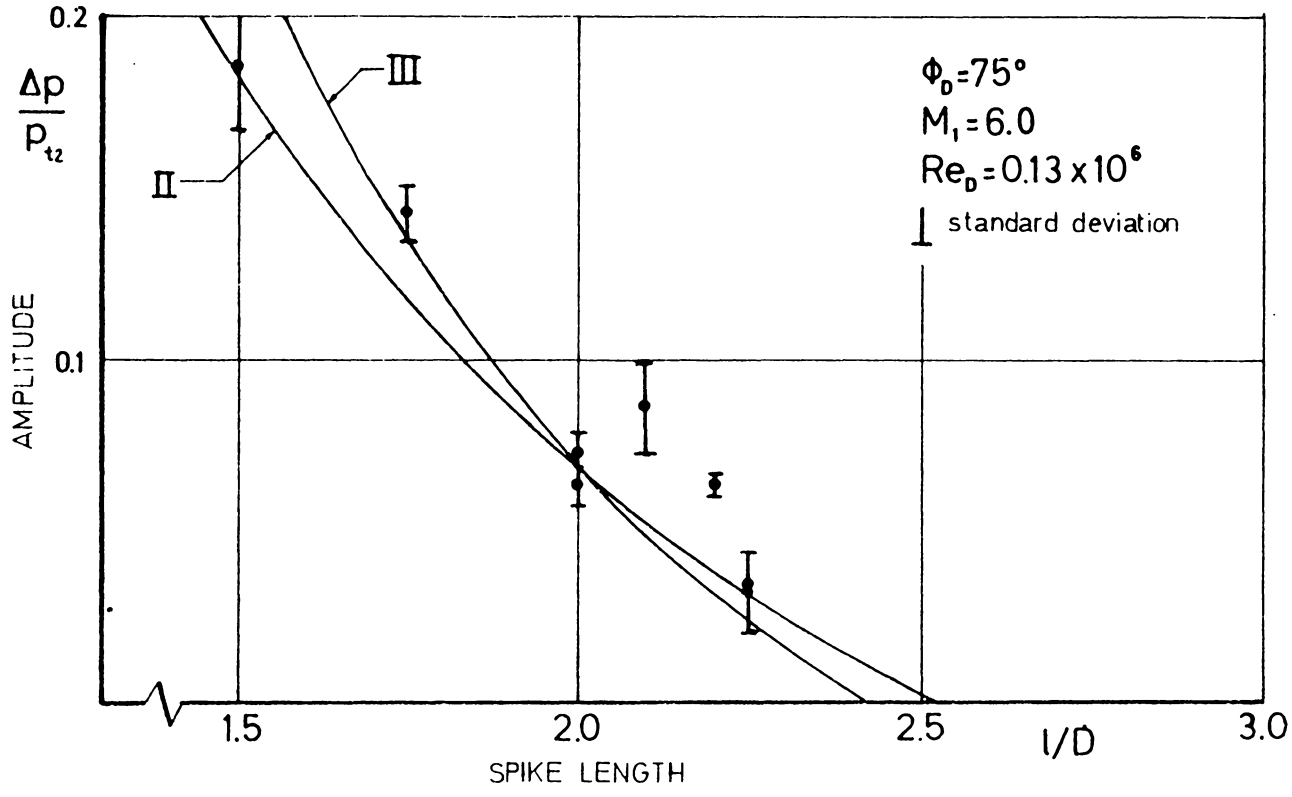

FIG. 64 A COMPARISON OF SHEAR LAYER OVERPRESSURE AND MEASURED PRESSURE WAVE AMPLITUDE, $\Phi_D = 75°$

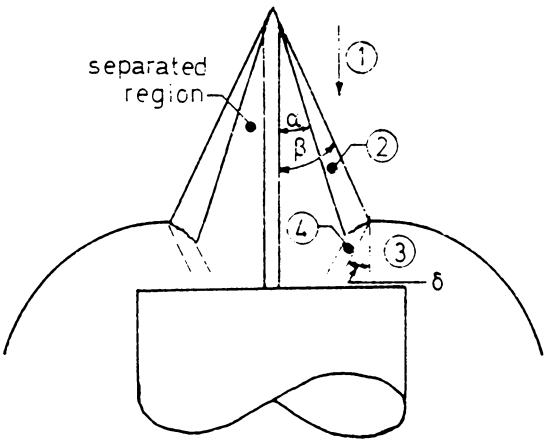

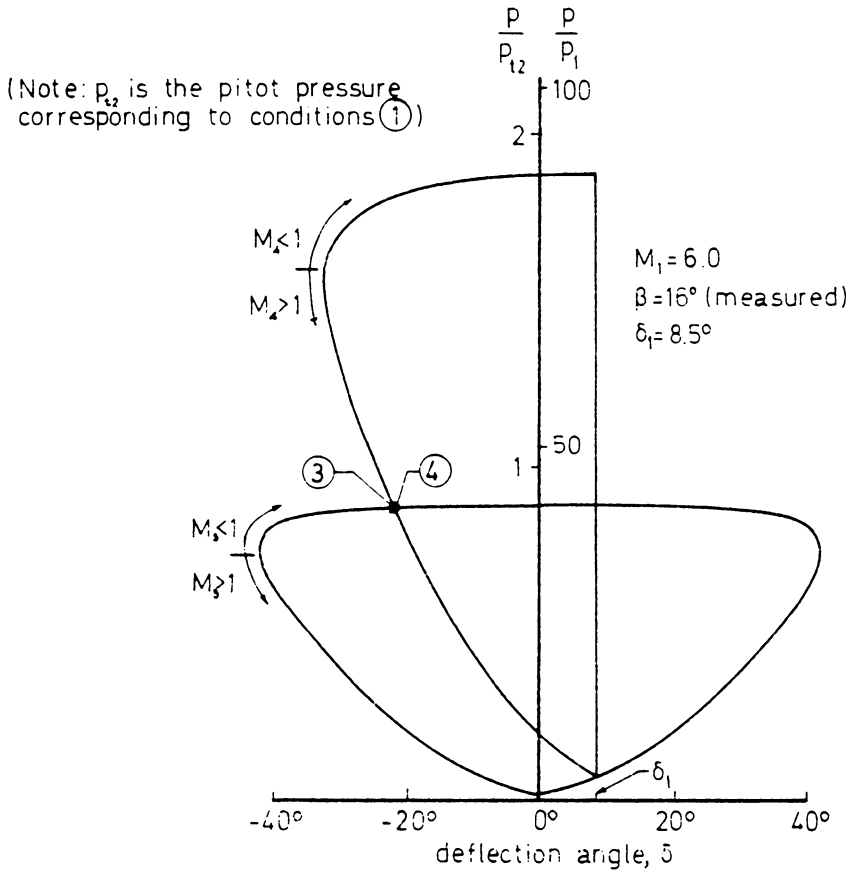

FIG. 65 HEART DIAGRAM, $M_1 = 6.0$

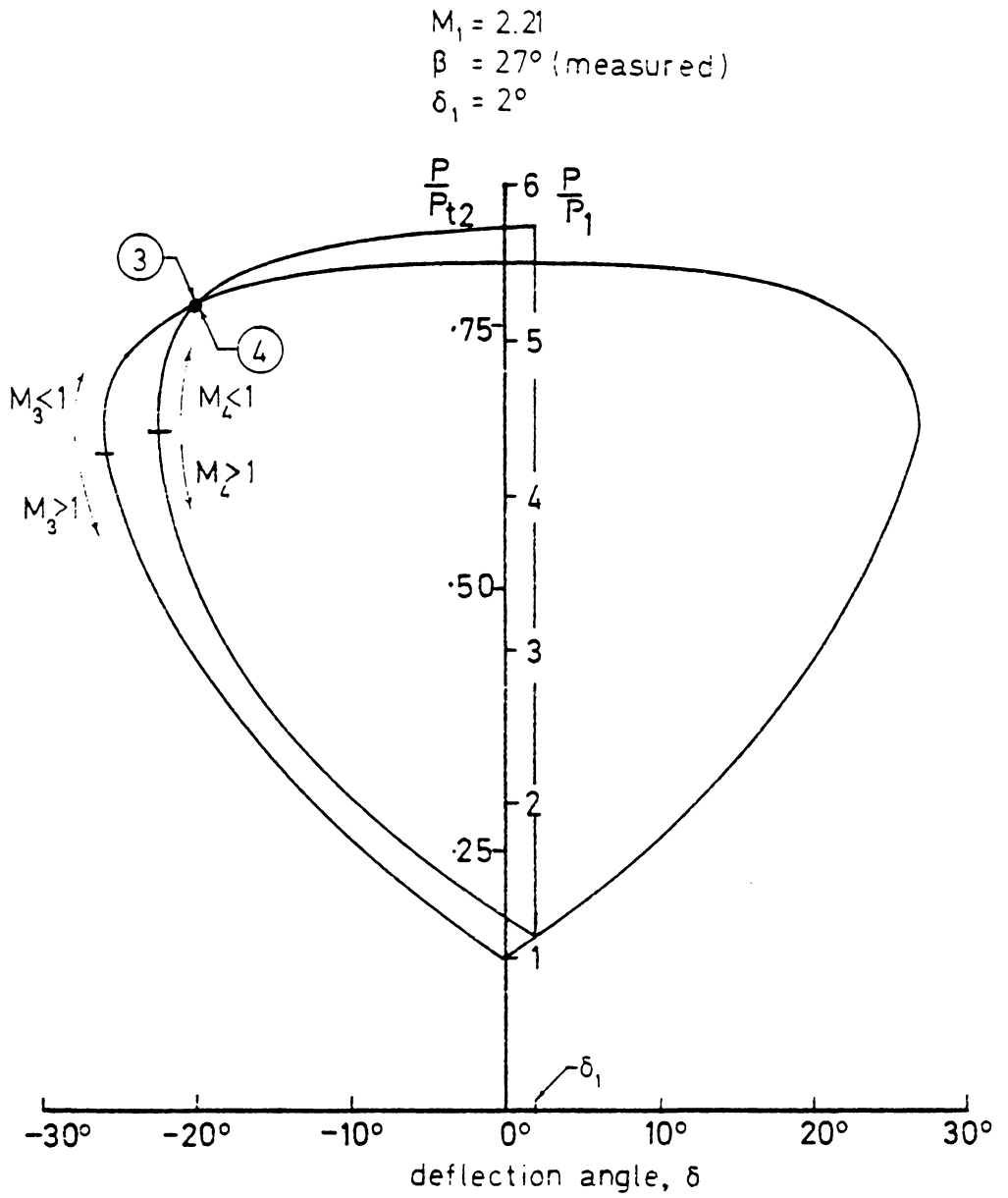

FIG. 66 HEART DIAGRAM, $M_1 = 2.21$

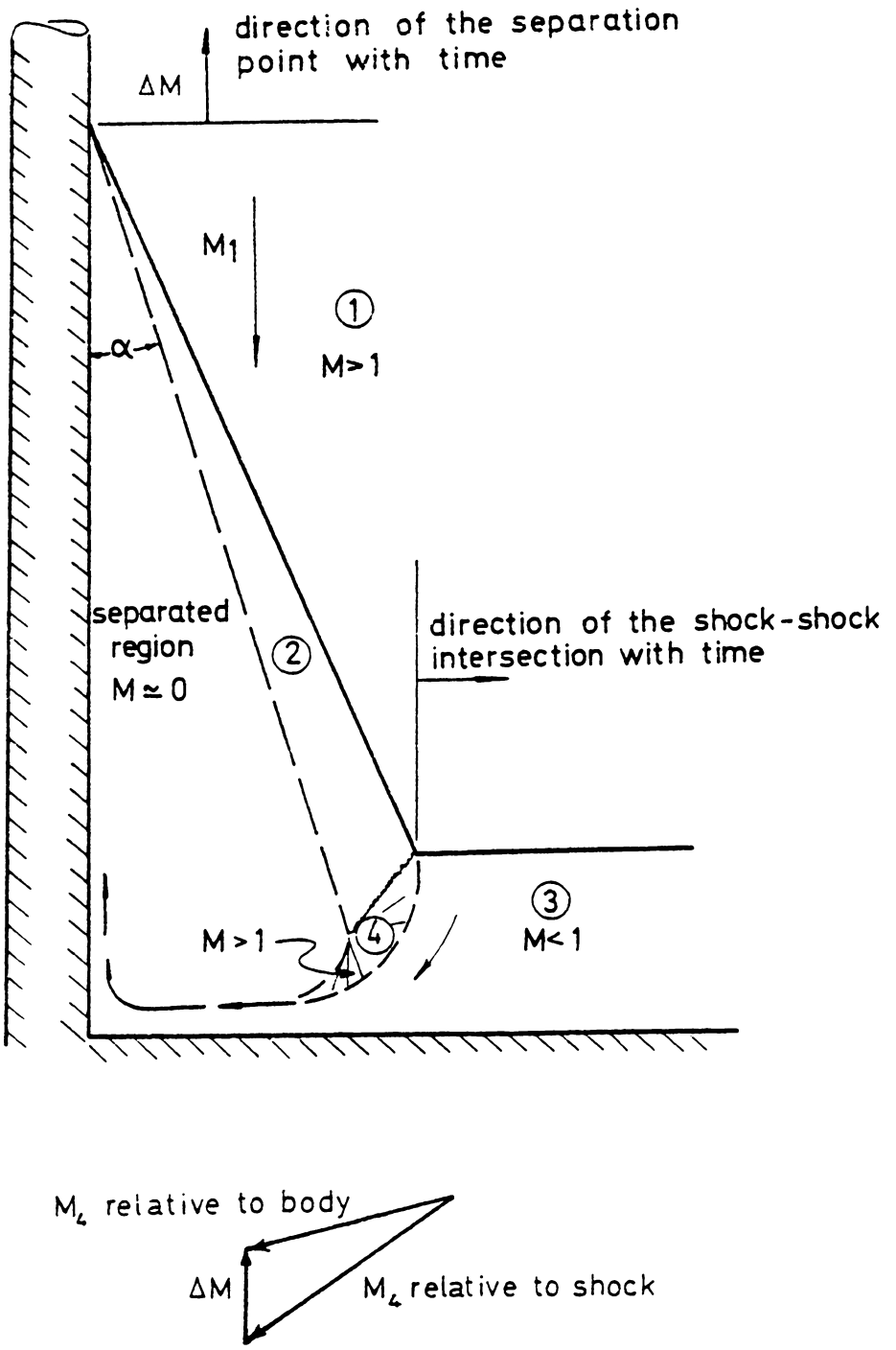

FIG. 67 SCHEMATIC OF THE SEPARATION POINT MOVEMENT AND RESULTING VELOCITY TRIANGLE FOR PULSATION

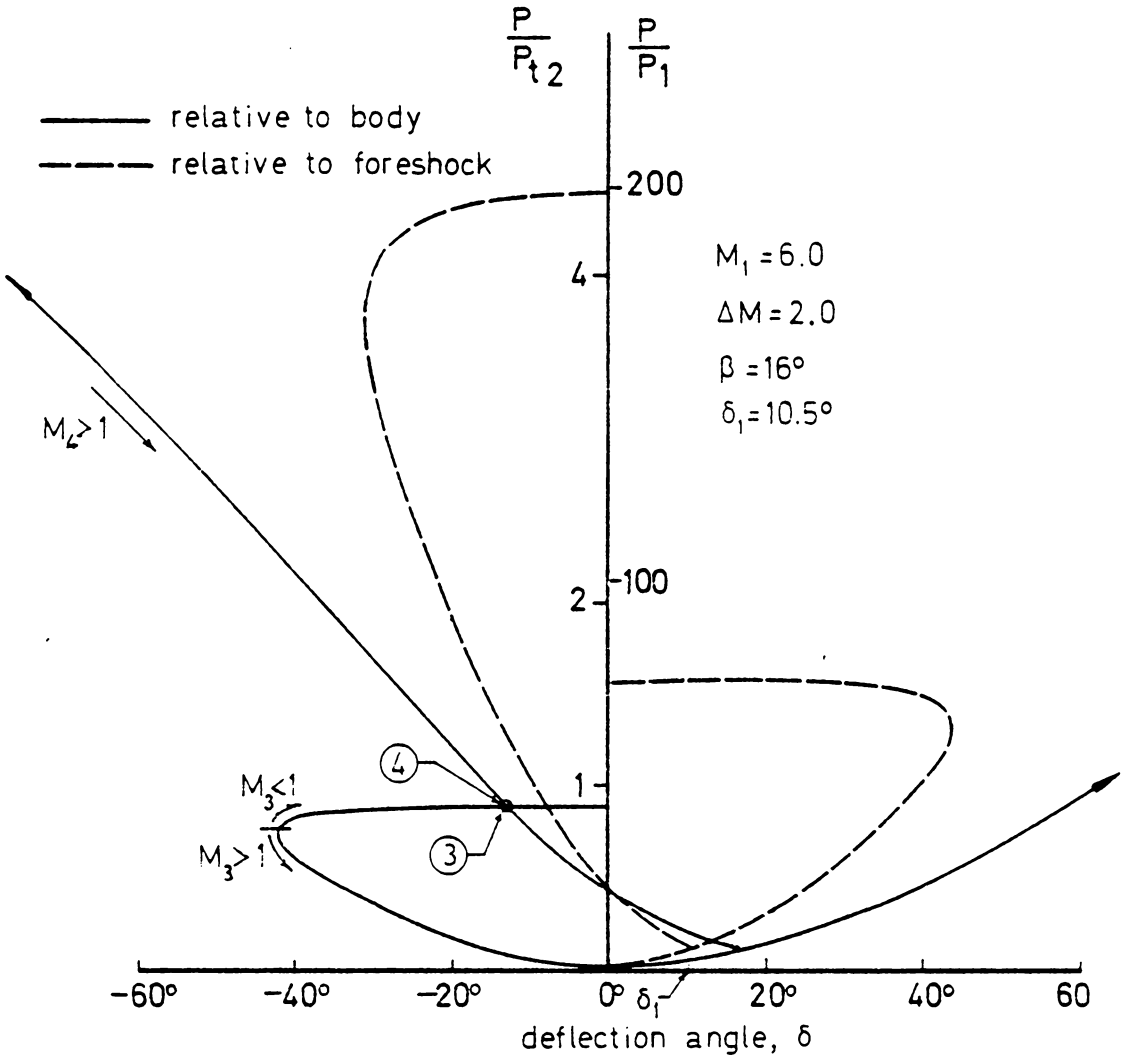

FIG. 68 DYNAMIC HEART DIAGRAM, $M_1 = 6.0$

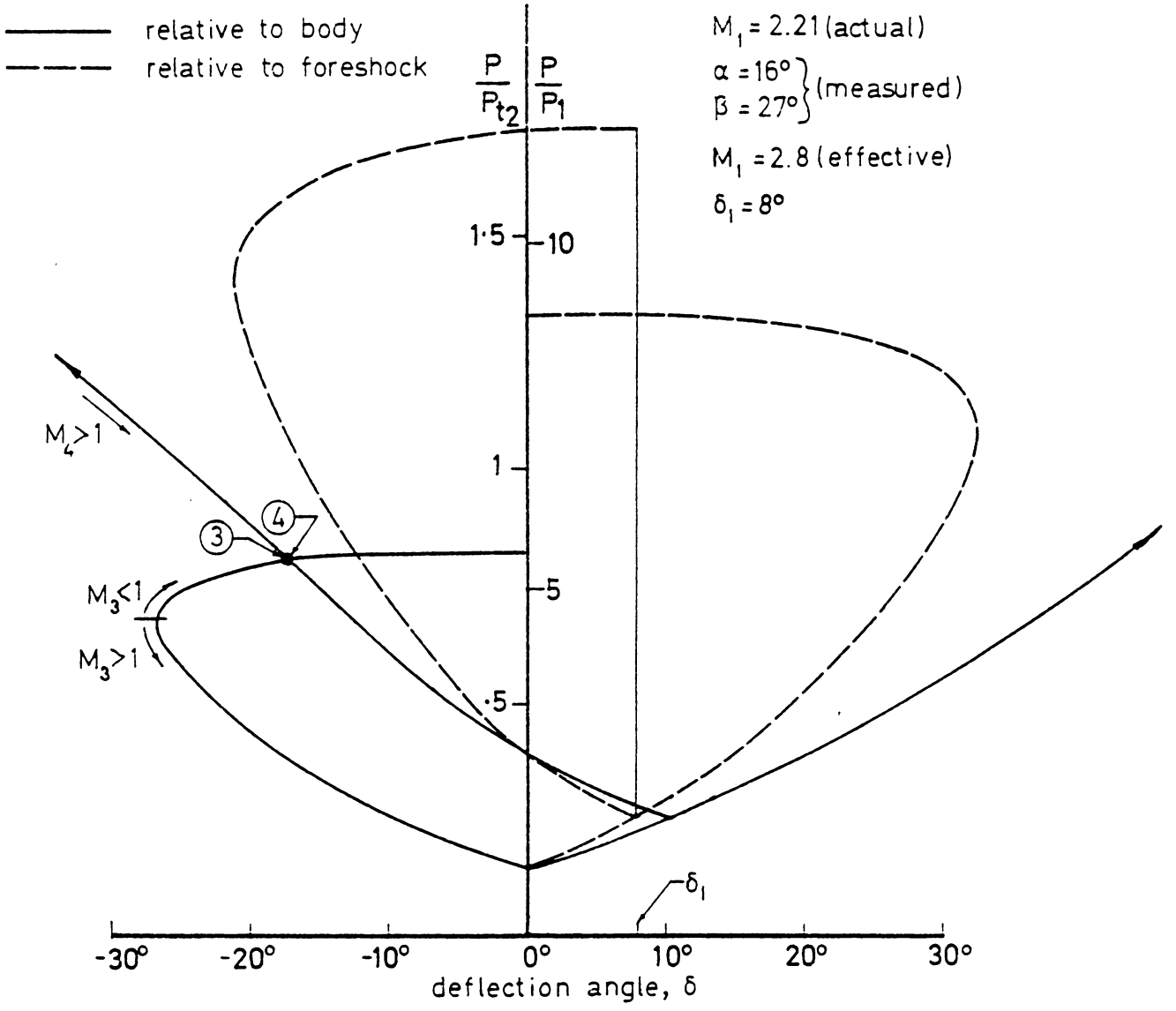

FIG. 69 DYNAMIC HEART DIAGRAM, M = 2.21

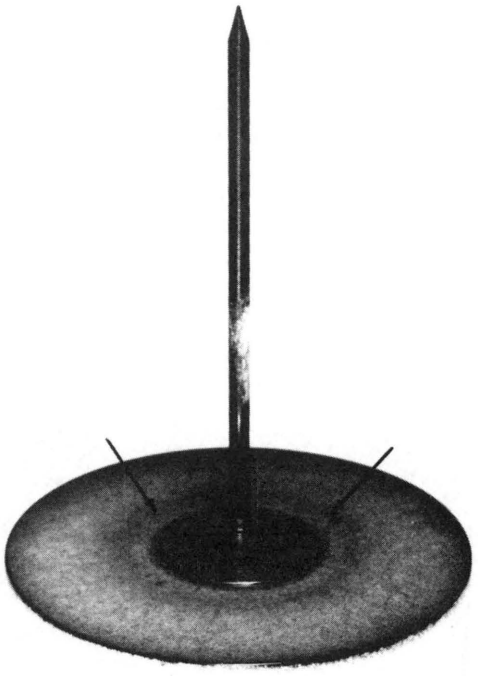

Fig. 70 Sublimation Test Results

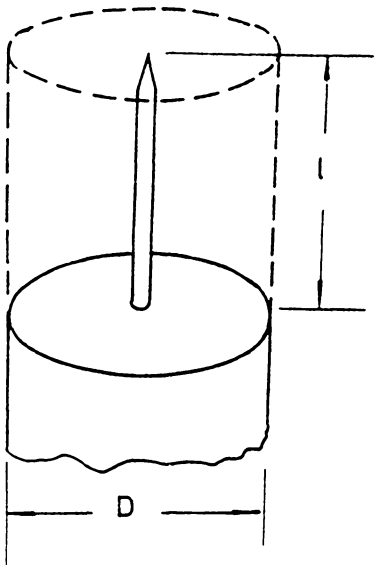

a) THE CONTROL VOLUME

$$V_c = \frac{\pi}{4} D^2 l$$

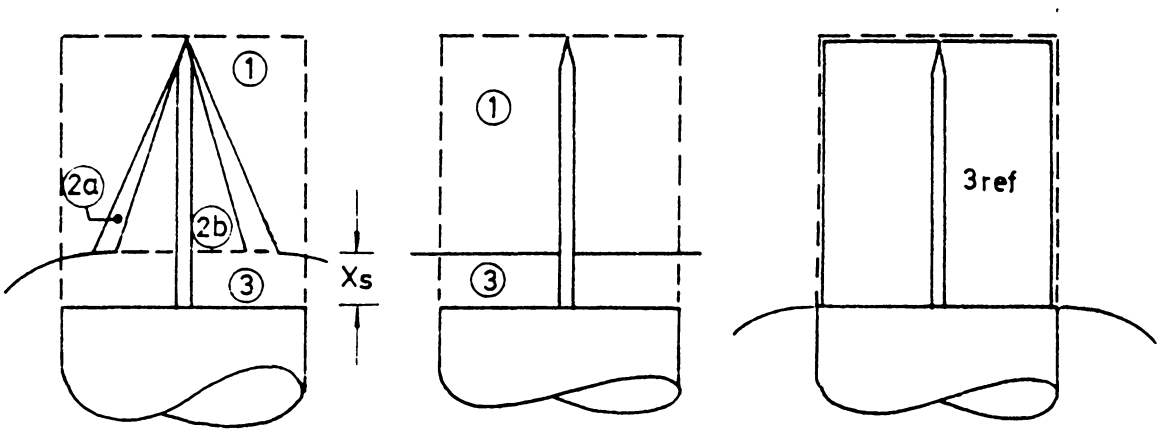

b) ACTUAL INITIAL CONDITIONS c) SIMPLIFIED INITIAL CONDITIONS d) FINAL CONDITIONS

FIG. 71 THE FORESHOCK EXPANSION MODEL

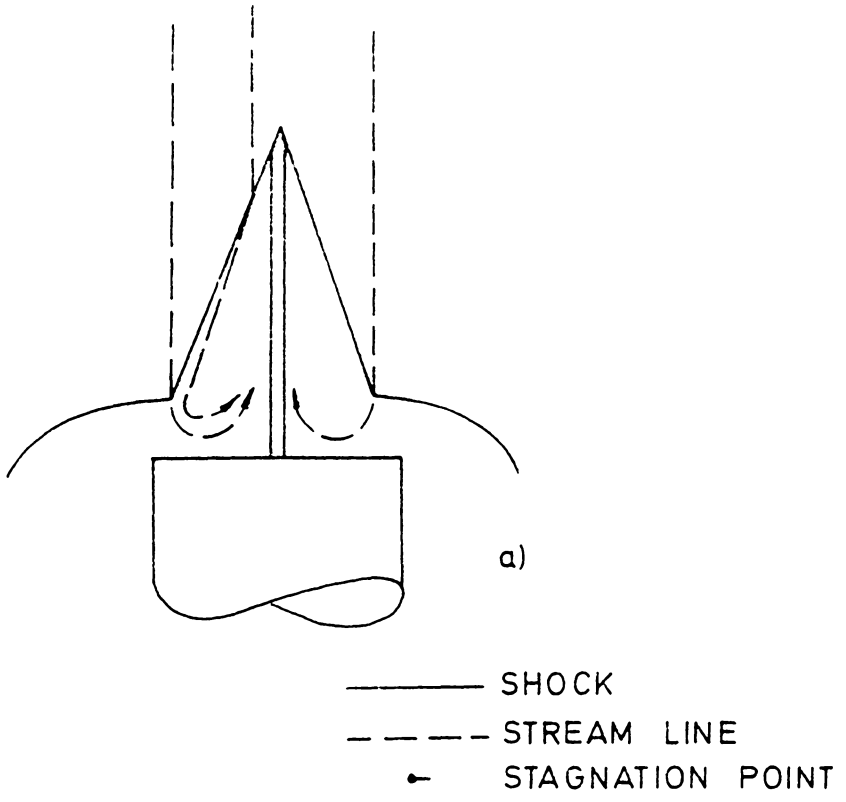

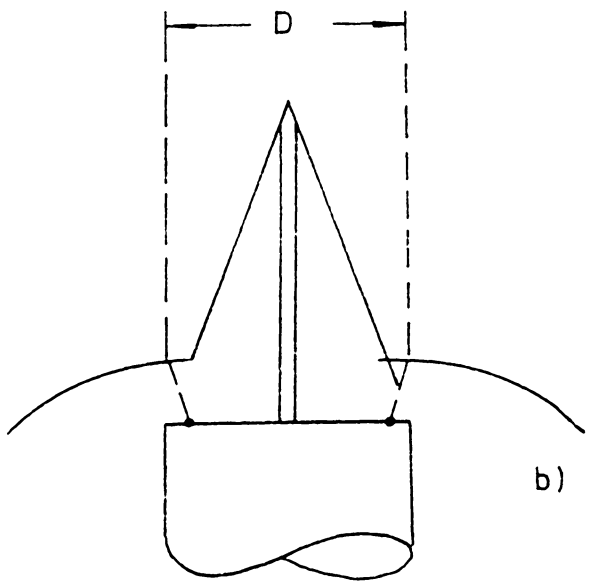

FIG. 72 THE CAPTURE AREA

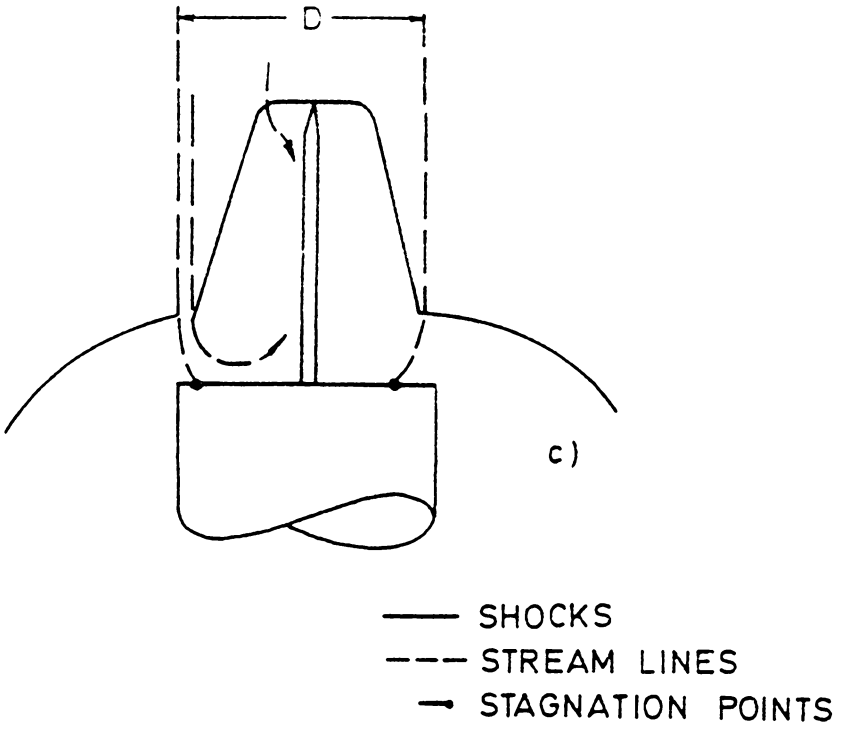

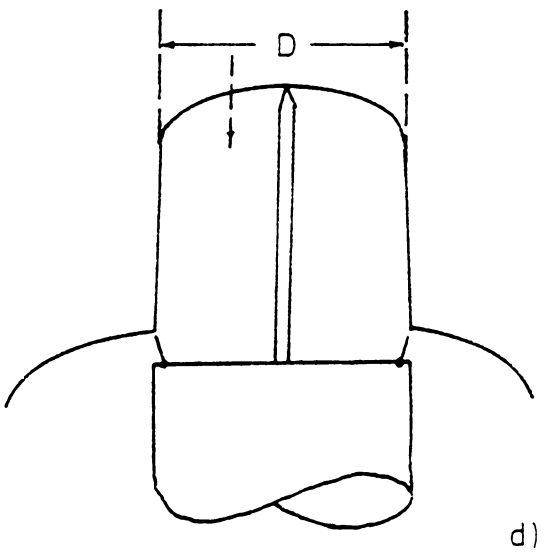

FIG. 72 THE CAPTURE AREA (CONCLUDED)

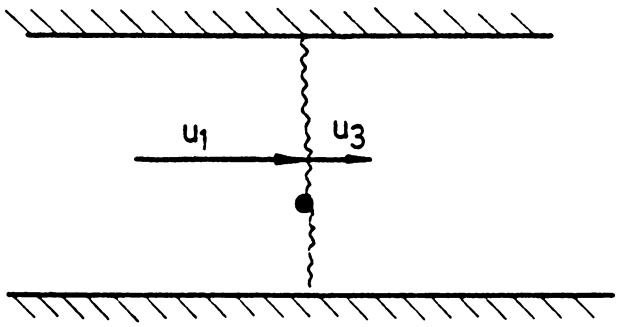

a) $U_S = 0$

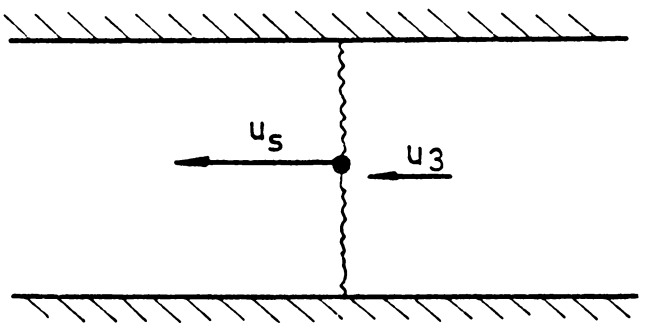

b) $U_S \neq 0$

$U_1 = 0$

FIG. 73 NORMAL SHOCK VELOCITIES

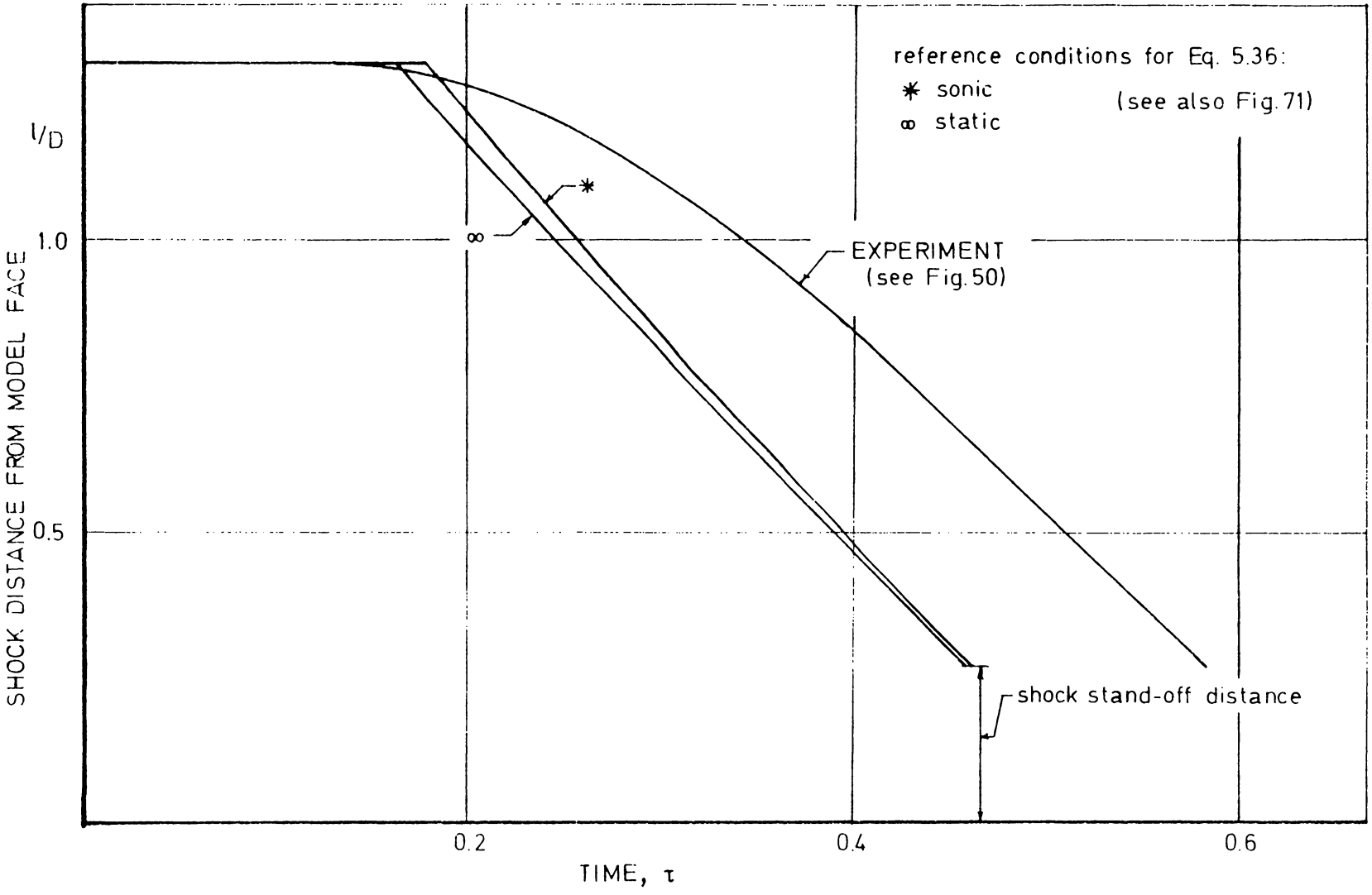

FIG. 74 A COMPARISON OF THE EXPERIMENTAL AND THEORETICAL SHOCK COLLAPSE HISTORIES

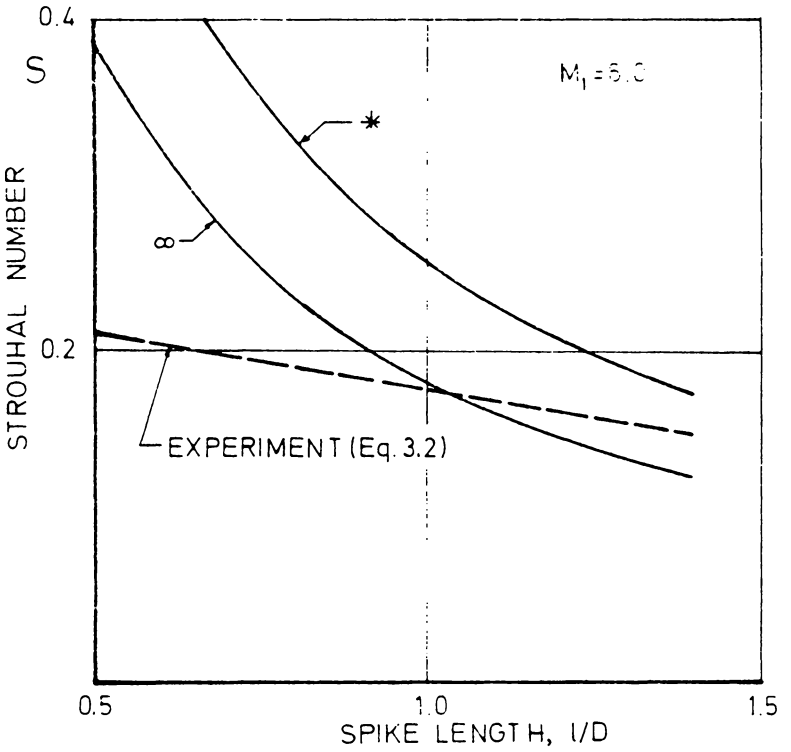

(See Fig. 74 for key to symbols)

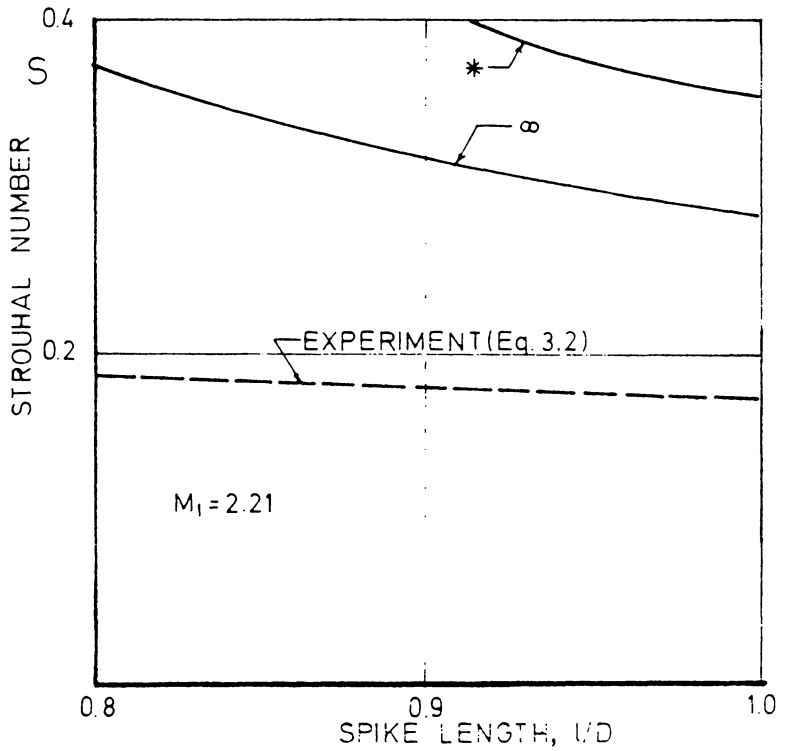

FIG. 75 A COMPARISON OF THE EXPERIMENTAL AND THEORETICAL FREQUENCY OF PULSATION

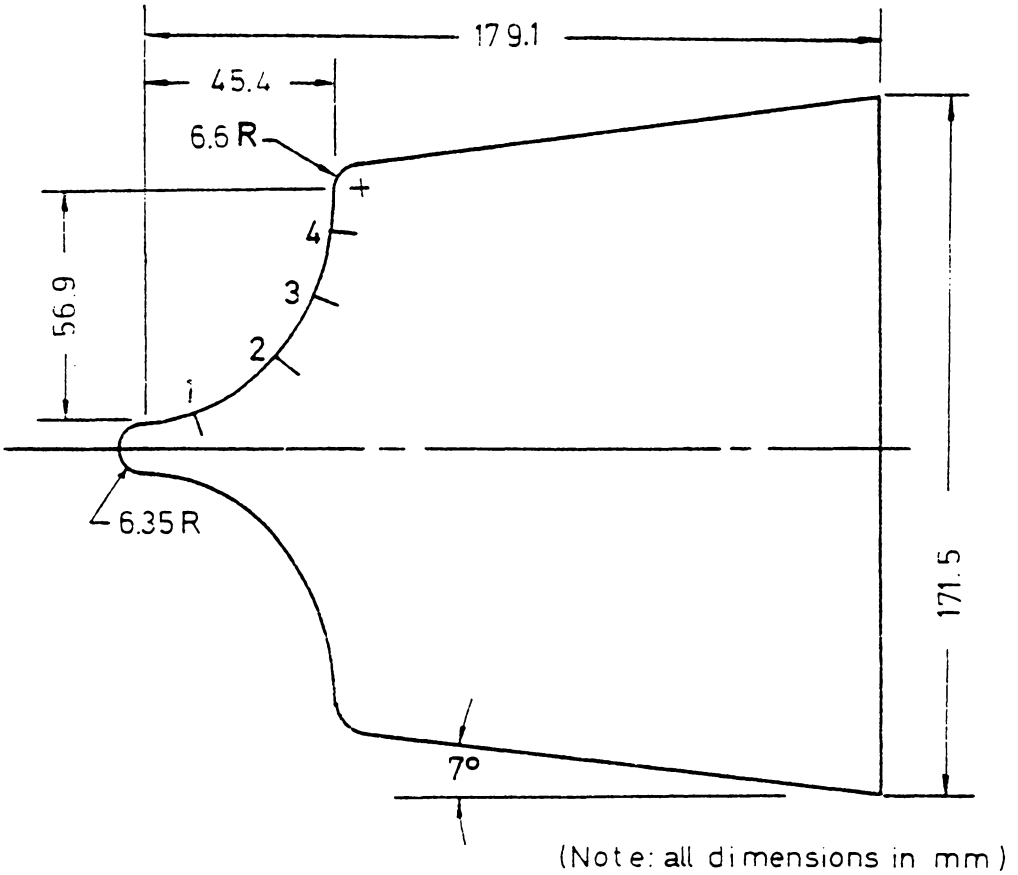

FIG. 76 AEROTHERM ELLIPTICAL TRICONIC MODEL

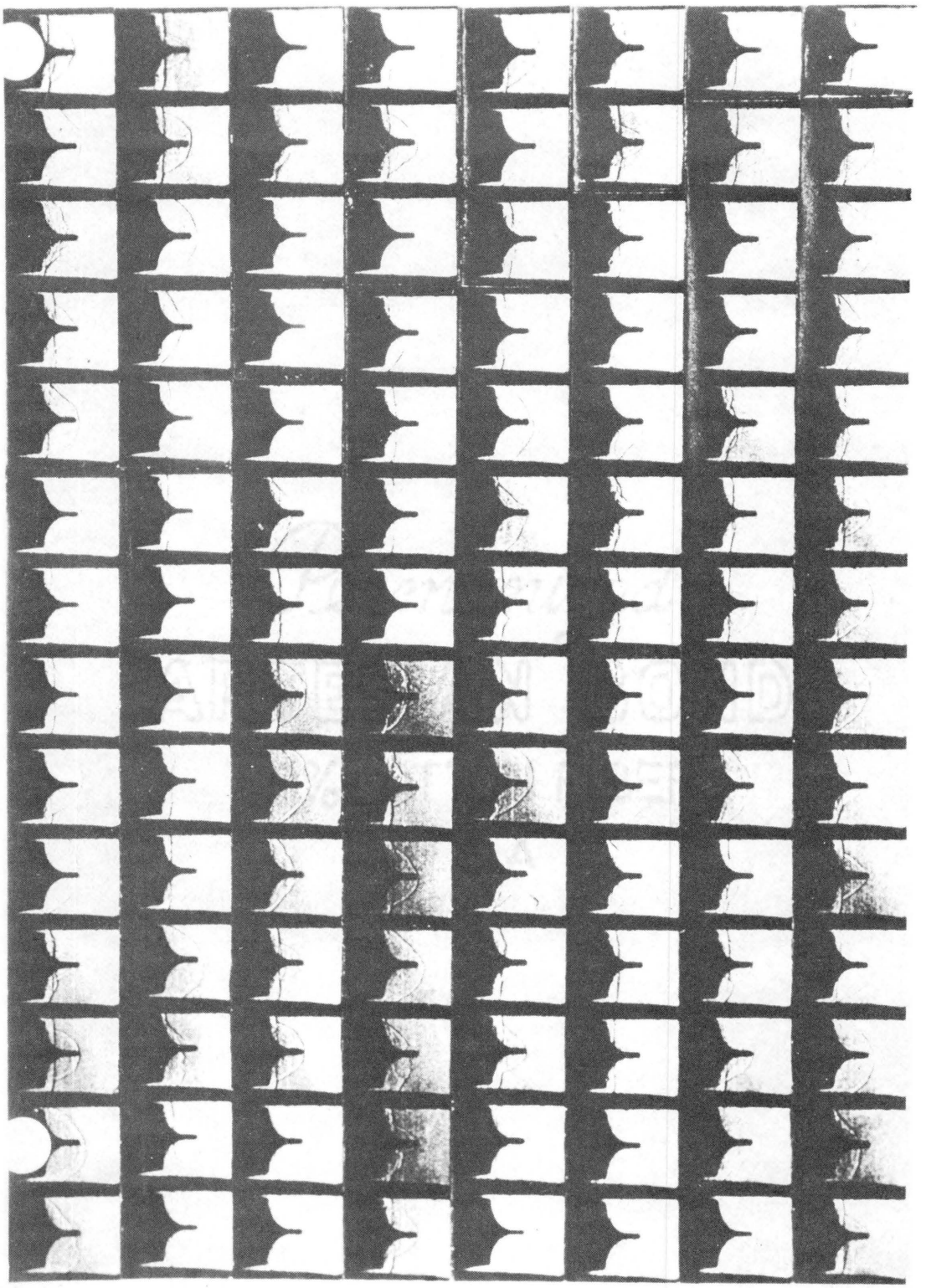

FIGURE 77 SIGH SPEED FILM OF THE ABLATION MODEL

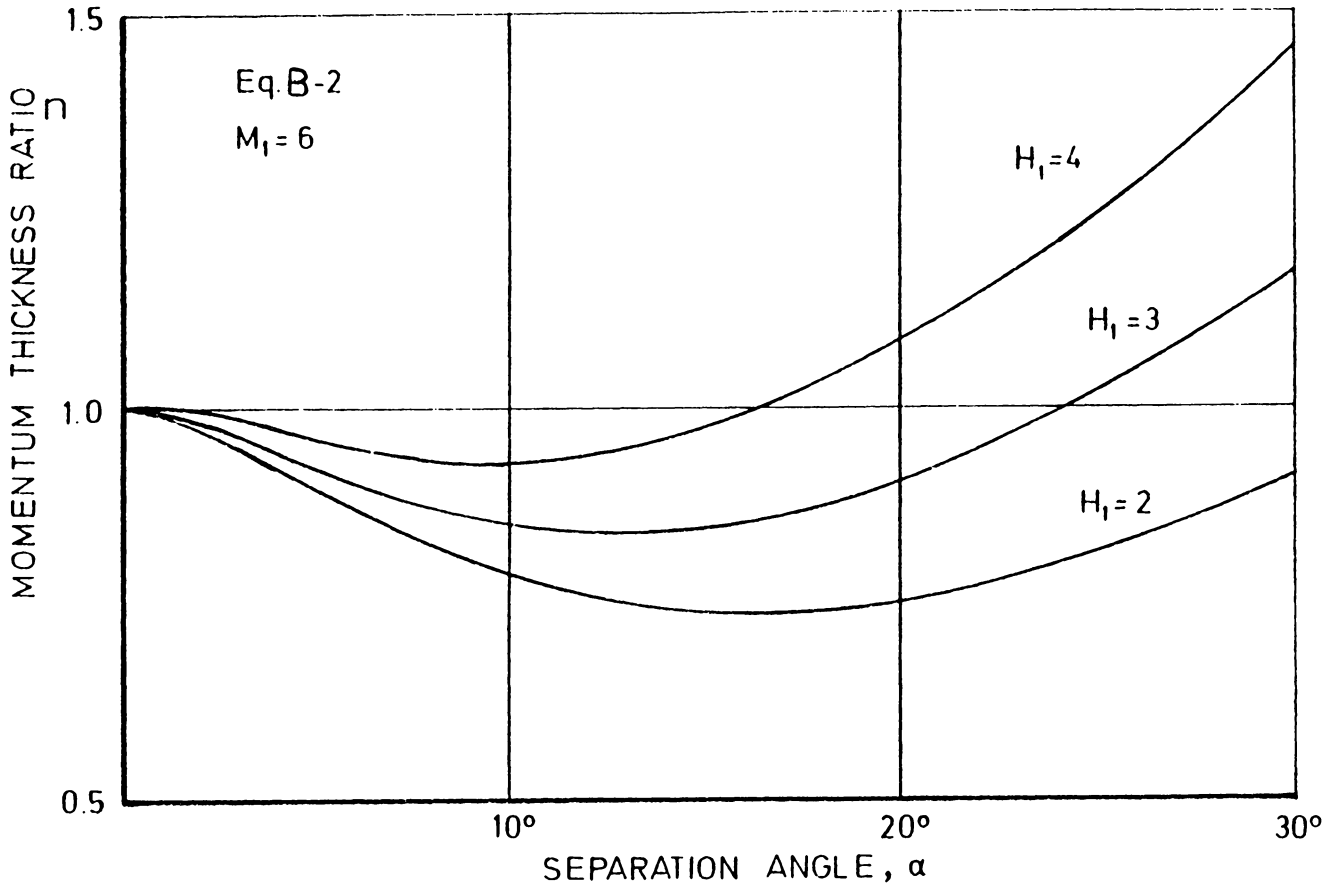

FIG. 78 THE RATIO OF MOMENTUM THICKNESSES

The vita has been removed from the scanned document

A STUDY OF UNSTABLE AXISYMMETRIC SEPARATION IN HIGH SPEED FLOWS

by

Michael Allen Kenworthy

(ABSTRACT)

A study of unstable axisymmetric separation was conducted using spiked cones in flows with free stream Mach numbers, M, of 6.0 and 2.21. Reynolds numbers based on the model diameter, Re_D, were 0.13×10^6 and 0.9×10^6 at M = 6.0 and 0.05×10^6 and 0.12×10^6 at M = 2.21. The body cone half angle, Φ_D, for the range $30° \leq \Phi_D \leq 90°$, and non-dimensional spike length, ℓ/D, up to $\ell/D = 3$ were varied in small increments. Pressure measurements made on the model face using fast response instrumentation showed the pressure to exhibit a regular or periodic wave form. These wave forms were analyzed in terms of the time averaged frequency, f, and amplitude, Δp.

Based on these pressure measurements synchronized with spark photographs of the flow, two distinct modes of unstable axisymmetric flow were observed namely, oscillation and pulsation. Both modes showed the non-dimensional frequency to decrease as ℓ/D was increased indepndent of Φ_D, Re_D, and M. The amplitude, Δp was found to be a strong frunction of ℓ/D, Φ_D, Re_D and M. However, the maximum Δp

of the oscillation mode was one tenth that of the pulsation mode which was of the order of magnitude of the pitot pressure.

To provide further information on which a theoretical analysis could be based specialized experiments were carried out on specific models. These techniques included thin film gauges and a high speed ciné in the streak mode.

These data were then examined with the purpose of establishing the mechanisms of the modes of unstable flow. An original hypothesis was developed for the oscillation mode based on a viscous mechanism. Comparison with experiment was made which showed this hypothesis to be a sound physical model. The pulsation mode was similarly treated revealing this mechanism to be of an inviscid nature.

Finally, the results of this study were used to predict the unstable flow parameters of an idealized ablation model of current practical interest. A comparison of this with experiment shows the results of the present study to provide a useful engineering guideline.

M. A. Kenworthy